

UNIVERSITY OF LIVERPOOL



UNIVERSITY OF
LIVERPOOL

Local Interaction Region Coupling
Correction for the LHC

Submitted by:
Félix SOUBELET

Supervised by:
Dr. Tobias PERSSON
Dr. Rogelio TOMÁS
Dr. Ozgur APSIMON
Prof. Carsten WELSCH

Thesis submitted in accordance with the requirements of the
University of Liverpool, School of Physical Sciences
for the degree of Doctor in Philosophy

October 22, 2023

Declaration of Authorship

I, Félix SOUBELET, declare that this thesis and the work presented in it are my own, done while in candidature for a doctorate degree. This thesis was not used, in whole or in part, to achieve an academic degree. No external sources were used without declaration in the text: any thoughts from others or literal quotations are clearly marked and where I have quoted from the work of others, the source is always given. Except for such quotations, this thesis is entirely my own work.

Several studies and results presented in this document have already been published, either in proceedings of the [International Particle Accelerator Conference \(IPAC\)](#) or as a peer-reviewed article in [Physical Review Accelerators and Beams \(PRAB\)](#), and a summary of these references is given below.

The following articles report on work that was included in this thesis:

[1]: F. Soubelet *et al.*, "Prospects for Local Interaction Region Coupling Correction at the LHC in Run 3", in Proceedings of 12th Int. Particle Accelerator Conf. (IPAC'21), Campinas, Brazil, MOPAB007, 2021.

[2]: F. Soubelet *et al.*, "First Interaction Region Local Coupling Corrections in the LHC Run 3", in Proceedings of 13th Int. Particle Accelerator Conf. (IPAC'22), Bangkok, Thailand, WEPOPT007, 2022.

[3]: F. Soubelet *et al.*, "Supervised Machine Learning for Local Coupling Sources Detection in the LHC", in Proceedings of 13th Int. Particle Accelerator Conf. (IPAC'22), Bangkok, Thailand, WEPOPT008, 2022.

[4]: F. Soubelet *et al.*, "Rigid Waist Shift: A New Method for Local Coupling Corrections in the LHC Interaction Regions", *Phys. Rev. ST Accel. Beams* 26, 2023.

[5]: F. Soubelet *et al.*, "Prospect of Operating with Limited Skew Quadrupole Corrector Availability in the LHC Interaction Regions", in Proceedings of 14th Int. Particle Accelerator Conf. (IPAC'23), Venice, Italy, MOPL044, 2023.

The following articles are studies that were contributed to by myself but are not included in this thesis:

[6]: F. Carlier *et al.*, "LHC Run 2 Optics Commissioning Experience in View of HL-LHC", in Proceedings of 10th Int. Particle Accelerator Conf. (IPAC'19), Melbourne, Australia, MOPMP033, 2019.

- [7]: R. Tracey *et al.*, "AI-Driven Holistic Approach to Energy Efficient HPC", in ISC High Performance 2020: High Performance Computing, pp 267-279, 2020.
- [8]: I. Béjar Alonso *et al.*, "High-Luminosity Large Hadron Collider (HL-LHC): Technical Design Report", in CERN Yellow Reports: Monographs, 2020.
- [9]: T. Persson *et al.*, "Optics Correction Strategy for Run 3 of the LHC", in Proceedings of 12th Int. Particle Accelerator Conf. (IPAC'21), Campinas, Brazil, WEPAB027, 2021.
- [10]: E. Maclean *et al.*, "Optics Measurement by Excitation of Betatron Oscillations in the CERN PSB", in Proceedings of 12th Int. Particle Accelerator Conf. (IPAC'21), Campinas, Brazil, THPAB168, 2021.
- [11]: T. Persson *et al.*, "Optics Measurements and Correction Plans for the HL-LHC", in Proceedings of 12th Int. Particle Accelerator Conf. (IPAC'21), Campinas, Brazil, WEPAB026, 2021.
- [12]: X. Buffat *et al.*, "Optics Measurement and Correction Strategies for HL-LHC", in CERN ATS Notes, 2022.
- [13]: T. Persson *et al.*, "Optics Correction Strategy for Run 3 of the LHC", in Proceedings of 13th Int. Particle Accelerator Conf. (IPAC'22), Bangkok, Thailand, WEPOST008, 2022.
- [14]: E. Fol *et al.*, "Experimental Demonstration of Machine Learning Application in LHC Optics Commissioning", in Proceedings of 13th Int. Particle Accelerator Conf. (IPAC'22), Bangkok, Thailand, MOPOPT047, 2022.
- [15]: F. Carlier *et al.*, "Challenges of k-Modulation Measurements in the LHC Run 3", in Proceedings of 14th Int. Particle Accelerator Conf. (IPAC'23), Venice, Italy, MOPL014, 2023.
- [16]: F. Carlier *et al.*, "LHC Run 3 Optics Correction", in Proceedings of 14th Int. Particle Accelerator Conf. (IPAC'23), Venice, Italy, MOPL015, 2023.
- [17]: J. Dilly *et al.*, "First Operational Dodecapole Correction in the LHC", Phys. Rev. ST Accel. Beams 26, 2023.

UNIVERSITY OF LIVERPOOL

*Abstract*CERN
School of Physical Sciences

Doctor of Philosophy

Local Interaction Region Coupling Correction for the LHC

by Félix SOUBELET

In order to further expand our knowledge of the structure of matter and the workings of our universe, scientists are constantly seeking to collide particles at ever-increasing energies and with higher [luminosity](#). So is the task of the [Large Hadron Collider \(LHC\)](#) at [CERN](#), the highest energy particle accelerator and collider to date, and the goal of its future upgrade into the [High-Luminosity Large Hadron Collider \(HL-LHC\)](#). This constant progress in performance requires more intense beams and smaller beam sizes at collisions points as well as a tight control of these parameters. Thus, successful operation of large-scale particle colliders heavily depends on the precise correction of magnet field or alignment errors present in the machine.

In the [LHC](#), transverse [betatron coupling](#) has been shown to have a significant impact on both the beam dynamics and luminosity production due to uncompensated sources close to the [Interaction Points \(IPs\)](#). However, current measurement methods are not sufficient for precise local coupling measurement at the [IP](#), and the impact of these sources has so far been left uncompensated. This thesis covers work done in an effort to determine and correct [Interaction Region \(IR\)](#) local coupling.

A key tool presented in this document is the designed [Rigid Waist Shift \(RWS\)](#), a new optics configuration which allows the determination of local coupling corrections based on correlated global variables such as the closest tune approach $|C^-|$. The validity of this new method has been demonstrated through simulations and experimental measurements taken during the [LHC Run 3](#) commissioning in 2022, where determined corrections were applied and led to a measured luminosity increase of 9.7% and 3.5% at the [ATLAS](#) and [CMS](#) detectors, respectively. Additionally, the application of machine learning techniques for high complexity problems such as the detection of coupling sources in the [LHC](#) has been explored, yielding promising results but requiring some more improvements to be operationally viable. Finally, optics studies which revealed avenues for improvements in the optics measurements done at the LHC are also presented.

Acknowledgements

Now that the main results of several years of work have been summarized in this little document and, as this writing comes to an end, it is time to look back and thank the many people that have contributed and supported me along the way.

First and foremost, I wish to thank Tobias Persson with all my heart for his kind supervision and unwavering support during those years. I consider this PhD to be divided into a before and an after, and you to be the turning point. I can never thank you enough for your patience, advice, guidance, encouragements and enthusiasm, without which I know I would not have crossed the finish line. My heartfelt thanks go to Rogelio Tomás as well for keeping my best interest in mind, and for your continuous help and wise feedback throughout.

A few special people now need to be thanked here. They have all, each in their own way, significantly contributed to helping me through this long journey.

A big thanks to Joschua Dilly for your enthusiasm for programming, "clean code" and scientific computing. Thanks for the reviews, for the late night pull requests, the scientific discussions, the coffees, the control room banter and for your L^AT_EX black magic knowledge. This document would not have looked as good without you.

To Félix Carlier, or "Félix number 1", thank you for taking the time to explain so much of the non-linear dynamics theory to me, and for providing advice on the writing of this document. Your thesis, that you so kindly gave me a physical copy of, has been a great source of inspiration and has set a high standard of quality.

Thank you to Michael Hofer for the countless questions you have answered, for being the first to guide me through the perilous land of Resonance Driving Terms, and for being such an encyclopedia of knowledge and Indico links.

To Elena Fol, thank you for showing me how to teach the machines, for the coffee talks and for being such a little ray of sunshine every day (except when it's cold).

To Axel Poyet, thank you for being you and being there every step of the way, from close and afar. Thanks for the friendship, the help, the jokes, the sarcasm, the shared struggle and all of the silliest moments: it has been great.

Thank you to Konstantinos Paraschou for being a great flatmate through part of this journey, and getting through the pandemic lockdowns with me: shared mental breakdowns are strangely cathartic. As you already (don't) know, "book boom".

Thanks also go to my family for their support, patience and encouragements.

Many other people - so many, actually - have contributed one way or another to this adventure, and a few group mentions are in order.

My thanks go to all the past and current members of the OMC team for the great work environment of this group, and for their cheerful company during all these hours - mostly nights and weekends - spent in the control room. I am equally grateful to the LHC Operations team for their collaboration, for accepting me in their midst for a short time, and in particular to Michi Hostettler for being such a source of knowledge

and always eager to provide help and advice. Similar thanks go to the wonderful folks at the IBM Hartree center for taking me in during my placement, especially Vadim Elisseev and Rob Tracey for their close supervision.

Many thanks to some special teachers who have played a bigger part than they know turning me into the scientist I am today: Mr. Bourquard for fostering my curiosity in all things physics-related, and Mr. Beck for helping me find - at my own speed - the beauty in mathematics. Thank you to Jonathan Ferreira for the passionate and passionating plasma lectures, Alexis Nuttin for equally great neutronics classes; and Elsa Merle-Lucotte for the degree of her involvement helping students find their way.

To all the people I have walked the PhD road with - Thibault, Marie, Eva, Mathilde, Anaïs, Floriane, Guillaume, Mathieu, Nico, Elsa, Élisabeth, Diane, Pauline, Laurène, Émilien, Marouane, Luis and many more - a thousand thanks for your comradeship and the myriad of great moments we have shared. I wish you to find success and happiness in your journey, wherever it may take you.

As a final word, a big "thank you!" to all scientists who have advanced this beautiful field of physics, have led to the design, creation and operation of the LHC, and overall have made my PhD possible. As was put so well into words by Sir Isaac Newton: "If I have seen further, it is by standing on the shoulders of giants."

“Everything always breaks...”

Tobias Persson.

Contents

Glossary	xiii
Nomenclature	xiii
Acronyms	xv
Symbols	xvi
List of Figures	xix
List of Tables	xxvii
1 Introduction	1
1.1 Motivations	1
1.2 Thesis Outline	2
2 Relevant Theory of Beam Dynamics	5
2.1 Linear Beam Dynamics	5
2.2 Non-Linear Magnetic Multipoles	14
2.3 Non-Linear Formalism and Resonance Driving Terms	16
2.4 Betatron Coupling	22
2.5 Luminosity	27
3 Optics Measurements and Corrections at the LHC	31
3.1 The LHC Lattice	32
3.2 The Operational Cycle of the LHC	42
3.3 Optics Measurements and Corrections	43
4 Interaction Region Local Coupling Correction in the LHC	57
4.1 Local Betatron Coupling in the LHC Interaction Regions	57
4.2 Current Correction Methods and Their Limitations	61
4.3 The Colinearity Knob	65
4.4 Rigid Waist Shift for Local Coupling Correction	67
4.5 Local Coupling Correction in the LHC 2022 Commissioning	80
4.6 Relevance to Other Colliders	92
4.7 Operation with Limited Correctors Availability	95
4.8 Summary	104
5 Machine Learning for Interaction Region Local Coupling	107
5.1 Relevant Concepts of Machine Learning	107
5.2 Identification of Local Coupling Sources	111
5.3 Summary	119

6	Optics Studies	121
6.1	Phase Error Dependency on BPM Type and Location	121
6.2	Simulations of Sextupolar Amplitude Detuning in the LHC	129
6.3	Summary	132
7	Conclusion	135
	Appendices	138
A	Thin Kick Hamiltonian Derivation	139
A.1	Multinomial Expansion	139
A.2	Hamiltonian Derivation	140
B	Element Naming Conventions in the LHC	143
C	Experimental Knobs Designed for the LHC	147
C.1	Definitions of the Colinearity Knobs	147
C.2	Definitions of the Rigid Waist Shift Knobs	147
C.3	Definitions of the Optics Rematching Knobs	148
D	Negative Rigid Waist Shift Measurements	151
E	List of LHC Fills Used for Measurements	155
E.1	Fills Used During the LHC Run 2	155
E.2	Fills Used During the 2021 Beam Tests	155
E.3	Fills Used During the LHC Run 3 2022 Commissioning	156
E.4	Fills Used During the LHC 2022 Physics Run	156
F	Software Developments	157
	Bibliography	159

Glossary

Nomenclature

AC Dipole Dipole magnet attached to an AC power source with variable frequency and strength, allowing the imposition of forced oscillations on the [beam](#). See [Section 3.3.1](#).

ALICE (A Large Ion Collider Experiment) An [experiment](#) optimized to study heavy-ion collisions at the [Large Hadron Collider \(LHC\)](#) .

Amplitude detuning Tune change with the transversal amplitude of a particle. See [Section 2.3.5](#).

ATLAS (A Toroidal LHC Apparatus) One of two general purpose detectors at the [LHC](#). It investigates a wide range of physics, from the search for the Higgs boson to extra dimensions and particles that could make up dark matter. Although it has the same scientific goals as the [CMS experiment](#), it uses different technical solutions and a different magnet-system design .

Beam Short for "Particle Beam". The name for the collection of all particles in an accelerator traveling in the same direction. In the [Large Hadron Collider \(LHC\)](#) there are two beams (Beam 1 and Beam 2) traversing in opposite directions and colliding at the [Interaction Points \(IPs\)](#).

Beta-beating Relative difference of the [\$\beta\$ -functions](#) between measurement and model: $(\beta_{\text{measured}} - \beta_{\text{model}})/\beta_{\text{model}}$. It is a good indicator of the quality of the linear optics. See [Section 3.3](#).

Beta-function Value of the [Twiss parameters](#) β as a function of longitudinal location. This value is closely related to the amplitude \mathcal{A} of the betatron-oscillations and hence the size of the [beam](#) at that location via the [action \$J\$](#) by $\mathcal{A} = \sqrt{2J\beta}$.

Betatron coupling Coupling between the horizontal and vertical transverse motion of a particle. Common sources of coupling are [skew](#) quadrupoles and solenoids. See [Section 2.4](#).

Closed Orbit The orbit of a particle with reference momentum, sometimes also called "reference orbit" or "ideal orbit". See [Section 2.1.1](#).

CMS (Compact Muon Solenoid) One of two general purpose detectors at the [LHC](#). It investigates a wide range of physics, from the search for the Higgs boson to extra dimensions and particles that could make up dark matter. Although it has the same scientific goals as the [ATLAS experiment](#), it uses different technical solutions and a different magnet-system design .

Courant-Snyder Parameters Set of quantities describing the distribution of positions and momenta of the particles in a [beam](#). Also known as [Twiss parameters](#). See for instance the [\$\beta\$ -function](#).

Experiment In the context of the [LHC](#), an "experiment" denotes one of the particle physics detector experiments and its accompanying data-collecting research structure. The four largest detectors, [ATLAS](#), [CMS](#), [ALICE](#), [LHCb](#) are located at the four colliding [IPs](#) of the [LHC](#).

Feed-down Particles passing off-center through a multipole field experience effects akin to the influence of lower-order multipoles due to the orbit offset.

Flat optics [Optics](#) in which the β^* is different for both transverse planes, usually much smaller in one than in the other. See also [round optics](#).

Hadron Composite subatomic particles consisting of two or more quarks, held together by strong interactions.

IP (Interaction Point) The specific point at which the two counter-rotating [beams](#) interact, i.e. their particles collide. In the [LHC](#) these are located in the center of [Insertion Regions \(IRs\)](#) 1, 2, 5 and 8 inside the detectors, or [experiments](#) .

IR (Insertion Region) Straight section between the arcs of a synchrotron, housing larger facilities such as detectors ([experiments](#)), acceleration ([RF](#)), etc. In this document the shorthand IR mostly refers to an "Interaction Region", a.k.a. an Insertion Region hosting an [IP](#) where [beams](#) are made to collide .

Knob A group setting of magnets powerings to be changed together.

LHCb (LHC-beauty) A specialized b-physics [experiment](#), designed primarily to measure the parameters of CP violation in the interactions of b-[hadron](#), heavy particles containing a bottom quark .

Long Shutdown Planned shutdown periods of the [LHC](#) between [Runs](#) spanning multiple years, as opposed to the [Year-End Technical Stop \(YETS\)](#), which only lasts a few months. This time is used for repairs and upgrades of the machine, as well as general maintenance.

Luminosity The ratio of the number of events, i.e. collisions, detected per cross section, either per time interval ("instantaneous luminosity") or in total ("integrated luminosity", e.g. since the beginning of a year, a [run](#) or of operation). See [Section 2.5](#).

MAD-X Current version of the [Methodical Accelerator Design \(MAD\)](#) framework developed in [BE-ABP](#) at [CERN](#).

MD (Machine Development) Studies dedicated to understanding and improving the machine, e.g. by trying to reveal error-sources or attempting their correction, or testing possible future procedures and machine configurations. They usually involve [beam-time](#), i.e. measurements in the [CERN Control Center \(CCC\)](#) .

Normal magnets Magnet with a "normal" oriented multipole field with pole-tips off the horizontal axis. Opposed to a [skew](#) magnet of the same order n , for which the field is rotated by $\pi/(2n)$ rad.

Optics Refers to accelerator [beam](#) optics, describing the particle motion through an accelerator as defined by the elements (i.e. magnets) of the machine. As the behaviour of a particle beam in magnetic fields shows similarities to a light beam propagating through lenses and can be described with similar equations, a lot of theory and nomenclature has been borrowed from ray optics.

RF (Radio Frequency) Shorthand for the acceleration part of a synchrotron, as the frequency of the accelerating electric field is usually in the radio-frequency range (at the [LHC](#) ≈ 400 MHz) .

Round optics [Optics](#) in which the β^* is identical for both planes. See also: [flat optics](#).

Run Consecutive years of [LHC](#) operation, separated by long shutdowns. [Run 1](#) has taken place from 2008 to 2013, [Run 2](#) from 2015 to 2018 and [Run 3](#) started in 2022.

RWS (Rigid Waist Shift) A specific perturbation of the optics in an [IR](#) that moves all four betatron waists of the beam simultaneously. See [Section 4.4](#) .

Skew magnets Magnet with a "skew" oriented multipole field, with pole-tips on the horizontal axis. Opposed to a [normal](#) magnet of the same order n , for which the field is rotated by $\pi/(2n)$ rad.

Synchronous particle The ideal particle that defines the reference trajectory in a circular accelerator. See [Section 2.1.1](#).

Trim A trim refers to powering adjustments of a given electrical circuit powering one or several magnets in series or according to a given scheme.

Tune Number of betatron oscillations per turn in a circular accelerator. See also: [\$\beta\$ -function](#).

Twiss Parameters See [Courant-Snyder Parameters](#).

Acronyms

ABP Accelerator and Beam Physics group at [CERN](#).

ALICE [A Large Ion Collider Experiment](#).

ATLAS [A Toroidal LHC Apparatus](#).

ATS Achromatic Telescopic Squeeze.

BBQ Base Band Tune.

BE Beams Department.

BPM Beam Position Monitor.

CCC CERN Control Center.

CERN European Organization for Nuclear Research.

CMS [Compact Muon Solenoid](#).

FCC Future Circular Collider.

HEP High Energy Physics.

HL-LHC High-Luminosity Large Hadron Collider.

IP [Interaction Point](#).

IPAC International Particle Accelerator Conference.

IR [Insertion Region](#).

LHC Large Hadron Collider.

LHCb [LHC-beauty](#).

LINAC Linear Accelerator.

LIV.DAT Liverpool Big Data Science Center for Doctoral Training.

LSA LHC Software Architecture.

MAD Methodical Accelerator Design.

MD [Machine Development](#).

OMC Optics Measurements and Corrections.

PRAB Physical Review Accelerators and Beams.

PS Proton Synchrotron.

PSB PS Booster.

PTC Polymorphic Tracking Code.

RDT Resonance Driving Term.

RF [Radio Frequency](#).

RWS [Rigid Waist Shift](#).

SPS Super Proton Synchrotron.

SVD Singular Value Decomposition.

YETS Year-End Technical Stop.

Symbols

- J** Action. One of the phase space coordinates in the Courant-Snyder normalization and closely related to the invariant of (linear) motion $\varepsilon = 2J$. Usually subscripted with x or y giving the transversal plane. Unit: m.
- $B\rho$** Magnetic rigidity. Used as a normalization factor for [normal magnetic field strength](#) and [skew magnetic field strength](#). Unit: T m.
- β^* The [\$\beta\$ -function](#) at the [IP](#). Usually subscripted with x or y giving the transversal plane. Unit: m.
- $|C^-|$ The minimum tune separation. It is a quantification of the amount of global linear coupling in the machine. Dimensionless.
- J_n** Skew magnetic field strength. Skew field component normalized to the [magnetic rigidity](#). Usually subscripted with an integer n giving the field order. Unit: m^{-n} .
- K_n** Normal magnetic field strength. Normal field component normalized to the [magnetic rigidity](#). Usually subscripted with an integer n giving the field order. Unit: m^{-n} .

List of Figures


2.1	The Frenet-Serret coordinate system used in accelerator physics. Here \hat{x} , \hat{y} , and \hat{s} form the right-handed orthogonal basis, while ρ is the local bending radius.	6
2.2	Illustration of a design reference orbit (blue), a closed orbit (orange) and a single turn particle trajectory (red).	7
2.3	Schematic of a FODO cell. A focusing quadrupole is denoted with an F while a defocusing one is denoted with a D.	7
2.4	Magnetic fields in an LHC dipole and quadrupole, with a $\cos(\theta)$ and $\cos(2\theta)$ current distribution in the circular coil, respectively. Currents in the dipole and quadrupole coils are indicated in color. These visuals were taken from [35].	8
2.5	Phase space ellipse in the transverse (z, p_z) plane, where z represents either transverse coordinate x or y	12
2.6	Illustrative representation of phase-space in physical coordinates (left) and normalized, or Courant-Snyder, coordinates (right) for an accelerator with linear elements only. Courtesy of F. Carlier [41].	13
2.7	Phase space in normalized coordinates from tracking 200 particles in a simple FODO-based lattice, when exciting a third order resonance. Points of each color corresponds to the trajectory of a given particle.	17
2.8	Illustrative exaggerated representations of phase space in the three different coordinate systems: physical (left), normalized (middle) and normal form (right) coordinates. Courtesy of F. Carlier [41].	18
2.9	Tunes diagram showing resonance lines up to order $n = 5$. The LHC working points are indicated by the two dots: in blue for injection tunes and red for collision tunes.	19
2.10	Illustration of the coordinate transformations and change of the one-turn map. This diagram reads from Courant-Snyder coordinates at turn N in the top left, and shows both paths to reach the Courant-Snyder coordinates at turn $N + 1$ in the top right.	21
2.11	Illustration of a normal (left) and skew (right) magnetic quadrupole and their magnetic field lines.	22
2.12	Illustration of coupled and uncoupled fractional tunes versus the uncoupled tune split. Courtesy of J. Keintzel [67].	26
3.1	The CERN Accelerator Complex in 2022, not to scale [71]. For typical LHC operation, a proton beam is produced in LINAC4 and follows the chain: LINAC4 \rightarrow PSB \rightarrow PS \rightarrow SPS \rightarrow LHC.	31
3.2	Schematic of the LHC layout, adapted from [102].	32
3.3	Schematic of an LHC arc cell [103].	33

3.4	Simplified layout (top) and optics functions (bottom) of an LHC arc cell for the $\beta^* = 30$ cm optics.	34
3.5	Simplified layout (top) and optics functions (bottom) of the LHC arc23 for the $\beta^* = 30$ cm optics.	35
3.6	The horizontal and vertical β -functions in the LHC around IP5 at injection optics (top) and collision optics (bottom). Notice the drastically different scales on the vertical axes.	36
3.7	The simplified element layout (top) and β -functions (bottom) in the close vicinity of IP5 at $\beta^* = 30$ cm collision optics, without crossing angles.	37
3.8	Layout of the triplet magnets and the linear and non-linear correctors in the LHC experimental insertions [110], showing common aperture magnets. The skew quadrupole correctors correspond to order a_2 and are located in the C2 package.	38
3.9	Crossing schemes for IR1 and IR5 at collision optics.	39
3.10	Simplified layout and optics functions in the dispersion suppressor leading beam 1 to IP5, for the $\beta^* = 30$ cm optics.	40
3.11	Simplified layout and optics functions in the matching section and dispersion suppressor leading beam 1 to IP5, for the $\beta^* = 30$ cm optics.	40
3.12	The β -functions in sectors 45 and 56 at different points in the squeeze for the 2022 optics: at the end of the pre-squeeze (top) and at the end of the tele-squeeze (bottom).	41
3.13	Simplified illustration of the LHC nominal cycle.	42
3.14	The measured β -beating at the beginning (blue) and end (orange) of the LHC 2022 commissioning, for beam 2.	44
3.15	Comparison of turn-by-turn data obtained from a single free kick (top) and an AC dipole excitation (bottom).	46
3.16	Resulting vertical β -functions in a FODO lattice in the case of free (orange) and driven (blue) oscillations.	47
3.17	AC dipole induced β -beating as a function of δ_D , for various phase advances between the AC dipole and a given location in the ring where the observation would be made. The results are shown for the horizontal (left) and vertical (right) planes with a common working point used for measurements.	48
3.18	Horizontal spectrum from the frequency analysis of a measurement taken during the Run 2 commissioning in 2022. The main (orange) and natural (green) tune lines are indicated, where for instance $(0, 1)$ corresponds to the $0 \cdot Q_x + 1 \cdot Q_y = Q_y$ tune in the horizontal spectrum.	49
3.19	The β -beatings obtained when reconstructing the β -functions from phase (blue) and from amplitude (orange) in an LHC measurement in 2022.	50
3.20	Example data from the k -modulation of the first quadrupole left of IP1. The top plot shows the quadrupole strength variation over time and the bottom plot the resulting horizontal (blue) and vertical (orange) tune variations.	51

3.21	Local phase correction in IR5 (vertical line indicates IP5) from the LHC 2022 commissioning at flat-top. The blue line shows the measured phase deviation from model values, while the orange line shows the effect of the reconstructed errors on the model. The green line shows the expected phase deviation after applying the correction.	55
3.22	Local coupling RDTs correction in IR2 (vertical line indicates IP2) from the LHC 2021 beam test. The blue line shows the measured RDTs, while the orange line shows the attempt at canceling the contribution at the edges of the segment with the two available correctors in the IR.	56
4.1	Amplitudes of the coupling RDTs (bottom) f_{1001} (blue) and f_{1010} (orange) from tilts in the triplet quadrupoles around IP1. The top plot shows the magnets' powering while the middle plot shows the assigned tilts in each element.	58
4.2	Relative values of the RMS beam size at IP1 (blue) as well as relative instantaneous luminosity (orange) for different strengths of a local coupling bump around the IP generated with skew quadrupoles, for the LHC (filled) and HL-LHC v1.5 (dashed) collision optics.	59
4.3	Relative deviation between beam sizes calculated from Ripken parameters according to Eq. (4.1) and from tracking a particle distribution, at an IP affected by coupling for the horizontal (blue) and vertical (orange) planes.	60
4.4	Transverse beam sizes at IP5 at 6.8 TeV and $\beta^* = 30$ cm with normalized emittances $\varepsilon_x = \varepsilon_y = 3.75 \mu\text{m}$ and for different strengths of a local coupling bump around the IP. The ellipses are reconstructed through the σ_{11} , σ_{13} and σ_{33} terms of the sigma matrix, obtained from MAD-X.	61
4.5	Similar looking coupling RDTs from two measurements (top and bottom) taken during the LHC 2022 commissioning. One scenario leads to a 20% instantaneous luminosity decrease at IP1 compared to the other.	62
4.6	Propagation of the measured $ f_{1001} $ and $ f_{1010} $ for beam 1 around IP1 (dashed vertical line), measured with two different correction settings. The 2022 measurement (orange) leads to a beam size smaller by 9.2% than the 2021 one (blue).	63
4.7	Reconstructed CRDT $ \hat{F}_{XY} $ around IP2 from measurements at $\beta^* = 50$ cm during a 2018 MD. The blue lines correspond to 2 measurements with the nominal optics, and orange lines correspond to 3 measurements with a local coupling bump implemented around IP2. The percentages indicate the strength of the AC dipole kicks.	64
4.8	Amplitude of the f_{1001} RDT in the vicinity of IP1 for various settings of the colinearity knob, in the absence (blue, orange and purple) and presence (red) of global coupling. The locations of the MQSX corrector magnets are highlighted as green vertical lines.	66
4.9	Simulated effect of the designed Rigid Waist Shift knob as defined in Table 4.2 on the $\beta^* = 30$ cm optics of 2022. The blue line represents the waist displacement from the design location. The orange and green lines represent, respectively, the horizontal and vertical β -function change at the IP as the waist is displaced.	68

4.10	Simulated effect of the designed RWS knob on the β -functions around IP1, with the $\beta^* = 30$ cm optics of 2022. The β -functions for both the horizontal (blue) and vertical (red) planes are shown for the nominal (full lines) and shifted waists (dashed lines) scenarios. An identical result is found for IP5.	69
4.11	Simulated β -beating induced across beam 1 in both the horizontal (blue) and vertical (orange) planes, from applying an RWS as defined in Table 4.2 at IP1. A 20 to 30% β -beating is observed through most of the machine, with (wanted) outliers close to IP1.	70
4.12	Simulated β -beating induced across the machine in the beam 1 horizontal plane from applying an RWS at IP1, before (blue) and after (orange) applying the optics rematching knob.	71
4.13	Simulated β -functions around IP1 when applying an RWS, before (full lines) and after (dashed lines) application of the rematching knobs, with the $\beta^* = 30$ cm optics of 2022.	72
4.14	Amplitudes of the linear coupling RDTs in the vicinity of IP1 under a coupling bump, with (red) and without (blue) an RWS. The vertical green lines represent the positions of the skew quadrupoles correctors (MQSX.3[RL]1) used to implement the coupling bump. A colinearity knob setting of 10 and a rigidity waist shift knob setting of 1 were used.	73
4.15	Impact of the colinearity knob on the global $ C^- $, calculated according to Eq. (2.73), with (blue) and without (orange) applying an RWS.	74
4.16	Resulting $ C^- $ (Eq. (2.73)) for various combinations of tilt error and colinearity knob settings, when applying an RWS.	75
4.17	Resulting beam size (Eq. (4.1)) increase for identical settings of tilt error and colinearity knob settings as Fig. 4.16, but without an RWS.	75
4.18	Resulting $ C^- $ under an RWS (orange) and IP1 beam size (Eq. (4.1)) without an RWS relative to the nominal scenario (blue), for various colinearity knob settings. The black dotted line represents the threshold of a 1% beam size increase from the nominal scenario.	76
4.19	Resulting $ C^- $ in simulations as done for Fig. 4.18, with (blue) and without (orange) local coupling sources in IR1.	77
4.20	Relative IP beam sizes when compared to the nominal scenario (blue) when inputting the local errors used in the study for Fig. 4.19 (orange) and after applying the suggested correction (green). The black dotted line represents the threshold of a 1% beam size increase from the nominal scenario.	78
4.21	Resulting simulated $ C^- $ under an RWS during a scan of the colinearity knob, for various implementations of global coupling in the machine. For each case a vertical dashed line highlights the location of the minimization point.	79
4.22	Propagation of the measured $ f_{1001} $ (blue) around IP5 (dashed grey line) and of the reconstructed values from the determined correction (orange), measured at 450 GeV and $\beta^* = 11$ m.	81
4.23	Propagation of the measured $\Re f_{1001}$ (blue) around IP1 (dashed grey line) and the reconstructed values from the determined correction (orange), measured at 6.8 TeV and $\beta^* = 30$ cm.	82

4.24	Propagation of the measured $\Im f_{1001}$ (blue) around IP1 (dashed grey line) and the reconstructed values from the determined correction (orange), measured at 6.8 TeV and $\beta^* = 30$ cm.	83
4.25	The beam 1 β -beating observed at 6.8 TeV and $\beta^* = 30$ cm for the corrected machine (yellow), from the implementation of the RWS in IR5 (blue) and after applying the optics re-matching knob (red). The highlighted area (orange) shows where magnetic elements are affected by the knobs.	85
4.26	Measurement scan done at IR1 for beam 1 (red) and simulations for the same setup (blue). The minima of both curves are highlighted by vertical dashed lines and the delta between the two, suggesting the remaining error to correct, is displayed on the graph.	86
4.27	Measurement scan done at IR1 for beam 2 (red) and simulations for the same setup (blue). The minima of both curves are highlighted by vertical dashed lines and the delta between the two, suggesting the remaining error to correct, is displayed on the graph.	86
4.28	Measurement scan done at IR5 for beam 1 (red) and simulations for the same setup (blue). The minima of both curves are highlighted by vertical dashed lines and the delta between the two, suggesting the remaining error to correct, is displayed on the graph.	87
4.29	Measurement scan done at IR5 for beam 2 (red) and simulations for the same setup (blue). The minima of both curves are highlighted by vertical dashed lines and the delta between the two, suggesting the remaining error to correct, is displayed on the graph.	87
4.30	Trim of the colinearity knob setting (blue) and observed IP1 instantaneous luminosity change (orange) at 6.8 TeV and $\beta^* = 30$ cm. The blue area highlights the trim values suggested by the RWS method, which varies for beam 1 and beam 2.	89
4.31	Trim of the colinearity knob setting (blue) and observed IP5 instantaneous luminosity change (orange) at 6.8 TeV and $\beta^* = 30$ cm. The blue area highlights the trim values suggested by the RWS method, which varies for beam 1 and beam 2.	90
4.32	Zoomed view of the colinearity knob setting (blue) and observed IP5 instantaneous luminosity change (orange) at 6.8 TeV and $\beta^* = 30$ cm. The blue area highlights the trim values suggested by the RWS method, which varies for beam 1 and beam 2.	90
4.33	The expected (lines) and observed (triangular markers) instantaneous luminosity changes at 6.8 TeV for the various optics in the LHC cycle, for IP1 (blue) and IP5 (orange). Vertical dashed lines indicate the $\beta^* = 30$ cm and $\beta^* = 42$ cm data points.	92
4.34	Phase advances relative to IP5 in the FCC-ee V22 lattice, in the Z operation mode at 45.6 GeV and $\beta^* = 10$ cm.	93
4.35	Simulated amplitude of coupling RDTs f_{1001} (blue) and f_{1010} (orange) from a 1 mrad tilt in the first Q1 quadrupoles around the FCC-ee's IP5.	94
4.36	Expected instantaneous luminosity reduction for various trims of the colinearity knob at IP1/IP5 for different β^* optics. Each line corresponds to the trim necessary to compensate for a specific corrector's powering.	96

4.37	Relative change in horizontal (blue) and vertical (orange) beam sizes from carrying over the correction of the MQSX left of IP1 to the MQSX right of IP1.	97
4.38	Magnets powering (top) and horizontal (middle) and vertical (bottom) aperture limitations around IP1, at $\beta^* = 30$ cm. The blue and red shaded areas represent, in each plane, the 3σ , 6σ and 11σ beam envelopes, from darkest to lightest respectively. The grey blocks represent the physical locations of various elements.	98
4.39	Instantaneous luminosity drop from correction carry-over to the right MQSX at IR1 at $\beta^* = 30$ cm. The vertical grey line indicates the nominal operating point after the RWS correction adjustments.	99
4.40	Instantaneous luminosity drop from correction carry-overs in both directions at IR5 at $\beta^* = 30$ cm. The vertical grey line indicates the nominal operating point after the RWS correction adjustments.	100
4.41	Integrated luminosity loss over a day for each missing MQSX and for two different baselines of instantaneous luminosity. Data is a courtesy of S. Kostoglou 	101
4.42	The amplitude of the coupling RDTs at IP1 for various tilts of the triplet quadrupole Q3 left of the IP, assuming a failure of the skew quadrupole corrector MQSX.3L1.	102
4.43	The amplitude of the coupling RDTs at IP5 for various tilts of the triplet quadrupole Q2 right of the IP, assuming a failure of the skew quadrupole corrector MQSX.3R5.	103
5.1	Three examples showcasing models approximating (blue) a true function (orange) after training on provided samples (dark blue). Of the three models one is too simple and underfits (left), one generalizes properly (middle), and one is too complex and overfits (right). This plot was reproduced from the <i>scikit-learn</i> documentation [223, 224].	110
5.2	Beam 1 (top) and Beam 2 (bottom) coupling RDTs f_{1001} (blue) and f_{1010} (orange) after the implementation of tilt errors in the independently powered IR quadrupoles Q1 to Q11 in IRs 1, 2, 5 and 8, for the 6.8 TeV and $\beta^* = 30$ cm optics.	112
5.3	Conceptual representation of the dataset generation and supervised model training. This diagram is heavily inspired from [216].	113
5.4	Standard deviation of the coupling RDTs at BPMs for Beam 1, from a batch of measurements taken on April 3, 2018. These data points were later divided into IR and arc BPMs to determine applied noise levels.	114
5.5	Normalized mean absolute error (top) and R^2 scores (bottom) of a ridge regressor on various datasets corresponding to different noise levels added to the coupling RDTs. The σ values indicated correspond to the standard deviation of the Gaussian noise distributions added to the coupling RDTs data.	116
5.6	Histograms of the true applied DPSI values (purple), the values predicted by the Ridge model (blue) and the deviations from the predictions to the true values (pink) for a noised sample in the test dataset ($\sigma_{\text{DPSI}} = 10^{-4}$ rad and $\sigma_{\text{Arcs,IRs}} = 10^{-5}$).	117

5.7	True assigned (blue) and predicted (orange) DPSI values with a ridge model for a given test dataset sample. Here the magnet names have been switched for numbers in order to improve clarity.	117
6.1	Distribution of BPM β -functions across the machine for the Run 2 measurements used. A small amount of BPMs located at much higher β are not shown on this plot.	122
6.2	Chi-square distribution of the squares of phase measurement errors for different BPM combinations, differentiated by the β -functions at the locations of the measuring BPMs. For this plot a BPM was considered "low" below $\beta = 100$ m, "high" above $\beta = 200$ m and "medium" in between.	123
6.3	Distribution of the phase measurement errors for different BPM combinations, differentiated by the β -functions at the locations of the measuring BPMs. For this plot a BPM was considered "low" below $\beta = 100$ m, "high" above $\beta = 200$ m and "medium" in between.	124
6.4	A randomly generated chi-square distribution (blue) with $k = 4$ degrees of freedom, and a numerically fit probability density function (orange). The determined mode (red) is indeed located at $k - 2 = 2$. Here 'df' (degrees of freedom), 'loc' (horizontal offset) and 'scale' (a scaling factor) are parameters determined during the fit. The horizontal axis is in units of σ^2	125
6.5	Phase error distributions for different BPM β combinations, between standard arc BPMs.	127
6.6	Computed standard deviations on phase advances between standard arc BPMs for the LHC Run 2 (2018, $\beta^* = 30$ cm) for different β -functions combinations of these BPMs.	128
6.7	Computed standard deviations on phase advances between <i>warm</i> type BPMs for the LHC Run 2 (2018, $\beta^* = 30$ cm) for different β -functions combinations of these BPMs. Empty slots correspond to β -functions ranges where no BPMs of this type are present.	128
6.8	Natural horizontal tune Q_x shift with horizontal free or forced action (J_x or A_x), in the case of free oscillations (blue) and driven motion with $\Delta Q_x = -0.01$ (red) and $\Delta Q_x = -0.005$ (orange).	131
6.9	Natural vertical tune Q_y shift with horizontal free or forced action (J_x or A_x), in the case of free oscillations (blue) and driven motion with $\Delta Q_x = -0.01$ (red) and $\Delta Q_x = -0.005$ (orange).	131
B.1	Naming scheme in a segment of the LHC [241].	143
D.1	Measurement scan with a negative RWS done at IR1 for beam 1 (red) and simulations for the same setup (blue).	151
D.2	Measurement scan with a negative RWS done at IR1 for beam 2 (red) and simulations for the same setup (blue).	152
D.3	Measurement scan with a negative RWS done at IR5 for beam 1 (red) and simulations for the same setup (blue).	153
D.4	Measurement scan with a negative RWS done at IR5 for beam 1 (red) and simulations for the same setup (blue).	153

List of Tables

3.1	Description and purpose of the straight sections in the LHC. Out of the experiments only the four major ones are mentioned.	35
3.2	Value of the $\beta_{x,y}^*$ at different IPs for different optics configurations as of Run 3.	37
4.1	Definition of one unit of the colinearity knob, a powering setting of the IR skew quadrupole correctors.	65
4.2	Definition of one unit of the rigid waist shift knob.	67
4.3	Values of the $\sqrt{\beta_x\beta_y}$ term in Eq. (4.5) at the MQSX magnets around IP1 or IP5 without (left) and with (right) the application of an RWS, with the $\beta^* = 30$ cm optics of 2022.	72
4.4	Local IR skew quadrupole correctors powering at the four main LHC IRs as determined with the segment-by-segment technique in the 2022 commissioning and their values as used during the LHC Run 2.	84
4.5	Correction adjustments suggested from the Rigid Waist Shift scans analysis, on top of the existing segment-by-segment corrections that were in the machine (see Table 4.4).	88
4.6	Instantaneous luminosity gains observed at the main experiments ATLAS and CMS from the method's suggested corrections.	91
4.7	Final values of local IR skew quadrupole correctors powering at the two main LHC experiments, as determined with segment-by-segment (middle), compared to the values used in the LHC Run 2 (left) and the values after RWS adjustments (right).	91
4.8	Expected total received dose of the MQSX magnets in the main IRs in Run 3. Table reproduced based on data from [197].	95
4.9	Necessary tilt angles of either Q2 or Q3 triplet elements to compensate for the loss of the closest skew quadrupole corrector/ Results are shown for IR2 and IR8, but only IR1 and IR5 are at risk of failure.	103
5.1	Comparison of the R^2 score averaged over 1000 samples taken from the test dataset for different models. For the results in this table, the standard deviations of the applied noise were $\sigma = 10^{-4}$ for IR BPMs and $\sigma = 10^{-6}$ for arc BPMs. The distribution of tilt errors had a standard deviation of $\sigma = 10^{-4}$ rad.	118
6.1	Direct and cross term detuning coefficients for free and forced motion, determined from tracking data with a linear regression.	132
B.1	Example prefixes for different LHC element types. An extensive list of all elements can be found at [236].	144

C.1	Definitions of the colinearity knobs for IR1 (left) and IR5 (right) as implemented in LSA.	147
C.2	Definitions of the Rigid Waist Shift knobs for IR1 (left) and IR5 (right) as implemented in LSA.	148
C.3	Definition of the optics rematching knob for IR1 as implemented in LSA. These settings rematch the optics for a Rigid Waist Shift knob trimmed with a factor 1.	148
C.4	Definition of the optics rematching knob for IR1 as implemented in LSA. These settings rematch the optics for a Rigid Waist Shift knob trimmed with a factor -1	149
C.5	Definition of the optics rematching knob for IR5 as implemented in LSA. These settings rematch the optics for a Rigid Waist Shift knob trimmed with a factor 1.	150
C.6	Definition of the optics rematching knob for IR5 as implemented in LSA. These settings rematch the optics for a Rigid Waist Shift knob trimmed with a factor -1	150
E.1	List of the LHC fills used in the experimental campaign, during the LHC Run 2.	155
E.2	List of the LHC fills used in the experimental campaign, during the LHC 2021 beam tests.	155
E.3	List of the LHC fills used in the experimental campaign, during the LHC 2022 commissioning.	156
E.4	List of the LHC fills used in the experimental campaign, during the LHC 2022 physics Run.	156

CHAPTER 1

Introduction



In this document a distinction is made between glossary items and acronyms, and locally relevant terms and concepts. The former will appear in [blue](#) and are clickable links bringing the reader back to the glossary such as the following: [optics](#). The latter will appear in [orange](#) and are an indication of a term or concept that is important to the content at hand but does not necessarily warrant its own entry in the glossary.

1.1 Motivations

Accelerator physics as a branch of physics has its roots nearly a century ago with the pioneering work of E. Lawrence [18] inventing the cyclotron, and shortly after in 1932 when J. Cockcroft and E. Walton [19–21] built the first particle accelerator that could produce nuclear reactions. Since then accelerator physics has grown into a mature field of research with applications ranging from cancer treatment and the production of medical isotopes to material science such as the analysis of archeological items, but also many industrial uses.

However, [High Energy Physics \(HEP\)](#) - the study of the fundamental constituents of matter - has historically been the main drive to push the boundaries of accelerator science. One of the most significant contributions of this field has been the design, construction and operation of particle colliders providing data for experiments at the forefront of [HEP](#) research, such as the [Large Hadron Collider \(LHC\)](#) at [CERN](#), the highest energy and most technologically advanced particle accelerator yet built. These contributions recently culminated with the discovery of the Higgs boson by the [ATLAS](#) and [CMS](#) experiments at the [LHC](#) in 2012 [22, 23], which Peter Higgs and François Englert were awarded the 2013 Nobel Prize in Physics for predicting nearly 50 years prior [24, 25].

Since then experiments at the [LHC](#) keep analyzing data from collisions to probe in more detail the now uncovered mechanisms, as well as attempt to discover physics beyond the Standard Model such as supersymmetry or dark matter. To this end, the LHC has kept pushing its performance to even higher energies and [luminosity](#). The machine has already undergone two [Long Shutdowns](#) during which it was upgraded, and is currently in the [Run 3](#) of its operation. Another shutdown is planned a few years

from now to upgrade the accelerator to the [High-Luminosity Large Hadron Collider \(HL-LHC\)](#) [26], which aims to increase the [luminosity](#) of the collider by a factor of 10.

Increasing the luminosity of the machine however is not without its challenges and limitations, and in order to achieve an optimal performance an understanding and control of the dynamics of the particle beams is essential. One such limitation to the delivery of optimal [luminosity](#) is the so-called local linear [betatron coupling](#) in the [Insertion Regions \(IRs\)](#), which can lead to a significant decrease in collision numbers if left uncorrected.

The focus of this thesis is on the handling of local linear coupling in the [IRs](#) of the [LHC](#), and the development of a new method to measure and correct the phenomenon, improving the performance of the accelerator. By addressing this issue, the research presented in this document aims to contribute to the ongoing efforts to push the performance of the [LHC](#) to even greater heights, and to hopefully enable new discoveries in the field of particle physics.

1.2 Thesis Outline

This document describes work done on the matter of local linear coupling correction in the [LHC](#), and of this thesis at large. Across studies a focus is kept on the main [IRs](#) of the [LHC](#), 1 and 5, which are more error-sensitive due to their optics configurations.

As a first step and to allow the reader to follow the details of this work, [Chapter 2](#) gives an in-depth introduction to the world of accelerator physics and beam dynamics. The chapter starts with the linear beam dynamics as the core foundation to any particle accelerator, then carries on with non-linear phenomenology present in more complex machines in order to introduce necessary concepts and quantities of interest to the work presented in this document, such as [Resonance Driving Terms \(RDTs\)](#). A section is dedicated to [betatron coupling](#) and its parametrization, and another to [luminosity](#) as a key performance indicator of a collider.

[Chapter 3](#) opens with a comprehensive overview of the [LHC](#) machine and its operation in [Run 3](#), with particular attention given to the main [IRs](#). The second half of the chapter dives into the practice of [Optics Measurements and Corrections \(OMC\)](#) as done at the [LHC](#) by the [OMC](#) team. Insight is given on each step, from data acquisition methods and devices to the reconstruction of quantities of interest and the determination of adjustments that would bring the machine closer to its desired, nominal state.

The main body of work for this thesis, which offers a new experimental setup and correction method for local linear coupling in the [LHC IRs](#), is detailed in [Chapter 4](#). The chapter opens by providing the reader with a justification of the need for local linear coupling correction both for the [LHC](#) and the future [HL-LHC](#) machine. An overview of the local coupling situation in the [LHC](#) is given, including current correction methods and their limitations which stem from the specific conditions of the [LHC IRs](#). The theoretical basis for the new correction method is laid out, which relies on the leakage of [RDTs](#) from the [IRs](#) to the rest of the machine, and the various experimental setup tools that were developed are thoroughly presented. Experimental measurements and data analysis from the method's application in the [LHC 2022](#) commissioning are presented as well as the resulting [luminosity](#) improvements observed from the application of the determined corrections. A short section is dedicated to the relevance of this method

for other existing or future colliders. Finally, the chapter offers an assessment of the realistic eventuality of one or more failure of the dedicated magnets used for coupling correction and the explored solutions.

In line with the themes of the [Liverpool Big Data Science Center for Doctoral Training \(LIV.DAT\)](#) [27] a machine learning-based approach to the subject of local linear coupling has been explored, that is presented in [Chapter 5](#), which starts with a minimal overview of the relevant machine learning concepts. The new approach to local linear coupling is presented with a focus on the data preparation, model training and achieved results. A discussion on the potential of this machine learning approach is held, as well as the challenges to overcome to make it fully viable in [LHC](#) operations.

Some additional work performed during this thesis is presented in [Chapter 6](#). While not relating directly to the main subject of this thesis, the work presented in this chapter is nonetheless relevant to either the [LHC](#) and its operation or to the [OMC](#) team's activities at large.

Finally, [Chapter 7](#) restates the main results and conclusions from the work done in this thesis. A discussion is held on the findings and any missing element to this work, as well as the potential avenues for future developments. The chapter closes with a look at the future of [LHC](#) operations and potential implications of this work to other colliders.

Some additional material is provided in the appendices of this document. [Appendix A](#) offers a detailed derivation for the Hamiltonian thin kick expansion which would have been too cumbersome to include in [Chapter 2](#). [Appendix B](#) provides complementary, illustrated supporting material regarding the naming conventions in use for the [LHC](#), which the reader might find useful considering the inevitable amount of machine specific jargon used in this document. In the spirit of completeness, [Appendices C to E](#) provide details on the experimental campaign relating to the studies in this thesis. The former lists the different experimental knobs used for measurements in the [LHC](#) for the results shown in [Chapter 4](#), and the latter provides a comprehensive list of the [LHC](#) fills used for measurements. [Appendix D](#) provides details on additional measurements not presented in detail in [Chapter 4](#). Finally, [Appendix F](#) succinctly presents the main software development contributions done over the course of this PhD.

CHAPTER 2

Relevant Theory of Beam Dynamics

The design, operation, performance, and safety of a particle accelerator depend on the [beam](#) dynamics. This chapter provides an overview of the beam dynamics theories relevant to the material in this thesis, and more specifically beam [optics](#). For a more complete treatment of relevant accelerator physics the reader is best referred to textbooks by Wilson [28], Lee [29], Wiedemann [30], Minty and Zimmermann [31], Wolski [32] or Chao [33, 34]. Most of the material herein can be found in the aforementioned literature, and when not in these works explicit references to the relevant content are given.

This chapter starts out with a description of linear dynamics and a parametrization of turn-by-turn motion in a circular accelerator. It then moves on to aspects of non-linear dynamics and the use of normal form to obtain the non-linear motion and introduce [Resonance Driving Terms \(RDTs\)](#), then follows up with an introduction to [betatron coupling](#) and ends with a discussion of [luminosity](#).

2.1 Linear Beam Dynamics

The linear dynamics of an accelerator are, mainly, the endeavor to bend and focus particle [beams](#) to confine them within the machine's aperture.

2.1.1 Transport and Guiding of Charged Particles

To force the beam's particles into a closed trajectory, they are subjected to magnetic fields that deflect their trajectories. The force exerted on the beam is the Lorentz force F_L given by the equation:

$$\vec{F}_L = \frac{d\vec{p}}{dt} = q(\vec{E} + \vec{v} \times \vec{B}) , \quad (2.1)$$

where \vec{p} is the particle momentum, q the particle charge, \vec{E} the electric field, \vec{v} the particle velocity and \vec{B} the magnetic field. In most accelerators, including the [Large Hadron Collider \(LHC\)](#), the particles' speed is close to the celerity of light c and the force from the magnetic field is significantly stronger than that produced by the electric field for realistic values of \vec{E} and \vec{B} . As a result, while electric fields are used for acceleration, in high energy particle accelerators magnetic fields are typically used to

guide particles. The guiding magnetic field can be expanded into a series of multipolar fields, for instance here in the horizontal plane:

$$B_y = \underbrace{B_{y0}}_{\text{dipole}} + \underbrace{\frac{dB_y}{dx}x}_{\text{quadrupole}} + \underbrace{\frac{1}{2!} \frac{d^2 B_y}{dx^2} x^2}_{\text{sextupole}} + \underbrace{\frac{1}{3!} \frac{d^3 B_y}{dx^3} x^3}_{\text{octupole}} + \dots \quad (2.2)$$

Bending forces are supplied by dipole magnets with a magnetic field perpendicular to the beam trajectory, while focusing is typically performed with the use of quadrupole magnets. Higher orders belong to the non-linear dynamics and will be discussed later on in this chapter. Figure 2.1 illustrates the Frenet-Serret coordinate system traditionally used in linear beam dynamics.

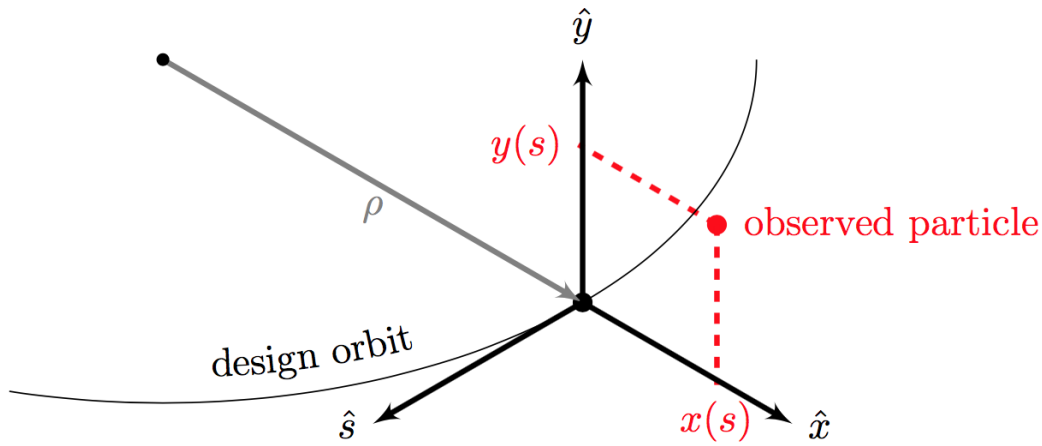


FIGURE 2.1: The Frenet-Serret coordinate system used in accelerator physics. Here \hat{x} , \hat{y} , and \hat{s} form the right-handed orthogonal basis, while ρ is the local bending radius.

The coordinate system travels longitudinally with the particle, along a reference trajectory defined by an ideal, or *synchronous*, particle. The longitudinal curvilinear coordinate is s , and denotes the position of the particle along the ideal orbit with respect to an arbitrary initial point at $s = 0$. One can define a local radius of curvature, $\rho(s)$, which depends on the local magnetic field \vec{B} and varies along the ring. The transverse *phase space* is defined by (x, x', y, y') , where x and y are a particle's coordinates in the transverse planes relative to the reference trajectory. The x' and y' coordinates are divergent angles, with the prime indicating differentiation with respect to s .

In the linear regime, magnetic dipoles define the ideal orbit for a particle of *reference momentum* p_0 . This ideal orbit goes through the magnetic center of all elements in the machine to close back on itself after a revolution, and is called the *closed orbit*. In practice however the real closed orbit will deviate from the ideal orbit due to various effects such as dipolar field errors, and the two are distinct. Particles within the beam are distributed in amplitude and oscillate around the closed orbit, which corresponds to the path of a particle with zero amplitude within the beam, because of focusing forces. This is illustrated in Fig. 2.2 where a conceptualized design orbit, a closed orbit and an actual particle trajectory are shown.

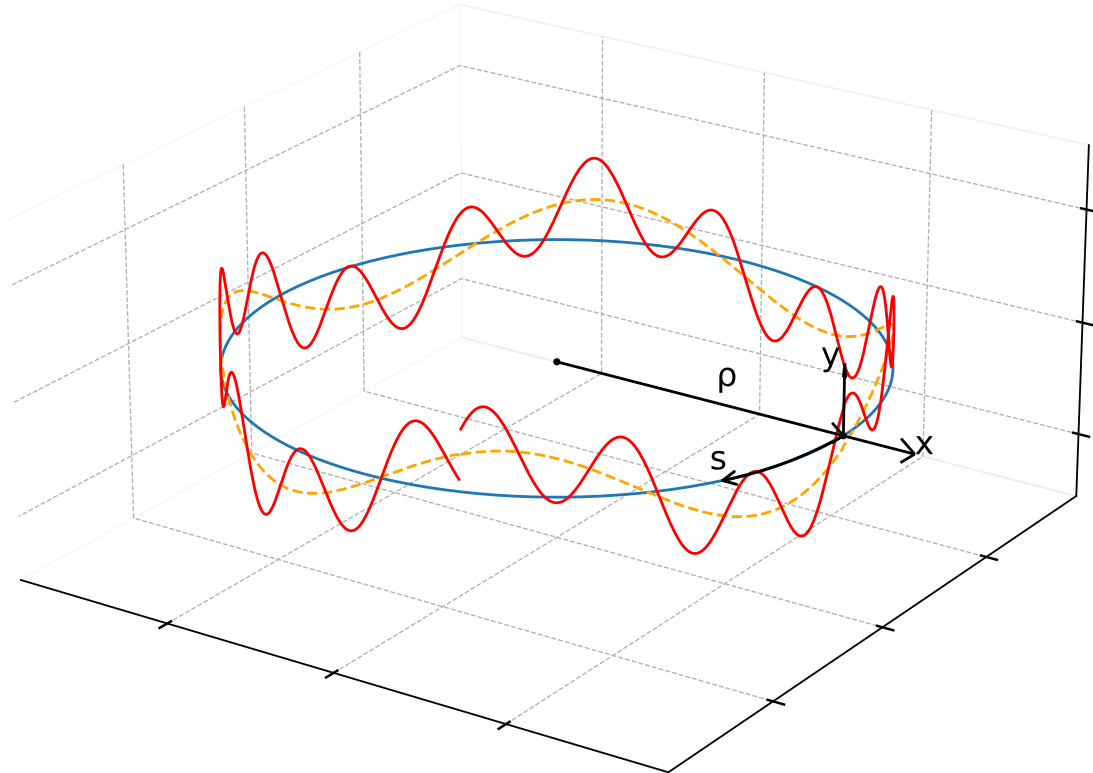


FIGURE 2.2: Illustration of a design reference orbit (blue), a closed orbit (orange) and a single turn particle trajectory (red).

Focusing forces are typically provided by magnetic quadrupoles: a quadrupolar field acting on a charged particle displaced from the closed orbit will provide a restoring (focusing) force proportional to the displacement in one transverse plane, while simultaneously providing a diverging (defocusing) force in the other. As a convention, a quadrupole focusing in the horizontal plane and defocusing in the vertical one is referred to as a **focusing quadrupole**. Respectively, a quadrupole defocusing in the horizontal plane but focusing in the vertical one is referred to as a **defocusing quadrupole**.

A net focusing effect in both planes can be obtained with a setup of quadrupoles of alternating polarity in equal distance, a widely used configuration named the **FODO cell**. A schematic of a FODO cell is shown in Fig. 2.3, and Fig. 2.4 illustrates magnetic fields in an LHC dipole and quadrupole.

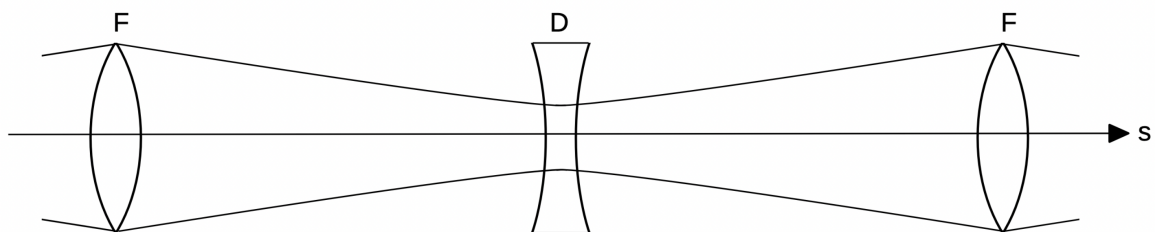


FIGURE 2.3: Schematic of a FODO cell. A focusing quadrupole is denoted with an F while a defocusing one is denoted with a D.

For each magnet applying a field B one can define the **magnetic rigidity** $B\rho$, which is an indication of the field's ability to alter a particle's course based on its charge q and momentum p , as:

$$B\rho = \frac{p}{q}. \quad (2.3)$$

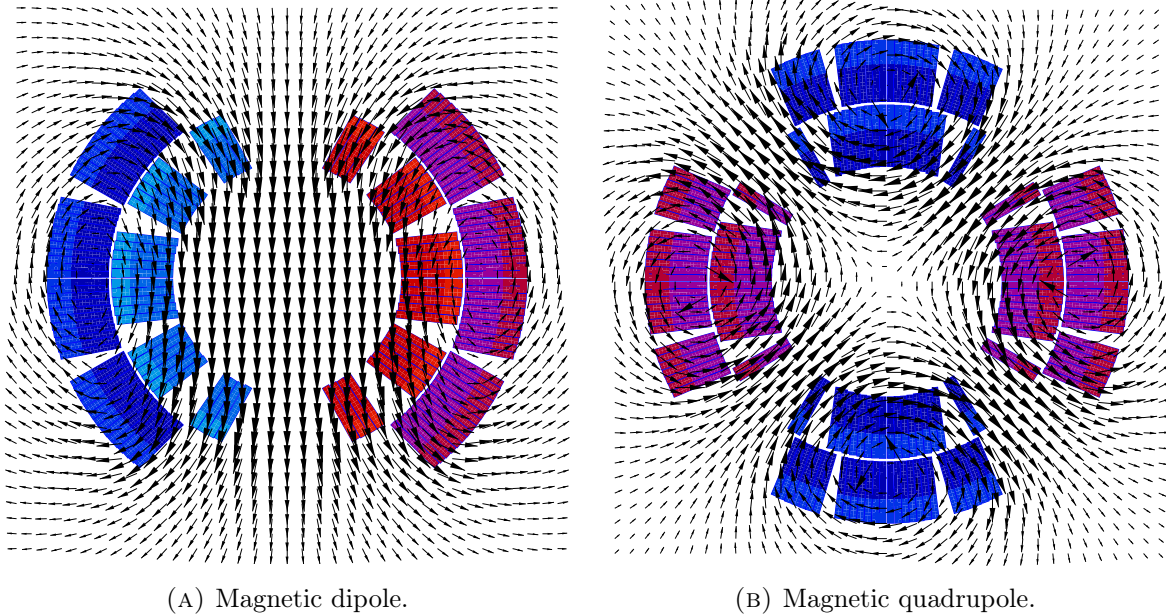


FIGURE 2.4: Magnetic fields in an LHC dipole and quadrupole, with a $\cos(\theta)$ and $\cos(2\theta)$ current distribution in the circular coil, respectively. Currents in the dipole and quadrupole coils are indicated in color. These visuals were taken from [35].

2.1.2 Equations of Motion and Twiss Parameters



The dynamics described in the material below apply similarly for both transverse planes. From now on, for clarity of the exposed expressions z will be used to denote either x or y , and when explicitly needed a distinction will be made between the two transverse planes.

The focusing from quadrupoles in a circular accelerator such as the LHC is periodic in s , with a period of at most the circumference of the machine. Assuming the existence of a **closed orbit**, the transverse motion of a single particle in a synchrotron with a periodic lattice is described by **Hill's equation**:

$$z''(s) + K_z(s)z(s) = 0; \quad z = x, y; \quad z' = \frac{dz}{ds}, \quad (2.4)$$

where K_z represents the focusing effect of dipoles and quadrupoles in the transverse plane z and varies with s given that it is dictated by the magnetic elements traversed by particles.

This focusing effect can be expressed according to:

$$\begin{aligned} K_x(s) &= \frac{1}{\rho(s)^2} - k_1(s) , \\ K_y(s) &= k_1(s) , \end{aligned} \quad (2.5)$$

where $k_1(s)$ is the normalized quadrupole strength. A **focusing quadrupole** has a $K > 0$, a **defocusing quadrupole** has $K < 0$, and a drift space has $K = 0$. The term $(1/\rho^2)$ in the horizontal component arises from the weak focusing caused by dipoles.

According to the theorem of Floquet [29], the solution with periodic boundary conditions to Hill's equation takes the form of Eq. (2.6):

$$\begin{aligned} z(s) &= \sqrt{\beta_z(s)\varepsilon_z} \cos(\phi_z(s) + \phi_{z,0}) , \\ z'(s) &= -\sqrt{\frac{\varepsilon_z}{\beta_z(s)}} [\sin(\phi_z(s) + \phi_{z,0}) + \alpha(s) \cos(\phi_z(s) + \phi_{z,0})] . \end{aligned} \quad (2.6)$$

These equations describe a harmonic oscillation in the transverse planes. Here ε_z is the **geometric emittance** of a particle and is a constant of the motion at a given energy. The $\phi_z(s)$ and $\alpha_z(s)$ terms are the **phase advance** and the **alpha-function**, respectively. $\beta_z(s)$ is the **beta-function** and represents the beam envelope, or size, around the ring. It describes the transverse position dependent amplitude of the oscillation and has the dimension of a length. In particle colliders such as the **LHC** the **β -functions** at the **Interaction Points (IPs)**, where the beams are made to collide, are commonly referred to as the β^* . The solution of Hill's equation (Eq. (2.4)) can also be written in matrix form as:

$$\begin{pmatrix} z \\ z' \end{pmatrix}_s = M \begin{pmatrix} z \\ z' \end{pmatrix}_0 . \quad (2.7)$$

In this form, which makes the assumption that the magnetic field of an element is constant along the longitudinal direction, M is called a **transfer matrix**. Below are the transfer matrices corresponding to a drift space (M_{drift}), a dipole ($M_{\text{dip.}}$), a focusing quadrupole ($M_{\text{foc.quad.}}$) and a defocusing quadrupole ($M_{\text{defoc.quad.}}$), respectively:

$$M_{\text{drift}} = \begin{pmatrix} 1 & L \\ 0 & 1 \end{pmatrix} , \quad (2.8)$$

$$M_{\text{dip.}} = \begin{pmatrix} \cos \theta & \rho \sin \theta \\ \frac{-1}{\rho} \sin(\theta) & \cos \theta \end{pmatrix} , \quad (2.9)$$

$$M_{\text{foc.quad.}} = \begin{pmatrix} \cos(\sqrt{k_1}L) & \frac{1}{\sqrt{k_1}} \sin(\sqrt{k_1}L) \\ -\sqrt{k_1} \sin(\sqrt{k_1}L) & \cos(\sqrt{k_1}L) \end{pmatrix} , \quad (2.10)$$

$$M_{\text{defoc.quad.}} = \begin{pmatrix} \cosh(\sqrt{|k_1|}L) & \frac{1}{\sqrt{|k_1|}} \sinh(\sqrt{|k_1|}L) \\ \sqrt{|k_1|} \sinh(\sqrt{|k_1|}L) & \cosh(\sqrt{|k_1|}L) \end{pmatrix} , \quad (2.11)$$

where L is the element length and $\theta = L/\rho$ is the bending angle of the dipole.

The above correspond to a 2D case and should be appropriately used depending on the plane. For instance, for a focusing quadrupole $M_{\text{foc.quad.}}$ (Eq. (2.10)) should be used to transform the horizontal coordinates, and since the element will be defocusing in the vertical plane $M_{\text{defoc.quad.}}$ (Eq. (2.11)) should be used to transform the vertical coordinates.

Larger transfer matrices can be constructed in 4D (or even 6D when including the longitudinal coordinates) to be applied to (x, x', y, y') directly. In the uncoupled case, this corresponds to a 4×4 matrix with the respective 2D transfer matrices on the diagonal and zeros elsewhere. The 4D transfer matrix of a **normal** focusing quadrupole is then expressed as:

$$M = \begin{pmatrix} M_{\text{foc.quad.}} & \begin{pmatrix} 0 & 0 \\ 0 & 0 \end{pmatrix} \\ \begin{pmatrix} 0 & 0 \\ 0 & 0 \end{pmatrix} & M_{\text{defoc.quad.}} \end{pmatrix}. \quad (2.12)$$

Some elements will have non-zero terms outside the diagonal in their transfer matrix. This is the case of a **skew** quadrupole for example, which gives a horizontal kick proportional to the vertical offset of the particle, and vice-versa. This leads to **coupled motion**, or **betatron coupling**, where the horizontal and vertical coordinates no longer evolve independently. Betatron coupling will be discussed in more detail later on, and for now only the 2D case of a given plane will be considered.

The transfer matrix of a group of elements is obtained by multiplying the transfer matrices of all individual elements. For example, the transfer matrix corresponding to the FODO cell of Fig. 2.3 is:

$$M_{\text{FODO}} = M_{\text{foc.quad.}} \cdot M_{\text{drift}} \cdot M_{\text{defoc.quad.}} \cdot M_{\text{drift}}. \quad (2.13)$$

For a complete machine with hundreds to thousands of elements, the maps of linear elements can still be combined to obtain the coordinates of a particle after a full revolution. This specific transfer map is called the **one-turn map** and fully describes the linear evolution of a particle's coordinates over one revolution of the accelerator. It can be expressed as:

$$M_{\text{OTM}} = M_N \cdot M_{N-1} \cdot \dots \cdot M_2 \cdot M_1, \quad (2.14)$$

where M_i is the transfer matrix of the i^{th} in the machine. The transformation of coordinates over a revolution is then given by:

$$\begin{pmatrix} z \\ z' \end{pmatrix}_{s_0+C} = M_{\text{OTM}} \cdot \begin{pmatrix} z \\ z' \end{pmatrix}_{s_0}. \quad (2.15)$$

The phase advance $\phi_z(s)$ mentioned above corresponds to the difference of the betatron phase functions at two points, typically also taken with respect to an arbitrary initial point at $s = 0$. The phase advance between two points at longitudinal positions s_1 and s_2 in the lattice is defined as:

$$\phi_{s_1 \rightarrow s_2} = \phi(s_2) - \phi(s_1) = \int_{s_1}^{s_2} \frac{1}{\beta(s)} ds. \quad (2.16)$$

As particles go around the ring, they oscillate around the closed orbit within an envelope defined by the β -functions and the emittance. The number of these so-called **betatron oscillations** per revolution is the **tune** Q_z . The tune is defined in Eq. (2.17), where $\Delta\phi_z$ is the total betatron phase advance of a particle over a full circumference:

$$Q_z = \frac{1}{2\pi} \Delta\phi_z = \frac{1}{2\pi} \oint_C \frac{ds}{\beta_z(s)}. \quad (2.17)$$

The α -function is defined via the derivative of the β -function by:

$$\alpha_z(s) = -\frac{1}{2} \beta_z'(s). \quad (2.18)$$

Similarly to the β -function, the **gamma-function** $\gamma_u(s)$ describes the envelope of oscillations in z' . Both quantities are related by the α -function according to:

$$\gamma_z(s) = \frac{1 + \alpha_z^2(s)}{\beta_z(s)}. \quad (2.19)$$

The $\alpha_z(s)$, $\beta_z(s)$, $\gamma_z(s)$ and $\phi_z(s)$ are also called the **Twiss parameters** [36]. The transfer matrix can be expressed with Twiss parameters according to [37]:

$$M = \begin{pmatrix} m_{11} & m_{12} \\ m_{21} & m_{22} \end{pmatrix} = \begin{pmatrix} \cos(\phi_z) + \alpha_z \sin(\phi_z) & \beta_z \sin(\phi_z) \\ -\gamma_z \sin(\phi_z) & \cos(\phi_z) - \alpha_z \sin(\phi_z) \end{pmatrix}, \quad (2.20)$$

where the s dependency of the Twiss parameters is omitted for simplicity.

2.1.3 Phase Space Ellipse



Strictly speaking, the (z, z') plane forms the **trace space** for the transverse coordinate z while the (z, p_z) plane forms the **phase space**. However, for monochromatic beams with constant momentum (e.g. no acceleration) the angular displacement z' is linked to the transverse momentum p_z by $p_z = \beta_r \gamma_r m_0 c z'$, with m_0 the particle's rest mass and β_r, γ_r the relativistic factors. Therefore, in the following we will consider trace space and phase space as equivalent and simply refer to *phase space*.

In the linear regime all particle trajectories describe ellipses in (z, z') , or (z, p_z) phase space. The geometric emittance ε_z introduced in Eq. (2.6), also named the **Courant-Snyder invariant**, defines together with the **Twiss parameters** $\alpha_z(s)$, $\beta_z(s)$ and $\gamma_z(s)$ the equation of the phase space ellipse:

$$\gamma_z(s) z(s)^2 + 2\alpha_z(s) z(s) z'(s) + \beta_z(s) z'(s)^2 = \varepsilon_z. \quad (2.21)$$

Figure 2.5 shows a schematic illustration of the phase space ellipse, the area A of which is defined by the geometric emittance according to:

$$A = \pi \varepsilon_z. \quad (2.22)$$

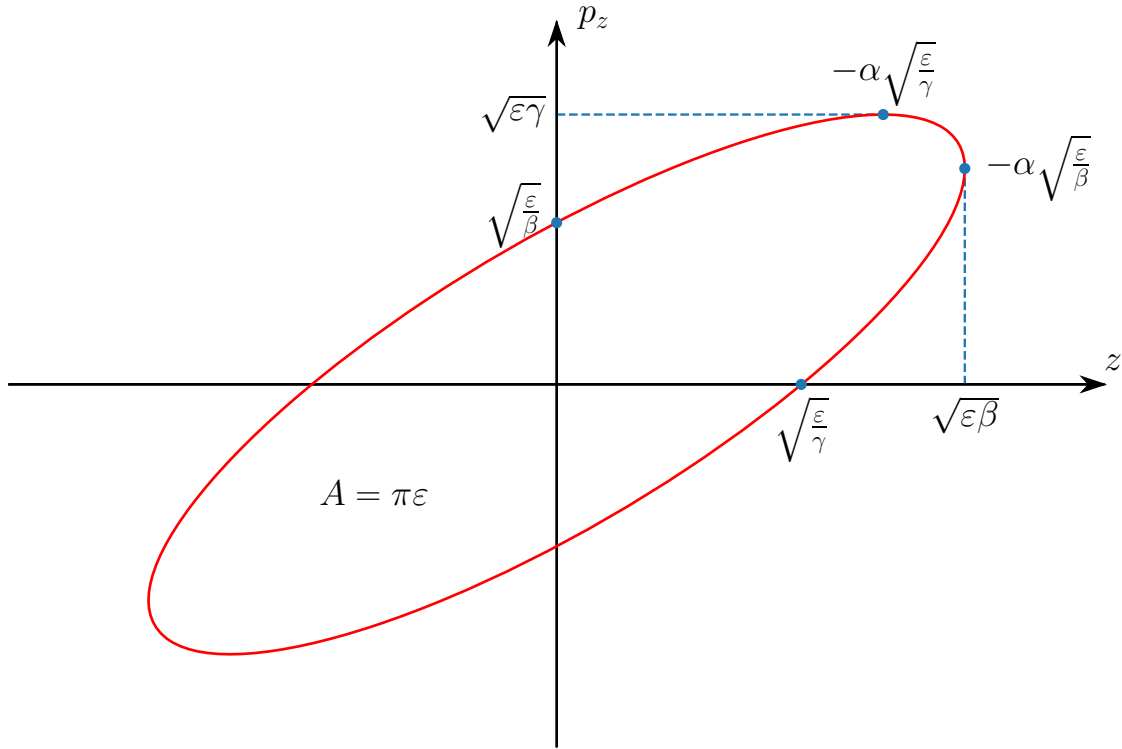


FIGURE 2.5: Phase space ellipse in the transverse (z, p_z) plane, where z represents either transverse coordinate x or y .

According to the **Liouville theorem**, the phase space volume - the ellipse area A - is a constant in a closed system. When accelerating the beam this theorem no longer holds true and the geometric emittance ε_z will decrease as the beam energy increases. One can then construct the **normalized emittance**, which is invariant with beam energy, based on the relativistic beta and gamma:

$$\varepsilon_z^{\text{norm}} = \beta_{\text{rel}} \gamma_{\text{rel}} \varepsilon_z . \quad (2.23)$$

When referring to the emittance of a specific particle one uses the term **single particle emittance**. The **action** J_z is related to the single particle emittance by:

$$2J_z = \varepsilon_z . \quad (2.24)$$

The state of particles in phase space can be fully characterized by the action variable J_z and the corresponding phase variable ϕ_z seen previously. Different particles in the beam will have different single particle emittances and will undergo betatron oscillations of varying amplitudes. For a Gaussian shaped beam the transverse beam size is:

$$\sigma_z = \sqrt{\beta_z \varepsilon_z^{\text{beam}}} , \quad (2.25)$$

with $\varepsilon_z^{\text{beam}}$ the beam emittance, typically defined as the emittance corresponding to a 1σ amplitude of the Gaussian charge distribution. In the case of more general particle distributions, an alternative definition of the beam emittance is often used [38, 39]:

$$\varepsilon_z^{\text{rms}} = \sqrt{\langle z \rangle^2 \langle z' \rangle^2 - \langle z z' \rangle^2} . \quad (2.26)$$

The phase space trajectory of a particle depends on the **Twiss parameters** $\alpha(s)$, $\beta(s)$, and $\gamma(s)$. One can remove this dependency by performing a coordinate transformation to the **Courant-Snyder coordinates** [40], defined as:

$$\begin{pmatrix} \hat{z} \\ \hat{z}' \end{pmatrix} = \begin{pmatrix} \frac{1}{\sqrt{\beta_z}} & 0 \\ \frac{\alpha_z}{\sqrt{\beta_z}} & \sqrt{\beta_z} \end{pmatrix} \begin{pmatrix} z \\ z' \end{pmatrix}, \quad (2.27)$$

where the Courant-Snyder coordinates are denoted with a hat $\hat{\cdot}$. An identical transformation exists to go from (z, p_z) to (\hat{z}, \hat{p}_z) coordinates. In this new system, particles follow circular trajectories in phase space. **Figure 2.6** provides an illustrative representation of phase space in both physical and normalized coordinates for an accelerator with linear elements only. In the new representation, the elliptical phase space is transformed into a simpler circular phase space where the motion corresponds to simple rotations, fully described by, and depending only on, the **action** and angle variables (J_z, ϕ_z) .

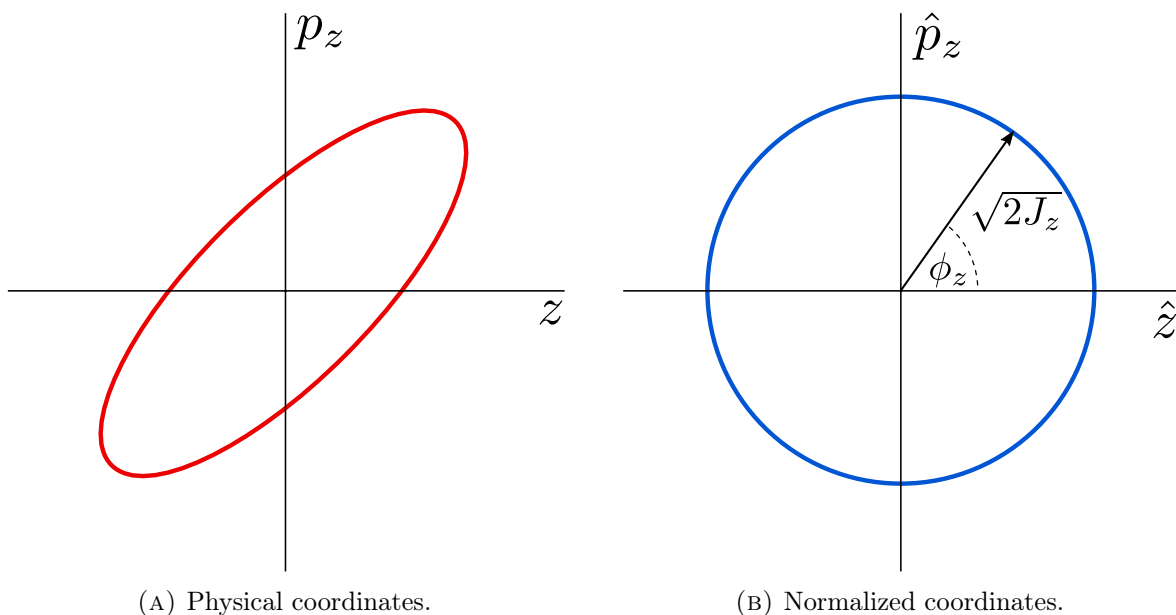


FIGURE 2.6: Illustrative representation of phase-space in physical coordinates (left) and normalized, or Courant-Snyder, coordinates (right) for an accelerator with linear elements only. Courtesy of F. Carlier [41].

2.1.4 Chromatic Effects

Until now, it was assumed that all particles had the intended design momentum p_0 . Naturally, in practice particles within the beam have a distribution in energy and momentum. For a particle with a momentum $p \neq p_0$ one defines and uses the **relative momentum deviation** δ_p :

$$\delta_p = \frac{p - p_0}{p_0} = \frac{\Delta p}{p_0}. \quad (2.28)$$

Such momentum offsets introduce **chromatic errors** in the beam dynamics. Effects and parameters depending on δ_p are called **chromatic effects**.

From the definition of the **magnetic rigidity** in Eq. (2.3), it follows that particles of different momenta will have different local radii of curvature when going through dipoles and therefore follow different orbits along the machine. The orbit deviation of an off-momentum particle from that of the synchronous particle is defined by the **dispersion function** $D(s)$. Its contribution to a particle's orbit in a region of non-zero dispersion is described by:

$$\Delta z_{\text{dispersion}} = D_z(s)\delta_p . \quad (2.29)$$

Off-momentum particle positions scale linearly with dispersion, and in its presence Eq. (2.6) is extended to [30]:

$$z(s) = \sqrt{\varepsilon_z \beta_z(s)} \cos(\phi_z(s) + \phi_{z,0}) + D_z(s)\delta_p . \quad (2.30)$$

Another chromatic parameter is the **chromaticity** Q'_z , which describes the tune shift ΔQ_z with particle momentum by:

$$Q'_z = \frac{\Delta Q_z}{\delta_p} . \quad (2.31)$$

The effective focusing strength of quadrupoles, which is inversely proportional to the momentum, differs for off-momentum particles. The change of focusing strength due to energy deviation is:

$$\Delta k_1 = -\frac{e}{p^2} \frac{dB_y}{dx} \Delta p = -k_1 \delta_p . \quad (2.32)$$

This quadrupole error results in a tune shift proportional to the energy offset:

$$\Delta Q = \frac{1}{4\pi} \int \beta(s) \Delta k_1(s) ds = \left[-\frac{1}{4\pi} \int \beta(s) k_1(s) ds \right] \delta_p . \quad (2.33)$$

The natural chromaticity of a linear lattice can then be approximated by [42]:

$$Q'_z \approx -\frac{1}{4\pi} \oint \beta_z(s) K_z ds . \quad (2.34)$$

2.2 Non-Linear Magnetic Multipoles

Magnetic fields of sextupolar and higher order are called **non-linear** magnetic fields. While only dipolar and quadrupolar magnetic fields are considered in the linear approximation, non-linear magnetic fields are present in most accelerators. They can be introduced by design or by the presence of flaws in lower order magnets, the latter having the potential to seriously disrupt the beam.



We label n the order of a multipole. This document uses the *European convention* for field indices, in which $n = 1$ corresponds to a magnetic dipole, $n = 2$ to a quadrupole, etc.

The magnetic field of a multipole of order n is given by:

$$B_y(x, y, s) + iB_x(x, y, s) = \sum_{n=1}^{\infty} [B_n(s) + iA_n(s)] (x + iy)^{n-1},$$

$$B_n(s) = \frac{1}{(n-1)!} \left. \frac{\partial^{n-1} B_y}{\partial x^{n-1}} \right|_{(0,0,s)},$$

$$A_n(s) = \frac{1}{(n-1)!} \left. \frac{\partial^{n-1} B_x}{\partial x^{n-1}} \right|_{(0,0,s)}.$$
(2.35)

Here $B_n(s)$ and $A_n(s)$ are the **normal** and **skew multipole coefficients**, respectively, where a skew magnet of order n is rotated by $\pi/(2n)$ with respect to its normal counterpart. Starting from the Hamiltonian equations:

$$\frac{d\vec{p}_z}{dt} = -\frac{\partial \mathcal{H}}{\partial \vec{z}}, \quad \frac{d\vec{z}}{dt} = \frac{\partial \mathcal{H}}{\partial \vec{p}_z},$$
(2.36)

the Hamiltonian for the transverse planes for a multipole of order n is given by Eq. (2.37) [43, 44]:

$$\mathcal{H}_n = \frac{q}{p} \operatorname{Re} \left[(B_n + iA_n) \frac{(x + iy)^n}{n} \right].$$
(2.37)

In the linear regime, this Hamiltonian may then be written as:

$$\mathcal{H} = \frac{1}{2} p_x^2 + \frac{1}{2} p_y^2 + \frac{1}{2} K(s) x^2 - \frac{1}{2} K(s) y^2,$$
(2.38)

where $K(s)$ describes the variation of the focusing strength around the ring. More generally, if the Hamiltonian for a **normal** multipole of order n is labeled N_n and that of a **skew** multipole of order n is labeled S_n , then [45, 46]:

$$N_n \propto \operatorname{Re} [(x + iy)^n]$$

$$\propto \operatorname{Re} \left[\sum_{k=0}^n \binom{n}{k} i^k \beta_x^{\frac{n-k}{2}} \beta_y^{\frac{k}{2}} \left(\sqrt{2J_x} \cos(\phi_x) \right)^{n-k} \left(\sqrt{2J_y} \cos(\phi_y) \right)^k \right],$$
(2.39)

$$S_n \propto \operatorname{Im} [(x + iy)^n]$$

$$\propto \left[\sum_{k=0}^n \binom{n}{k} i^k \beta_x^{\frac{n-k}{2}} \beta_y^{\frac{k}{2}} \left(\sqrt{2J_x} \cos(\phi_x) \right)^{n-k} \left(\sqrt{2J_y} \cos(\phi_y) \right)^k \right].$$
(2.40)

The powering of non-linear magnets and the presence of magnetic errors can have a significant impact on the beam dynamics. Geometric errors can also contribute to the presence of non-linear components. For instance, when a particle does not pass through the magnetic center of an element it will see not only the primary field component but also perturbations of all lower orders to that of the traversed element [30]. This effect is called **feed-down** and can be introduced by misalignment of lattice elements, which would cause the closed orbit to deviate from the ideal one and the beam to pass off-axis in magnets.

Should that happen with a sextupole, for instance, the beam would experience a sextupolar field but also encounter quadrupolar and dipolar components. The rotational misalignment of elements is also a concern, as rotating a purely normal or skew multipole results in the beam experiencing a combination of both normal and skew fields.

2.3 Non-Linear Formalism and Resonance Driving Terms

The material below takes inspiration from [43–46] where some aspects are described in more detail than given here. For the curious reader, a very thorough approach to normal forms can be found in [41] and [47].

2.3.1 Non-Linear Transfer Maps

As introduced in Eq. (2.14), the dynamics of a circular accelerator can be parametrized in terms of **transfer maps** relating final to initial phase space coordinates. This approach is described in [40, 48]. While the transfer map of a linear element is described by a matrix, that of a non-linear element is itself described by the exponential **Lie operator** $e^{-:f:}$ defined as [32]:

$$\begin{aligned} e^{-:f:}g &= g + [f, g] + \frac{1}{2} [f, [f, g]] + \dots, \\ [f, g] &= \sum_i \frac{\partial f}{\partial q_i} \frac{\partial g}{\partial p_i} - \frac{\partial f}{\partial p_i} \frac{\partial g}{\partial q_i}, \end{aligned} \quad (2.41)$$

where q_i and p_i are the canonical coordinates and momenta, respectively. Here $[f, g]$ is the **Poisson bracket** of f and g . When including non-linear sources, the one-turn map introduced in Eq. (2.14) becomes:

$$M_{\text{OTM}} = e^{-:h_N:} e^{-:h_{N-1}:} \dots e^{-:h_2:} e^{-:h_1:} R, \quad (2.42)$$

where R is a matrix describing the linear dynamics of the machine, and the h_i terms represent the thin kick Hamiltonians of the non-linear elements in the accelerator.

Relevant properties of the exponential Lie operator can be found in [43, 44], one of which being that the product of exponential Lie operators can be expressed as another exponential Lie operator following the Baker-Campbell-Hausdorff theorem [49]. The one-turn map becomes:

$$M_{\text{OTM}} = e^{-:h:} R, \quad (2.43)$$

in which, in the case that the h_i are small, h can be approximated as:

$$h = \sum_{n=1}^N h_n + \sum_{n,m < n} [h_m, h_n] + \dots \quad (2.44)$$

Using only the first order in h_n , the thin kick h can be expressed in expanded terms using the action and angle variables according to [44]:

$$h = \sum_{jklm} h_{jklm} (2J_x)^{\frac{j+k}{2}} (2J_y)^{\frac{l+m}{2}} e^{i[(j-k)(\phi_x + \phi_{x,0}) + (l-m)(\phi_y + \phi_{y,0})]}, \quad (2.45)$$

with h_{jklm} being the **Hamiltonian coefficient** encompassing the contribution of all multipoles of order $n = j + k + l + m$. The derivation for the result of Eq. (2.45) can be found in [Appendix A](#). A multipole of order $n = j + k + l + m$ gives rise to terms $\propto x^{j+k}y^{l+m}$ in the Hamiltonian. In the case of a **skew quadrupole** ($n = 2$) for example, one will see terms in the Hamiltonian $\propto xy$, meaning a contribution to h_{1010} , h_{1001} , h_{0110} and h_{0101} .

2.3.2 Normal Form, Resonance Driving Terms and Resonances

Due to the presence of non-linear sources the linear invariant J_z introduced in [Section 2.1.3](#) is no longer a constant. This leads to the phase space trajectory in normalized, or Courant-Snyder, coordinates no longer describing a circle. An example of this situation is given in [Fig. 2.7](#), where the horizontal phase space trajectories of 200 particles are shown in normalized coordinates when exciting a third order resonance.

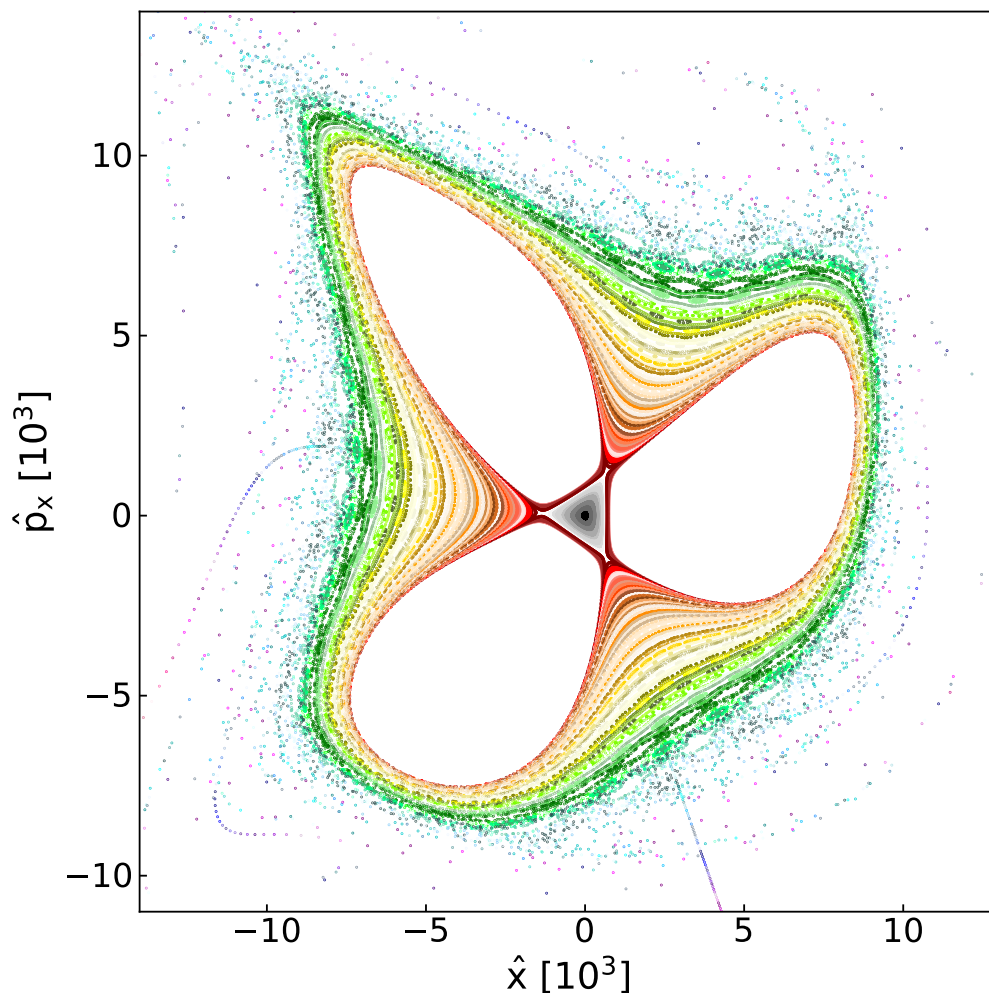


FIGURE 2.7: Phase space in normalized coordinates from tracking 200 particles in a simple FODO-based lattice, when exciting a third order resonance. Points of each color corresponds to the trajectory of a given particle.

One may wish to create a new transformation, akin to that to normalized coordinates, that would allow describing betatron motion in phase space by a pure rotation in the presence of non-linear sources. The change of coordinates is represented by a similarity transformation of the one turn map, written as [43]:

$$e^{-iF} e^{ih} Re^{iF} , \quad (2.46)$$

where F is the **generating function** of the transformation. The coordinates resulting from the transformation are called **normal form coordinates**. The different coordinate systems are illustrated in Fig. 2.8.

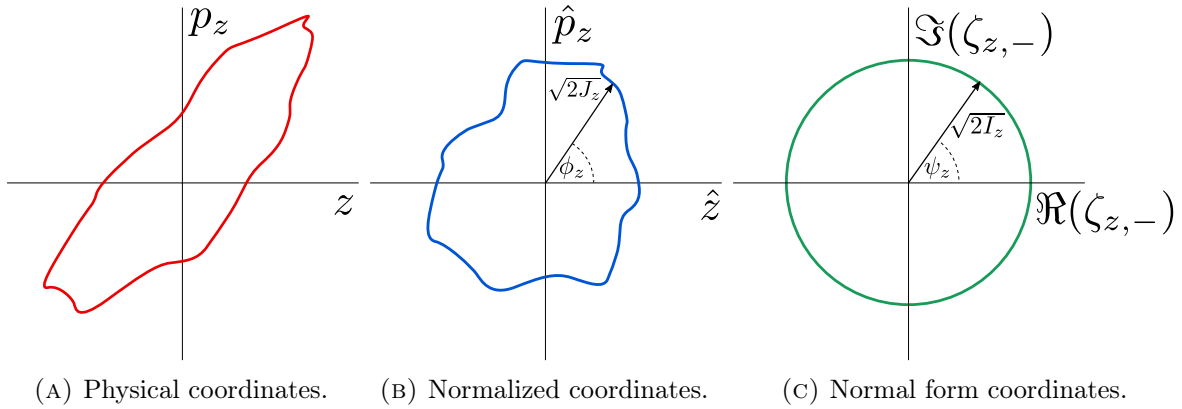


FIGURE 2.8: Illustrative exaggerated representations of phase space in the three different coordinate systems: physical (left), normalized (middle) and normal form (right) coordinates. Courtesy of F. Carrier [41].

The generating function of the transformation F contains a large portion of the information describing the non-linear dynamics, and a new non-linear invariant I_z can be introduced. Similarly to h in Eq. (2.45), the generating function F can be expanded in terms of the normal form coordinates according to [44]:

$$F = \sum_{jklm} f_{jklm} (2I_x)^{\frac{j+k}{2}} (2I_y)^{\frac{l+m}{2}} e^{i[(j-k)(\psi_x+\psi_{x0})+(l-m)(\psi_y+\psi_{y0})]} , \quad (2.47)$$

where (I_z, ψ_z) are to normal form coordinates what (J_z, ϕ_z) are to normalized coordinates. The f_{jklm} coefficients are related to the h_{jklm} terms by:

$$f_{jklm} = \frac{h_{jklm}}{1 - e^{i2\pi[(j-k)Q_x+(l-m)Q_y]}} . \quad (2.48)$$

From Eq. (2.48) one can see that the f_{jklm} coefficients diverge for certain values of the tunes. Specifically, divergence happens when the following relation is satisfied:

$$(j - k) Q_x + (l - m) Q_y = p , \quad \text{where } j, k, l, m, p \in \mathcal{Z} . \quad (2.49)$$

A divergence of the f_{jklm} terms leads to a divergence of the transformation to normal form coordinates, which generally indicates an unclosed phase space trajectory due to a **resonance** in the beam motion. The condition in Eq. (2.49) corresponds to situations where particles lie on resonant frequencies, typically causing their amplitudes to grow unboundedly by the dynamics. Therefore the f_{jklm} terms are called **Resonance Driving Terms**.

For this reason, the tune is one of the single most important design parameters in synchrotrons. The chosen operational transverse tunes of a synchrotron are known as its **working point**, and should be selected carefully in order to avoid resonances. Resonances up to order $n = 5$ are shown in Fig. 2.9, with lines of different orders differentiated from one another.

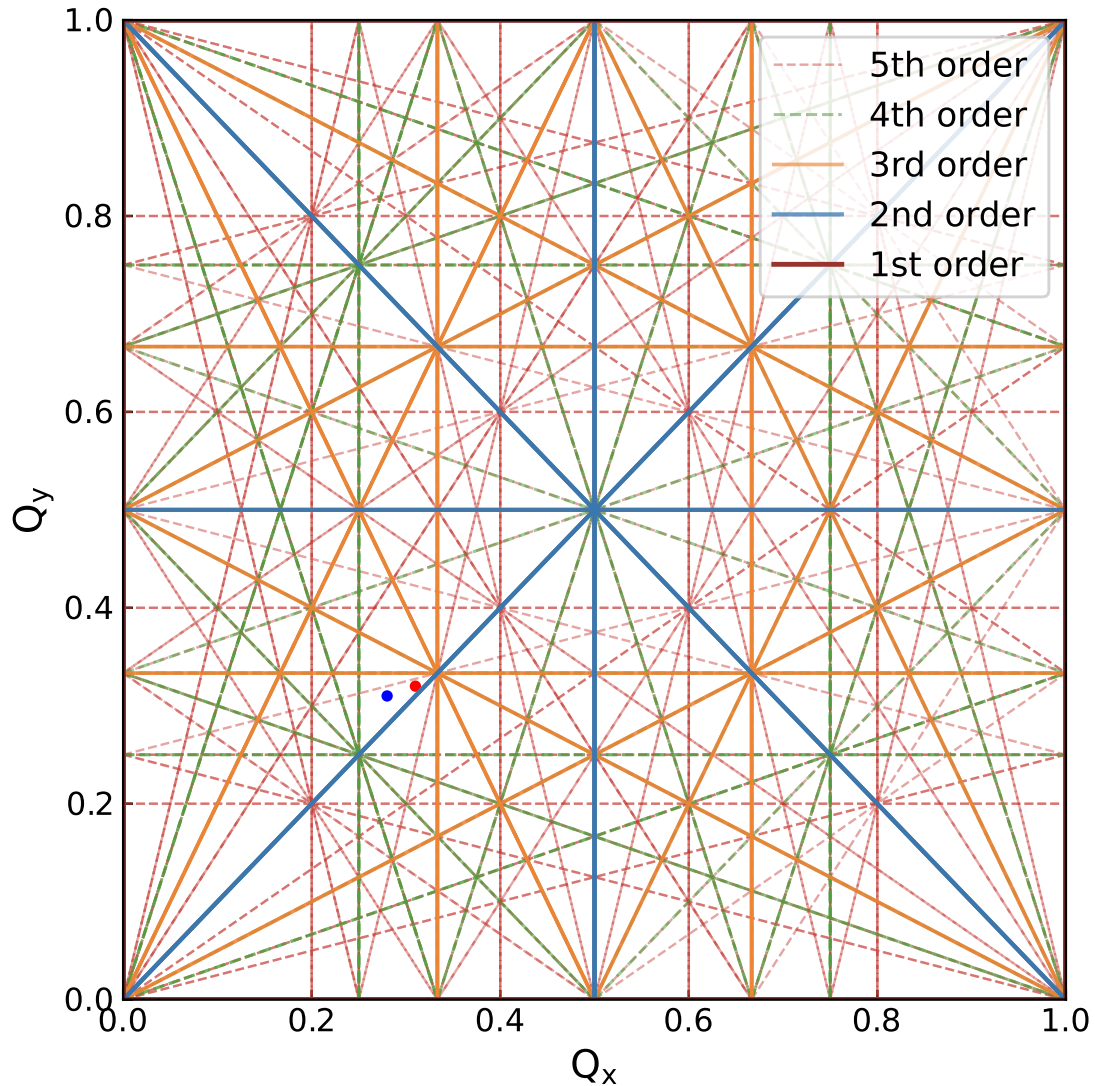


FIGURE 2.9: Tunes diagram showing resonance lines up to order $n = 5$. The LHC working points are indicated by the two dots: in blue for injection tunes and red for collision tunes.

Commonly, the label of a given resonance is written as (n_1, n_2) , where $n_1 = (j - k)$ and $n_2 = (l - m)$. Every generating function term f_{jklm} and, equivalently, every Hamiltonian term h_{jklm} , is associated with a specific resonance defined by the values of j , k , l , and m .

The **RDTs** vary in amplitude through the machine as they depend on the local multipole strength of contributing sources. Characteristically, the f_{jklm} terms show abrupt jumps at the location of relevant sources.

2.3.3 Resonance Basis and Normal Form Coordinates

The normalized Courant-Snyder coordinates (\hat{z}, \hat{p}_z) are related to the action and angle variables (J_z, ϕ_z) by:

$$\begin{aligned}\hat{z} &= \sqrt{2J_z} \cos(\phi_z + \phi_{z0}) , \\ \hat{p}_z &= -\sqrt{2J_z} \sin(\phi_z + \phi_{z0}) .\end{aligned}\tag{2.50}$$

One can define the **resonance basis** $(h_x^+, h_x^-, h_y^+, h_y^-)$ by the relation:

$$h_z^\pm = \hat{z} \pm i\hat{p}_z = \sqrt{2J_z} e^{\mp i(\phi_z + \phi_{z0})} .\tag{2.51}$$

The transformation to the **normal form coordinates** introduced in the previous section, $(\zeta_x^+, \zeta_x^-, \zeta_y^+, \zeta_y^-)$, is expressed as:

$$\zeta_z^\pm = \sqrt{2I_z} e^{\mp i(\psi_z + \psi_{z0})} = e^{-:F:} h_z^\pm .\tag{2.52}$$

where (I_z, ψ_z) are the terms introduced in Eq. (2.47).

By definition of the transformation, the one-turn map in normal form coordinates is an amplitude dependent rotation. It follows that the motion of these coordinates as a function of the turn number N is then given by:

$$\zeta_z^\pm(N) = \sqrt{2I_z} e^{\mp i(2\pi Q_z N + \psi_{z0})} ,\tag{2.53}$$

with Q_z the transverse tunes. The inverse transformation from the new normal form coordinates to the resonance basis coordinates is written, to first order, as:

$$h_z^\pm = e^{:F:} \zeta_z^\pm \simeq \zeta_z^\pm + [F, \zeta_z^\pm] .\tag{2.54}$$

Using Eq. (2.53) and Eq. (2.54), the linearly normalized coordinates can be expressed after N turns as [44, 50]:

$$\begin{aligned}h_x^-(N) &= \sqrt{2I_x} e^{i(2\pi Q_x N + \psi_{x0})} - \\ &\quad 2i \sum_{jklm} j f_{jklm} (2I_x)^{\frac{j+k-1}{2}} (2I_y)^{\frac{l+m}{2}} e^{i[(1-j+k)(2\pi Q_x N + \psi_{x0}) + (m-l)(2\pi Q_y N - \psi_{y0})]} \\ h_y^-(N) &= \sqrt{2I_y} e^{i(2\pi Q_y N + \psi_{y0})} - \\ &\quad 2i \sum_{jklm} l f_{jklm} (2I_x)^{\frac{j+k}{2}} (2I_y)^{\frac{l+m-1}{2}} e^{i[(k-j)(2\pi Q_x N + \psi_{x0}) + (1-l+m)(2\pi Q_y N - \psi_{y0})]} .\end{aligned}\tag{2.55}$$

Figure 2.10 shows a schematic of the different transformations and changes to the one-turn map. While one can calculate the evolution of the Courant-Snyder coordinates by applying the map \mathcal{M} , the approach is complicated to solve in the presence of non-linearities. Solving the one-turn map for the next turn is best done by performing a transformation to normal form coordinates ζ_z^\pm using the generating function F , applying the amplitude dependent rotation map R , and transforming back to Courant-Snyder coordinates. These calculations are in practice simpler than the former method, and conserve non-linearities.

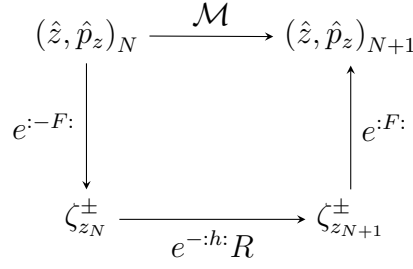


FIGURE 2.10: Illustration of the coordinate transformations and change of the one-turn map. This diagram reads from Courant-Snyder coordinates at turn N in the top left, and shows both paths to reach the Courant-Snyder coordinates at turn $N + 1$ in the top right.

2.3.4 Spectral Contribution

Each term in the summations of Eq. (2.55) corresponds to a certain mode in the beam motion and contributes to a specific frequency in the spectrum of the motion [51]. Said spectrum may be determined by a frequency analysis of the turn-by-turn beam position data, through means of a Fourier transform. In this spectrum, an RDT f_{jklm} at a specific location in the machine contributes to lines in the horizontal and vertical spectra according to [51, 52]:

$$\begin{aligned} H(1 - j + k, m - l) &= 2j |f_{jklm}| (2I_x)^{\frac{j+k-1}{2}} (2I_y)^{\frac{l+m}{2}}, \\ V(k - j, 1 - l + m) &= 2l |f_{jklm}| (2I_x)^{\frac{j+k}{2}} (2I_y)^{\frac{l+m-1}{2}}, \end{aligned} \quad (2.56)$$

where in the parentheses multiples of the fractional tunes are given. For example, $H(0, 1)$ indicates an observed line at $1 \times Q_y$ in the horizontal spectrum.

In principle the $|f_{jklm}|$ may be determined by a comparison of the amplitude of various spectral lines. In practice, some additional considerations need to be taken, as decoherence of a kicked beam can lead to a reduction in the amplitude of the spectral lines observed, or the fact that the contributions of different RDTs might not be distinct. More details are given in Chapter 3.

2.3.5 Amplitude Detuning

The **amplitude detuning** is the variation of the **tune** with the single particle emittance. It can be described with a Taylor expansion of the tune Q_z around the unperturbed tune $Q_{z,0}$ as:

$$\begin{aligned} Q_z(\varepsilon_x, \varepsilon_y) &= Q_{z,0} + \frac{\partial Q_z}{\partial \varepsilon_x} \varepsilon_x + \frac{\partial Q_z}{\partial \varepsilon_y} \varepsilon_y \\ &+ \frac{1}{2!} \left(\frac{\partial^2 Q_z}{\partial \varepsilon_x^2} \varepsilon_x^2 + \frac{\partial^2 Q_z}{\partial \varepsilon_x \partial \varepsilon_y} \varepsilon_x \varepsilon_y + \frac{\partial^2 Q_z}{\partial \varepsilon_y^2} \varepsilon_y^2 \right) + \dots, \end{aligned} \quad (2.57)$$

where $\varepsilon_z = 2J_z$ is the invariant of motion in the transverse plane z . The first order terms of the amplitude detuning, $\frac{\partial Q_z}{\partial \varepsilon_x}$ and $\frac{\partial Q_z}{\partial \varepsilon_y}$, are generated by octupoles and by the second order contribution of sextupoles [40]; while the following terms come from

higher order multipoles. The amplitude detuning is a good indication of the machine non-linearities.

2.4 Betatron Coupling

When the betatronic motion of particles in transverse planes are independent of each other, they are said to be **uncoupled**. In particle colliders such as the LHC this is the desired behaviour. When these motions share a dependency, they are said to be **coupled**, and one refers to this phenomenon as **betatron coupling**, or linear coupling. The transverse motions of particles in an accelerator may couple due to a variety of factors, with solenoid and **skew** quadrupole fields being the primary sources of linear coupling.

In the LHC the main contribution to coupling comes from unwanted **skew** quadrupolar fields. These mostly arise from **normal** quadrupoles mounted with a rotation error with respect to the longitudinal axis, but also from field imperfection from other magnets and feed-down from higher order magnets. An example of a normal and skew quadrupole is given in Fig. 2.11.

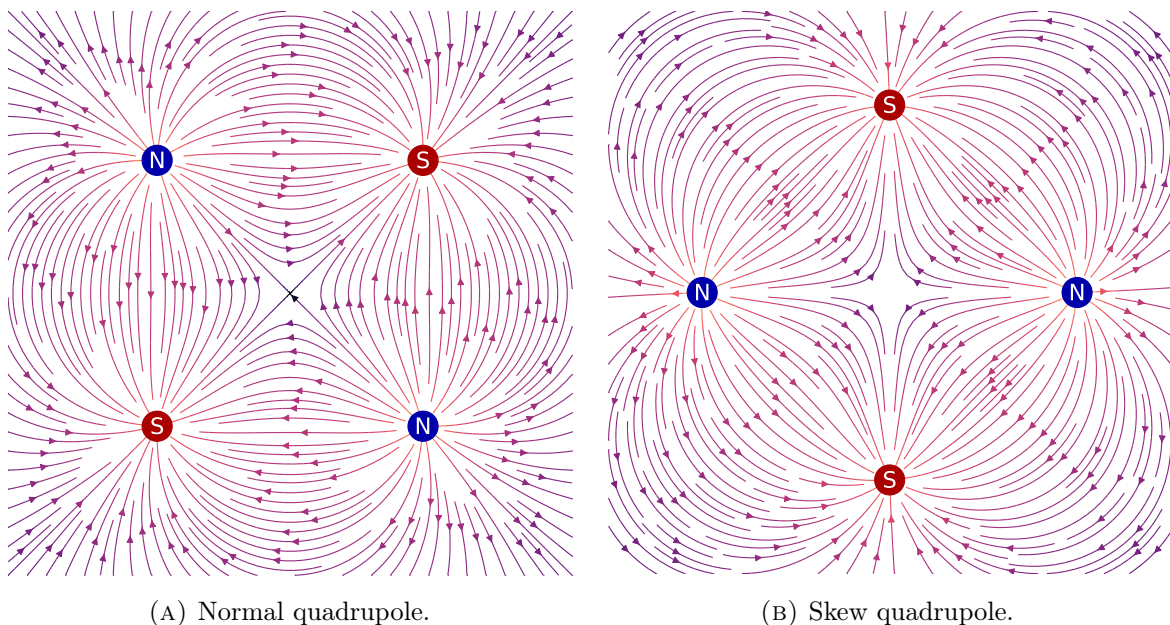


FIGURE 2.11: Illustration of a **normal** (left) and **skew** (right) magnetic quadrupole and their magnetic field lines.

Betatron coupling needs to be kept under control as it can perturb the tune feedback systems and push tunes into resonances, lead to a reduction in the dynamic aperture [53] or loss of beam stability [54, 55].

2.4.1 Parametrization of Betatron Coupling

There are different ways to parametrize coupled motion in a particle accelerator, the two most common being the Edwards-Teng [56] and Mais-Ripken [57] parametrizations. For coupled motion a dependency between the horizontal and vertical planes is introduced,

and as mentioned in [Section 2.1.2](#) the transverse motion can no longer be described by two independent 2×2 matrices. Instead, it is described by a 4×4 matrix $\hat{\mathbf{M}}$ such that

$$\hat{\mathbf{M}} = \begin{pmatrix} \mathbf{P} & \mathbf{p} \\ \mathbf{q} & \mathbf{Q} \end{pmatrix}, \quad (2.58)$$

where \mathbf{P} , \mathbf{p} , \mathbf{q} and \mathbf{Q} are 2×2 matrices. In the absence of [betatron coupling](#), it follows that \mathbf{p} and \mathbf{q} are 0. Magnetic elements introducing coupling between the horizontal and vertical planes have non-zero terms in the respective \mathbf{p} and \mathbf{q} of their transfer matrices. For instance, the transfer matrix of a [skew quadrupole](#) can be written

$$\mathbf{M}_{\text{skew quad.}} = \begin{pmatrix} \mathbf{M}_x & \mathbf{M}_{xy} \\ \mathbf{M}_{yx} & \mathbf{M}_y \end{pmatrix}, \quad (2.59)$$

where, using $\omega = \sqrt{k_{1s}} \geq 0$ for clarity, the various 2×2 matrices are expressed as [\[58\]](#):

$$\begin{aligned} \mathbf{M}_x &= \begin{pmatrix} \frac{1}{2}(\cos(\omega L) + \cosh(\omega L)) & \frac{1}{2\omega}(\sin(\omega L) + \sinh(\omega L)) \\ -\frac{\omega}{2}(\sin(\omega L) - \sinh(\omega L)) & \frac{1}{2}(\cos(\omega L) + \cosh(\omega L)) \end{pmatrix}, \\ \mathbf{M}_{xy} &= \begin{pmatrix} \frac{1}{2}(\cos(\omega L) - \cosh(\omega L)) & \frac{1}{2\omega}(\sin(\omega L) - \sinh(\omega L)) \\ -\frac{\omega}{2}(\sin(\omega L) + \sinh(\omega L)) & \frac{1}{2}(\cos(\omega L) - \cosh(\omega L)) \end{pmatrix}, \\ \mathbf{M}_{yx} &= \begin{pmatrix} \frac{1}{2}(\cos(\omega L) - \cosh(\omega L)) & \frac{1}{2\omega}(\sin(\omega L) - \sinh(\omega L)) \\ -\frac{\omega}{2}(\sin(\omega L) + \sinh(\omega L)) & \frac{1}{2}(\cos(\omega L) - \cosh(\omega L)) \end{pmatrix}, \\ \mathbf{M}_y &= \begin{pmatrix} \frac{1}{2}(\cos(\omega L) + \cosh(\omega L)) & \frac{1}{2\omega}(\sin(\omega L) + \sinh(\omega L)) \\ -\frac{\omega}{2}(\sin(\omega L) - \sinh(\omega L)) & \frac{1}{2}(\cos(\omega L) + \cosh(\omega L)) \end{pmatrix}. \end{aligned} \quad (2.60)$$

Edwards-Teng Parametrization

The effect of [betatron coupling](#) can, figuratively, be seen as a rotation of the beam ellipse. In the Edwards-Teng parametrization presented in [\[56\]](#), the linear coupling is then described by a symplectic rotation \mathbf{R} of $\hat{\mathbf{M}}$ into its normal modes form $\bar{\mathbf{M}}$, as shown in [Eq. \(2.61\)](#). In this new frame the motion is decoupled, and all the information on the coupling is held by the matrix \mathbf{R} .

$$\bar{\mathbf{M}} = \begin{pmatrix} \mathbf{X} & 0 \\ 0 & \mathbf{Y} \end{pmatrix} = \mathbf{R}\hat{\mathbf{M}}\mathbf{R}^{-1}. \quad (2.61)$$

Edwards and Teng have characterized the transformation \mathbf{R} with the symplectic matrix:

$$\mathbf{R} = \begin{pmatrix} \mathbf{I} \cos \theta & -\mathbf{K}^{-1} \sin \theta \\ \mathbf{K} \sin \theta & \mathbf{I} \cos \theta \end{pmatrix}, \quad (2.62)$$

where \mathbf{I} is the 2×2 unit matrix and \mathbf{K} is a 2×2 symplectic matrix, such that $\det(\mathbf{K}) = 1$. The coupled motion may then be described by the uncoupled [Twiss parameters](#) seen in [Section 2.1.2](#), together with the elements of matrix \mathbf{K} and Teng's angle of rotation θ . In the case that $\theta = 0$, the matrix \mathbf{R} is the identity matrix and as a result it will not rotate any of the modes: this corresponds to uncoupled motion.

The Edwards-Teng parameterization is used in the MAD-X code [59] when handling coupled motion. In MAD-X the relevant parameters are $\alpha_{x,y}$, $\beta_{x,y}$, $\mu_{x,y}$, $\gamma_{x,y}$ and r_{11} , r_{12} , r_{21} , r_{22} , where $r_{11} \dots r_{22}$ correspond to the elements of \mathbf{K} multiplied by $\tan(\theta)$.

Mais-Ripken Parametrization

The approach of Mais and Ripken was developed in [60] and is more accessible in [57, 61]. It defines so-called **Ripken parameters** α_{kj} , β_{kj} and γ_{kj} , where $k = 1 \dots 3$ refers to the plane (x, y, \dots) and the index j refers to the eigenmodes, that are accurate in the presence of coupling. In the coupled case, all β_N are non-zero and β_{11}, β_{22} are distinctively different from β_x, β_y , respectively. The relations linking these new parameters to the **Twiss parameters** can be found in [62].

The Mais-Ripken parameterization is the basis of the **Polymorphic Tracking Code (PTC)** [63]'s handling of coupled dynamics.

Coupling and Beam Matrix

Considering the 2D case of a given transverse direction the so-called **beam matrix** or **sigma matrix**, which is the covariance matrix of the particle distribution, is expressed as:

$$\sigma = \begin{pmatrix} \sigma_{11} & \sigma_{12} \\ \sigma_{21} & \sigma_{22} \end{pmatrix} = \begin{pmatrix} \langle z^2 \rangle & \langle zp_z \rangle \\ \langle p_z z \rangle & \langle p_z^2 \rangle \end{pmatrix}. \quad (2.63)$$

where the brackets indicate an average over all particles in the beam. Note that this matrix is symmetric with $\sigma_{12} = \sigma_{21}$.

Considering that the **Twiss parameters** and the emittance defining the phase space ellipse are related to the various moments of the beam distribution as

$$\begin{aligned} \epsilon_z &= \sqrt{\langle z^2 \rangle \langle p_z^2 \rangle - \langle zp_z \rangle^2}, \\ \beta_z &= \frac{\langle z^2 \rangle}{\epsilon_z}, \\ \alpha_z &= -\frac{\langle zp_z \rangle}{\epsilon_z}, \\ \gamma_z &= \frac{\langle p_z^2 \rangle}{\epsilon_z}, \end{aligned} \quad (2.64)$$

one can relate them to the sigma matrix via the emittance through:

$$\sigma = \epsilon_z \begin{pmatrix} \beta_z & -\alpha_z \\ -\alpha_z & \gamma_z \end{pmatrix}. \quad (2.65)$$

When considering the full 4D transverse space one can express the beam matrix Σ as a block diagonal 4×4 matrix with the respective horizontal and vertical sigma matrices on the diagonal and zeros elsewhere. In the presence of coupling, the general covariance matrix has non-zero terms outside its diagonal and takes the form of Eq. (2.66):

$$\Sigma = \begin{pmatrix} \sigma_{11} & \sigma_{12} & \sigma_{13} & \sigma_{14} \\ \sigma_{21} & \sigma_{22} & \sigma_{23} & \sigma_{24} \\ \sigma_{31} & \sigma_{32} & \sigma_{33} & \sigma_{34} \\ \sigma_{41} & \sigma_{42} & \sigma_{43} & \sigma_{44} \end{pmatrix} = \begin{pmatrix} \langle x^2 \rangle & \langle xp_x \rangle & \langle xy \rangle & \langle xp_y \rangle \\ \langle xp_x \rangle & \langle p_x^2 \rangle & \langle p_x y \rangle & \langle p_x p_y \rangle \\ \langle xy \rangle & \langle p_x y \rangle & \langle y^2 \rangle & \langle yp_y \rangle \\ \langle xp_y \rangle & \langle p_x p_y \rangle & \langle yp_y \rangle & \langle p_y^2 \rangle \end{pmatrix}. \quad (2.66)$$

Through Σ the coupling can be characterized by the values of the cross-plane elements $\langle xy \rangle$, $\langle xp_y \rangle$, $\langle p_x y \rangle$ and $\langle p_x p_y \rangle$. Through the symmetry (for instance, $\langle xy \rangle = \langle yx \rangle$) only those four terms are needed.

The angle of rotation θ in the Edwards-Teng parametrization is related to these terms through [64]:

$$\tan(2\theta) = \frac{2\Sigma_{xy}}{\Sigma_{xx} - \Sigma_{yy}} = \frac{2\sigma_{13}}{\sigma_{11}\sigma_{33}}. \quad (2.67)$$

In the Mais-Ripken parameterization, the Ripken parameters are constructed in order to be related to the Σ matrix in a similar way to that shown in Eq. (2.65) for the 2D uncoupled case.

2.4.2 Coupled Motion

To the first order, according to Eq. (2.49), linear coupling drives the two resonances $Q_x + Q_y = p$ and $Q_x - Q_y = p$, with $p \in \mathcal{Z}$. These are respectively called the **sum and difference resonances**, and in their vicinity the beam dynamics are heavily influenced.

The impact of linear coupling on the beam motion has been studied through Hamiltonian perturbation theory [30, 65], and through the normal form and RDT formalism [44]. As the transverse tunes approach the difference resonance, the emittance is described by:

$$\varepsilon_x + \varepsilon_y = \text{const}, \quad (2.68)$$

and as the resonance is approached the beam motion may not become unstable. Instead, there is a periodic exchange of emittance between the transverse planes, which leads to a beating in the betatron oscillation amplitudes.

The relation between the **unperturbed tunes** (Q_x, Q_y) and the **coupled tunes** (Q_1, Q_2) is given by [66]:

$$\begin{aligned} Q_1 &= Q_x - \frac{\Delta}{2} + \frac{\sqrt{\Delta^2 + |C^-|}}{2}, \\ Q_2 &= Q_y + \frac{\Delta}{2} - \frac{\sqrt{\Delta^2 + |C^-|}}{2}, \end{aligned} \quad (2.69)$$

with Δ being the unperturbed fractional tune split and $|C^-|$ the linear coupling coefficient, a parameter describing the strength of the coupling.

When $\Delta \gg |C^-|$, away from the resonance, the observed oscillation modes (Q_1, Q_2) are almost identical to the uncoupled tunes (Q_x, Q_y). When the tunes are moved closer together, approaching the difference resonance ($\Delta \rightarrow 0$), the perturbed tunes are forced apart by the coupling and a minimal tune separation ΔQ_{\min} can be observed. The $|C^-|$ of Eq. (2.69), named the **closest tune approach**, corresponds to this separation. Figure 2.12 shows an illustration of the phenomenon in the vicinity of the resonance,

where both the unperturbed (dashed) and coupled (colored) fractional tunes are plotted against the uncoupled tune split.

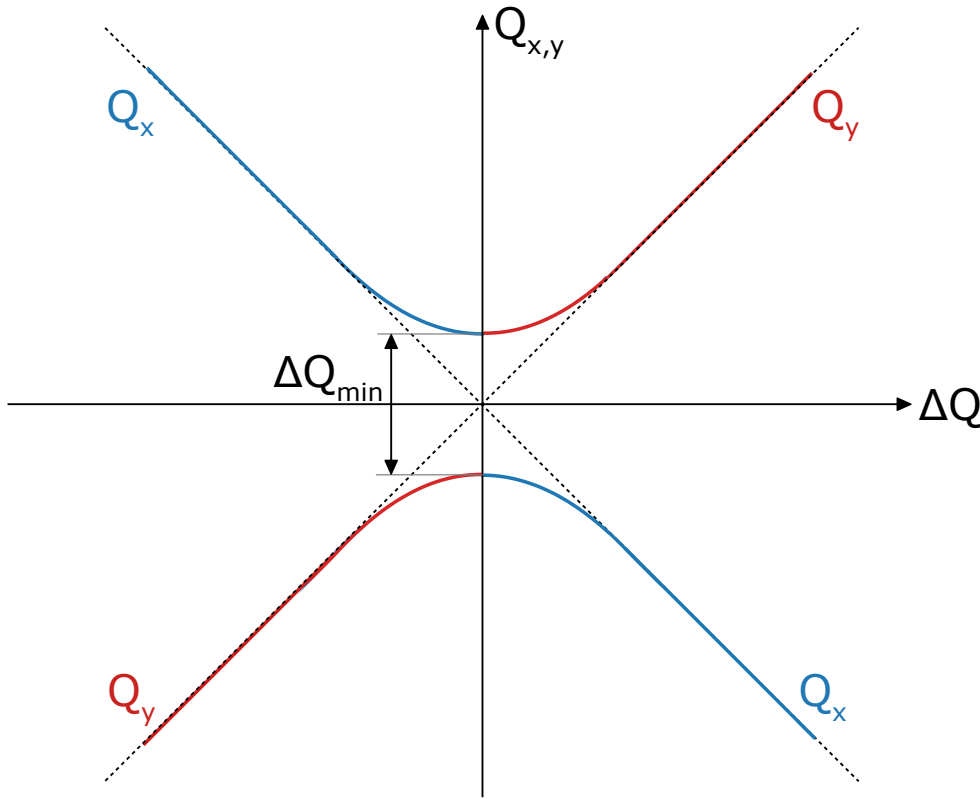


FIGURE 2.12: Illustration of coupled and uncoupled fractional tunes versus the uncoupled tune split. Courtesy of J. Keintzel [67].

On the other hand, when approaching the sum resonance the emittances follow:

$$\varepsilon_x - \varepsilon_y = \text{const} . \quad (2.70)$$

This resonance allows for unstable motion as only the difference in emittance is constrained. Therefore, it is common to choose a working point far from the sum resonance. In the LHC, the working points (visible on Fig. 2.9) are set such that the linear coupling is dominated by the difference resonance: the fractional tunes are $(Q_x, Q_y) = (0.28, 0.31)$ at injection and $(Q_x, Q_y) = (0.31, 0.32)$ for squeezed beams and collisions¹.

2.4.3 Linear Coupling Resonance Driving Terms

Linear coupling in the LHC is dominated by the contribution of skew quadrupole fields, which lead to terms $\propto xy$ in the Hamiltonian. According to the resonance relation of Eq. (2.49) and as seen in Section 2.4.2, this gives rise to the RDTs f_{1001} and f_{0110} , which correspond to the $Q_x - Q_y = p$ difference resonance; and f_{1010} which corresponds to the $Q_x + Q_y = p$ sum resonance.

¹The LHC working point is actually more diverse and will be discussed in more detail in the next chapter.

The f_{1001} and f_{0110} describe the same dynamics but the former is for the horizontal plane while the latter is for the vertical plane. Since they describe the same dynamics it is customary to label both of them as f_{1001} , which is a convention used throughout this document.

It was mentioned in [Section 2.4.2](#) that the [LHC](#) working point is selected to be close to the stable difference resonance, and as a consequence in the LHC the $|f_{1001}|$ dominates relative to the $|f_{1010}|$. These [RDTs](#) can be expressed as a function of the uncoupled lattice parameters at the location of both the coupling-contributing elements and the observation point s as [\[65\]](#):

$$\begin{aligned} f_{1001}(s) &= -\frac{1}{4(1 - e^{2\pi i(Q_x - Q_y)})} \sum_l k_l \sqrt{\beta_x^l \beta_y^l} e^{i(\Delta\phi_x^{sl} - \Delta\phi_y^{sl})}, \\ f_{1010}(s) &= -\frac{1}{4(1 - e^{2\pi i(Q_x + Q_y)})} \sum_l k_l \sqrt{\beta_x^l \beta_y^l} e^{i(\Delta\phi_x^{sl} + \Delta\phi_y^{sl})}, \end{aligned} \quad (2.71)$$

where k_l is the l^{th} integrated [skew](#) quadrupole strength, $\beta_{x,y}^l$ are the [\$\beta\$ -functions](#) at the location of the l^{th} skew quadrupole, $Q_{x,y}$ are the horizontal and vertical tunes, and $\Delta\phi_{x,y}^{sl}$ are the phase advances from the l^{th} skew quadrupole to the observation point at the longitudinal coordinate s . The summation is done over all contributing [skew](#) quadrupoles.

These [RDTs](#) can be related to the strength of the coupling ΔQ_{min} , and as such the $|C^-|$ can be expressed in relation to the f_{1001} [RDT](#). In [\[44\]](#) a simple version of this relation was established as:

$$|C^-| \approx 4\Delta \frac{1}{N} \sum_{i=1}^N |f_{1001}|_i, \quad (2.72)$$

where the summation is done over the N observation points, and Δ is the fractional tune split. A more accurate relation was established in [\[68\]](#), which is:

$$|C^-| = \left| \frac{4\Delta}{2\pi R} \oint ds f_{1001} e^{-i(\phi_x - \phi_y) + is\Delta/R} \right|, \quad (2.73)$$

where the dependence of variables on the position s was omitted for clarity.

In [\[65\]](#) the equations of motion are solved perturbatively under the influence of a weak [skew](#) quadrupole strength $j(s)$. Assuming that the machine is close to the difference coupling resonance, $\Delta = Q_x - Q_y \rightarrow 0$, the $|C^-|$ can be approximated as:

$$|C^-| = \frac{1}{2\pi} \left| \oint ds \sqrt{\beta_x(s)\beta_y(s)} j(s) e^{-i(\phi_x - \phi_y) + i\frac{s\Delta}{R}} \right|, \quad (2.74)$$

where s is the position around the ring, $\beta_{x,y}$ are the horizontal and vertical [\$\beta\$ -functions](#), $\phi_{x,y}$ are the phase advances and R is the radius of the machine.

2.5 Luminosity

The [LHC](#) machine being a particle collider, it is operated to produce collisions between two counter-rotating beams and to produce data for [High Energy Physics \(HEP\) experiments](#). As the studied interactions coming from these collisions are rare, a

substantial interaction rate is required. Naturally, the performance of the machine is then described by the number of collisions provided to experiments as well as the center-of-mass energy of these collisions.

As a figure of merit for the number of collisions the **luminosity** is used. The **instantaneous luminosity** \mathcal{L} is the proportionality factor between the number of events per unit of time dR/dt and the process cross-section σ_{cross} :

$$\frac{dR}{dt} = \mathcal{L}\sigma_{\text{cross}} . \quad (2.75)$$

The instantaneous luminosity is given in units of inverse barns per second ($\text{b}^{-1} \text{s}^{-1}$), where $[b] = 10^{-24} \text{cm}^2$. For a collider with Gaussian beams, it can be expressed as [69]:

$$\mathcal{L} = \frac{f_{\text{rev}} N_1 N_2}{4\pi\sigma_x\sigma_y} S , \quad (2.76)$$

where f_{rev} is the revolution frequency of particle bunches, N_1 and N_2 are the number of particles in each beam, and $\sigma_{x,y}$ are the transverse beam sizes at the interaction points. S is the **luminosity reduction factor** and depends on various parameters such as crossing angles, orbit offsets, beam-beam interactions, beam tilts in the case of **flat optics** etc. For Gaussian bunches colliding with a **crossing angle** θ , where $\sigma_s \gg \sigma_{x,y}$ and neglecting other contributions, the luminosity reduction factor is approximated by [69]:

$$S \approx \frac{1}{\sqrt{1 + \left(\frac{\theta}{2} \frac{\sigma_s}{\sigma_x}\right)^2}} . \quad (2.77)$$

The luminosity can be influenced by the local presence of **betatron coupling** through its impact on beam size, as will be discussed in **Chapter 4**. As seen in **Eq. (2.25)** the beam sizes directly depend on the β -function at the **IP**, β^* , which then defines the collider's performance from the point of view of the optics. Indeed, the smaller the β^* the smaller the beam sizes, and the more collisions will be produced per bunch crossing.

The **integrated luminosity**, the accumulated luminosity over a given period of time, is given by:

$$\mathcal{L}_{\text{int}} = \int_{t_1}^{t_2} \mathcal{L} dt . \quad (2.78)$$

The integrated luminosity is usually in units of $\text{fb}^{-1} = 10^{39} \text{cm}^{-2}$. The total number of collisions, or events, over said time period is then:

$$N_{\text{events}} = \mathcal{L}_{\text{int}}\sigma_{\text{cross}} . \quad (2.79)$$

Throughout luminosity production, the instantaneous luminosity naturally decreases as more and more particles are lost to collisions [70]. Any particle losses happening before colliding the beams will lead to a reduction of the initial $N_{1,2}$ and of the resulting integrated luminosity of the given fill.

Luminosity production requires a good control of the linear optics, both for the quality of the optics themselves but also for a smooth and safe operation. Many non-linear contributions may also influence the dynamics away from the linear regime,

leading to a deterioration of the dynamics and, down the line, the luminosity. Therefore for a particle collider like the [LHC](#) a good control of all effects influencing the beam dynamics is required, and methods to both measure and correct any deviations from the ideal machine are a necessity. An overview of these is given in [Chapter 3](#).

CHAPTER 3

Optics Measurements and Corrections at the LHC

The **Large Hadron Collider (LHC)** is a 26.659 km long synchrotron collider located at the **European Organization for Nuclear Research (CERN)**, on the French-Swiss border. It is part of **CERN's Accelerator Complex**, illustrated in **Fig. 3.1**, a chain of particle accelerators progressively bringing protons and heavy ions up to an energy of 6.8 TeV per beam as of 2023.

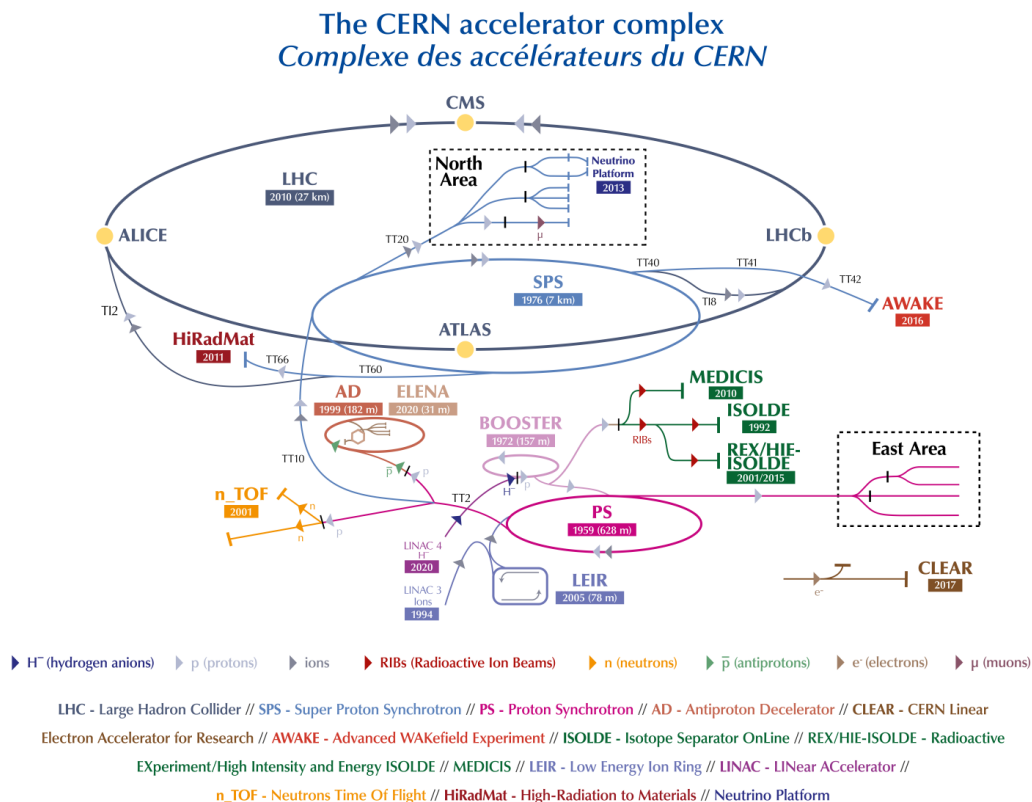


FIGURE 3.1: The CERN Accelerator Complex in 2022, not to scale [71]. For typical LHC operation, a proton beam is produced in LINAC4 and follows the chain: LINAC4 \rightarrow PSB \rightarrow PS \rightarrow SPS \rightarrow LHC.

Particles go through a chain of different particle accelerators before reaching their experimental destinations. For protons colliding in the LHC, the first step is a linear accelerator, LINAC4, which accelerates them up to a kinetic energy of 160 MeV. Next, the protons are injected into the PS Booster (PSB), where they are accelerated to an energy of 1.4 GeV. The next stages are the Proton Synchrotron (PS), in which they will reach 25 GeV; then the Super Proton Synchrotron (SPS) where they are accelerated to 450 GeV before being finally injected into the LHC.

The LHC circulates two counter-rotating hadron beams, each in their ring, which are made to collide at four Interaction Points (IPs) to provide data for High Energy Physics (HEP) experiments. The main data-taking experiments on the LHC are ATLAS [72–74], ALICE [75–77], CMS [78–80], and LHCb [81–83]; with other notable experiments being LHCf [84–86], MATHUSLA [87–89], FASER [90–92], SND [93–95], TOTEM [96–98], and MoEDAL [99–101]. The LHC is currently the world’s highest energy particle accelerator, colliding beams at 13.6 TeV center-of-mass energy as of Run 3, 2023.

3.1 The LHC Lattice

The LHC lattice consists of eight octants each intersected by an Insertion Region (IR). Conventionally, the segment between two IRs is called an arc and the arc between IR1 and IR2 is named Arc12, and similarly for other arcs. An octant is defined as going from mid-arc to mid-arc around a given IR which is located at its center. Each octant is named according to the IR at its center: the octant with IR1 at its center is named Octant1, and similarly for other octants. An illustration and a detailed description on naming conventions can be found in Appendix B.

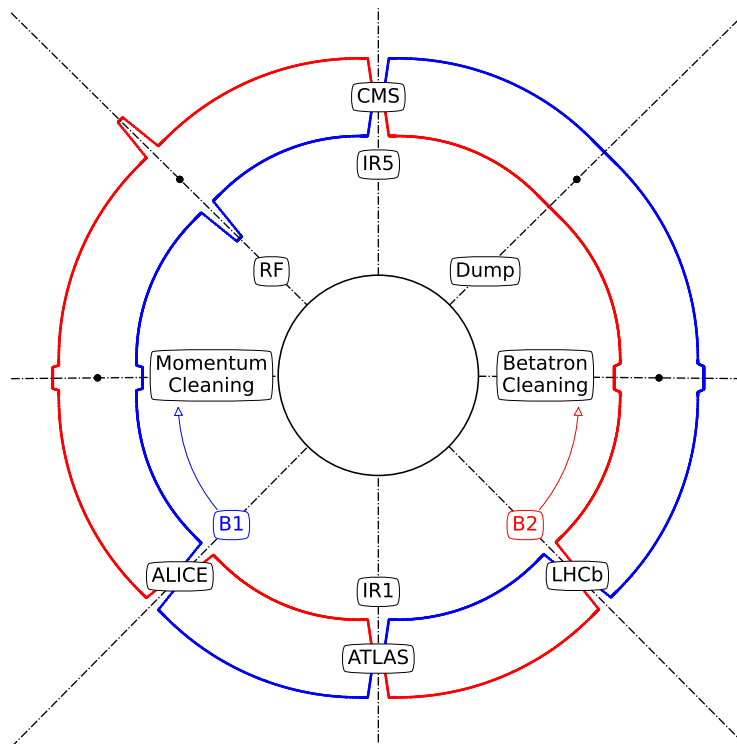
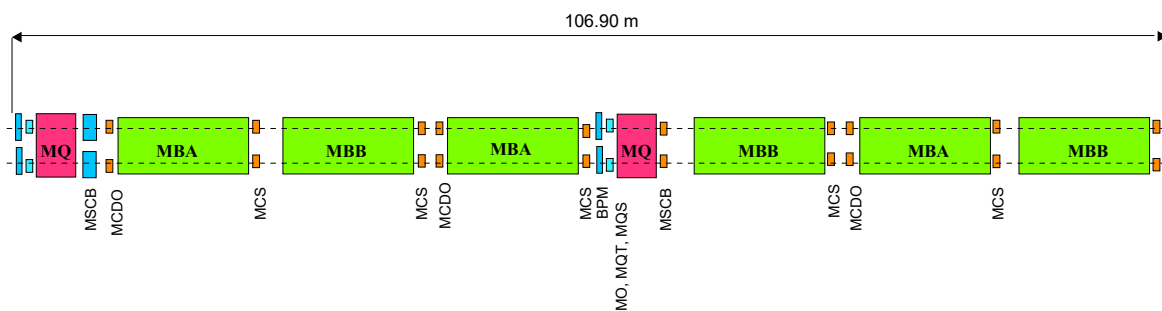


FIGURE 3.2: Schematic of the LHC layout, adapted from [102].

Beam 1 rotates clockwise in its ring when viewing the LHC from above, and Beam 2 rotates counter-clockwise as viewed from above. The beams occupy separate apertures - or beam pipes - side by side except in the IRs where they are made to collide. The layout of the LHC can be seen in simplified schematic form in Fig. 3.2, and full details can be found in the LHC Design Report [103–105].

3.1.1 The LHC Arcs

Each arc in the LHC is made up of 23 cells and is approximately 2.45 km long. The layout of an LHC arc cell is given in Fig. 3.3, and a clearer schematic representation can be found in [106]. The cell is based on an FBDB (FODO with Bends) layout alternating focusing and defocusing quadrupoles interspaced with dipoles. These elements are all superconducting and are commonly labeled MQF, MQD and MB, respectively.



MQT: trim quadrupole

MCS: spool piece sextupole

MQS: skew trim quadrupole

MCDO: spool piece octupole + decapole

MO: lattice octupole

MSCB: sextupole (skew sextupole) + orbit corrector

FIGURE 3.3: Schematic of an LHC arc cell [103].

Each cell contains two MQ (one MQF, one MQD) with three MBs in between, for a total of 6 MBs per cell. The MBs are all powered in series and, for size constraint reasons [103], are of a dual bore design. The MQs are themselves also powered in series but split in two families: one power circuit is dedicated to MQF magnets and another circuit for the MQD magnets, where each arc holds a circuit for each family. As a consequence, these elements can only be trimmed in groups.

Part of the main assemblies are superconducting *spool piece magnets*, correctors used for the local compensation of magnetic errors in the main arc magnets [103]. These include sextupole correctors, sextupolar spool pieces named MCS and mounted on the ends of every main dipole, used to correct b_3 errors of the MBs. Similarly, octupole and decapole spool pieces are included and used for the compensation of b_4 and b_5 errors in the main arc magnets, respectively. The octupole correctors are named MCO while the decapole correctors are named MCD, and both are nested together in an assembly named MCDO which is mounted on the end of every second MB. The spool piece magnets in the LHC are single aperture and powered in series similarly to the MQs, with one circuit assigned for each magnet family.

In addition to spool piece magnets, linear and non-linear **lattice correctors** are mounted on the main arc quadrupoles MQs. These lattice correctors are powered in series per family, and independently for each beam. Horizontal and vertical orbit correctors, respectively **MCBH** and **MCBV**, are installed at each focusing and defocusing MQ. Normal **trim** quadrupoles, named **MQT**, are primarily used for tune correction. In each arc four MQTs are rotated by 45° to form **skew** quadrupoles, named **MQS**, used for **betatron coupling** correction. **Normal** and **skew** sextupoles **MS** and **MSS**, used for natural chromaticity and chromatic coupling correction respectively, are mounted on the MQs. Landau octupoles **MO** provide damping of coherent oscillations, and are split into two families (focusing and defocusing) powered in series, such that there are two families per arc and per beam.

Figure 3.4 shows a simplified layout of an LHC arc cell's elements as well as β and dispersion functions for 2022 optics at $\beta^* = 30$ cm. In the layout (top) part of the plot the powering of elements is indicated, with MBs in blue, MQs in red, MSs in yellow and MOs in green. Beam position monitors (BPMs) are indicated as grey patches. Note that not all elements are indicated. Figure 3.5 shows a similar plot but across LHC arc23 for the same optics.

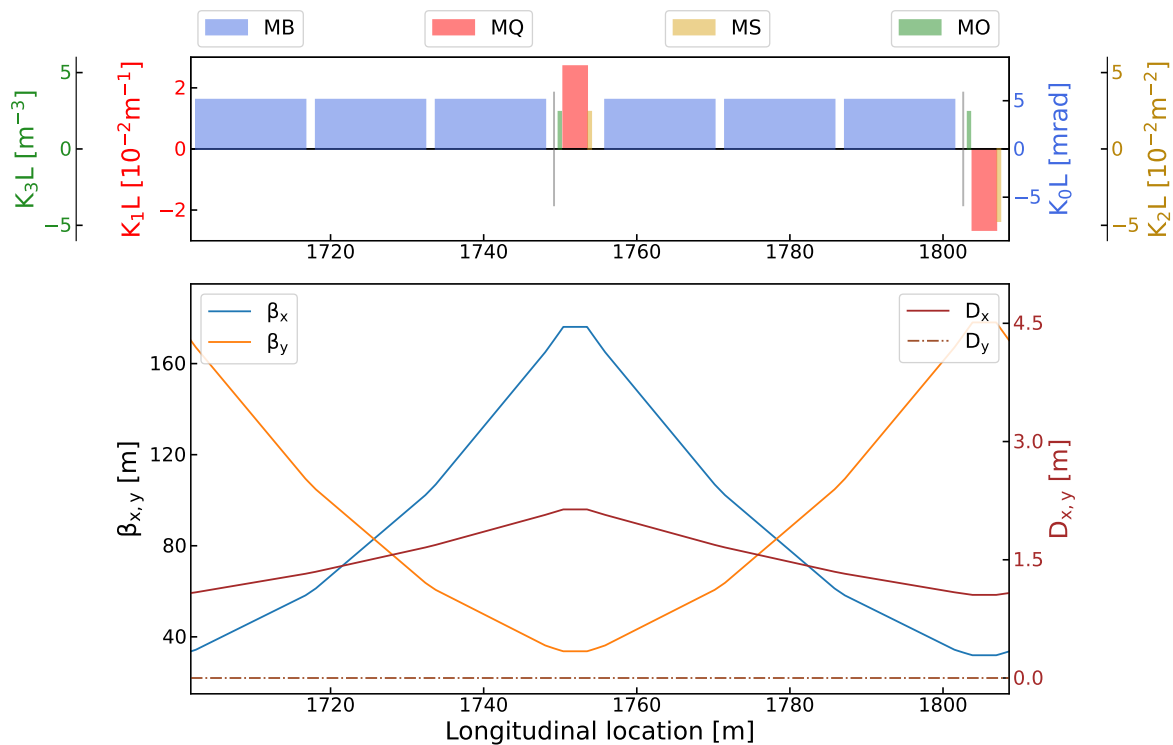


FIGURE 3.4: Simplified layout (top) and optics functions (bottom) of an LHC arc cell for the $\beta^* = 30$ cm optics.

The purpose of the arcs is that of beam transport to the more purpose-specific parts of the machine located in the **IRs**.

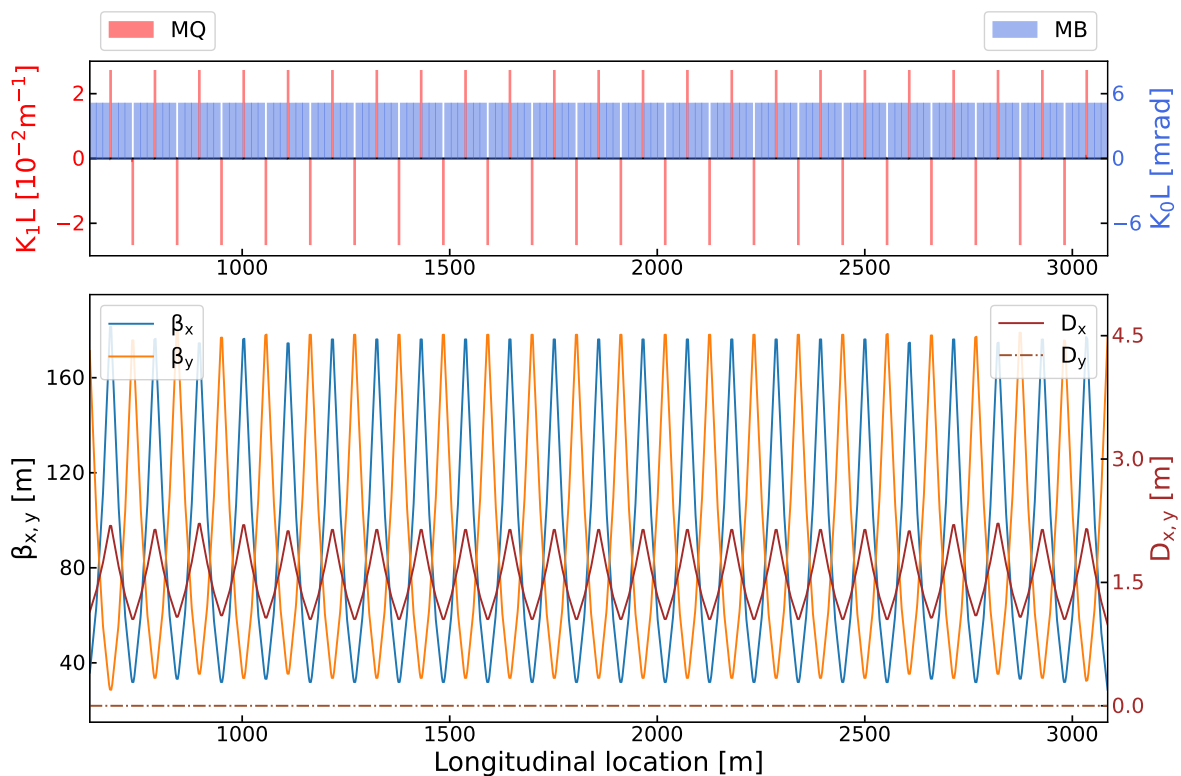


FIGURE 3.5: Simplified layout (top) and optics functions (bottom) of the LHC arc23 for the $\beta^* = 30$ cm optics.

3.1.2 The LHC Experimental Interaction Regions

In the middle of each octant, in between arcs, the LHC hosts **long straight sections** (see [Appendix B](#) for details) with specific purposes. Each of these is centered around an **Insertion Region (IR)** where a dedicated layout is in place to fulfill the section's purpose. The purpose of each straight section is briefly stated in [Fig. 3.2](#) and detailed in [Table 3.1](#).

Straight Section	Description
IR1	ATLAS Experiment
IR2	ALICE Experiment and B1 Injection
IR3	Momentum Cleaning (Collimation)
IR4	RF Systems and LHC Instrumentation
IR5	CMS Experiment
IR6	Beam Dump System
IR7	Betatron Cleaning (Collimation)
IR8	LHCb Experiment, and B2 Injection

TABLE 3.1: Description and purpose of the straight sections in the LHC. Out of the experiments only the four major ones are mentioned.

Of interest to this thesis are the **experimental insertions**, located in IR1, IR2, IR5, and IR8, where the beams are made to collide. An insertion region in which beams are made to collide is called an **Interaction Region**, or sometimes Experimental Interaction Region.



Though in the strict sense the short form **IR** stands for Insertion Region, it is commonly used to refer to an Interaction Region. It is the case in this document, where when used **IR** should be taken as Interaction Region.

At the center of the **IR**, beams are made to collide at the **Interaction Point (IP)**. In order to achieve high luminosity during collisions, and as shown in [Section 2.5](#), the β -functions at the IPs are squeezed to very small values. [Figure 3.6](#) shows the β -functions in the LHC around IP5 at both injection and collision optics, where the effect of the squeeze is apparent.

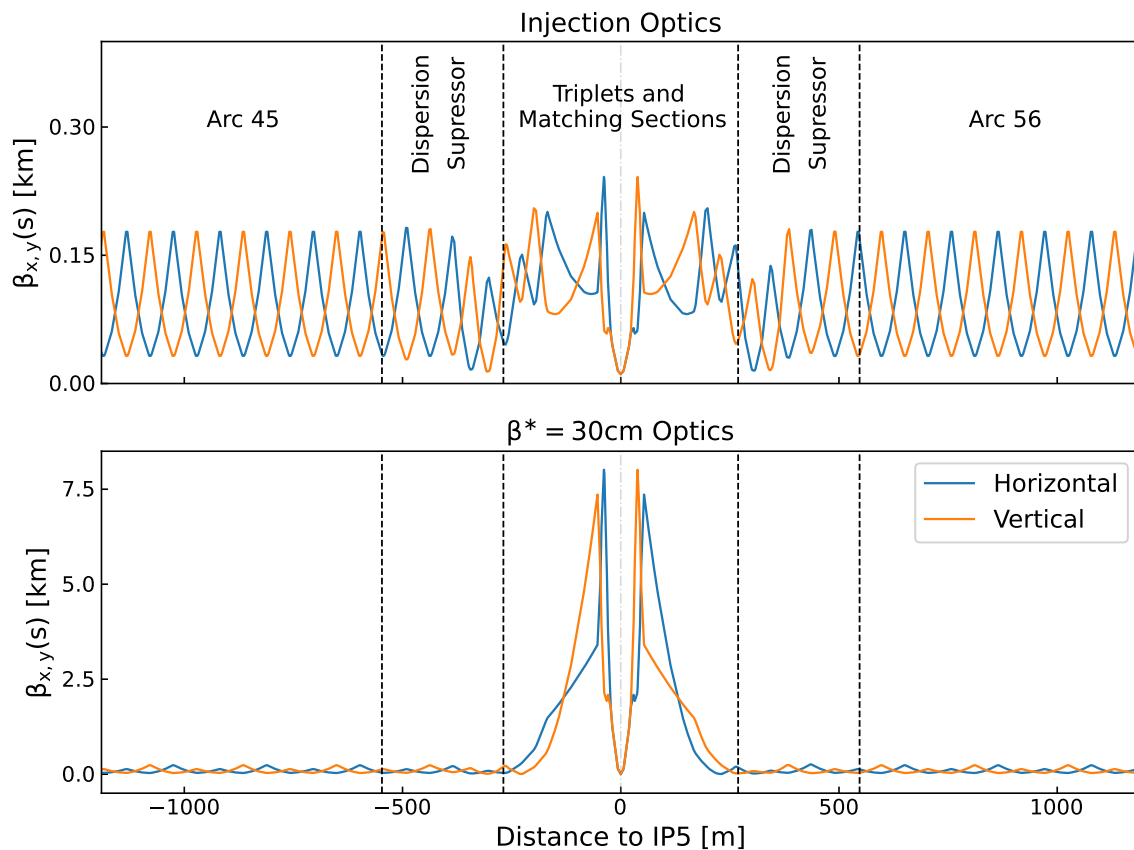


FIGURE 3.6: The horizontal and vertical β -functions in the LHC around IP5 at injection optics (top) and collision optics (bottom). Notice the drastically different scales on the vertical axes.

During normal operation for collisions the β^* at **ATLAS** and **CMS** is squeezed down to $\beta^* = 30$ cm. In this configuration, at **ALICE** and **LHCb** the β^* are only squeezed to higher values, 10 m and 2 m respectively in 2023. During collisions involving ions (Pb-Pb and p-Pb) the β^* is reduced at **ALICE** and **LHCb**. [Table 3.2](#) summarizes the β^* values for the different experiments and configurations.

IP	Lowest β^*		
	Injection Optics	Proton Collisions	Ion Collisions
IP1	11 m	30 cm	50 cm
IP2	11 m	10 m	50 cm
IP5	11 m	30 cm	50 cm
IP8	11 m	2 m	150 cm

TABLE 3.2: Value of the $\beta_{x,y}^*$ at different IPs for different optics configurations as of Run 3.

In order to achieve a small β^* at the IPs, the beams are focused using a superconducting **triplet** of quadrupoles, on either side of and close to the IP [107]. The triplet is optimized to be symmetric [108], with Q1 and Q3 being the same length at 6.3 m and Q2 split into two sub-magnets Q2a and Q2b of 5.5 m each. All three magnets are powered in series but can be adjusted individually using dedicated **trim** converters [109].

This arrangement of three quadrupoles allows for a strong focusing of the β -functions in both transverse planes. However, such an arrangement leads to high β -functions in the triplet quadrupoles themselves and neighboring elements. An illustration of the area close to IP5 for collision optics with $\beta^* = 30$ cm is given in Fig. 3.7.

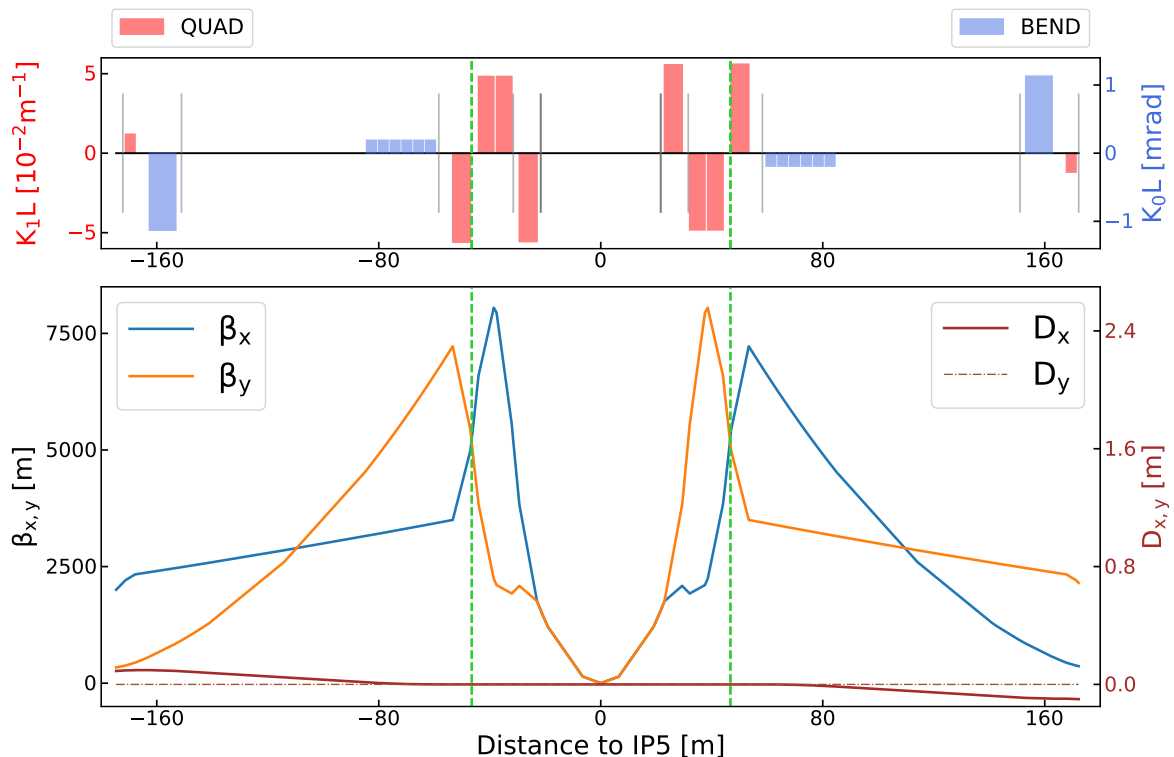


FIGURE 3.7: The simplified element layout (top) and β -functions (bottom) in the close vicinity of IP5 at $\beta^* = 30$ cm collision optics, without crossing angles.

On the layout plot the four **red patches** closest to the **IP** location correspond to Q1, Q2a, Q2b and Q3 respectively, the triplet quadrupoles. The **blue patches**

correspond to D1 (first batch closest to the IP) and D2 (the furthest dipole), the **separation/recombination dipoles** responsible for bringing the beams together/apart in the common region from/to their separate apertures in the arcs. The separation dipole D1 is made of six 3.4 m long normal conducting magnets while D2 is a superconducting twin aperture magnet 9.45 m long. Further quadrupoles after the triplet are matching quadrupoles and will be discussed later. The grey lines correspond to the location of **Beam Position Monitors (BPMs)**, measurement instrumentation.

Due to the large β -functions in the triplet quadrupoles, as can be seen in Fig. 3.7, any magnetic error in the elements of the IR would have a strong impact on the beam dynamics. To enable correction of these errors, linear and non-linear corrector magnets are installed along the IR, distributed symmetrically around the IP: every corrector magnet on one side of the IP has a counterpart on the other side. Of interest to this thesis are the a_2 **skew** quadrupole correctors installed just before Q3 on each side of the IP, the locations of which are highlighted in Fig. 3.7 by **green vertical lines**. A schematic of the corrector layout is shown in Fig. 3.8. All IR correctors are individually powered magnets.

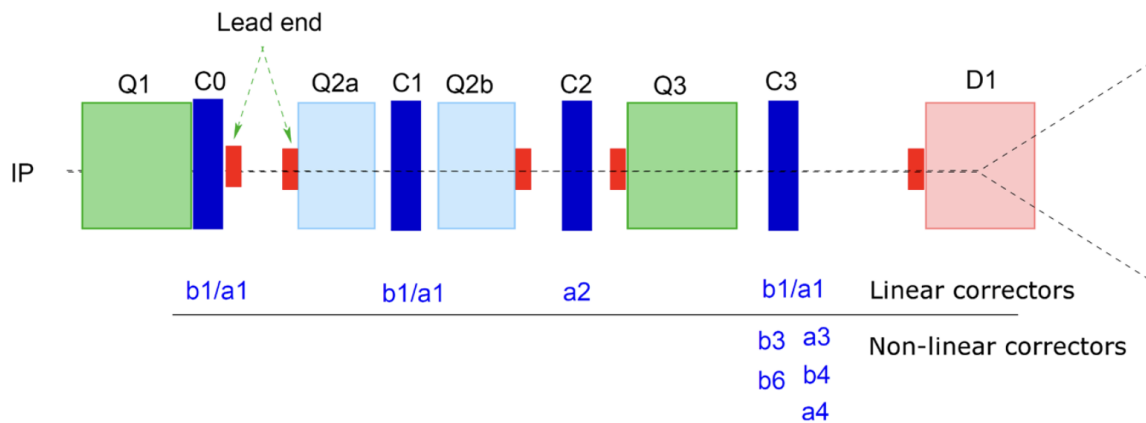


FIGURE 3.8: Layout of the triplet magnets and the linear and non-linear correctors in the LHC experimental insertions [110], showing common aperture magnets. The skew quadrupole correctors correspond to order a_2 and are located in the C2 package.

In order to prevent parasitic crossings between the two beams' bunches around the IP during collisions, **separation bumps** are implemented in a single transverse plane for each IP, in the form of closed orbit bumps. Due to the presence of these bumps, in order to reach collisions a **crossing angle** is introduced.

The optics in IR1 and IR5 are identical except for the crossing schemes. In IR1 the crossing angle is in the vertical plane while it is in the horizontal plane in IR5. Respectively, the separation bumps are in the horizontal plane in IR1 and in the vertical plane in IR5. On top of the opposite planes for the separation bump and crossing angles, the schemes themselves are slightly different.

Figure 3.9 shows the crossing schemes for both IR1 and IR5 for the $\beta^* = 30$ cm collision optics, with the location of the triplets highlighted in grey and that of the separation dipoles in yellow.

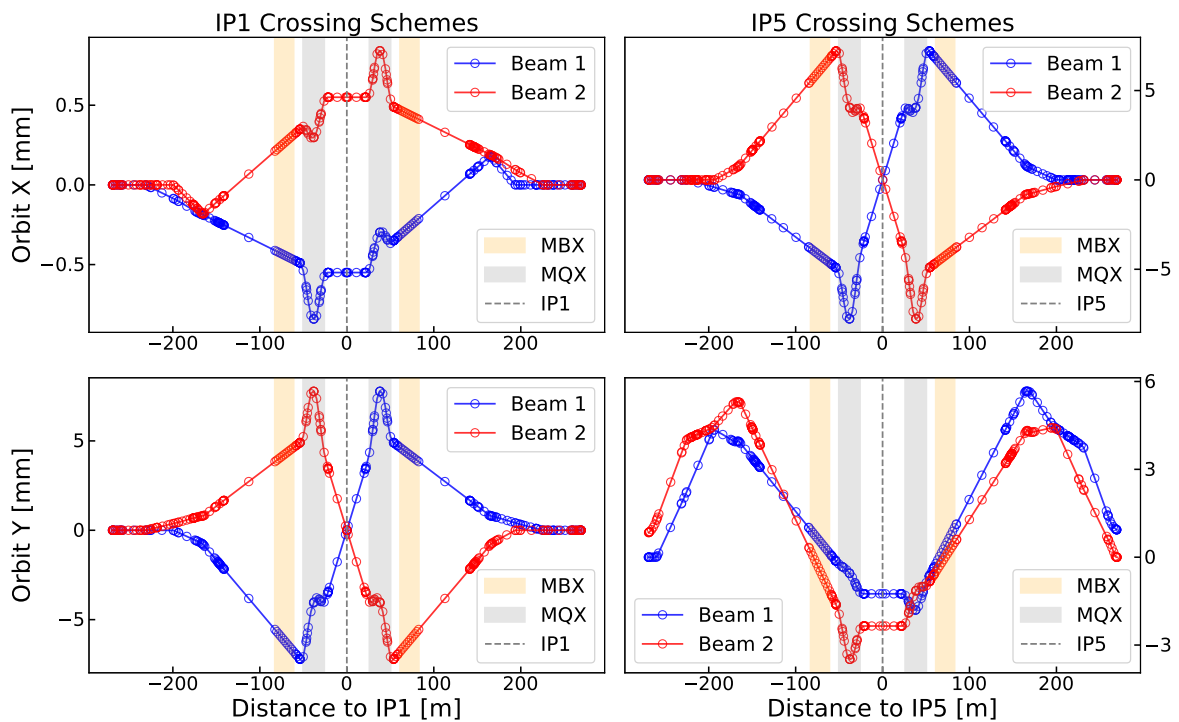


FIGURE 3.9: Crossing schemes for IR1 and IR5 at collision optics.

Other IRs, of lower interest to this thesis, have significantly different layouts which can be found in detail in [103, 111].

3.1.3 Matching Sections and Dispersion Suppressors

Assuring the transition between the arcs and the specific *optics* conditions of the IRs are *matching sections* and *dispersion suppressors*, the location of which is highlighted on Fig. 3.6. Together, the two segments are responsible for matching the *Twiss parameters* between the arcs and the IRs, and for reducing the dispersion to near-zero value at the IP, respectively.

The dispersion suppressor is made of two arc cells containing two instead of the regular three dipoles. The quadrupoles in these cells, Q7 to Q10, are powered individually. The dispersion suppressor leading to IP5 can be seen on Fig. 3.10, where the beam travels from left to right.

The matching section is made of individually powered superconducting quadrupoles Q4 to Q6. These are used to match the Twiss parameters from their values out of the arcs to that at the entrance of the triplets. In order to help the matching to the arcs the trim quadrupoles QT11 to QT13, adjacent to the FODO quadrupoles Q11 to Q13, are also individually powered and used for the matching. The full segment from the start of the dispersion suppressor to just before separation dipole D2 is shown in Fig. 3.11, where again the beam travels from left to right.

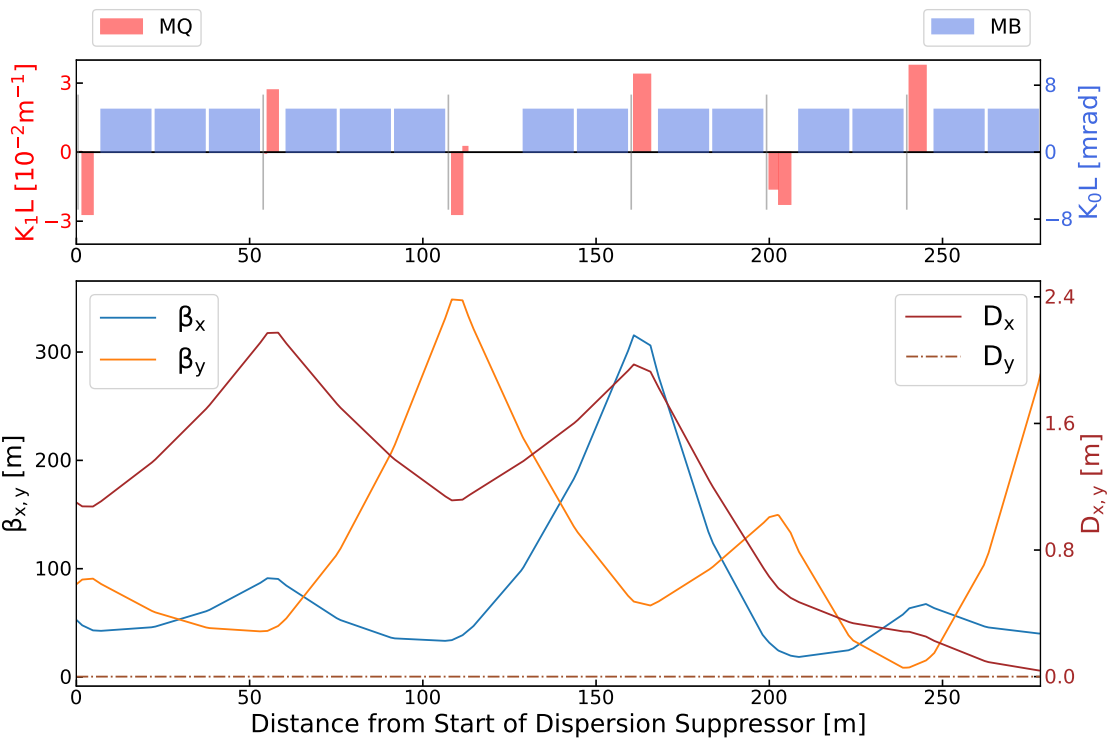


FIGURE 3.10: Simplified layout and optics functions in the dispersion suppressor leading beam 1 to IP5, for the $\beta^* = 30$ cm optics.

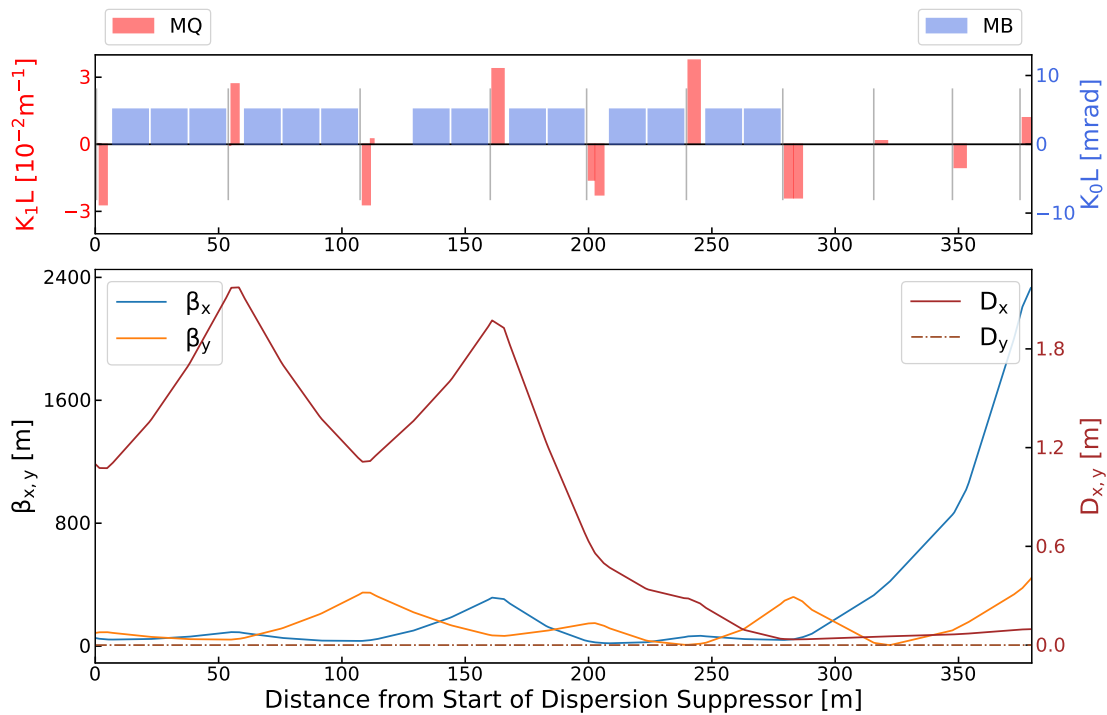


FIGURE 3.11: Simplified layout and optics functions in the matching section and dispersion suppressor leading beam 1 to IP5, for the $\beta^* = 30$ cm optics.

3.1.4 The ATS Optics Scheme

When pushing the β^* to smaller values, and therefore the β -functions in the triplets to higher ones, the chromatic effects produced by the triplet quadrupoles (Eq. (2.34)) increase drastically and need to be corrected. As the beam energy reaches its maximum, the beam size gets smaller and an aperture margin that allows to increase the β -functions appears in the arcs.

The **Achromatic Telescopic Squeeze (ATS)** optics scheme [112–114] consists of splitting the reduction of the β^* - the squeeze - into two stages. In the first one, the **pre-squeeze**, the β^* is reduced using the matching quadrupoles around the affected IP. To ease the strain on these quadrupoles (magnet strength, need for chromaticity correction and orbit control) a second stage is performed. In this stage, the **tele-squeeze**, the β^* is reduced by using the matching quadrupoles in the adjacent IRs: IR2 and IR8 for the tele-squeeze of IR1, and IR4 and IR6 for the tele-squeeze of IR5. Sectors 81, 12, 45 and 56 are therefore called ATS sectors. This modulation in the second stage sends β -beating waves down the arcs, which make the β -functions peak at the location of sextupoles and octupoles in those arcs, enhancing their efficiency.

The ratio between the peak β -functions induced in the arcs is called the **telescopic index**, or tele-index, and is denoted r_{Tele} [115]. It is defined as:

$$r_{Tele} = \beta_{ats}^{peak} / \beta_{non-ats}^{peak} \quad (3.1)$$

Figure 3.12 shows the β -functions around IP5, at two different steps in the squeeze, where one can see the β -beating waves in the neighboring ATS sectors 45 and 56.

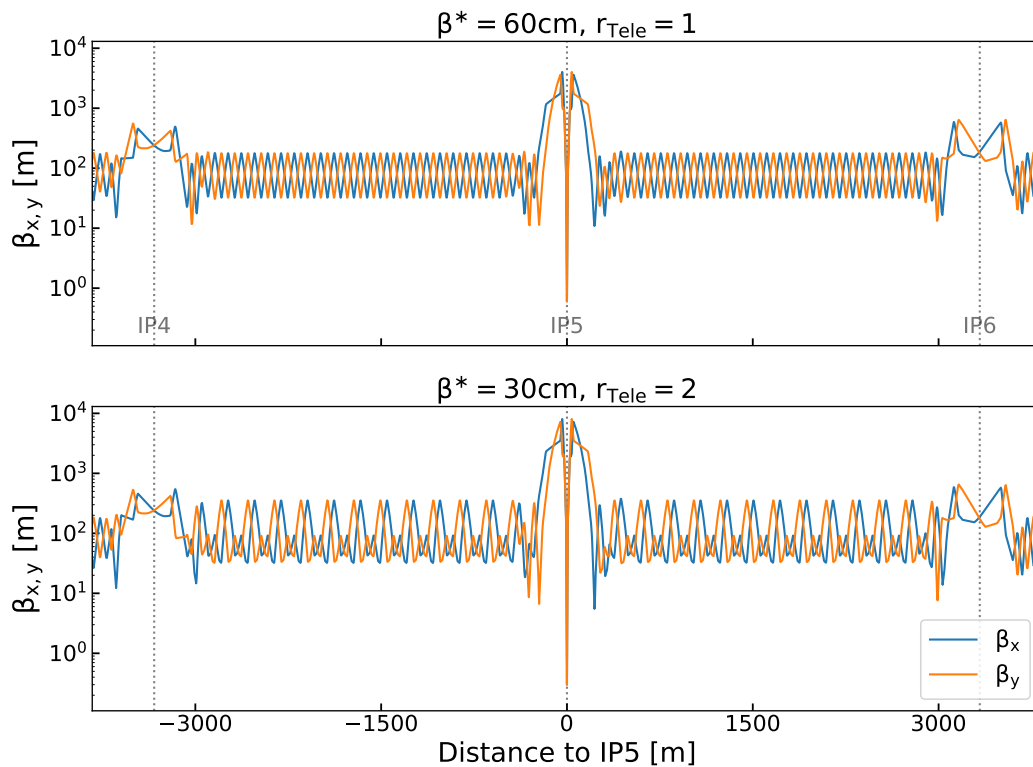


FIGURE 3.12: The β -functions in sectors 45 and 56 at different points in the squeeze for the 2022 optics: at the end of the pre-squeeze (top) and at the end of the tele-squeeze (bottom).

This ATS optics scheme has been used in the LHC since Run 2 and allowed the reduction of the collision optics β^* from its design value of 55 cm to 30 cm. It is the operational baseline for Run 3.

3.2 The Operational Cycle of the LHC

The LHC operational cycle [116], illustrated in Fig. 3.13, begins with a **pre-cycle** of certain magnetic elements [117]. A full pre-cycle is only done after an interruption of the machine operations, such as when a technical intervention is performed. During the pre-cycle no beams are present in the machine and the respective element currents are increased up to several TeV beam energy configuration, to ensure the reproducibility of the magnetic fields over successive fills. The exact nature of the pre-cycle depends on the magnetic elements.

After the pre-cycle comes the **injection** stage: beams are injected from the SPS at an energy of 450 GeV. First a probe beam consisting of just a single bunch is injected to check the validity of several systems (injection interlock, orbit, tune, chromaticity and coupling control), then a 12-bunches beam, and finally a physics beam meant for collisions is injected. At injection optics the $\beta_{x,y}^*$ at the main colliding IPs (IP1 and IP5) is 11 m. The number of bunches, their intensity and their filling pattern [118] depends strongly on the experimental demands. For **optics** measurements for instance, between one and three low intensity, non-colliding bunches of about 10^{10} protons per bunch are injected for each beam. For luminosity production a larger number of high intensity bunches is injected: of the order of a few 10^3 bunches, with $\geq 10^{11}$ protons per bunch.

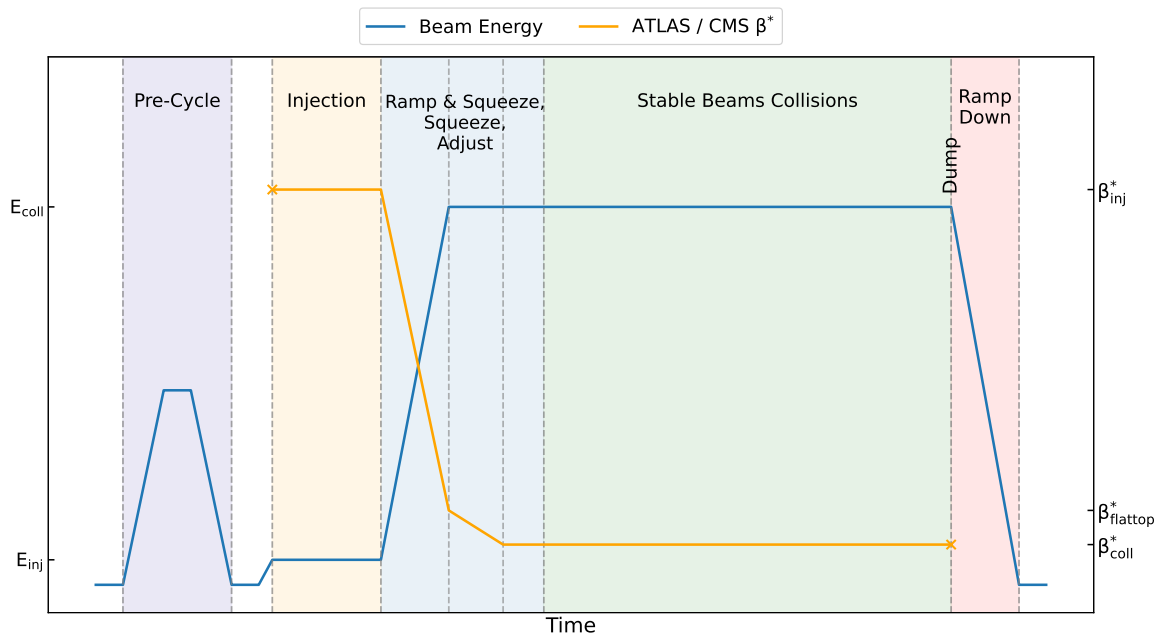


FIGURE 3.13: Simplified illustration of the LHC nominal cycle.

After injection, the beam energy is increased up to collision energy (6.8 TeV in Run 3) while the beams are squeezed and the β^* reduced. This process, called **combined ramp and squeeze**, has been used in the LHC since 2017 [119]. Before then, the squeezing process only started once the energy had reached collision value.

After reaching top energy, a configuration known as **flat-top**, another **squeeze** is performed to bring the β^* to collision value. This is when the **ATS** scheme mentioned in [Section 3.1.4](#) happens.

In a final step before luminosity production, called **adjust**, the last few needed parameters are adjusted to bring the beams into collision: tunes, crossing angles, collapse of the separation bumps. The resulting configuration, called **stable beams**, is kept throughout the fill for luminosity production. The fill ends when the beams are extracted from the machine, a.k.a. **beam dump**, after which the cycle ends by a **ramp down** of the magnets' currents. Some magnets pre-cycle during the ramp down.

The working point is changed several times along the cycle for stability reasons. As of 2022, at injection the transverse tunes are (62.275, 60.293). The working point is brought to (62.28, 60.31) during the ramp and squeeze, at the end of which it is moved to (62.311, 60.318). A final change is made in the adjust step, where the tunes are brought to (62.314, 60.319) before going into collisions. This last setting may be changed by machine operators during stable beams in order to optimize the beam lifetime.

Starting in [Run 3](#), some additional complexities were added to the cycle that are not shown in [Fig. 3.13](#). In 2022 a **β^* -leveling** was introduced, where collisions start at $\beta^* = 60$ cm and the β^* is progressively reduced to 30 cm during stable beams. This is done in order to limit pile-up for the experiments (at around 52 events per bunch crossing for the main **IPs** in 2022) and the impact on the triplets' cryogenics capacity [[120](#), [121](#)]. This β^* -leveling will start at $\beta^* = 1.2$ m in 2023 and 2024, with a higher pile-up value. Starting in 2023 an **anti-telescope** is performed in the ramp to allow this earlier leveling, and a crossing-angle rotation at **LHCb** (IP8) is done when reaching flat-top in order to maintain physics conditions at the IP regardless of the LHCb spectrometer polarity [[120](#)].

3.3 Optics Measurements and Corrections

The quality of the **LHC** optics has a significant impact on the machine's performance. For instance, the luminosity achieved by the machine is directly determined by the **β -functions** at the **IPs**, as seen in [Section 2.5](#). Furthermore, a good control of the β -functions is essential for safe beam operations due to the destructive power of the LHC beams, and the machine is subject to strict limits on the deviation from model values [[122](#)]. One can then define the **β -beating**, a good indicator of the quality of the linear **optics**, as the relative deviation of the machine's β -functions from that of the design values. It is defined as:

$$\frac{\Delta\beta_z(s)}{\beta_z(s)} = \frac{\beta_z(s)_{\text{measured}} - \beta_z(s)_{\text{model}}}{\beta_z(s)_{\text{model}}} \quad \text{where } z = x, y . \quad (3.2)$$

In order to verify the machine's beam optics and find any potential faults, or deviations from the model values, beam measurements are necessary. From these, comparisons to model values are made which allow for an assessment and understanding of the errors in the machine; and corrections can be calculated and applied to bring the optics as close to the nominal scenario as possible. As the linear optics functions impact the non-linear phenomenology of an accelerator, a well understood and corrected linear optics is a pre-requisite to study of the non-linear dynamics.

Figure 3.14 shows the β -beating for beam 2 of the LHC in its 2022 virgin¹ state and with all determined corrections trimmed in, at the end of the commissioning phase. Correction of the linear optics functions towards their nominal values also leads to an enhanced rms closed orbit around the ring since the orbit feedback algorithms in the LHC assume the nominal LHC model [123, 124].

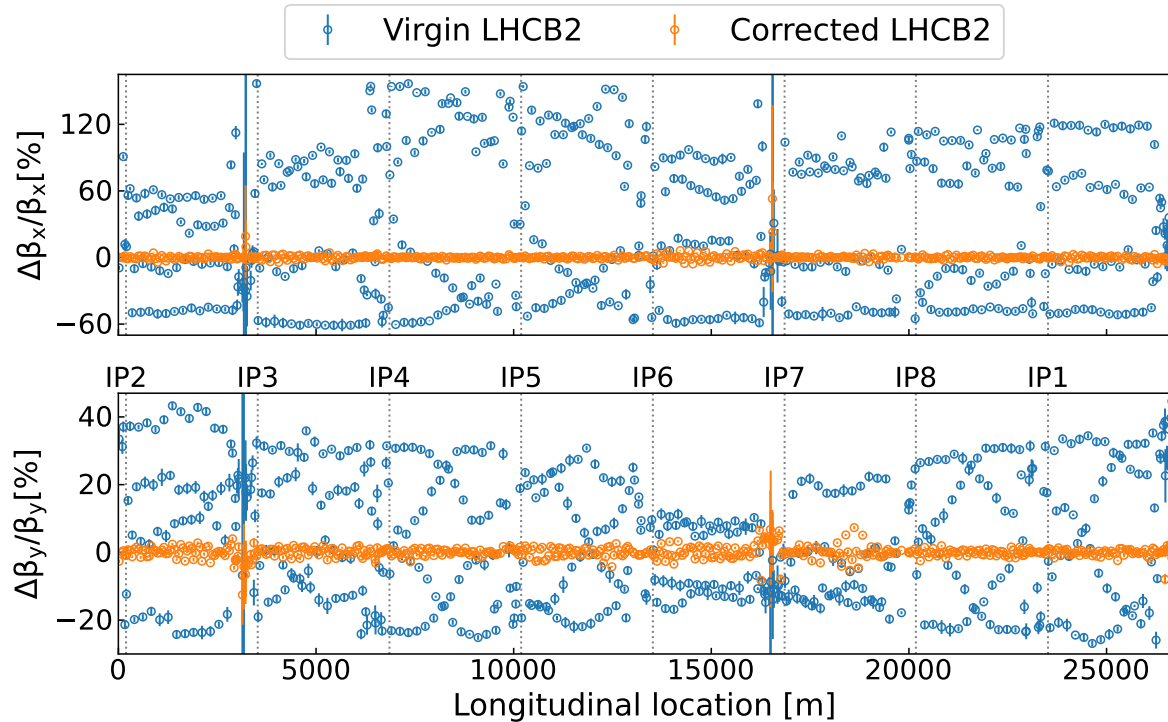


FIGURE 3.14: The measured β -beating at the beginning (blue) and end (orange) of the LHC 2022 commissioning, for beam 2.

3.3.1 Beam Instrumentation for Optics Measurements

Circular machines such as the LHC include a variety of beam instrumentation devices which serve various purposes, from injection kickers and feedback systems used in regular operations to dedicated devices for optics measurements. Below is an introduction to those of interest for optics measurements.

Beam Position Monitors and Tune Measurement

Beam Position Monitors (BPMs) are one of the most crucial devices for beam diagnostics. They measure the transverse center of charge of circulating bunches, either in a given plane for single plane BPMs, or in both planes simultaneously for dual plane BPMs. In the LHC, this centroid beam position can be measured on a turn-by-turn and bunch-by-bunch basis by around 500 dual plane BPMs across the machine. So-called stripline BPMs are employed in the common apertures as they can discriminate between counter-rotating bunches, while button BPMs are used in the remaining portions of the

¹The term *virgin* refers to the state of the machine without any corrections.

machine [103]. The location of BPMs in the lattice can be seen as vertical grey lines, in an insertion region such as IR5 in Figs. 3.7 and 3.11 and in the arcs in Fig. 3.4.

In the LHC, the **Base Band Tune (BBQ)** system [125, 126] provides continuous, passive monitoring of the tune by performing spectral analysis of the turn-by-turn data at a specific location in IR4. The **BBQ** is also capable of measuring an estimation of the linear coupling at the measurement location, which can be used as a rough first estimate for the coupling in the machine. While it is possible to assess tune and coupling with the **BBQ** without external excitation of the beam, the LHC chirp can generate small transverse oscillations to improve the quality of these measurements.

Experimental Kickers

For the study of beam dynamics, measurements are done by inducing large transverse oscillations of the beam to be picked up by the **BPMs**, typically much larger than natural beam size. Large oscillation amplitudes are required to provide a good signal-to-noise ratio. The spectral analysis of measured turn-by-turn positions provides valuable insights in all the modes contained in the particle motion, at each BPM location. In the **LHC** kicker dipole magnets are available for both beams, and are located in IR4. These magnets can operate in three possible modes, referred to as the **Tune Kicker (MKQ)**, **Aperture Kicker (MKA)**, and the **AC dipole**.

The tune and aperture kickers [127, 128] operate as traditional kicker magnets: ramping their magnetic field up and down in a single turn, applying a transverse kick to the beam and then allowing free motion. The name only refers to the amplitude of induced oscillations: lower strength to measure the tune and higher strength to measure the available dynamic aperture. Unfortunately, at top energy the amplitude of oscillations achievable with the kickers is considerably reduced. Additionally, the beam will decohere after being kicked: the momentum distribution of particles in the bunch will cause the observed centroid of the beam to show a decaying oscillation [129]. As a consequence a beam can only be kicked a certain number of times before needing to be replaced, and it can take up to several hours to reach the same machine configuration again, as the cycle detailed in Section 3.2 needs to be respected.

For **optics** measurements lasting oscillations are preferred, as they increase the spectral resolution and reduce the noise floor in the spectral analysis of turn-by-turn data. Furthermore, a non-destructive excitation method is preferred in order not to alter the beam state, which allows for repeated measurements.

Such a non-destructive, sustained excitation of the beams can be achieved with an **AC dipole**. It is a rapidly oscillating dipole magnet which can generate forced driven oscillations with large amplitudes by exciting the beam at frequencies close to the natural tunes [130, 131]. Moreover, the AC dipole strength can be ramped up and down adiabatically [132] and kept constant at high amplitudes, allowing for long lasting coherent oscillations of the beam. These properties, fulfilling the aforementioned requirements, make the AC dipole the most important tool for optics measurements in the LHC. A comparison of the turn-by-turn data obtained from beam excitation with a single free kick and an AC dipole is shown in Fig. 3.15.

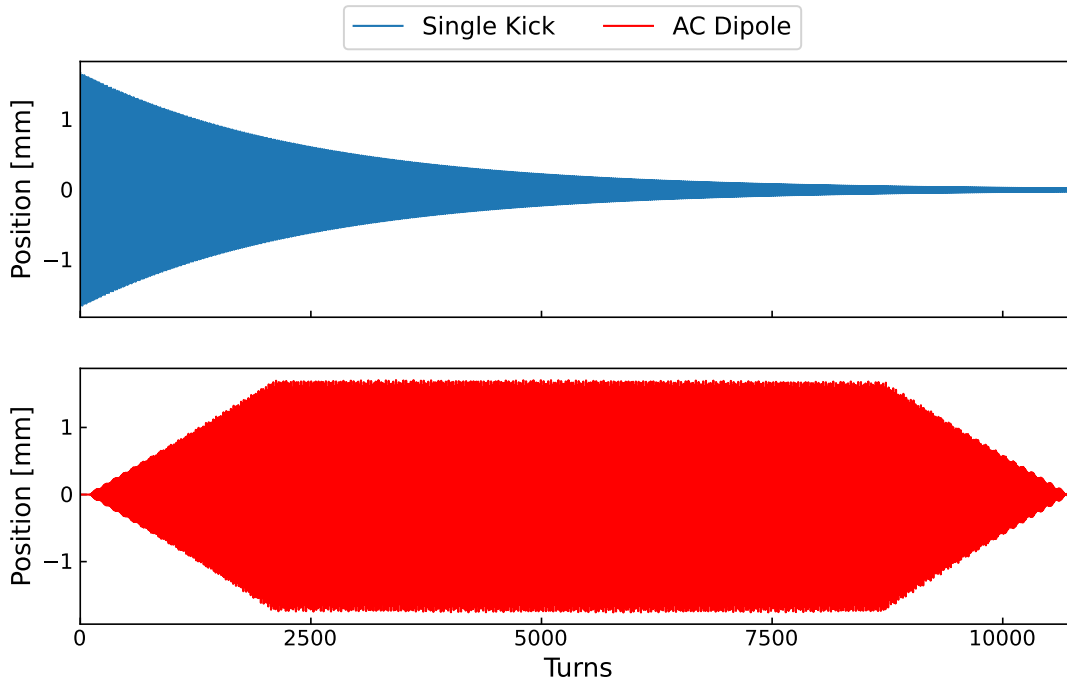


FIGURE 3.15: Comparison of turn-by-turn data obtained from a single free kick (top) and an AC dipole excitation (bottom).

3.3.2 Optics Measurements

Optics measurements are performed by exciting the beam and analyzing the resulting betatron oscillations. The various steps of the measurement and analysis process are described below.

Beam Excitation

The first step of optics measurements in the LHC is to excite the beams with the AC dipole. As excitation of the beams to large amplitudes can represent a risk to the safety of the machine, such measurements are only performed with one to three low intensity bunches of about 10^{10} protons each. In the LHC, the AC dipole has a ramp-up and ramp-down time of 2000 turns, and is able to drive excitations at maximum strength for 6600 turns before ramping down, as can be seen in Fig. 3.15. When exciting the beam, the turn-by-turn position of the bunch is measured by the BPMs across the machine and only the turns corresponding to the maximum AC dipole strength are used for analysis.

It is important to note that the forced oscillations introduce a perturbation on the optics. In the case of free oscillations, it was shown in Chapter 2 that the transverse motion goes according to Eq. (2.6). For the transverse plane z , by considering $\phi_{z,0} = 0$ at the start of machine one gets:

$$z(s) = \sqrt{2J_z\beta_z(s)} \cos(\phi_z) , \quad z = x, y , \quad (3.3)$$

where ϕ_z and J_z are the action and angle variables introduced in Section 2.1.3, respectively.

When the AC dipole is driving the beam, an equivalent parametrization exists, and denoting the transverse driven coordinate as $z_D(s)$ one can express it as [130, 133]:

$$z_D(s) = \sqrt{2J_z\beta_z(s)} \cos(\phi_z) + \sqrt{2A\beta_{D,z}(s)} \cos(\phi_D) , \quad (3.4)$$

where A and ϕ_D are respectively the action and angle variables of the forced oscillations, and $\beta_{D,z}(s)$ is the β -function modified by the AC dipole. The form of Eq. (3.4) makes the assumption that the forced oscillation term depends only on ϕ_D .

The β -function modified by the AC dipole, corresponding to the perturbed optics under forced oscillations, is given by [134]:

$$\beta_{D,z}(s) = \frac{1 + \lambda_D^2 - 2\lambda_D \cos(\psi_D(s))}{1 - \lambda_D^2} \beta_z(s) , \quad (3.5)$$

where $\psi_D(s)$ is the phase advance with respect to the AC dipole location. The λ_D term is dependent on the gap between the driven and natural tune, and is defined by [134]:

$$\lambda_D = \frac{\sin(\pi\delta_D)}{\sin(2\pi Q_z + \pi\delta_D)} , \quad (3.6)$$

where $\delta_D = Q_D - Q_z$ corresponds to the aforementioned gap, often called the tune delta. In the LHC, the AC dipole is usually driven with $\delta_{D,x} = -0.01$ and $\delta_{D,y} = 0.012$.

One can see in Fig. 3.16 the impact of an AC dipole on the vertical β -function in a simple FODO lattice, where the difference between the free and forced cases is apparent.

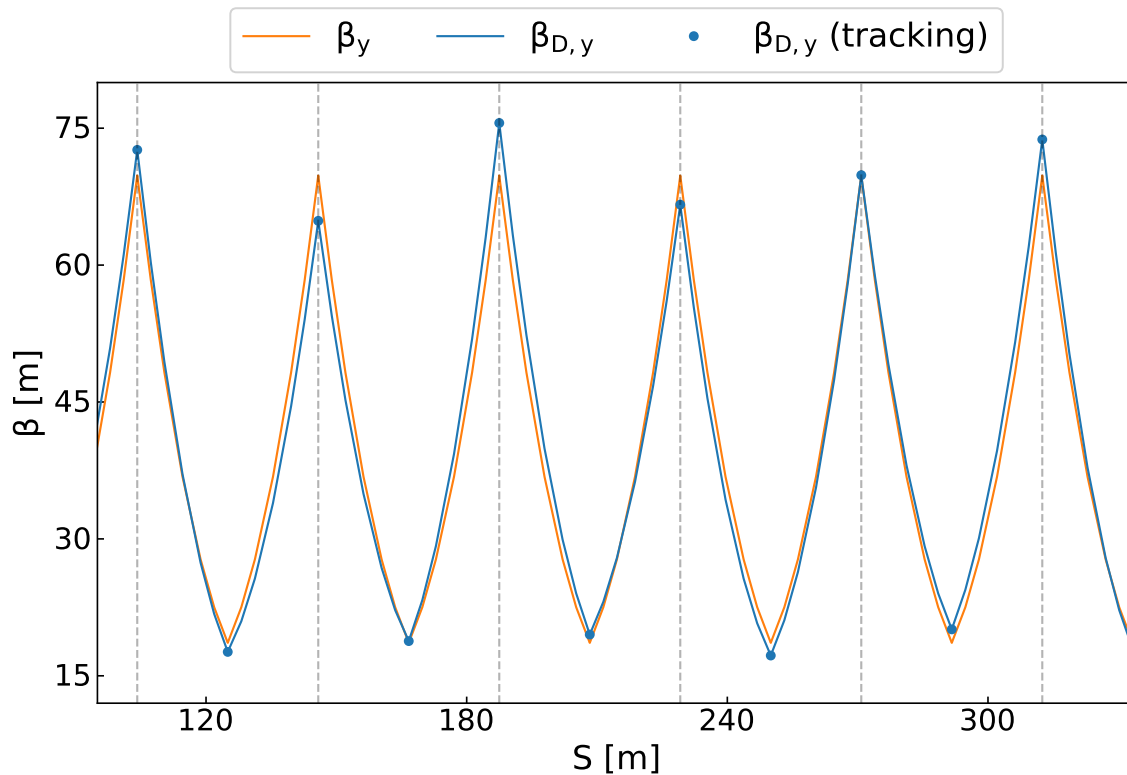


FIGURE 3.16: Resulting vertical β -functions in a FODO lattice in the case of free (orange) and driven (blue) oscillations.

One can then determine the β -beating induced by the AC dipole, as defined in Eq. (3.2). From Eq. (3.5) and Eq. (3.6) one can express this beating according to:

$$\frac{\beta_{D,z} - \beta_z}{\beta_z} = \frac{1 + \lambda_D^2 - \lambda_D \cos(2\psi_D - 2\pi Q_z)}{1 - \lambda_D^2} - 1, \quad (3.7)$$

with Q_z the natural transverse tune of the machine. Figure 3.17 shows this β -beating for various phase advances between the AC dipole and an element where the observation would be made. The vertical black lines correspond to the usual tune deltas used in LHC measurements, and the values are displayed for the two fractional tunes of a common working point for LHC measurements: $(Q_x, Q_y) = (0.28, 0.31)$. For these usual settings the AC dipole induced β -beating reaches no more than 9%.

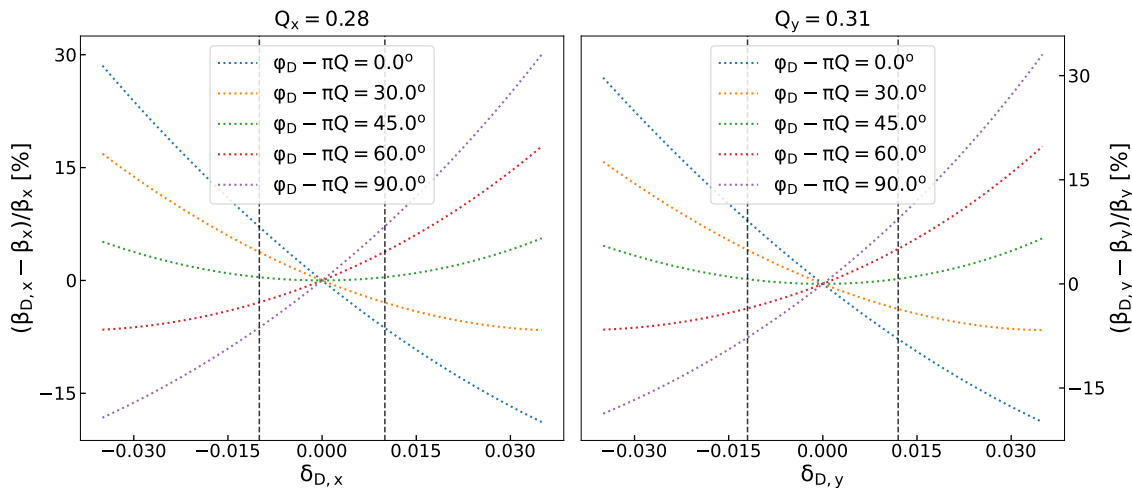


FIGURE 3.17: AC dipole induced β -beating as a function of δ_D , for various phase advances between the AC dipole and a given location in the ring where the observation would be made. The results are shown for the horizontal (left) and vertical (right) planes with a common working point used for measurements.

As a consequence, the measured oscillations, associated optics functions and [Resonance Driving Terms \(RDTs\)](#) will not be those of the natural machine. This impact of the AC dipole on the optics is taken into account and compensated in analysis steps [135], and this compensation is expanded later on in this chapter.

Spectral Analysis

As a first step, the recorded raw turn-by-turn data is cleaned of noise using a [Singular Value Decomposition \(SVD\)](#) approach [136]. An interpolated Fourier Transform is then performed on the cleaned data [137, 138], which provides information about the phase and the measured amplitude at each BPM. Automatic outlier detection is available based on the spectra of BPMs, both as an automated step [139] and a manual step (removing BPMs with exact-zero signals, wrong tune lines etc.). Figure 3.18 shows a horizontal spectrum obtained from a measurement during the Run 2 commissioning in 2022, with the main tune lines identified. The frequency space is zoomed for clarity.

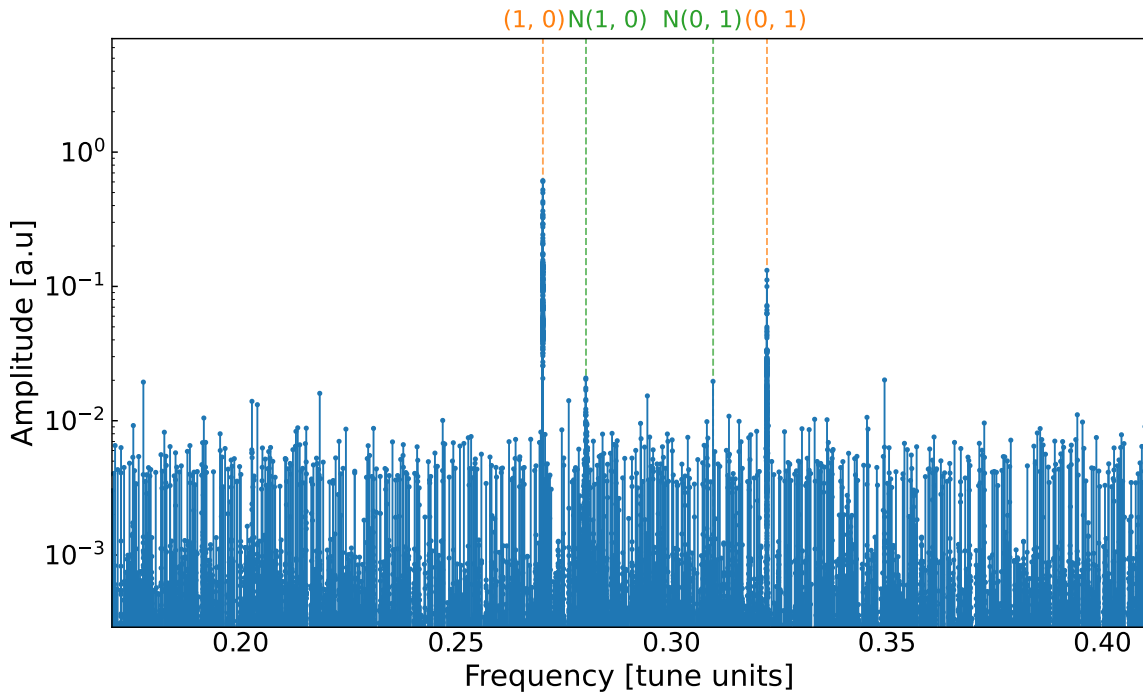


FIGURE 3.18: Horizontal spectrum from the frequency analysis of a measurement taken during the Run 2 commissioning in 2022. The main (orange) and natural (green) tune lines are indicated, where for instance (0,1) corresponds to the $0 \cdot Q_x + 1 \cdot Q_y = Q_y$ tune in the horizontal spectrum.

Optics Reconstruction

With knowledge of the phase information at each measuring BPM, and with knowledge of the model machine, the transverse optics functions can be determined. For LHC measurements the model knowledge traditionally comes from design studies done with the MAD-X code [59]. The β -function at a given BPM can be calculated from the measured phases of 3 BPMs (i, j, k), according to [31, 140]:

$$\beta_z^{\text{phase}}(s_i) = \frac{\cot(\phi_z(i \rightarrow j)) + \cot(\phi_z(i \rightarrow k))}{\cot(\phi_z^m(i \rightarrow j)) + \cot(\phi_z^m(i \rightarrow k))} \beta_z^m(s_i), \quad z = x, y, \quad (3.8)$$

where the superscript m denotes the model values and $\phi_z(i \rightarrow j)$ is the phase advance between the i^{th} and j^{th} BPMs. The BPMs do not necessarily need to be consecutive, and specific phase advances between the chosen BPMs increase the precision of the measurement. This method has also been extended to use specifically chosen combinations of N BPMs [141, 142], which improves its precision as it then only depends on the measured phase advances and is fully independent of BPM calibration [143].

From Eq. (2.24) one infers that the β -function can also be determined directly from the amplitude A of the oscillations recorded at BPMs:

$$\beta_z^{\text{amp}}(s_i) = \frac{A_z^2(s_i)}{2J_z}. \quad (3.9)$$

Using the peak-to-peak oscillation amplitude over N BPMs, one can determine the calibration-dependent [144] term J_z according to:

$$2J_z = \frac{\sum_{n=1}^N \left(\frac{\text{peak-to-peak}}{2} \right)_n^2 / \beta_z^m}{N}. \quad (3.10)$$

The reconstructed β -function from amplitude is dependent on the calibration of measuring BPMs. Figure 3.19 shows the β -beating reconstructed from phase and from amplitude for a 2022 LHC measurement at $\beta^* = 30$ cm, where the lower precision from reconstructing from amplitude can be seen.

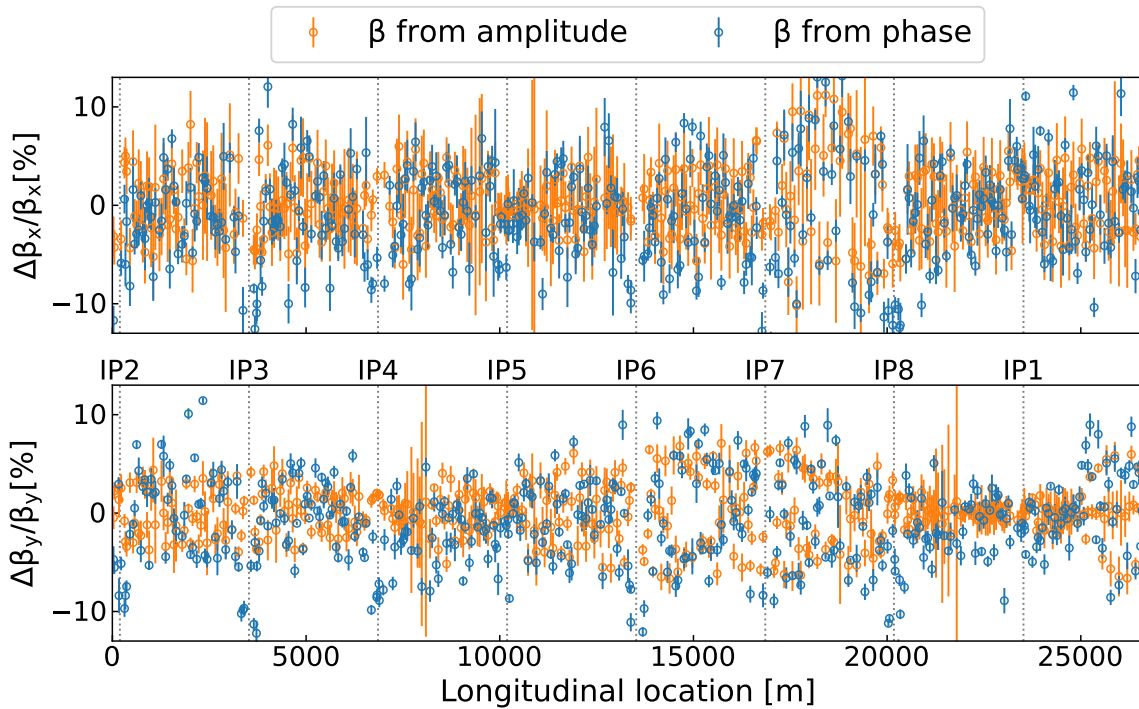


FIGURE 3.19: The β -beatings obtained when reconstructing the β -functions from phase (blue) and from amplitude (orange) in an LHC measurement in 2022.

Other Twiss parameters can be reconstructed from the phases and β -functions. Chromatic parameters are reconstructed by performing measurements at different momentum settings. By adjusting the frequency of the accelerating cavities, typically between -100 Hz and $+100$ Hz of the nominal setting, the energy of the beam is changed and the dispersion is then determined from the mean orbit recorded at different energies. Recent improvements have allowed doing so in a single measurement by modulating the RF frequency while transversely exciting the beam [137, 145].

One can also compute the normalized dispersion $D/\sqrt{\beta}$ which is independent from model values and BPM calibration [146].

K-Modulation

It is possible to directly measure the β^* at the IPs without beam excitation using the k -modulation technique [147]. By modifying the strength of individual quadrupoles and

recording the resulting tune changes, one can determine the average β -functions at the modulated quadrupole according to [31]:

$$\begin{aligned}\beta_z^{\text{avg}} &= \pm [\cot(2\pi Q_z) (1 - \cos(2\pi\Delta Q_z)) + \sin(2\pi\Delta Q_z)] \frac{2}{\Delta k L}, \\ &\approx \pm 4\pi \frac{\Delta Q_z}{\Delta k L},\end{aligned}\quad (3.11)$$

where Δk is the quadrupole strength variation, L its length and ΔQ_z the resulting tune variation in the machine. Figure 3.20 shows an example of the data retrieved from the k -modulation.

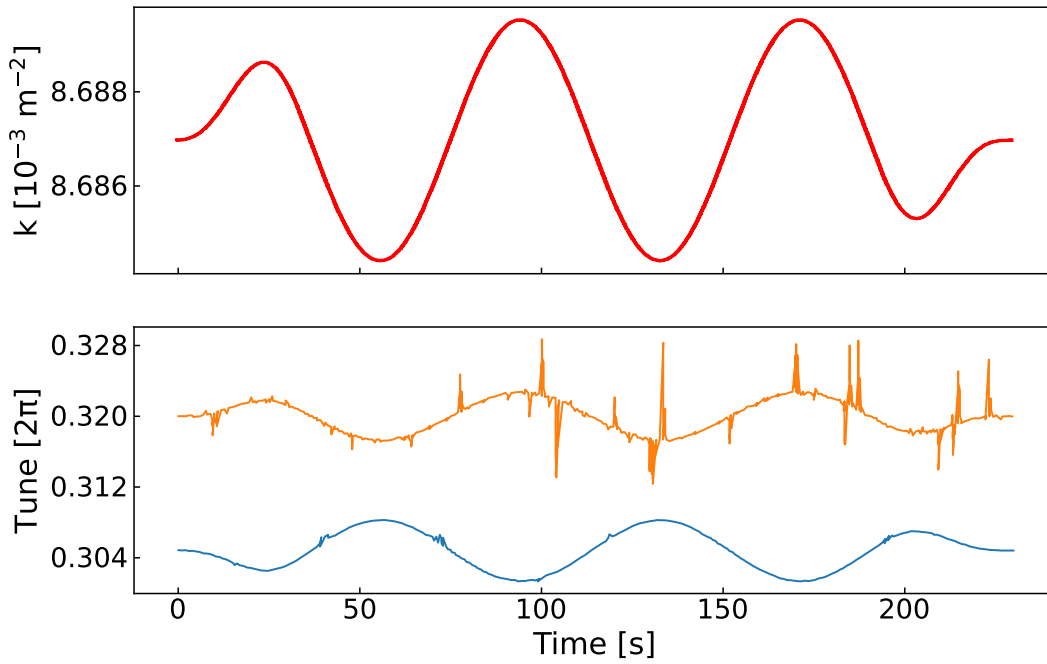


FIGURE 3.20: Example data from the k -modulation of the first quadrupole left of IP1. The top plot shows the quadrupole strength variation over time and the bottom plot the resulting horizontal (blue) and vertical (orange) tune variations.

By modulating both innermost quadrupoles near the IP, one determines the average β -functions in these quadrupoles, which can then be propagated through the drift space in between to determine both the β^* value as well as any potential waist shift [148]. In the LHC the k -modulation technique is the main method to determine the β^* at the IPs. Its results are also used as a better reconstruction of the β -function values in the inner BPMs.

3.3.3 Reconstruction of Linear Coupling RDTs

Of particular relevance to this thesis are the *betatron coupling RDTs* f_{1001} and f_{1010} , and it is worth spending some time detailing their reconstruction. As mentioned in Section 2.3.4, the f_{jklm} RDTs can be determined from the specific *spectral lines* arising during the spectral analysis of turn-by-turn data. By the term spectral lines one

refers here to the Fourier transform of the complex Courant-Snyder coordinate, which corresponds to:

$$\begin{aligned} H^\pm(n_x, n_y) &= \mathcal{F}\{h_x^\pm\}(n_x Q_x + n_y Q_y) , \\ V^\pm(n_x, n_y) &= \mathcal{F}\{h_y^\pm\}(n_x Q_x + n_y Q_y) , \end{aligned} \quad (3.12)$$

in which H indicates a line in the spectrum of horizontal turn-by-turn data, and V a line in the spectrum of vertical turn-by-turn data.

As seen in Eq. (3.12) the Courant-Snyder variables defined in Eq. (2.51) are needed. Since the momentum present in the expression of h_z^\pm is not a quantity directly measurable from a single BPM, it is reconstructed using two successive BPMs:

$$\hat{p}_{z_n} = \frac{\hat{z}_{n+1} - \hat{z}_n \cos(\Delta\phi_z)}{\sin(\Delta\phi_z)} , \quad z = x, y , \quad (3.13)$$

with $\Delta\phi_z$ the phase advance between the n^{th} and $(n+1)^{\text{th}}$ BPMs in the transverse z plane. In Eq. (3.13) it is assumed that the region between the two BPMs is free of coupling sources as well as non-linearities contributing to the main line and the coupling line in each spectrum.

With the information from two BPMs, one can compute the spectral lines according to Eq. (3.12). Starting from Eq. (2.56), one can for instance substitute $j = 1$, $k = 0$, $l = 0$, $m = 1$ and obtain $H(0, 1) = |f_{1001}| (2I_y)^{\frac{1}{2}}$, the amplitude of the line at Q_y in the horizontal spectrum.

With the proper values for j, k, l, m and using lines from the vertical spectrum one can cancel out the dependence on the action and look to obtain $|f_{1001}|$. However, it is possible - and likely - that the BPM calibrations aren't perfect, in which cases the measured and real coordinates differ:

$$\begin{aligned} x^{\text{meas}} &= C_x x^{\text{real}} , \\ y^{\text{meas}} &= C_y y^{\text{real}} . \end{aligned} \quad (3.14)$$

One can cancel out the $C_{x,y}$ factors by dividing any line amplitude by that of the main line, to create normalized spectral lines. Of interest for the coupling RDTs are the following:

$$\begin{aligned} A_{0,1} &= \frac{H(0, 1)}{|H(1, 0)|} , \\ B_{1,0} &= \frac{V(1, 0)}{|V(0, 1)|} , \\ A_{0,-1} &= \frac{H(0, -1)}{|H(1, 0)|} , \\ B_{-1,0} &= \frac{V(-1, 0)}{|V(0, 1)|} , \end{aligned} \quad (3.15)$$

where the $A_{0,1}$ and $B_{1,0}$ normalized spectral lines contain information on f_{1001} whereas the $A_{0,-1}$ and $B_{-1,0}$ ones contain f_{1010} .

By combining these normalized spectral lines, it has been shown that the amplitudes of the coupling RDTs may be expressed as [149, 150]:

$$\begin{aligned} |f_{1001}| &= \frac{1}{2} \sqrt{|A_{0,1} B_{1,0}|} = \frac{1}{2} \sqrt{\frac{H(0,1)V(1,0)}{V(0,1)H(1,0)}} , \\ |f_{1010}| &= \frac{1}{2} \sqrt{|A_{0,-1} B_{-1,0}|} = \frac{1}{2} \sqrt{\frac{H(0,-1)V(0,-1)}{V(0,1), H(1,0)}} , \end{aligned} \quad (3.16)$$

and the phases as:

$$\begin{aligned} q_{1001} &= \phi_{V(1,0)} - \phi_{H(1,0)} + \frac{\pi}{2} = \phi_{H(0,1)} - \phi_{V(0,1)} + \frac{\pi}{2} , \\ q_{1010} &= \phi_{H(0,-1)} - \phi_{V(0,1)} + \frac{\pi}{2} = \phi_{V(-1,0)} - \phi_{H(1,0)} + \frac{\pi}{2} . \end{aligned} \quad (3.17)$$

Here $H(1,0)$ corresponds to the line in the horizontal spectrum at Q_x while $H(0,1)$ corresponds to the line at Q_y in the same spectrum. In [47] a table is given that relates various spectral lines to amplitudes and phases of the corresponding resonances and RDTs. From the amplitude and phase information of Eqs. (3.16) and (3.17) the complex coupling RDTs are reconstructed as:

$$\begin{aligned} f_{1001} &= |f_{1001}| e^{iq_{1001}} , \\ f_{1010} &= |f_{1010}| e^{iq_{1010}} . \end{aligned} \quad (3.18)$$

In Fig. 3.18, which shows a spectrum from an LHC measurement during the 2022 commissioning, the coupling lines are visible and highlighted. This reconstruction method has successfully been used to measure linear coupling RDTs in the LHC since Run 1 [135, 151, 152].

AC dipole Compensation

Mentioned in Section 3.3.2 is the effect of AC dipole excitation on the observables, which differ from those of the natural machine. This effect is also present in the reconstructed coupling RDTs, and must be compensated for in order to obtain the natural machine's values. Several compensation methods exist, with the most straightforward being the application of a rescaling factor to the reconstructed RDTs.

Using this rescaling, one can express the driven RDTs as [153]:

$$\begin{aligned} f_{\pm,x}^{\text{driven}} &= \frac{\sin(Q_x \pm Q_y)}{\sin(Q_{D,x} \pm Q_y)} f_{\pm} , \\ f_{\pm,y}^{\text{driven}} &= \frac{\sin(Q_x \pm Q_y)}{\sin(Q_x \pm Q_{D,y})} f_{\pm} , \end{aligned} \quad (3.19)$$

where $f_+ = f_{1010}$ corresponds to the sum resonance, $f_- = f_{1001}$ corresponds to the difference resonance, $f_{\pm,x}^{\text{driven}}$ denotes the driven RDT as measured from horizontal turn-by-turn data, $Q_{D,z}$ is the driven tune in the transverse plane z and Q_z the natural tune in the same plane. Here the f_{\pm} notation is used for conciseness.

A fully analytical compensation of the AC dipole effect can be found in [135, 154] but will not be detailed in this document. A comparison of these methods' efficiency can be found in [155].

Single BPM

It is possible to approximate the coupling RDTs from the real coordinates using a single BPM, and doing the reconstruction without the momentum information. In this case, where only the position data is used, the spectral analysis will mix up lines $Z(a, b)$ and $Z(-a, -b)$ as it cannot distinguish one from the other. For the coupling RDTs this means that the f_{1001} and f_{1010} will contribute to the same resonance lines and cannot be separated [46]. It may, however, be possible to neglect one of them depending on their relative strengths.

Additionally, from the method described above it becomes clear that dual plane BPMs are required for coupling measurements. In case such instrumentation is not available, one can numerically construct a pseudo dual plane BPM by virtually shifting a vertical plane monitor towards the location of the nearest horizontal one, or inversely. To do so, the phases of the real spectral lines are shifted in accordance with the phase advance between the monitors, which assumes that the segment between these monitors is free of non-linear sources [111].

3.3.4 Correction Principles

Corrections of the linear optics in the LHC are based on two different approaches. Global corrections are better suited to compensate for widely distributed sources, while local corrections are focused towards the identification and compensation of strong, highly localized errors, and are mostly used around the IPs.

Local Corrections

In the LHC local optics errors are determined and corrected using the Segment-by-Segment (SbS) technique [150, 156]. The technique treats a section - or segment - of the accelerator as an independent beam line and propagates optics parameters measured at the start of the segment through the line using the MAD-X code [59]. The propagated optics parameters may be compared with the observation and one then tries to find correction settings - powering changes of selected magnets - that would best reproduce these propagated optics. Inverting the settings found and applying the inverted values in the machine corrects the measured errors.

This method is mostly used in the LHC IRs, where the β -beating is corrected by compensating the discrepancies in the betatron phase, which has the same impact as correcting the β -beating directly but proved to be a more precise and local observable [150]. For this one looks at the $\Delta\phi$ quantity through the segment and tries to minimize it:

$$\Delta\phi = \phi_{\text{model}} - \phi_{\text{measurement}} \quad (3.20)$$

An example of a local correction of the phase advance around IP5 from the LHC 2022 commissioning is shown in Fig. 3.21, where the phase deviation from the model values are shown across the segment together with the effect of the reconstructed errors.

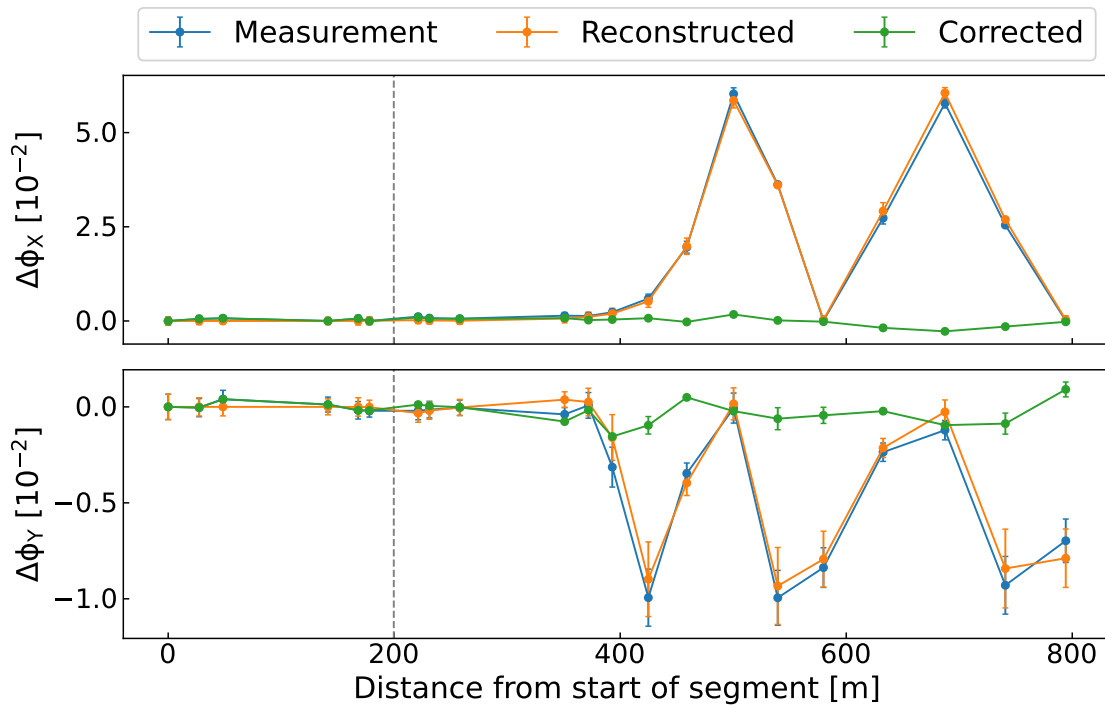


FIGURE 3.21: Local phase correction in IR5 (vertical line indicates IP5) from the LHC 2022 commissioning at flat-top. The blue line shows the measured phase deviation from model values, while the orange line shows the effect of the reconstructed errors on the model. The green line shows the expected phase deviation after applying the correction.

The concept from Eq. (3.20) can be applied to other observables such as the β -functions or the coupling RDTs. In the case of the coupling RDTs, due to the lower number of magnets available for adjustment one usually tries to compensate for the RDTs at the edges of the segment. One can also attempt to match for specific components of the RDTs specifically (real and imaginary parts). Figure 3.22 shows an example of a local correction of the coupling RDTs around IP2 from the LHC 2021 beam test. In this case, a good rematching at the edges of the segment means the contribution of the IR to the global coupling is well compensated. More details are given in the next chapter.

The segment-by-segment method has successfully been applied in the LHC for many years [123, 124, 157].

Global Corrections

Global corrections are based on a response matrix approach [111, 158]. This matrix, constructed from the machine model and simulation codes, holds the information on the response of the model optics functions to changes made in model settings, usually magnet powering changes. For instance, the response to a quadrupole knob trim of optics functions such as the phase advances, β -functions, normalized dispersion and tunes can be expressed as:

$$\mathbf{R}\Delta\vec{K} = \left(\Delta\vec{\phi}_x, \Delta\vec{\phi}_y, \frac{\Delta\vec{\beta}_x}{\beta_x}, \frac{\Delta\vec{\beta}_y}{\beta_y}, \Delta\frac{\vec{D}_x}{\sqrt{\beta_x}}, \Delta Q_x, \Delta Q_y \right). \quad (3.21)$$

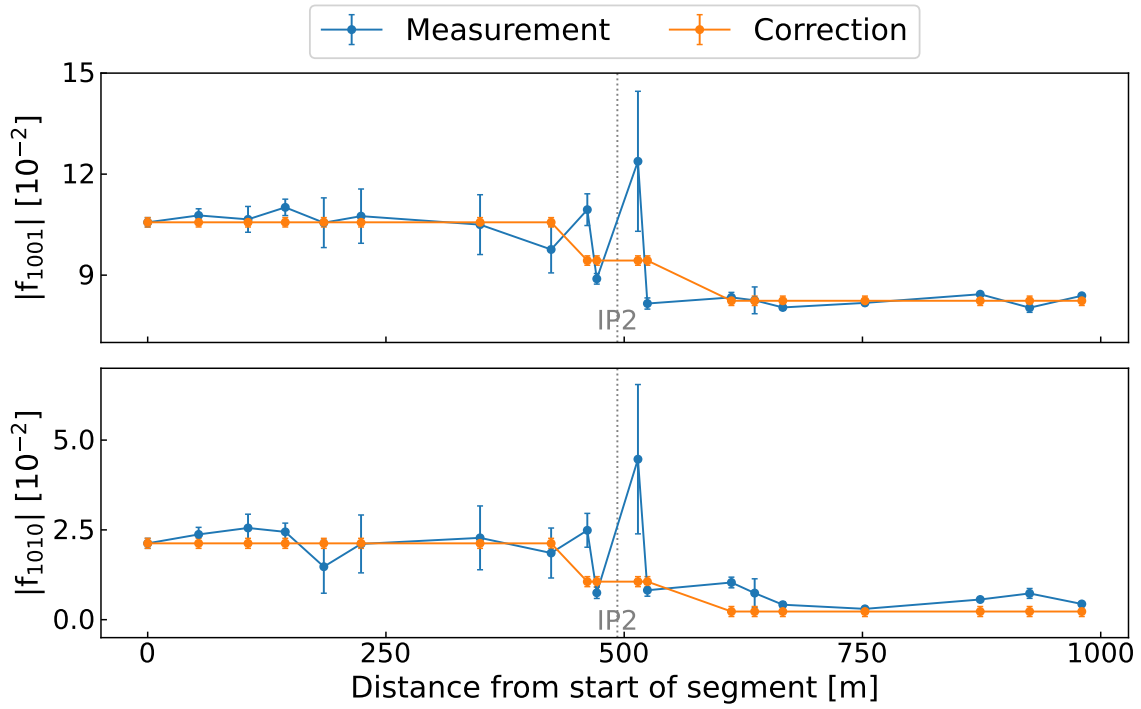


FIGURE 3.22: Local coupling RDTs correction in IR2 (vertical line indicates IP2) from the LHC 2021 beam test. The blue line shows the measured RDTs, while the orange line shows the attempt at canceling the contribution at the edges of the segment with the two available correctors in the IR.

Here \mathbf{R} is a $M \times N$ matrix, where N is the number of adjusted quadrupole knobs and M is the number of observation points, usually the number of BPMs. To calculate corrections the pseudo-inverse of the \mathbf{R} matrix, denoted \mathbf{R}^{-1} , is calculated and multiplied with the measured deviations from the model.

$$\Delta \vec{K} = \mathbf{R}^{-1} \left(w_1 \Delta \vec{\phi}_x, w_2 \Delta \vec{\phi}_y, w_3 \frac{\Delta \beta_x}{\beta_x}, w_4 \frac{\Delta \beta_y}{\beta_y}, w_5 \Delta \frac{\vec{D}_x}{\sqrt{\beta_x}}, w_6 \Delta Q_x, w_7 \Delta Q_y \right). \quad (3.22)$$

The $w_1 \dots w_7$ terms are weights which can be adjusted to either focus on correcting a given quantity, to ignore some parameters completely or to balance the corrections between all properties. By choosing weights and plugging measured optics deviations into Eq. (3.22), one can determine the knob trims that could correct said observed deviations.

CHAPTER 4

Interaction Region Local Coupling Correction in the LHC

The linear optics and coupling correction usually constitute the first phase of machine commissioning as both are major contributors to the performance of colliders, and are required to be under good control for the next phases of commissioning. In recent years, significant efforts have been made to improve the measurement and correction of linear and non-linear global coupling both in the [Large Hadron Collider \(LHC\)](#) [156, 159–167] and other synchrotrons [168–180], as their effects can lead to instabilities and unwanted dynamics in the machine [52, 55, 166, 181, 182].

In the LHC, local coupling correction has so far been done with the Segment-by-Segment technique [150]. The method, however, suffers inherent weaknesses making it not local enough for coupling corrections at the collisions points. This chapter, which constitutes the core of this thesis, presents a new method that was developed to determine corrections of [betatron coupling](#) at the [Interaction Points \(IPs\)](#). An overview of the various experimental measurements taken for this work can be found in [Appendix E](#).

4.1 Local Betatron Coupling in the LHC Interaction Regions

In the LHC, corrections of local [Insertion Region \(IR\)](#) linear coupling are of importance to keep a good control of beam sizes at the IPs and hence the luminosity performance, as well as to prevent a significant impact on the beam dynamics.

In [Eq. \(2.71\)](#), the contribution of elements to the linear coupling [Resonance Driving Terms \(RDTs\)](#) is given, where contributing elements are typically skew quadrupoles and solenoids. The amplitude of the contribution is dominated by the integrated strength of the magnet kL as well as the $\sqrt{\beta_x\beta_y}$ term at the location of the magnet. Given that a tilted quadrupole interacts with the beam as a straight quadrupole with an additional [skew](#) quadrupolar component, one can see from [Fig. 3.6](#) that any tilt in the triplet quadrupoles would generate a significant contribution to the coupling RDTs due to the very high β -functions in these magnets.

[Figure 4.1](#) shows the coupling RDTs' amplitudes from tilts in triplet quadrupoles, with the $\beta^* = 30$ cm 2022 optics [183]. In this [MAD-X](#) simulation, triplets around IP1 were assigned random tilts within ± 1.5 mrad, and these were the only contribution

to coupling in the machine. Nevertheless, this contribution amounted to a $|C^-|$ of 3.84×10^{-2} , already too high for machine operation.

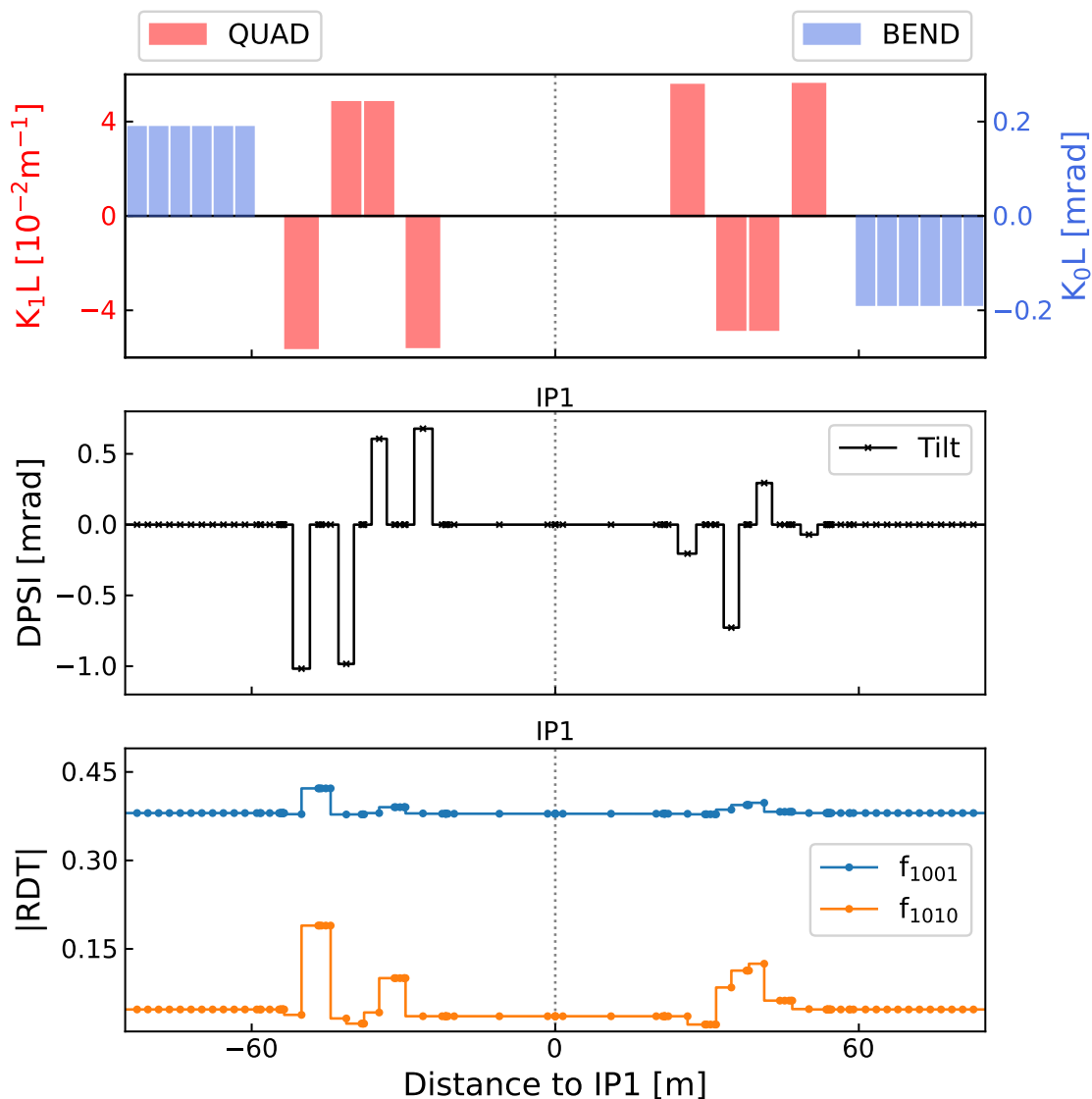


FIGURE 4.1: Amplitudes of the coupling RDTs (bottom) f_{1001} (blue) and f_{1010} (orange) from tilts in the triplet quadrupoles around IP1. The top plot shows the magnets' powering while the middle plot shows the assigned tilts in each element.

As a consequence, the IR contribution - mainly the triplets - to global coupling needs to be compensated. For this, in the LHC the local coupling correction is done by measuring the RDTs in the vicinity of the IP and using the MQSX skew quadrupole correctors introduced in Section 3.1.2 and showcased in Figs. 3.7 and 3.8 for correction. The corrections are determined with the Segment-by-Segment technique described in Section 3.3.4, and try to compensate for the triplets' contribution as well as possible. Though this compensation is rarely perfect, the residual contribution is usually small enough to be handled by the skew quadrupole correctors present in the LHC arcs (see Section 3.1.1). This correction is essential in order to reach low β^* with good optics control: at $\beta^* = 30$ cm, the local errors compensated in Run 2 [184] would contribute

to the $|C^-|$ by the amount of 0.33, too much for the arc correctors to handle. While such coupling in the machine is not inherently unstable in itself, it leads to other effects causing the machine to be unstable, for instance the impossibility of independently controlling the tunes, a change of working point or transverse instabilities from loss of Landau damping [54, 55].

Due to their location, the MQSX correctors are single aperture magnets, meaning that both beams pass through a single cavity in the element and feel the same magnetic field. This means finding a correction has the additional constraint that it is applied to both beam 1 and 2 simultaneously, and should be a compromise that works for both beams. As the triplet quadrupoles - also single aperture magnets - are expected to cause most of the contribution to local coupling, the local error to be corrected should be the same for both beams and such an arrangement of correctors is manageable.

During the late 2018 ion run in the LHC Run 2, it was observed that while global coupling was well corrected, a local coupling bump in IR2 had a significant impact on collisions and led to a reduction of the luminosity at the affected IP by up to 50% [6, 184, 185]. Investigations revealed that a coupling bump around IP2 led to a strong increase in beam size and a drop in collision rate. Importantly, the incident highlighted that no method existed to correct for the coupling specifically at the IP.

Figure 4.2 shows the expected beam size growth and luminosity decrease from various strengths of such a local coupling bump at one of the main IPs, for the LHC at $\beta^* = 30$ cm and for the HL-LHC at $\beta^* = 15$ cm. These results highlight the necessity of a proper handling of local coupling for the Run 3, as well as for the HL-LHC where the tolerance is about a factor 4 lower.

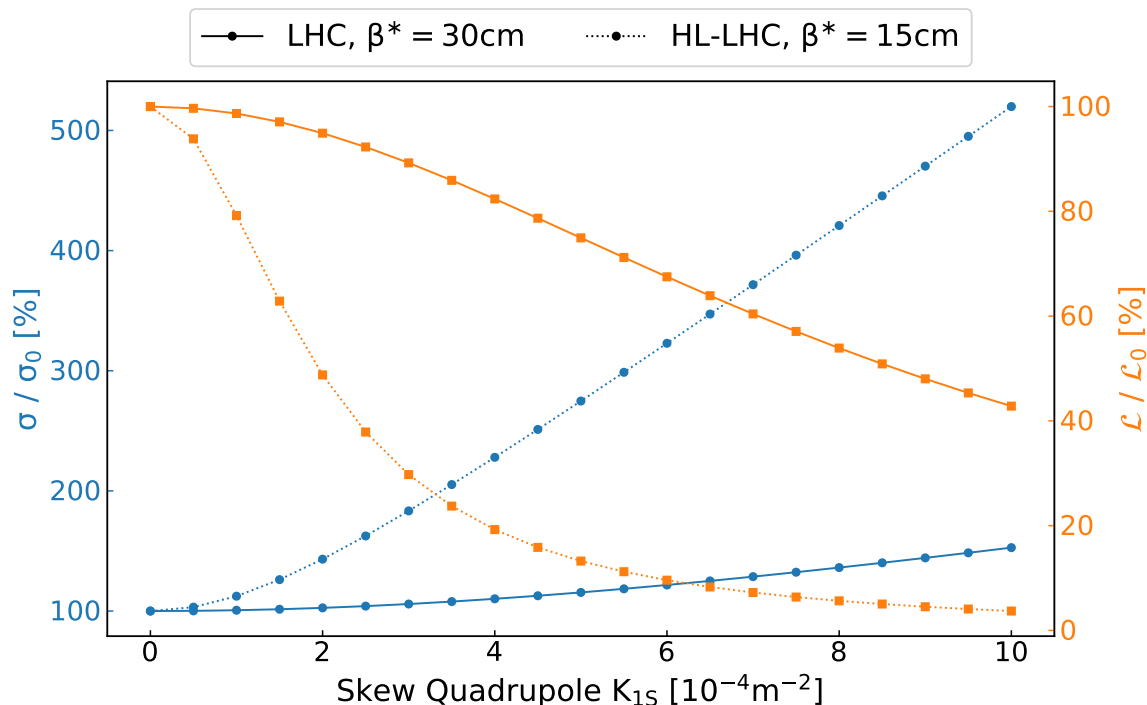


FIGURE 4.2: Relative values of the RMS beam size at IP1 (blue) as well as relative instantaneous luminosity (orange) for different strengths of a local coupling bump around the IP generated with skew quadrupoles, for the LHC (filled) and HL-LHC v1.5 (dashed) collision optics.

In the studies presented in this thesis, various calculations rely heavily on the Ripken parameters mentioned in Section 2.4.1. For instance, beam sizes are calculated from the β_{kj} terms according to [62]:

$$\langle z \rangle = \sqrt{\varepsilon_1 \beta_{1z} + \varepsilon_2 \beta_{2z}}, \quad z \in \{x, y\}, \quad (4.1)$$

in which the ε_1 and ε_2 terms represent the horizontal and vertical emittances, respectively.

The validity of this calculation has been verified in simulations by comparing its results to those obtained from other means. Figure 4.3 shows the relative deviation between computed beam sizes at IP5, calculated either according to Eq. (4.1) or from tracking a particle distribution, under various strengths of local coupling. In all cases the relative deviation is below 0.25 %.

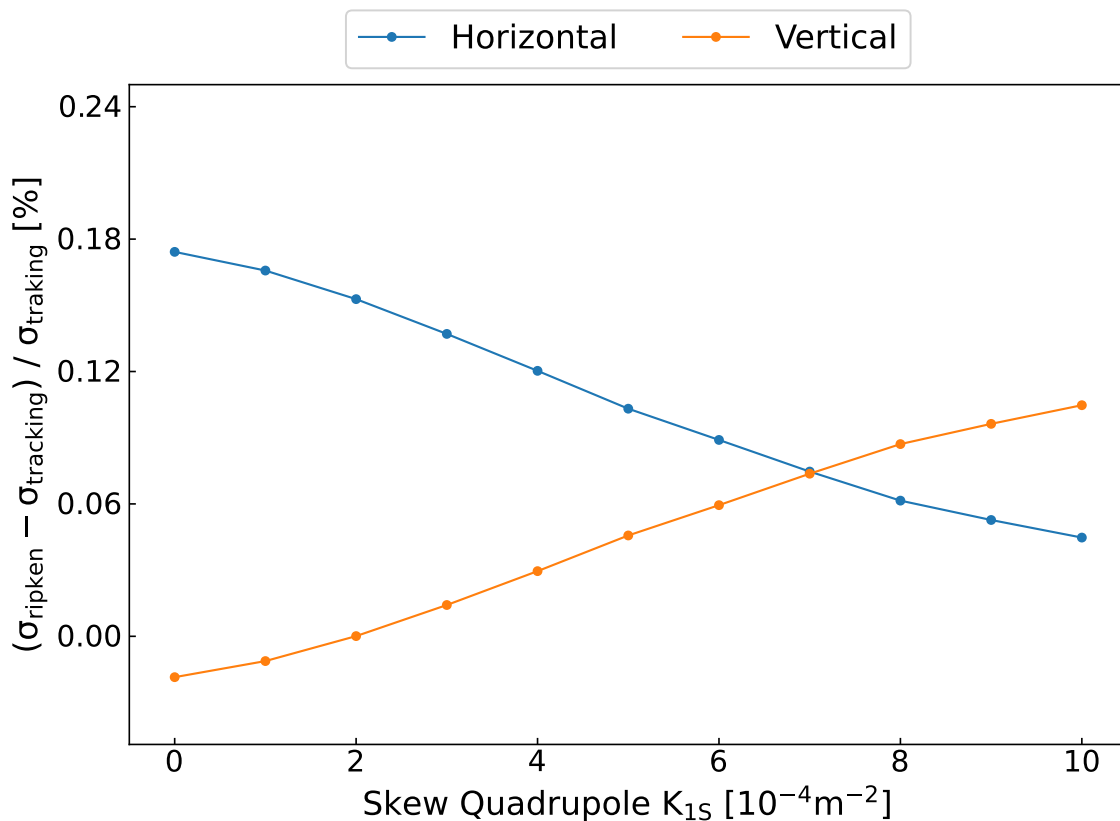


FIGURE 4.3: Relative deviation between beam sizes calculated from Ripken parameters according to Eq. (4.1) and from tracking a particle distribution, at an IP affected by coupling for the horizontal (blue) and vertical (orange) planes.

At the LHC IPs with round beams, as is the case in Run 3, the effect of the beam's tilt induced by linear coupling is negligible and its impact fully manifests as an increase in the beam size, as was the case at IP2 in 2018. Figure 4.4 shows a reconstruction of transverse beam sizes at IP1 (similar for IP5) for various strengths of a local coupling bump. While the beam ellipses show a $\gg 99\%$ overlap indicating a negligible tilt effect, the beam size in the most affected case is about 250% of the uncoupled case.

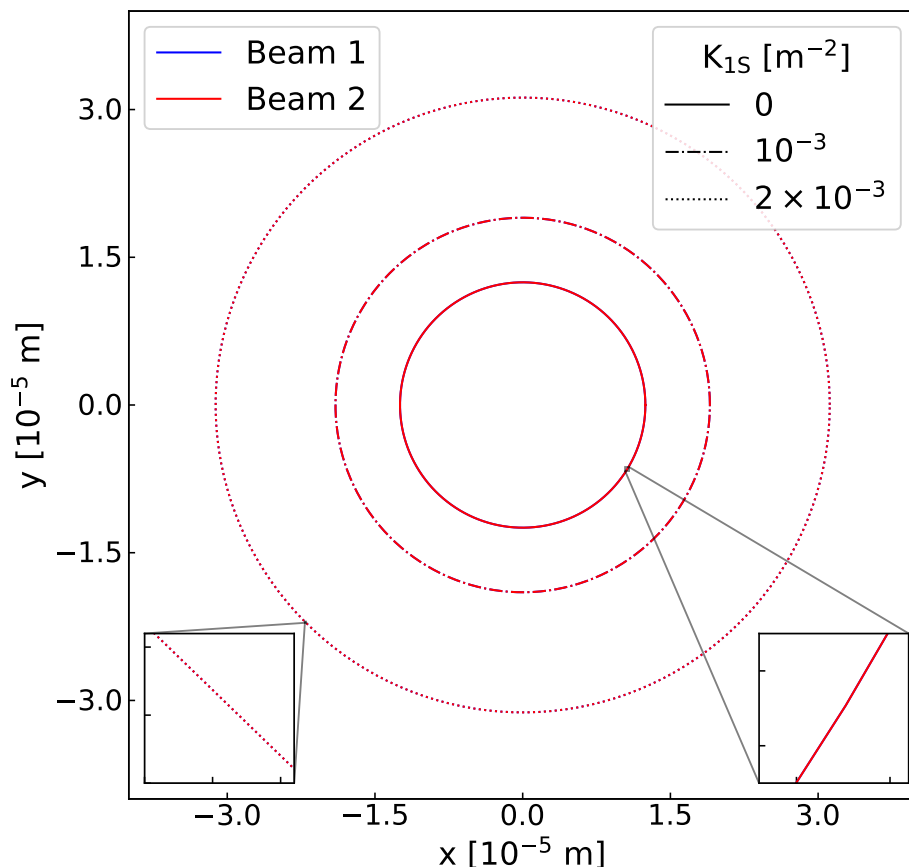


FIGURE 4.4: Transverse beam sizes at IP5 at 6.8 TeV and $\beta^* = 30$ cm with normalized emittances $\varepsilon_x = \varepsilon_y = 3.75 \mu\text{m}$ and for different strengths of a local coupling bump around the IP. The ellipses are reconstructed through the σ_{11} , σ_{13} and σ_{33} terms of the sigma matrix, obtained from MAD-X.

Instantaneous luminosities calculated for Fig. 4.2, in the absence of crossing angles, are given by [69]:

$$\mathcal{L} = \frac{N_1 N_2 f_{rev} N_b}{2\pi \sqrt{(\sigma_{x,1}^2 + \sigma_{x,2}^2)} \sqrt{(\sigma_{y,1}^2 + \sigma_{y,2}^2)}}, \quad (4.2)$$

where N_n is the number of protons per bunch in beam n , f_{rev} the revolution frequency of particles, N_b the number of bunches per beam and $\sigma_{z,n}$ is the size at the IP of beam n in the transverse plane z , calculated according to Eq. (4.1).

4.2 Current Correction Methods and Their Limitations

While the coupling RDTs contain information on the coupling situation in the machine, looking at their patterns along the ring is not a good indicator of the situation at an IP. For instance, Fig. 4.5 shows the reconstructed coupling RDTs from two measurements taken during the LHC 2022 commissioning. One of these measurements corresponds

to a 20% lower measured luminosity at IP1 compared to the other, however it is not possible to tell which is the better one from looking at the RDTs alone.

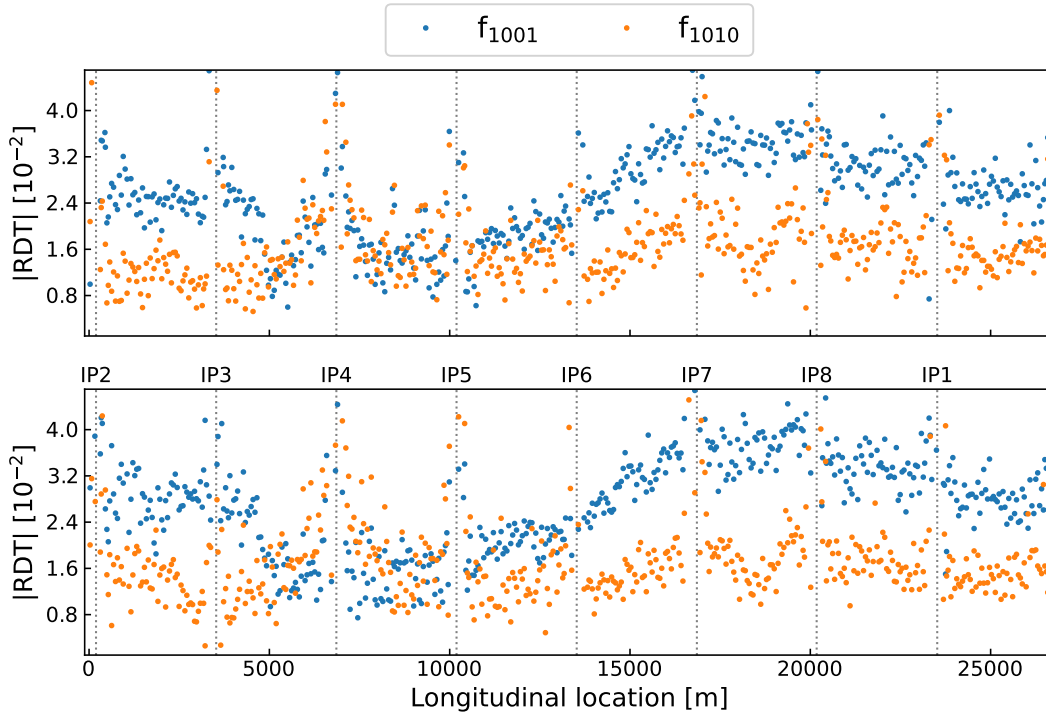


FIGURE 4.5: Similar looking coupling RDTs from two measurements (top and bottom) taken during the LHC 2022 commissioning. One scenario leads to a 20% instantaneous luminosity decrease at IP1 compared to the other.

Segment-by-Segment

The Segment-by-Segment technique mentioned in [Section 4.1](#) and used to implement local corrections in the LHC IRs suffers from inherent limitations making it unsuitable for the correction of coupling at the IP. Firstly, due to unfavorable phase advances in between [BPMs](#) in the IRs, it is difficult to get a good measurement of the coupling RDTs in these regions. As these are reconstructed from the h_z^\pm coordinates, they require reconstruction of the momentum (see [Section 3.3.3](#)). Knowing that the phase advance in the IRs is ~ 0 from BPM to BPM, and $\sim \pi$ from one side of the IP to the other, one can see through [Eq. \(3.13\)](#) why the momentum reconstruction is difficult at BPMs around an IP.

As a consequence, the reconstruction of coupling RDTs in close proximity to the IPs is inaccurate. [Figure 4.6](#) shows the amplitude of the coupling RDTs propagated with the SbS technique in the IR1 segment, from measurements taken during the LHC 2021 beam tests and 2022 commissioning. Not only can large error bars be noticed on the reconstructed data points, but no given case appears to be specifically better than the other while the [orange](#) line (2022 commissioning) corresponds to a better correction than the [blue](#) one (2021 beam tests). Given the data patterns and the fact that the orange case corresponds to a better correction, it does not appear that the SbS technique gives a good indication of the local coupling at the IP.

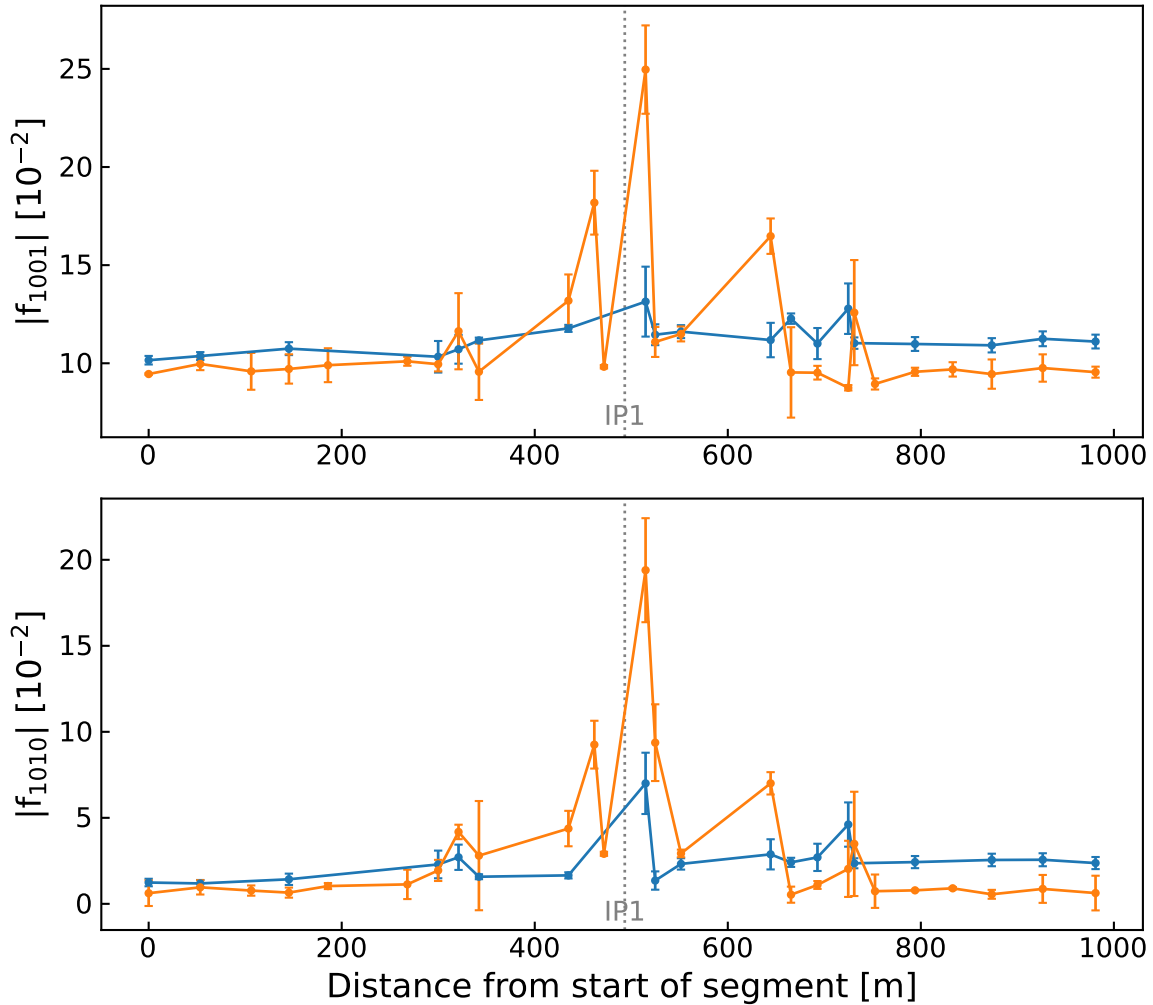


FIGURE 4.6: Propagation of the measured $|f_{1001}|$ and $|f_{1010}|$ for beam 1 around IP1 (dashed vertical line), measured with two different correction settings. The 2022 measurement (orange) leads to a beam size smaller by 9.2% than the 2021 one (blue).

Furthermore, the SbS technique does not allow to differentiate the contribution of one individual corrector from the other in the LHC IRs, making it difficult to find the correct balance of left and right powering settings. Indeed, as both correctors can compensate each other one might find a good compensation of the overall IR contribution to global coupling which also deteriorates the coupling situation at the IP. Additionally, as the coupling RDTs are reconstructed at BPMs the method cannot provide an estimate of coupling at the IP where there are no BPMs. In such a case where both correctors compensate for each other, SbS would not allow a degradation of the coupling at IP to be detected.

Combined Coupling Resonance Driving Terms

A candidate for a better observable that was considered are the **combined coupling RDTs** [47], also simply called Combined RDTs (CRDTs), denoted $|\hat{F}_{XY}|$ and $|\hat{F}_{YX}|$.

These can be expressed from the coupling RDTs, here with a scaling factor, as:

$$\begin{aligned}\hat{F}_{xy} &= \frac{\sinh 2\mathcal{P}}{\mathcal{P}} (f_{1001}^* - f_{1010}^*) , \\ \hat{F}_{yx} &= \frac{\sinh 2\mathcal{P}}{\mathcal{P}} (f_{1001} + f_{1010}^*) ,\end{aligned}\quad (4.3)$$

where $2\mathcal{P} = \sqrt{|2f_{1010}|^2 - |2f_{1001}|^2}$ and $*$ denotes the complex conjugate. These have the advantage that they can be reconstructed directly from the particle coordinates (x, y) without the need for momentum reconstruction [186].

Although the CRDTs seemed to work well in straightforward simulations, they were found to not be useful when it came to applying them to more realistic cases or real measurement data. Figure 4.7 shows the reconstructed CRDT $|\hat{F}_{XY}|$ from measurements done in a late 2018 Machine Development (MD), computed with the OMC team's analysis tools [187]. During the MD, the first investigations were made of local coupling at the IP, and while little data was collected due to a dump of beam 1, they provide a good test bed for a new observable candidate. Information about the MD fill can be found in Appendix E.

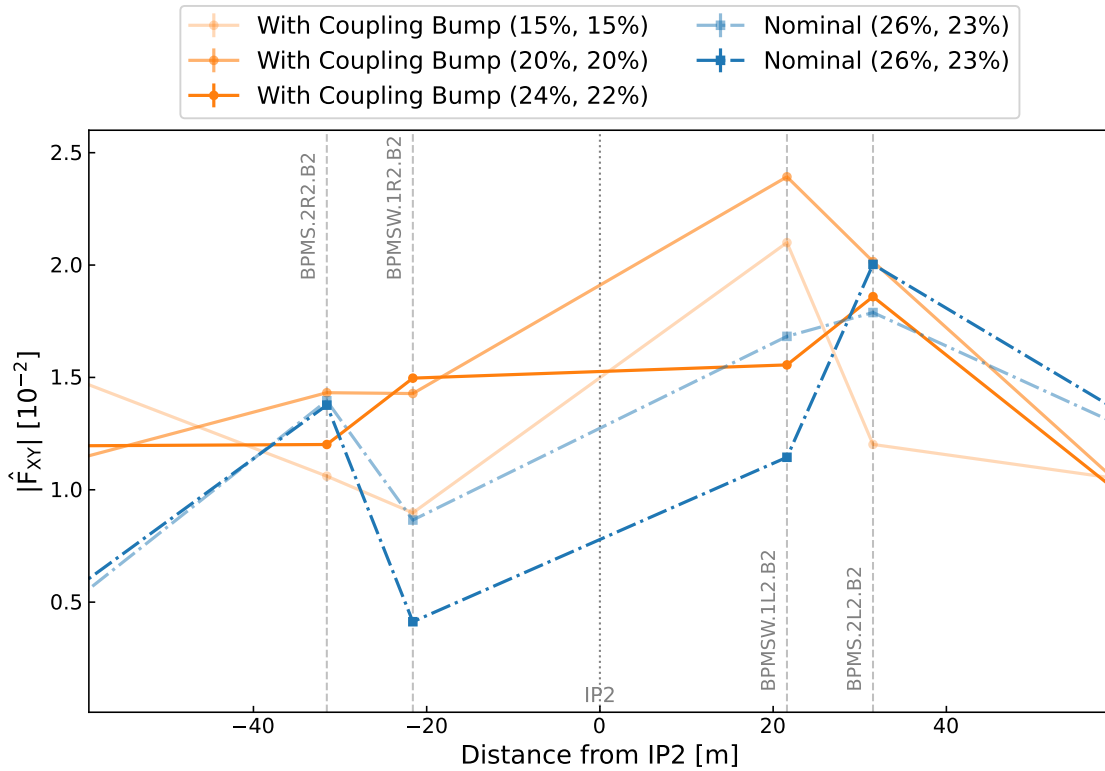


FIGURE 4.7: Reconstructed CRDT $|\hat{F}_{XY}|$ around IP2 from measurements at $\beta^* = 50$ cm during a 2018 MD. The blue lines correspond to 2 measurements with the nominal optics, and orange lines correspond to 3 measurements with a local coupling bump implemented around IP2. The percentages indicate the strength of the AC dipole kicks.

While the error bars are barely visible compared to the large ones in Fig. 4.6, the main observed issue was a lack of reproducibility between different measurements: different measurements done with identical settings give different results. Indeed, two

identical kicks with nominal optics (blue) give different values of the CRDTs at inner BPMs, sometimes differing by a factor two; and other measurements conducted in the presence of a constant coupling bump (orange) also demonstrate no consistency in the computed results. For this reason, the CRDTs were not considered further.

K-Modulation

The usual technique to get a measurement of the β -functions at the IP is k-modulation (see Section 3.3.2). Unfortunately, previous studies have shown that k-modulation measurements are robust against the presence of local coupling, both analytically [148, 186] and experimentally in a dedicated MD [188]. This prevents the possibility of driving a correction directly by measuring the β -function variations at an IP from coupling.

A Short Recap

To summarize so far, control of local coupling in the LHC IRs is an important goal that should be tackled for Run 3. Coupling corrections determined with the segment-by-segment method allow compensation of the IR's contribution to global coupling and are crucial to allow squeezing of the beams as well as safe machine operation. However, existing methods do not provide a reliable way to minimize coupling at the IP. To achieve this goal, two new things are needed:

1. A way of adjusting the coupling at the IP without affecting the rest of the machine, so as not to spoil the compensation of the IR's contribution to global coupling.
2. A reliable way of measuring coupling at the IP in order to derive the correction.

The former can be achieved with a knob described in Section 4.3, while the latter was achieved with a new optics configuration presented in Section 4.4.

4.3 The Colinearity Knob

The colinearity knob is a powering setting convention for the IR skew quadrupole correctors, the MQSX magnets. Originally designed for a flat optics MD [189], the knob acts anti-symmetrically on the left and right corrector magnets. The definition of the knob is given in Table 4.1. A full definition of the knobs as implemented and used in the LHC can be found in Appendix C.1.

Magnet	ΔK_{1S} [m^{-2}]
MQSX.3R[IP] $\rightarrow K_{1S}$	10^{-4}
MQSX.3L[IP] $\rightarrow K_{1S}$	-10^{-4}

TABLE 4.1: Definition of one unit of the colinearity knob, a powering setting of the IR skew quadrupole correctors.

In the case of only skew quadrupolar coupling sources, Eq. (2.74) becomes a summation over the individual sources and the $j(s)$ term becomes J_w - the integrated skew

quadrupole strength of the source indexed by w - in that summation:

$$\begin{aligned} |C^-| &= \left| \frac{1}{2\pi} \sum_w \sqrt{\beta_x^w \beta_y^w} J_w e^{-i(\phi_x - \phi_y) + i \frac{s\Delta}{R}} \right| \\ &= \left| \frac{1}{2\pi} \sum_w \sqrt{\beta_x^w \beta_y^w} J_w e^{i(\phi_x - \phi_y)} \right| + O(\Delta). \end{aligned} \quad (4.4)$$

In the case of the MQSX magnets, given the $\sim 180^\circ$ phase advance between the two correctors, the contribution to the global coupling can be written as:

$$\Delta C^- = \frac{1}{2\pi} \sum_w \sqrt{\beta_x^w \beta_y^w} J_w = \frac{1}{2\pi} \left(\sqrt{\beta_x^l \beta_y^l} k_S^l L + \sqrt{\beta_x^r \beta_y^r} k_S^r L \right), \quad (4.5)$$

with $k_S^w L = J_w$ the integrated strength of the skew quadrupole at position w . The l and r superscripts denote the corrector left or right of the IP, respectively.

Since, for **round optics** in the LHC the β -functions are by design identical at the correctors left and right of the IP (see Fig. 3.7) and those have identical lengths, with opposite powering settings as defined in Table 4.1 and assuming a good β -beating correction, this contribution reduces to 0. Therefore, the knob induces a closed coupling bump going from corrector to corrector around the IP without affecting the machine's global coupling. Figure 4.8 shows the effect of the colinearity knob on the f_{1001} .

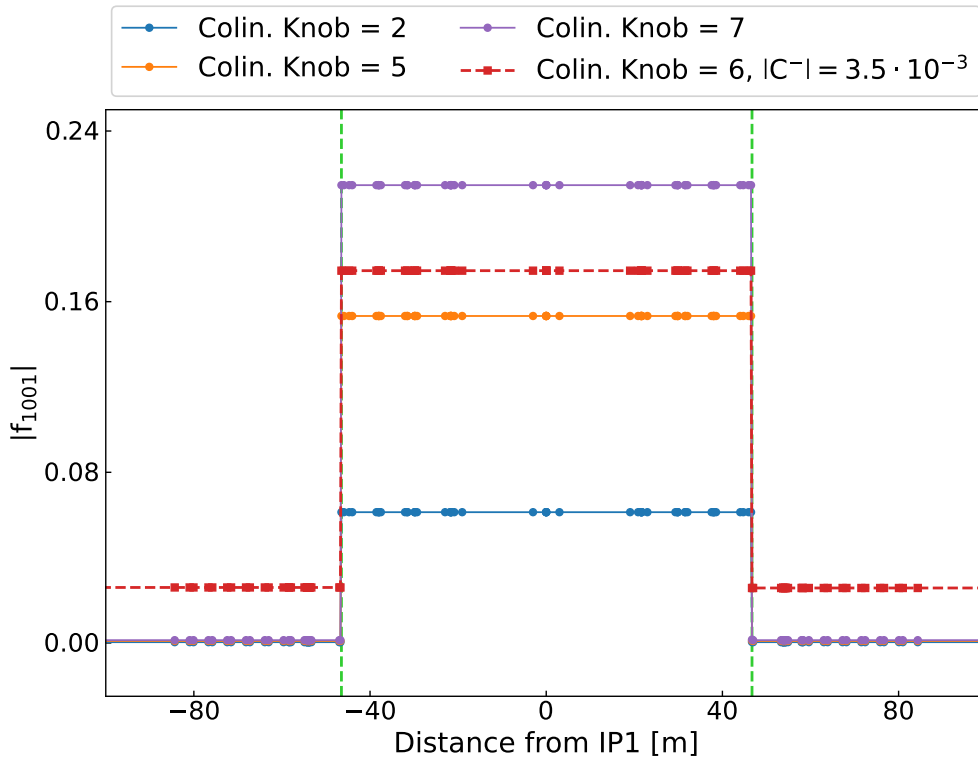


FIGURE 4.8: Amplitude of the f_{1001} RDT in the vicinity of IP1 for various settings of the colinearity knob, in the absence (blue, orange and purple) and presence (red) of global coupling. The locations of the MQSX corrector magnets are highlighted as green vertical lines.

One can observe that in all cases without global coupling (blue, orange and purple lines) the $|f_{1001}|$ falls down to 0 outside the MQSX to MQSX zone. When global coupling is present, the $|f_{1001}|$ goes back to its original value outside the limits of the bump. A similar plot can be obtained for the $|f_{1010}|$. The reader might notice how the amplitude of the RDT does not fall down to exactly 0 in the blue, orange and purple cases. As mentioned above the phase advance between the two magnets deviates from π by 1%, and similarly the $\sqrt{\beta_x\beta_y}$ term is not perfectly equal on each side but changes by 0.1%. For all intents and purposes though, these deviations are small enough for the contribution to be negligible.

Therefore, the colinearity knob is an effective tool to introduce a closed coupling bump in between the MQSXs. It can be used to modify the coupling specifically at the IP without changing the situation outside the IR, and can therefore act as a second step to adjust coupling locally without affecting the compensation of the IR coupling contribution. One now needs a way to relate the coupling at the IP to some reliable observable, which is achieved with a new optics setup as presented below.

4.4 Rigid Waist Shift for Local Coupling Correction

In order to circumvent the issues related to measuring the local coupling at the IP, it is necessary to find a way to relate it to other measurable quantities. This is achieved by the application of a Rigid Waist Shift (RWS), which changes the machine's optics configuration in the IRs, as presented below.

4.4.1 Rigid Waist Shift

Applying a Rigid Waist Shift to the beam - meaning all four betatron waists are moved simultaneously - breaks the (anti-)symmetry of the optics in the IR. An RWS is achieved by unbalancing the powering strength of the triplet quadrupoles Q1-Q3 on either side of the IP anti-symmetrically: over-powering one side and under-powering the other by the same amount.

The knob is designed so that a trim setting of 1 will result in a 0.5% change in the triplet knob powering (individual magnet trims are not used), which creates a waist shift of ~ 43.5 cm to the left or right of the IP depending on the unit setting of the knob. The definition of the knob is given in Table 4.2. A full definition of the RWS knobs as implemented and used in the LHC can be found in Appendix C.2.

Circuit	Powering Δ
KQX.R[IP]	-0.5%
KQX.L[IP]	0.5%

TABLE 4.2: Definition of one unit of the rigid waist shift knob.

Figure 4.9 shows how applying the knob in a given IR displaces the beam's waists away from the IP location, and also shows how the β -functions at the IP are modified. These were determined in MAD-X simulations, using the $\beta^* = 30$ cm optics of 2022, by

applying the RWS with different strength settings at IP1 and determining the waist, both numerically with a fine lattice slicing and analytically as described in [148]. Similar results are obtained when performing these simulations for IP5, as the design optics are identical for the two main experiments.

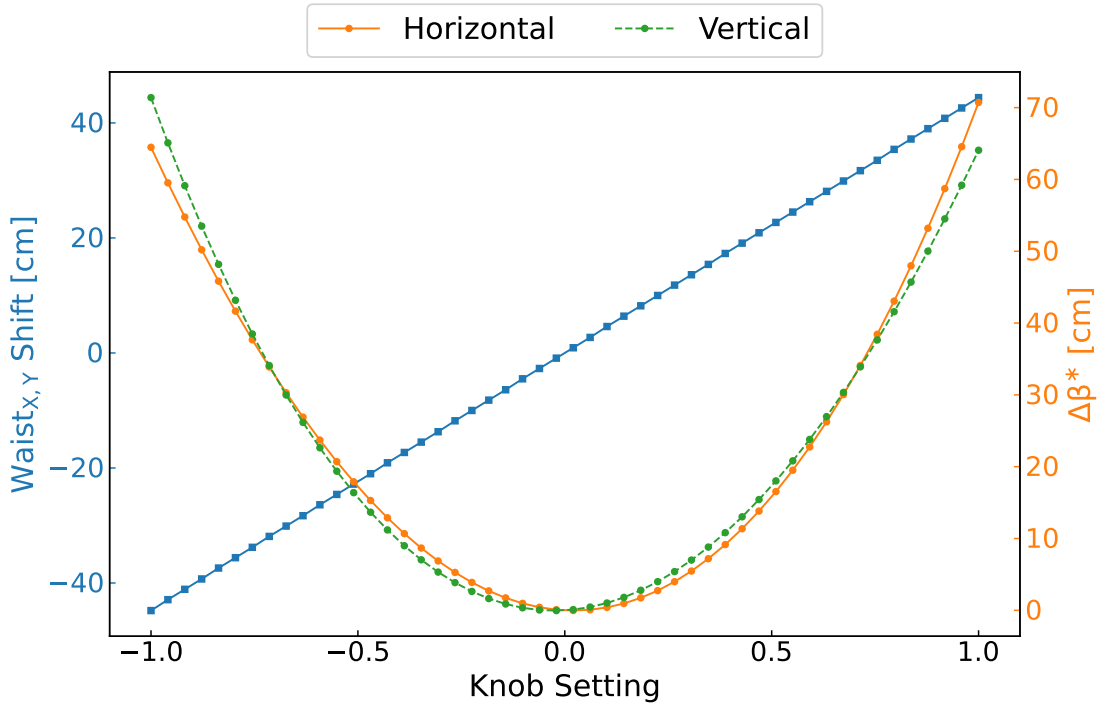


FIGURE 4.9: Simulated effect of the designed Rigid Waist Shift knob as defined in Table 4.2 on the $\beta^* = 30$ cm optics of 2022. The blue line represents the waist displacement from the design location. The orange and green lines represent, respectively, the horizontal and vertical β -function change at the IP as the waist is displaced.

The waist displacement from the design location (blue line) is almost completely linear with the knob setting. One can note that the minima of the parabolas indicating the change of β -functions at the IP (blue and orange curves) are not found at exactly the zero knob setting, which is because the LHC design optics include a very small waist at IP1 and IP5.

In Fig. 4.10 one can observe how the β -functions are affected by the application of an RWS, also simulated with the $\beta^* = 30$ cm optics of 2022. In this simulation, the lattice was sliced to improve the resolution of the data points, which explains the smoother lines compared to, for instance, Fig. 3.7. One can observe how the (anti-)symmetry of the optics in the IR is broken when applying the knob (full vs dashed lines): the horizontal (blue) and vertical (red) β -functions do not mirror each other anymore. Inset zooms are included around the location of the MQSX magnets (green vertical lines), showing how the horizontal and vertical β -functions are modified in their vicinity. The purpose of this setup is detailed in Section 4.4.2.

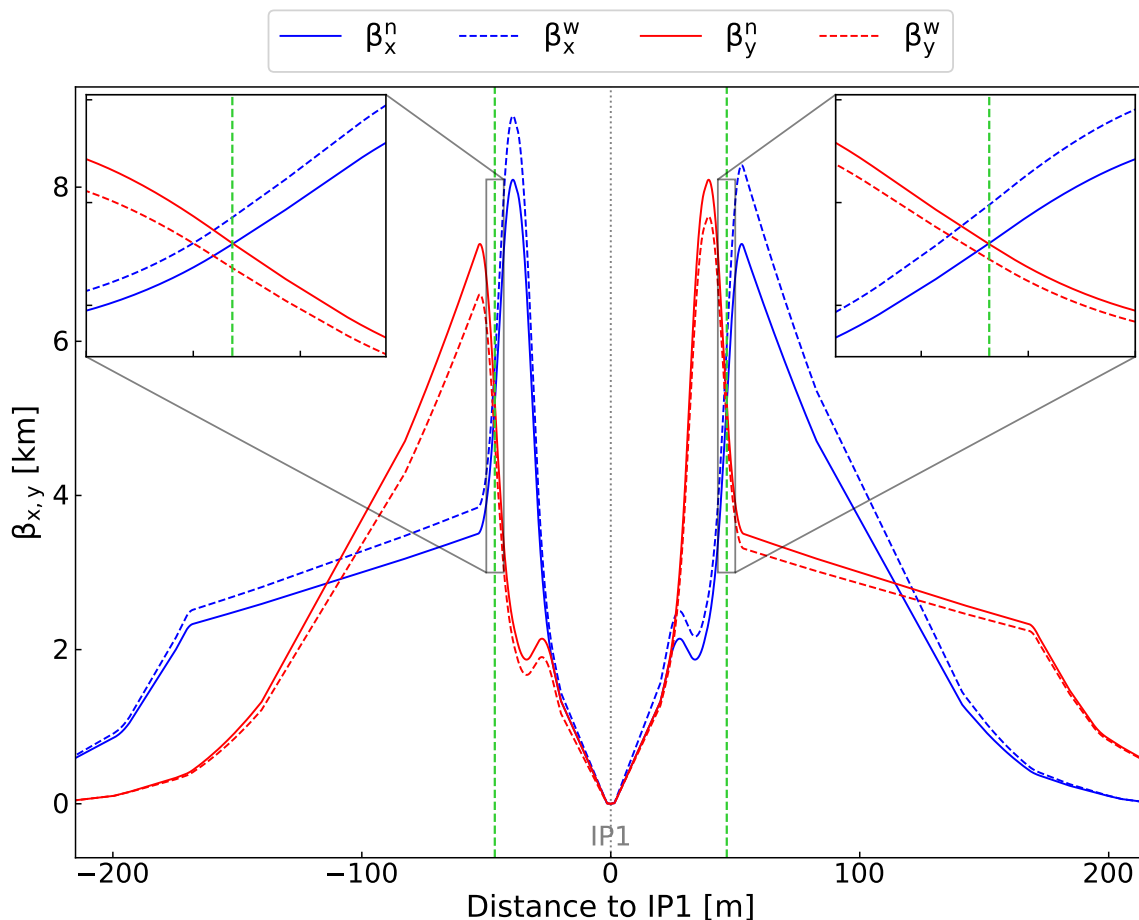


FIGURE 4.10: Simulated effect of the designed RWS knob on the β -functions around IP1, with the $\beta^* = 30$ cm optics of 2022. The β -functions for both the horizontal (blue) and vertical (red) planes are shown for the nominal (full lines) and shifted waists (dashed lines) scenarios. An identical result is found for IP5.

Optics Impact and Rematching

Predictably, the application of a Rigid Waist Shift as described above has a strong impact on the optics across the machine. This is due to the significant change of β -functions in the triplets, which sends a beating wave from the IR through the rest of the machine. Applying an RWS with a unit setting of 1, as defined in Table 4.2, leads to a 20–30% increase in peak β -beating throughout the machine, depending on the observed beam and plane.

This can be seen in Fig. 4.11, where in simulations an RWS was implemented with a unit setting of 1 at IP1 and the optics deviations from the nominal scenario were determined across the machine for both beams. The most affected beam and plane depends on the setting of the RWS: in Fig. 4.11 beam 1 horizontal and beam 2 vertical are most affected, but these would be beam 1 vertical and beam 2 horizontal if the RWS was applied with a setting of -1 . Strong outliers can be observed in the vicinity of the IP, which correspond to the desired deviation at the IP and in the triplets induced by the knob trim.

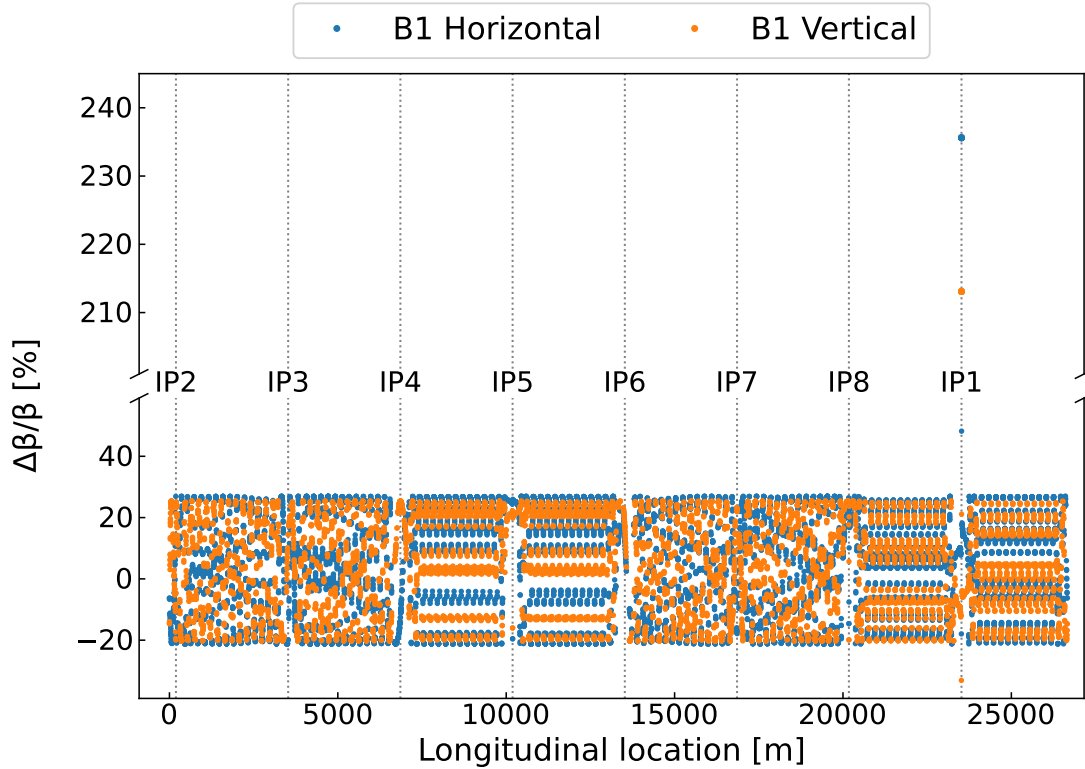


FIGURE 4.11: Simulated β -beating induced across beam 1 in both the horizontal (blue) and vertical (orange) planes, from applying an RWS as defined in Table 4.2 at IP1. A 20 to 30% β -beating is observed through most of the machine, with (wanted) outliers close to IP1.

Such a deviation of the optics has an impact on correction knobs. For instance, simulations show that the application of the RWS causes a 15% deviation of the $|C^-|$ from the target value set through the LHC global coupling knobs, used for coupling correction with the arc skew quadrupoles. Additionally, the optics deviations will change the impact of any errors probed while the RWS is trimmed in, namely the skew quadrupolar impact on the [closest tune approach](#) (see Eq. (2.74)).

In order to limit this impact on the optics and guarantee good measurements under an RWS, new correction knobs have been developed that make use of individually powered quadrupoles Q4 to Q10 (included). These knobs tune the optics functions and rematch them at the edges of the IR. They were designed with the [MAD-X](#) code and a software developed specifically that can create these experimental configurations for a given IP in the machine [190].

These knobs are obtained from simulations after applying an RWS in a given IR and iterating several matching routines for quantities of interest at different locations in the machine. Importantly, no involved magnet sees its powering change by more than $\sim 3\%$ with the application of these knobs, which allows for respecting the powering limits of individually powered elements. As the rematching knobs depend on the RWS setting and optics configuration, many variations are possible and no general definition table is available akin to Tables 4.1 and 4.2. A full definition of the rematching knobs for the $\beta^* = 30$ cm optics of 2022 as used in the LHC can be found in [Appendix C.3](#).

Figure 4.12 shows a comparison of the simulated optics deviation in the beam 1 horizontal plane, induced by the RWS before (blue) and after (orange) applying the rematching knob, here implemented at IP1. Across the machine the β -beating is brought down by $\sim 20\%$ to around $\sim 5\%$ depending on the beam and plane compared to the nominal scenario, except for the vicinity of the IP where the desired deviation is kept unchanged. A 5% β -beating across the machine is an acceptable level as it is similar to the level of control achieved during normal operation with all corrections trimmed in (see [124, 184]), as can be seen in Fig. 3.14.

While only beam 1 horizontal is shown in this figure, results are similar for all planes of beam 1 and beam 2. As the rematching depends on the desired configuration, for a given optics and setting of the RWS, a knob has to be designed for each beam, at each IR and for each RWS setting.

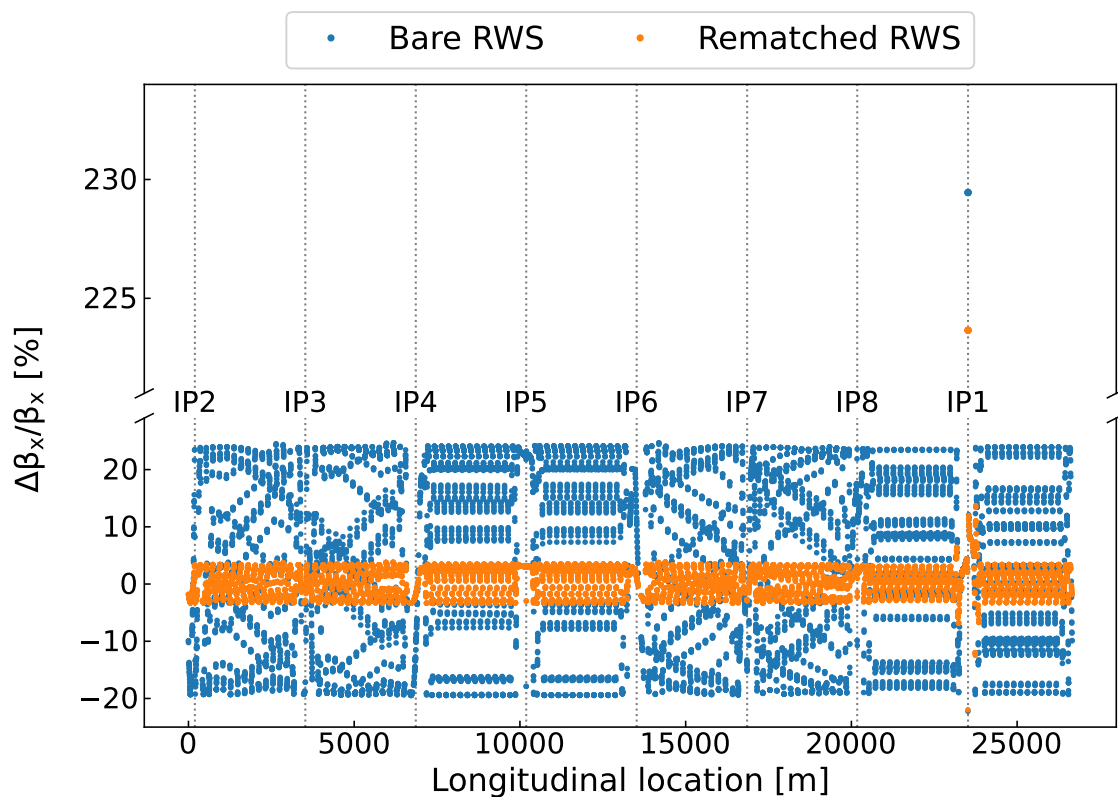


FIGURE 4.12: Simulated β -beating induced across the machine in the beam 1 horizontal plane from applying an RWS at IP1, before (blue) and after (orange) applying the optics rematching knob.

One can notice that, near the IP, the beating is also lowered by the rematching, but stays high enough to still break the symmetry of the optics in the IR. Figure 4.13 shows the β -functions around IP1 before (full lines) and after (dashed lines) application of the rematching knobs. One can observe how the deviation between the two cases is negligible close to the IP and, importantly, in both cases the symmetry of the IR is broken compared to, for instance, Fig. 3.7.

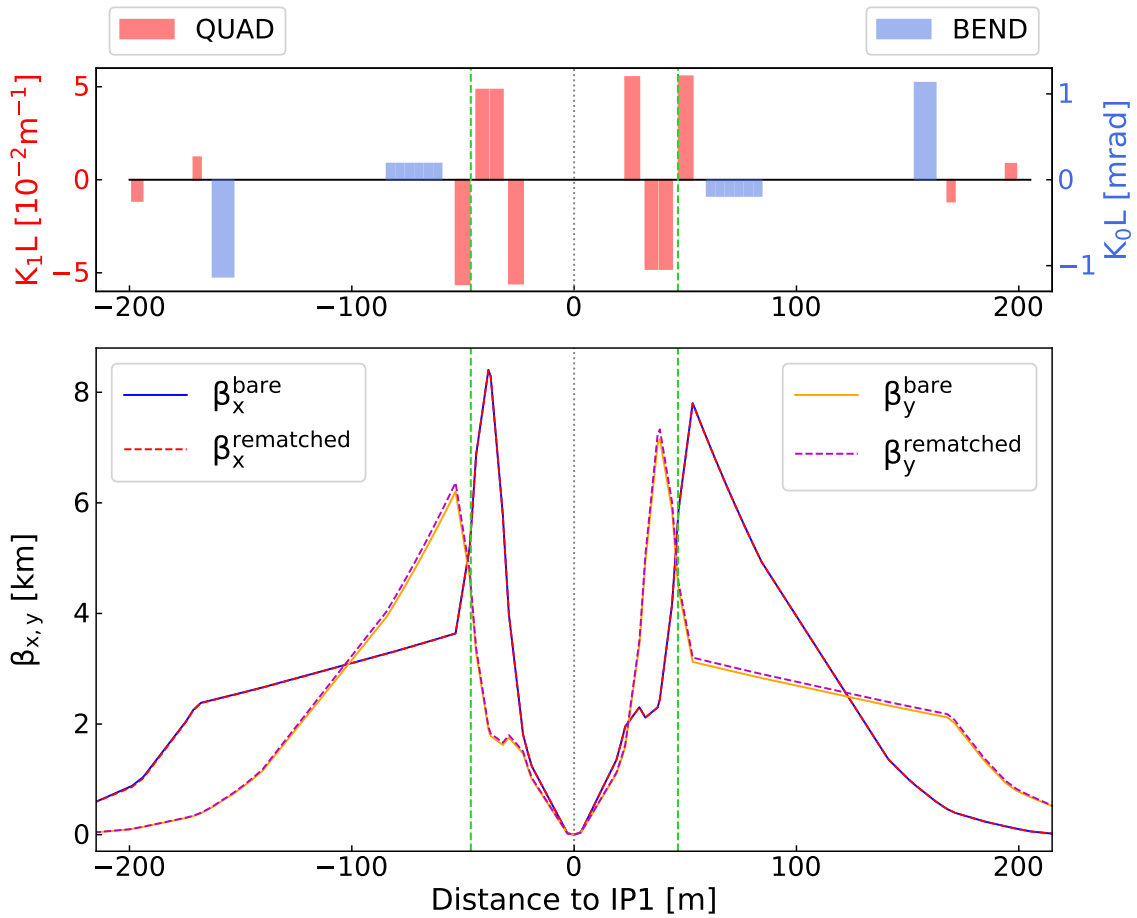


FIGURE 4.13: Simulated β -functions around IP1 when applying an RWS, before (full lines) and after (dashed lines) application of the rematching knobs, with the $\beta^* = 30$ cm optics of 2022.

4.4.2 Application Concept and Simulations

Making away with the optics symmetry of the IR allows to break the locality of any coupling bump, even a truly local one. As can be seen on the inset zooms of Fig. 4.10, with the application of an RWS the β -functions at the MQSX magnets change enough that the $\sqrt{\beta_x \beta_y}$ term in Eq. (4.5) are different at the two magnets. Table 4.3 shows the values of these terms with and without an RWS applied. Phase advances are also changed, but by a very small amount.

Magnet	$\sqrt{\beta_x \beta_y}$ [m]	
	Without an RWS	With an RWS
MQSX.3L[IP]	5193.084	5186.603
MQSX.3R[IP]	5199.142	5396.527

TABLE 4.3: Values of the $\sqrt{\beta_x \beta_y}$ term in Eq. (4.5) at the MQSX magnets around IP1 or IP5 without (left) and with (right) the application of an RWS, with the $\beta^* = 30$ cm optics of 2022.

Figure 4.14 shows the coupling RDTs from a closed coupling bump around the IP created through the colinearity knob, both in the presence (red) and absence (blue) of an RWS.

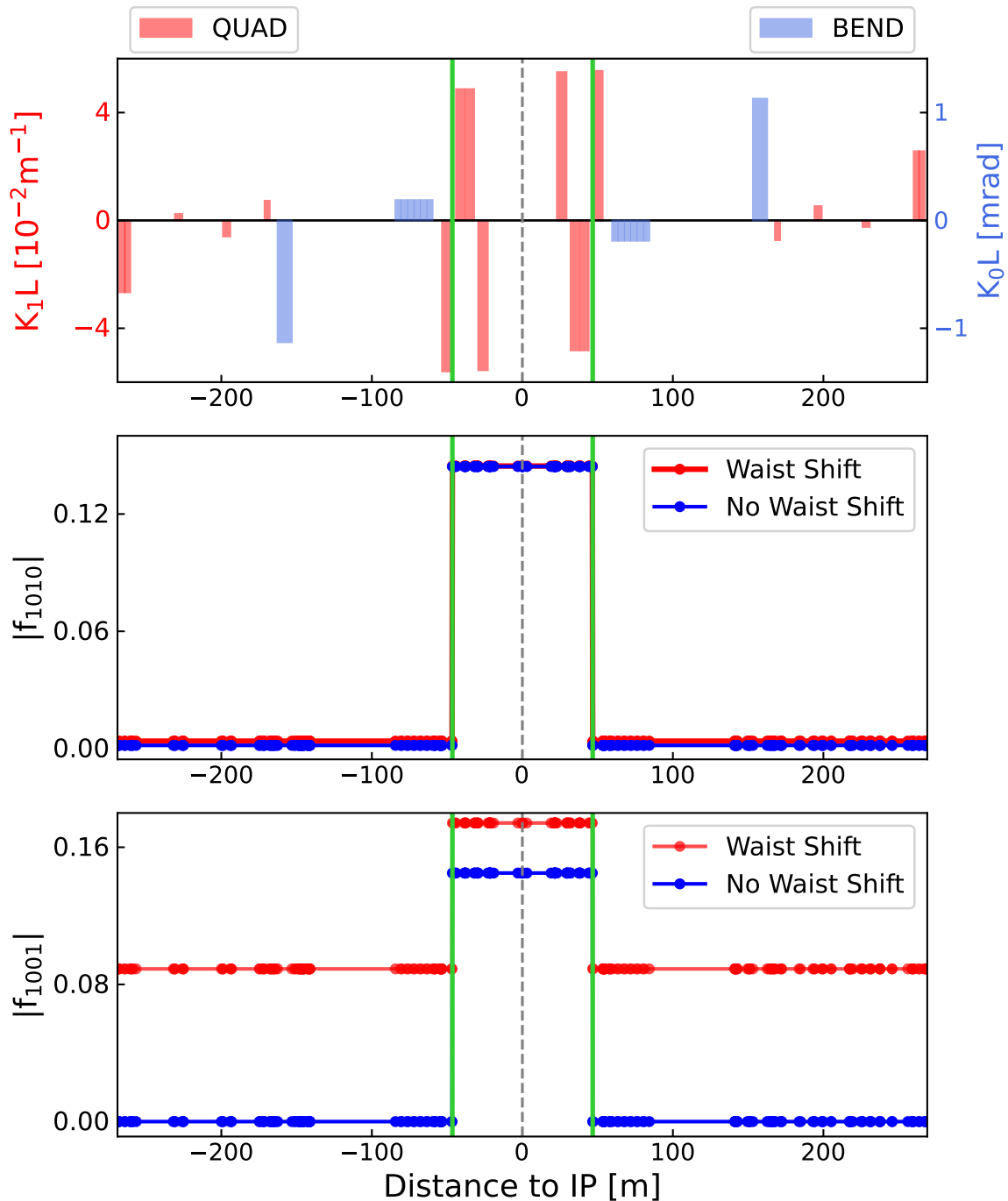


FIGURE 4.14: Amplitudes of the linear coupling RDTs in the vicinity of IP1 under a coupling bump, with (red) and without (blue) an RWS. The vertical green lines represent the positions of the skew quadrupoles correctors (MQSX.3[RL]1) used to implement the coupling bump. A colinearity knob setting of 10 and a rigidity waist shift knob setting of 1 were used.

When applying a Rigid Waist Shift and breaking the optics symmetry of the IR, one can observe a leakage of the coupling RDTs outside the limits of the initial coupling bump. These RDTs will then have a residual presence in the machine, which can be measured and reconstructed from turn-by-turn data from Beam Position Monitors (BPMs) with more suitable phase advances. As a consequence, under an RWS even a local coupling bump that would normally be invisible to the rest of the machine will have a direct impact on the global coupling, measured as the $|C^-|$. This can be seen in Fig. 4.15, where changes in the setting of the colinearity knob now have a strong effect on the $|C^-|$ when an RWS is applied in the relevant IR.

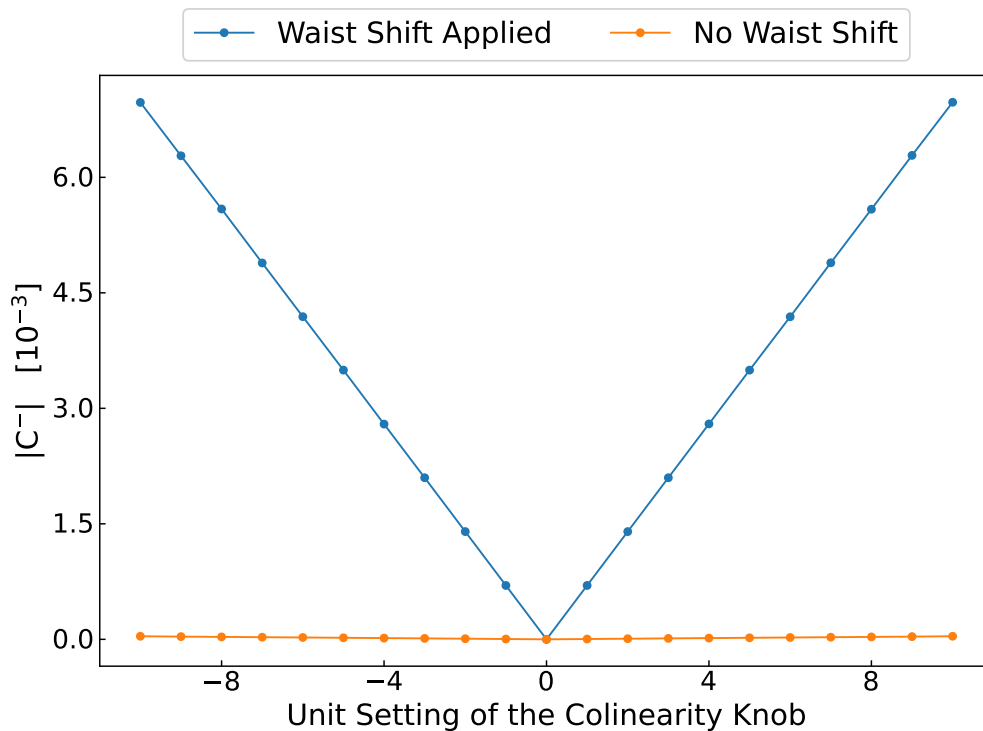


FIGURE 4.15: Impact of the colinearity knob on the global $|C^-|$, calculated according to Eq. (2.73), with (blue) and without (orange) applying an RWS.

As previously mentioned, since the bump is not actually perfectly closed the orange line in Fig. 4.15 is not completely flat and reaches up to $\sim 10^{-5}$, which is well below the measurement accuracy for the $|C^-|$. The behavior seen in Fig. 4.15, though theoretical, has been experimentally tested and confirmed in the machine [188]. Importantly, this behavior opens the possibility of using an RWS to probe IR local coupling through the measured global coupling.

Simulations have been done to investigate the feasibility of finding local coupling correction settings using an RWS, with the $\beta^* = 30$ cm optics of 2022. At both IR1 and IR5, a local coupling bump was created by introducing identical tilt errors in triplet quadrupoles Q3 - thus giving a skew quadrupolar component - and the colinearity knob was powered for compensation. The full parameter space was explored, both with and without an RWS applied. Figure 4.16 shows the values of the resulting $|C^-|$ when an RWS is applied. Figure 4.17 shows the resulting IP beam size increase as a ratio to the nominal beam size across the same parameter space.

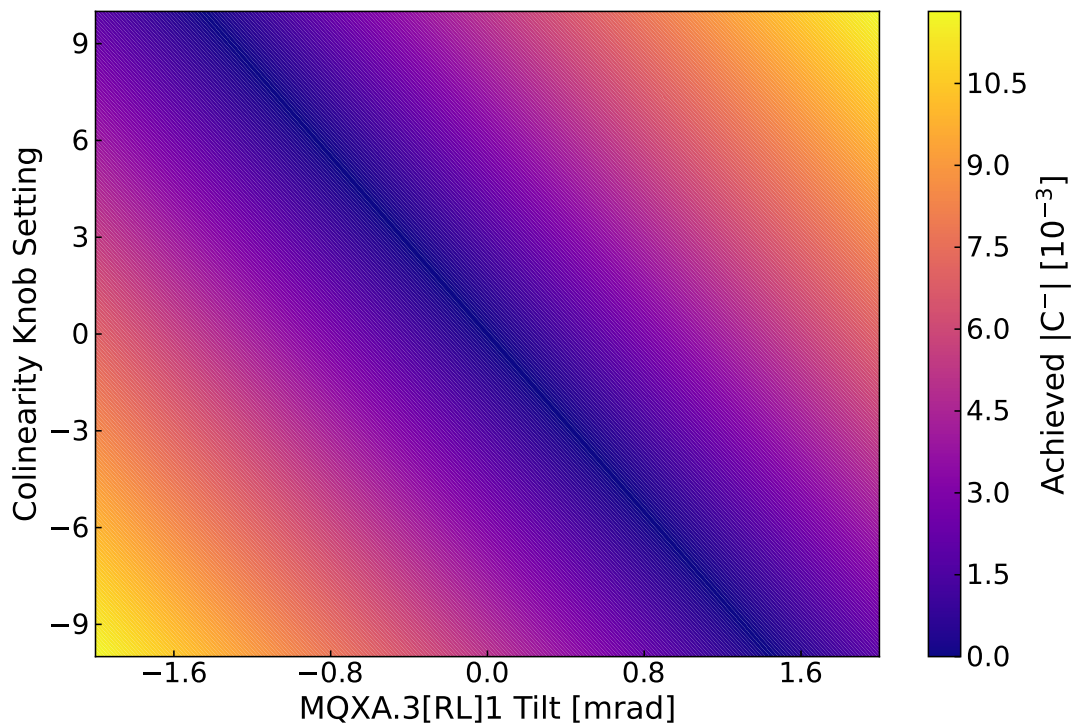


FIGURE 4.16: Resulting $|C^-|$ (Eq. (2.73)) for various combinations of tilt error and colinearity knob settings, when applying an RWS.

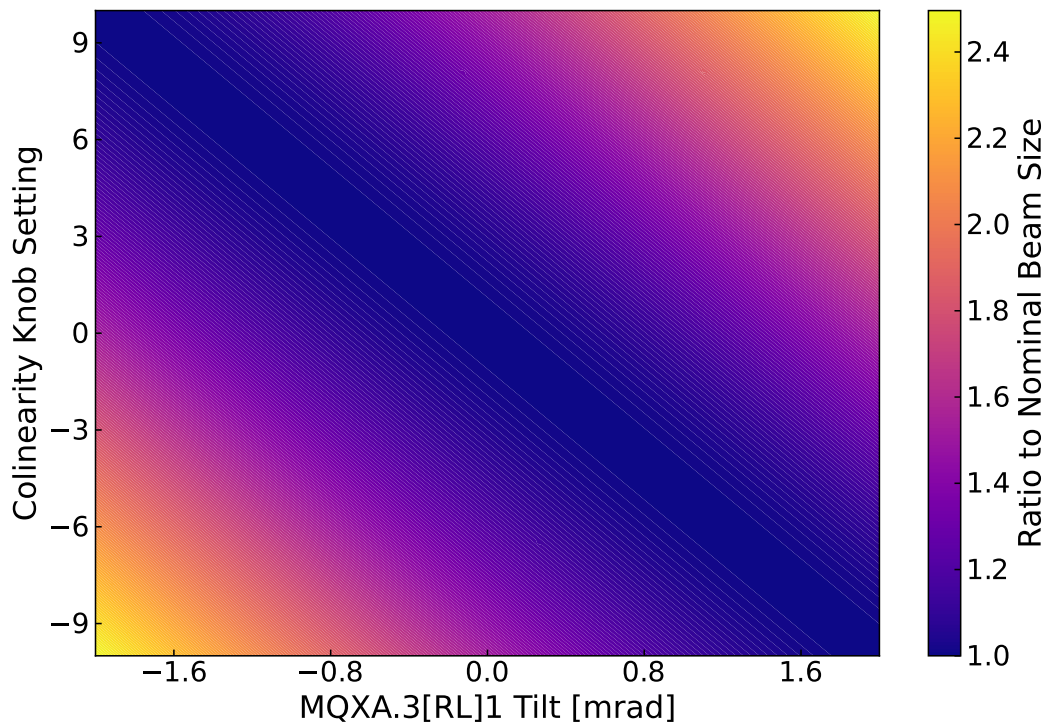


FIGURE 4.17: Resulting beam size (Eq. (4.1)) increase for identical settings of tilt error and colinearity knob settings as Fig. 4.16, but without an RWS.

The results of Fig. 4.17 highlight that minimization of the growth is possible, though a wrong setting would enhance the phenomenon. A strong correlation between beam size growth from the local coupling bump (without RWS, see Fig. 4.16) and the $|C^-|$ from leaked RDTs (with RWS, see Fig. 4.17) is observed.

Simulations replicating a more complex scenario - akin to operational conditions - were also performed. In these, tilt errors were introduced in triplet quadrupoles Q3 as previously to create a closed local coupling bump around the IP. Additionally, some tilt errors were added to an individually powered quadrupole in IR5 (for instance Q5) to simulate the presence of the expected residual local coupling errors in the other main IR, which contribute to the global coupling by the amount of 10^{-3} . Some global coupling sources were also added with a dedicated knob [191] that bring the global coupling to 10^{-2} , which was then corrected through a routine and brought down to $\sim 3 \times 10^{-3}$, a level similar to what can be achieved in the machine [192, 193]. The RWS and colinearity knobs were then powered to different settings, and the resulting $|C^-|$ and IP beam sizes were determined for all settings combinations.

Similar to the previous studies made for Figs. 4.16 and 4.17, an entire parameter space of implemented errors and corrections was explored. The evolution of both the $|C^-|$ and the beam size growth at IP1 for one of these simulations can be seen in Fig. 4.18. These curves would correspond to a vertical line in Figs. 4.16 and 4.17, but with a realistic scenario.

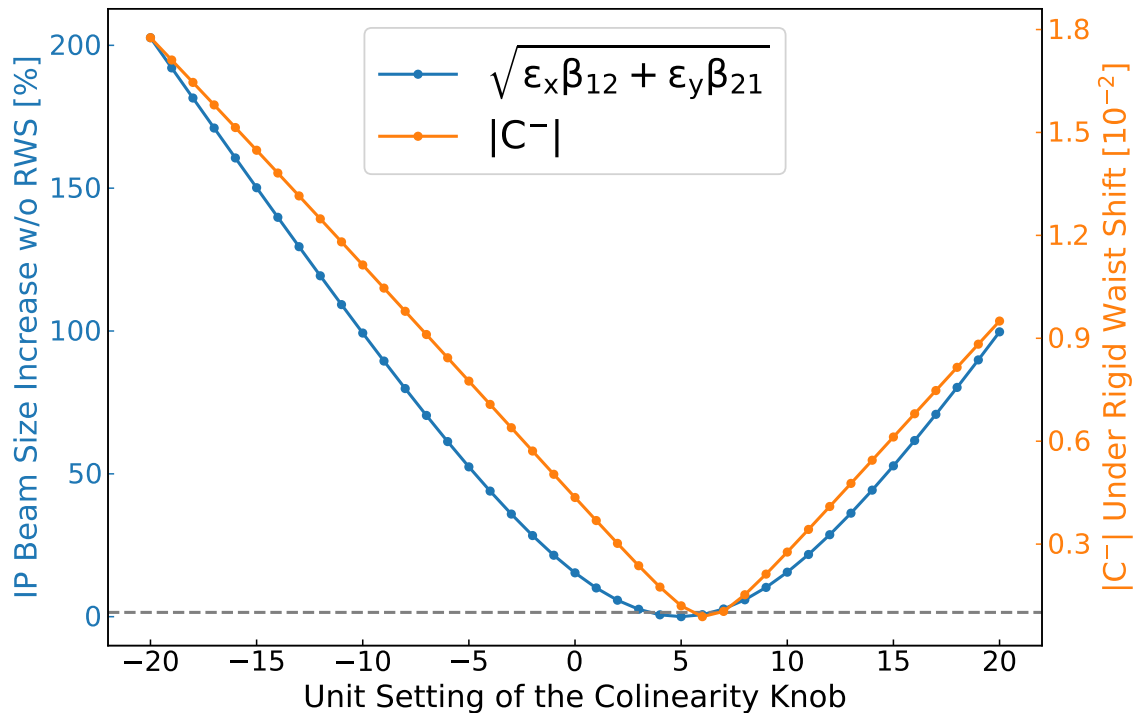


FIGURE 4.18: Resulting $|C^-|$ under an RWS (orange) and IP1 beam size (Eq. (4.1)) without an RWS relative to the nominal scenario (blue), for various colinearity knob settings. The black dotted line represents the threshold of a 1% beam size increase from the nominal scenario.

It can be observed that settings minimizing the measured $|C^-|$ under an RWS are very close to minimizing the coupling induced beam size increase without said RWS. Here, these settings also compensate for the contribution of the other added sources, on

top of the local ones. Similarly to previous studies a great correlation is observed, and across the parameter space one computes a 0.96 Pearson correlation coefficient between the quantities shown in Fig. 4.18. This confirms the link between the measured $|C^-|$ and the quantities of interest at the IP location. To summarize:

- Thanks to the RWS, sources leading to truly local coupling can be probed through their forced impact on global coupling.
- Using the correlation properties demonstrated above, one can find settings to minimize said local coupling and its effects at the IP.

4.4.3 Determining Corrections

The corrections which would compensate only the local sources are determined by comparing the measured $|C^-|$ to simulations, such as the orange line in Fig. 4.18.

In the real machine, some coupling will remain in the arcs due to a non-perfect global correction and non-local SbS corrections. As the method probes local errors' impact through the $|C^-|$, it will naturally be sensitive to the global coupling in the machine, which should be replicated in simulations. Although the overall behavior of simulations remains similar when including this component, an important change from the line seen in Fig. 4.18 is the location of the setting that minimizes the $|C^-|$. The relevance of this property will be discussed below. By comparing measurements from a colinearity knob scan to simulations - where the former includes the impact of local errors, but the latter does not - one can single out the contribution of the local sources to global coupling. This is illustrated in Fig. 4.19.

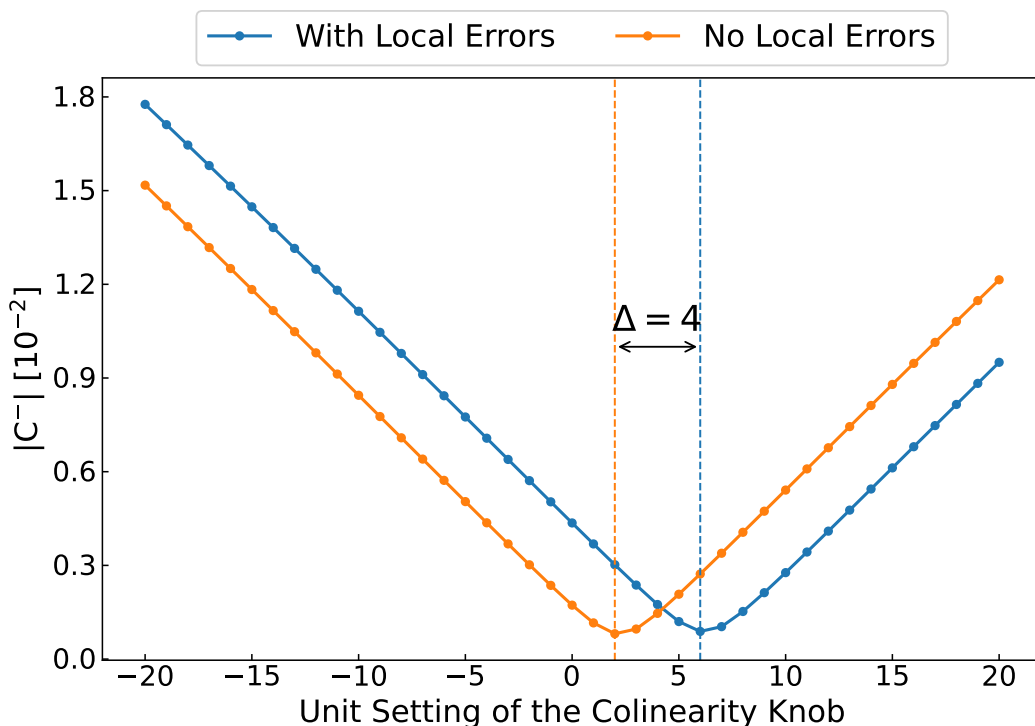


FIGURE 4.19: Resulting $|C^-|$ in simulations as done for Fig. 4.18, with (blue) and without (orange) local coupling sources in IR1.

Figure 4.19 shows the resulting $|C^-|$ values under an RWS during a colinearity knob scan, for one of the simulation scenarios mentioned previously (Fig. 4.18) (blue), and a similar scenario in which no local coupling sources were implemented in IR1 (orange). The former represents what would be measured in the machine, including the contribution of local sources. The latter represents a simulation to compare such a measurement to, which includes all contributions to global coupling except for the IR local sources. The difference between the two curves is then fully explained by the local sources.

Applying a trim of the colinearity knob setting linearly translates the curves of Fig. 4.19 horizontally. This behavior is valid and verifiable in both simulations and measurements. Therefore, one looks to determine a colinearity knob trim that, if applied in the machine, would bring the measurement's $|C^-|$ minimization point to that of the simulation. As this difference is fully explained by local sources, this trim contains the information on the local error in terms of colinearity knob setting: powering of the corrector magnets. In Fig. 4.19 the minima are highlighted with vertical lines and the aforementioned correction trim is determined from the relative position of these two minima. The value is different from that of the minimization in Fig. 4.18 as there global sources are also compensated while this correction aims at compensating only the local sources.

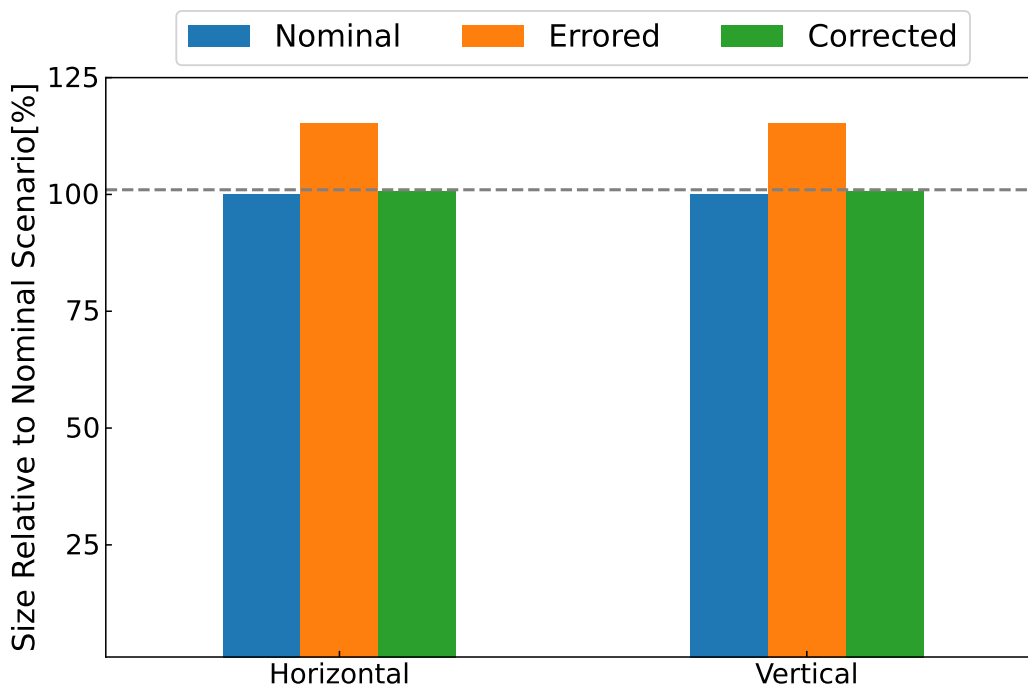


FIGURE 4.20: Relative IP beam sizes when compared to the nominal scenario (blue) when inputting the local errors used in the study for Fig. 4.19 (orange) and after applying the suggested correction (green). The black dotted line represents the threshold of a 1% beam size increase from the nominal scenario.

When only considering the local sources used for the results in Fig. 4.19 and inputting the correction trim suggested, one obtains a good compensation of the beam sizes at IP1. Figure 4.20 shows the impact of these local errors and the effect of applying the

suggested correction trim. The exactitude and effectiveness of the determined correction can be improved by performing higher resolution scans of the colinearity knob, but the values used are representative of what can be done in measurements.

Reproducing the Machine's Coupling

The reproduction of the machine's global coupling in simulations becomes necessary as soon as strong non-IR sources are present, which is likely in the real machine. Unfortunately the true distribution of sources in the machine is not known, and this reproduction can then be done in different ways. In studies, various implementations were tested: random tilts in all quadrupoles, LHC specific knobs [191], longitudinal misalignment of sextupoles, field errors in specific magnets or random combinations of the above. The resulting $|C^-|$ for these can be seen in Fig. 4.21, where for each scenario the minimization point is highlighted by a vertical dashed line.

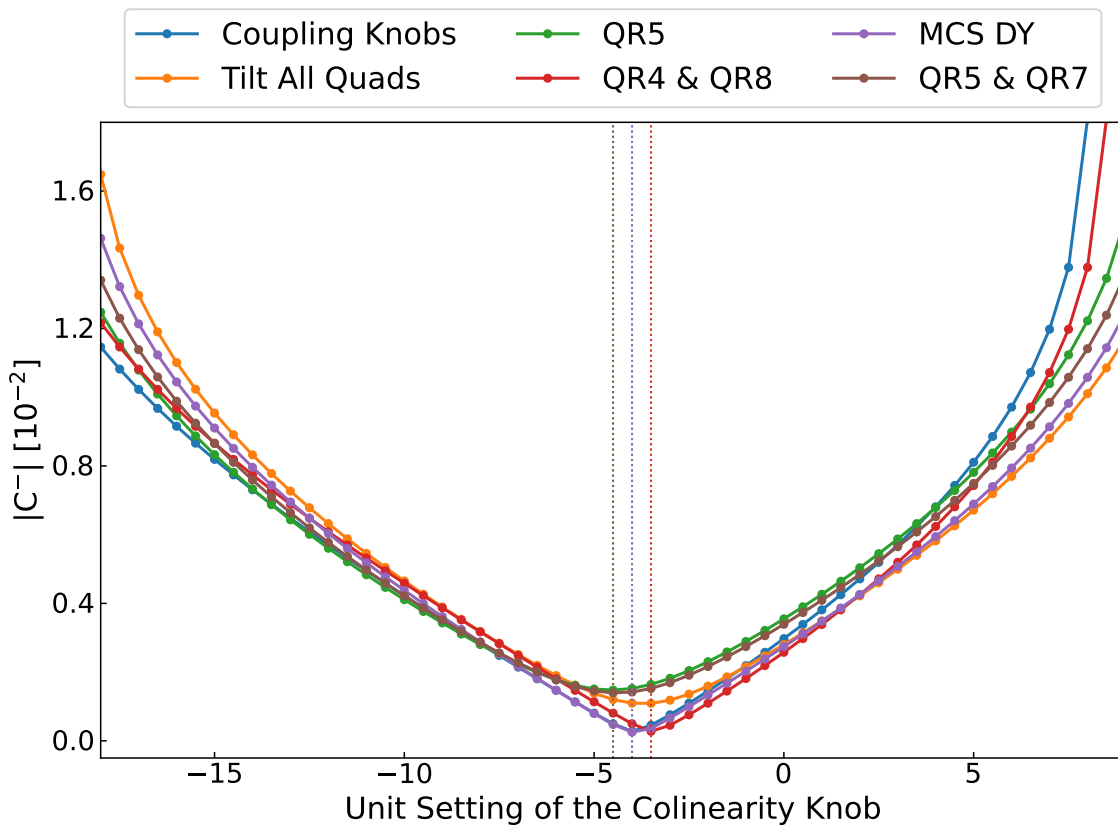


FIGURE 4.21: Resulting simulated $|C^-|$ under an RWS during a scan of the colinearity knob, for various implementations of global coupling in the machine. For each case a vertical dashed line highlights the location of the minimization point.

In all investigated scenarios the achieved $|C^-|$ before applying the RWS is the same value before ($\sim 10^{-2}$) and after ($\sim 2 \cdot 10^{-3}$) applying a correction routine. It was found that, to the levels of coupling we achieve after correcting the machine the distribution and implementation of sources had little impact on the minimization point of the $|C^-|$ curve under an RWS, as long as the overall pattern of the f_{1001} and the level of coupling measured in the machine were accurately reproduced.

One can see in Fig. 4.21 how the minimization point is relatively unchanged by the global coupling implementation method within the precision of the mesh step used for the scan, which was chosen to reflect that achievable in the machine. As a consequence, this coupling contribution was simulated using the coupling correction knobs implemented in the machine, as determined during earlier commissioning steps.

4.4.4 Rigid Waist Shift Procedure

To summarize so far, two tools have been developed and presented to tackle local coupling correction:

- The colinearity knob (Table 4.1) allows adjusting the coupling at the IP without affecting the rest of the machine, namely previously established corrections.
- The Rigid Waist Shift knob (Table 4.2) allows probing local errors through the $|C^-|$ (Figs. 4.14 and 4.15) and to find a correction setting of the colinearity knob that will minimize the coupling at the IP (Figs. 4.19 and 4.20).

Using those, the complete correction procedure for local linear coupling is then made of three steps:

1. Firstly, calculating and applying a correction of the IR contribution to global coupling based on RDTs from turn-by-turn measurements, using the SbS technique.
2. Secondly, breaking the optics symmetry between the right and left-hand side of the IP by applying an RWS, and performing a scan of the colinearity knob.
3. Finally, analyzing the data and comparing them to simulations in order to find a colinearity knob adjustment that minimizes the global coupling, without impacting the correction found in step 1.

These measurements can be performed for each IR and for each beam, and the subsequent determined corrections can then be directly applied in the machine.

4.5 Local Coupling Correction in the LHC 2022 Commissioning

Below are presented experimental results of local coupling correction in the LHC's first year of Run 3, during the 2022 commissioning, using the RWS procedure presented above. One can refer to Appendix E for information on the fills used for experimental measurements.

4.5.1 Segment-by-Segment Corrections

In October 2021 a week of beam tests was done in the LHC at injection energy. From the measurements at 450 GeV a first set of local coupling corrections were calculated for each of the four main IRs using the segment-by-segment technique. Figure 4.22 shows the segment-by-segment results for the absolute value of the f_{1001} RDT in IR5, from the 12th BPM left to right of IP5. The vertical grey line indicates the location of the IP

in the segment. Due to the [skew](#) quadrupole correctors in the IRs being single aperture magnets, one needs to find a single powering setting that works for both beams and both are shown on the figure.

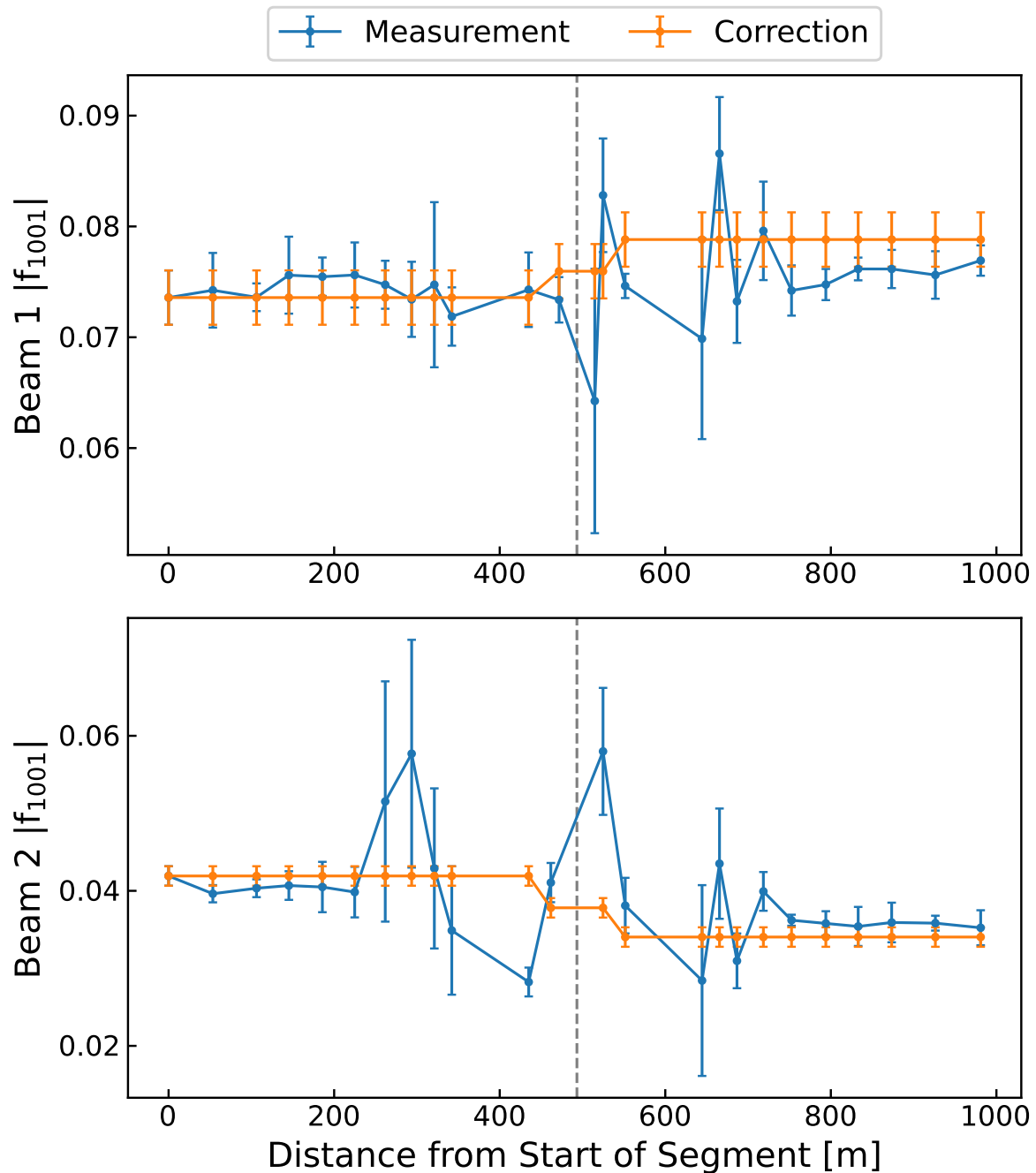


FIGURE 4.22: Propagation of the measured $|f_{1001}|$ (blue) around IP5 (dashed grey line) and of the reconstructed values from the determined correction (orange), measured at 450 GeV and $\beta^* = 11$ m.

One can see that the determined correction in IR5 matches the propagated measurement within the tolerance of the error bars at the edges of the segment. This guarantees a good compensation of the IR's contribution to global coupling.

During the LHC Run 3 commissioning, local coupling corrections determined during the previous year's beam test were trimmed in the machine from the start. After reaching the $\beta^* = 30$ cm optics, where the machine is more sensitive to local errors, a noticeable deviation around IP1 was observed and a refinement of the correction was determined, still with the segment-by-segment technique. Figures 4.23 and 4.24 show the effect of the new correction on the real and imaginary parts of the f_{1001} RDT in the segment, respectively.

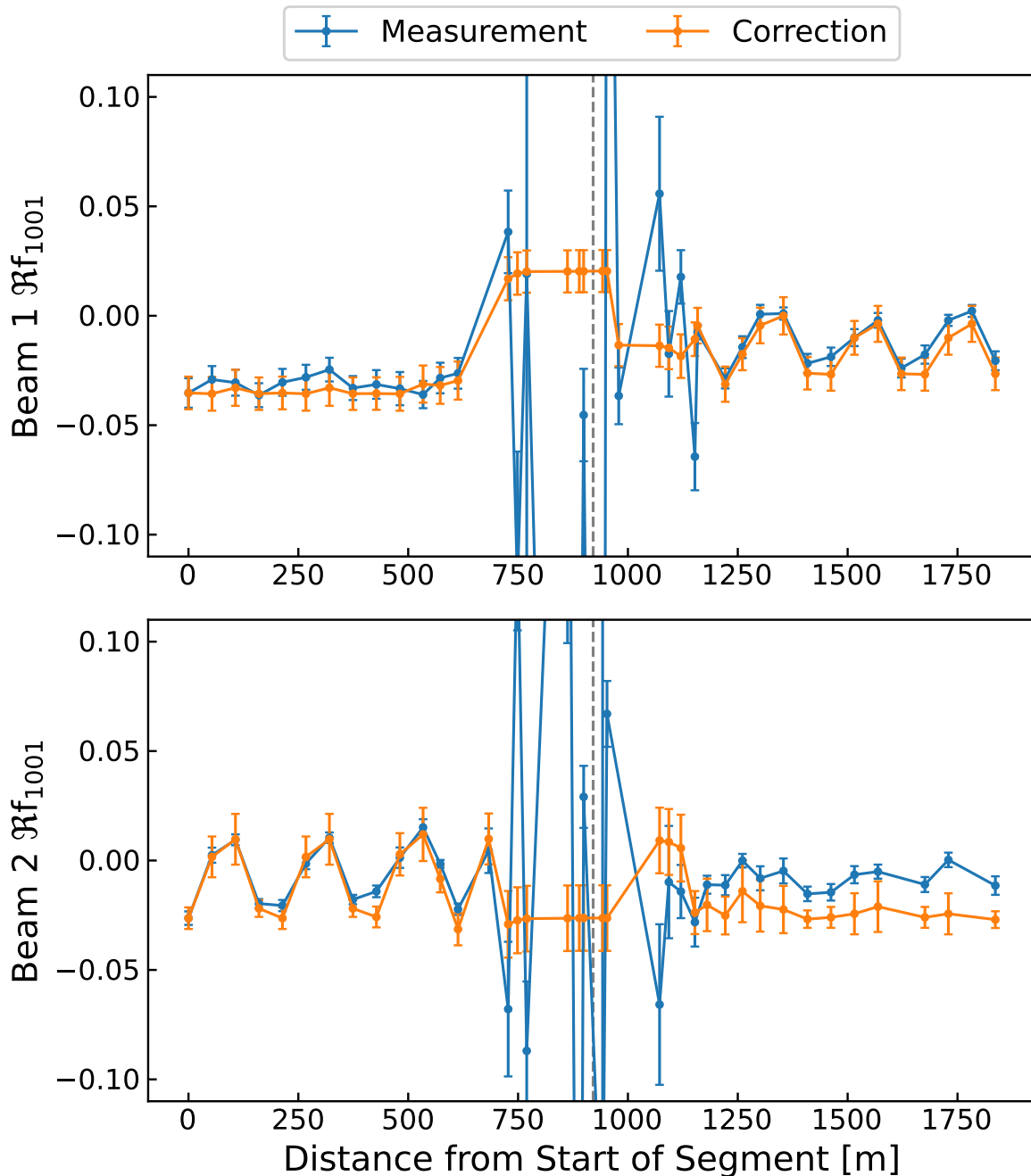


FIGURE 4.23: Propagation of the measured $\Re f_{1001}$ (blue) around IP1 (dashed grey line) and the reconstructed values from the determined correction (orange), measured at 6.8 TeV and $\beta^* = 30$ cm.

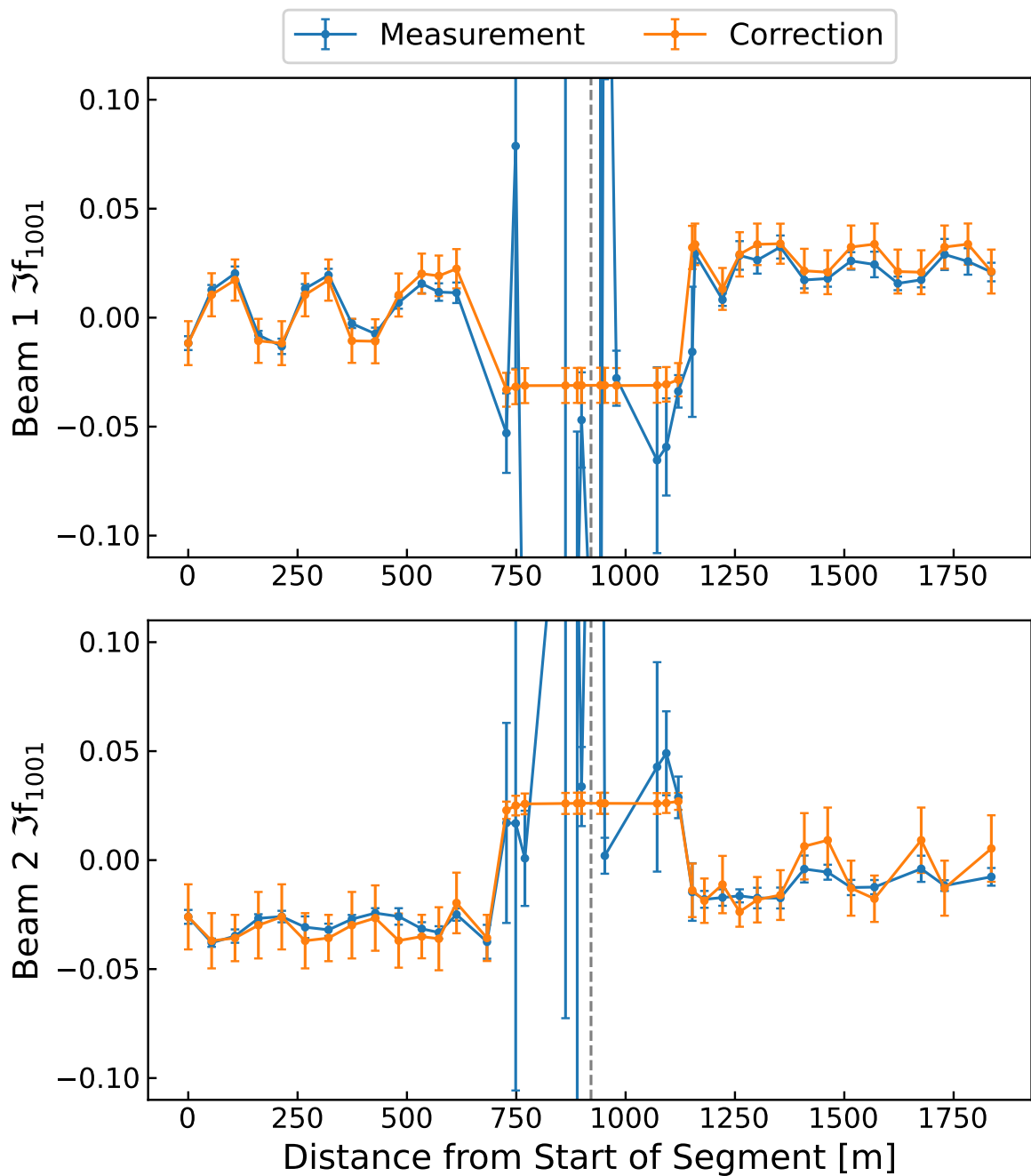


FIGURE 4.24: Propagation of the measured $\Im f_{1001}$ (blue) around IP1 (dashed grey line) and the reconstructed values from the determined correction (orange), measured at 6.8 TeV and $\beta^* = 30$ cm.

The beating observed from the old correction was re-matched thanks to a setting adjustment where the IR1 right-hand side corrector's powering was changed by 10^{-4} m^{-2} . The final correction settings determined with the segment-by-segment technique and trimmed in the machine at the four main IRs can be found in Table 4.4, along with their counterpart values from Run 2 for comparison.

IR	Circuit	K_{1S} [10^{-4} m^{-2}]	
		2016-2018 [184]	2022 SbS
IR1	RQXS.3L1	11	8
	RQXS.3R1	7	7
IR2	RQXS.3L2	-14	-14
	RQXS.3R2	-14	-14
IR5	RQXS.3L5	7	6
	RQXS.3R5	7	6
IR8	RQXS.3L8	-5	-5
	RQXS.3R8	-5	-5

TABLE 4.4: Local IR skew quadrupole correctors powering at the four main LHC IRs as determined with the segment-by-segment technique in the 2022 commissioning and their values as used during the LHC Run 2.

4.5.2 Rigid Waist Shift Corrections

The RWS method was implemented in both IR1 and IR5 at 6.8 TeV and $\beta^* = 30$ cm to determine final correction settings in the form of adjustments from the SbS corrections presented above. Relevant fills used for these measurements can be found in [Table E.3](#).

As a first step, the validity of the experimental setup was verified by trimming the RWS in the machine and then checking the efficiency of the optics rematching knobs. [Figure 4.25](#) shows the β -beating across the machine for beam 1 before any knob application (yellow), from applying the RWS in IR5 (blue) and after the application of the optics re-matching knob (red). Similar checks were done for both beams and both IRs. The β -functions in these measurements are reconstructed with the OMC codes according to [194].

The measured impact is in agreement with what was expected from earlier simulations (see [Section 4.4.1](#)), leading to a 15-25% additional β -beating in the machine depending on the observed beam and plane; while the re-matching knob brought this beating back to about 5% where it was previously kept thanks to existing corrections. Considering the state of the machine at the time of these measurements, it can be considered that the optics re-matching shows great efficiency. Naturally, some strong deviations are noticed close to IP5 (going out of range of the y-axis) as the optics there are changed on purpose, but also because β -function reconstruction close the IPs is of relatively low quality.

After confirming the validity of the optics knobs and with the waist shift in the machine, scans of the colinearity knob ([Table 4.1](#)) were performed. At each setting, a few measurements were taken by method of beam excitation, from which the coupling RDTs were computed. As the optics are affected - and re-matched - differently for beam 1 and beam 2, a scan of the colinearity knob was performed for each beam and for each IR. Different scans were done with different granularity due to time constraints.

For each measurement, the RDTs across the machine are normalized to the base case with no RWS, global coupling corrected and no colinearity knob trim. Only then

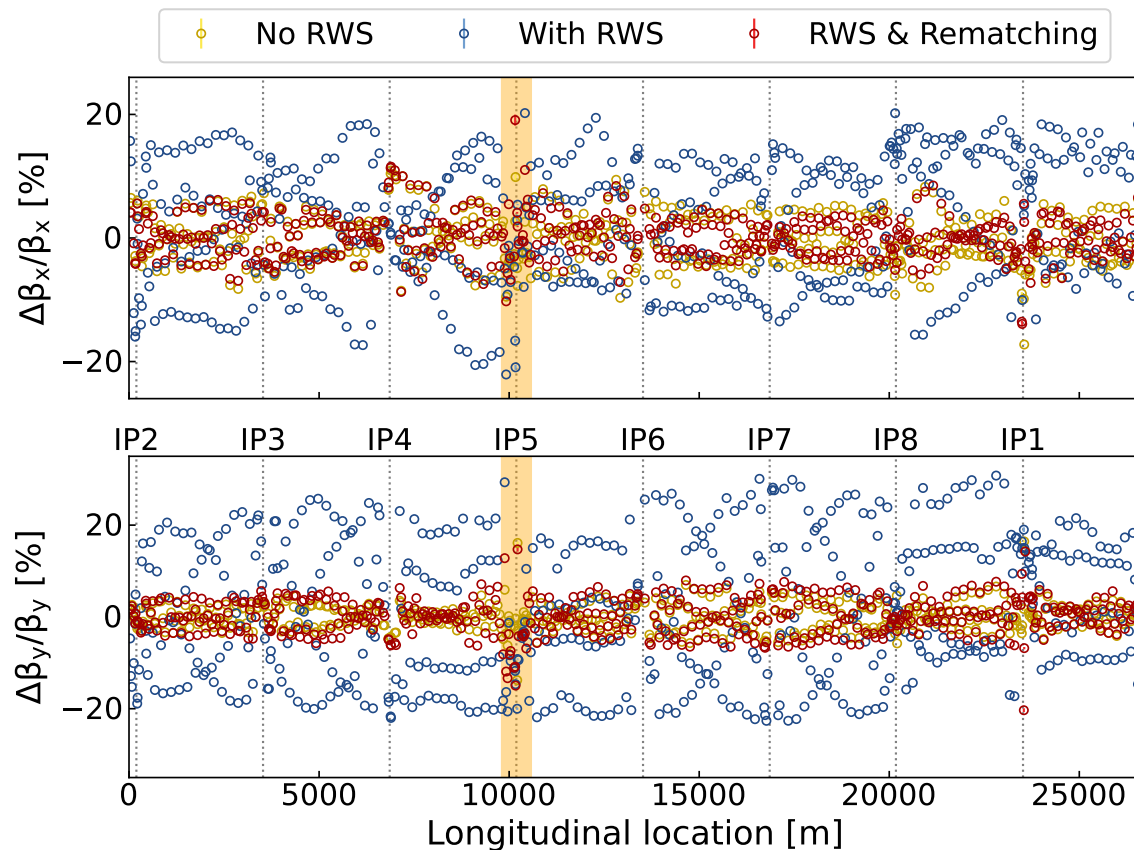


FIGURE 4.25: The beam 1 β -beating observed at 6.8 TeV and $\beta^* = 30$ cm for the corrected machine (yellow), from the implementation of the RWS in IR5 (blue) and after applying the optics re-matching knob (red). The highlighted area (orange) shows where magnetic elements are affected by the knobs.

is the $|C^-|$ computed according to Eq. (2.73). Then the variations due to the changes of the colinearity knob are visualized and compared to simulations. In said simulations, the global coupling of the machine is reproduced by introducing the coupling correction knobs implemented in the machine at the time of measurements.

In Figs. 4.26 to 4.29 comparisons are shown between simulations and scan measurements at IR1 for beam 1 and beam 2, then IR5 for beam 1 and beam 2, respectively. The delta between minimization settings, corresponding to the suggested correction adjustment, is highlighted on each plot. The relatively low range of achieved $|C^-|$ values is due to the aforementioned RDTs normalization. The noticeably different behavior of beam 1 and beam 2 simulations is explained by the different coupling situation in each beam: throughout commissioning beam 2 has required only small global coupling corrections while beam 1 required significantly stronger ones, as well as local adjustments for different arcs. As these are reproduced in simulations, this difference in behavior is unsurprising.

In Figs. 4.26 to 4.29, simulations for beam 2 suggest that the (small) reproduced global coupling has little effect on the procedure, and the colinearity knob scan could almost be used alone to determine the corrections. For beam 1 simulations, however, the impact of the reproduced global coupling appears much more

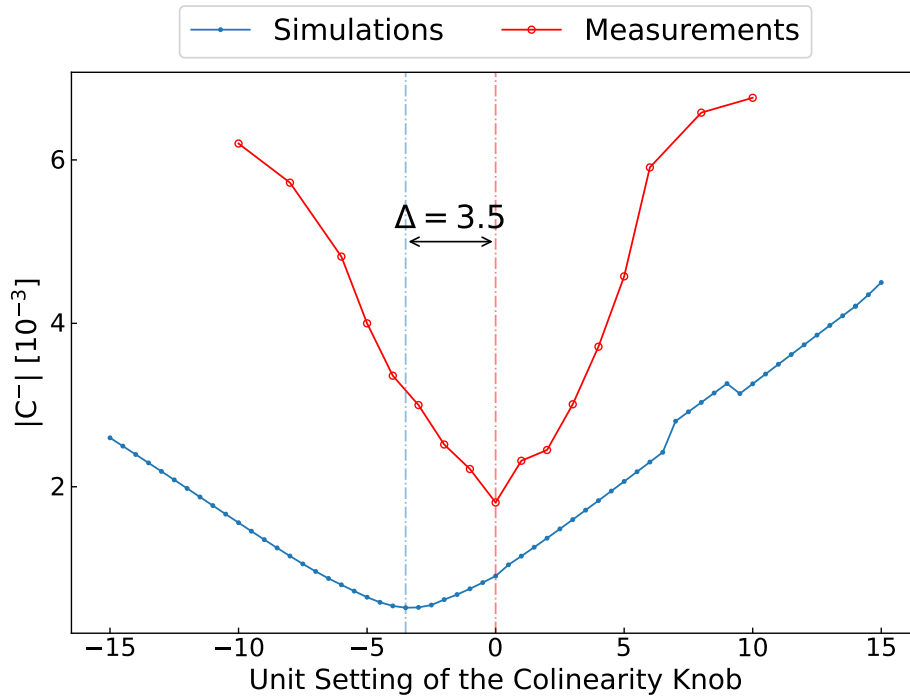


FIGURE 4.26: Measurement scan done at IR1 for beam 1 (red) and simulations for the same setup (blue). The minima of both curves are highlighted by vertical dashed lines and the delta between the two, suggesting the remaining error to correct, is displayed on the graph.

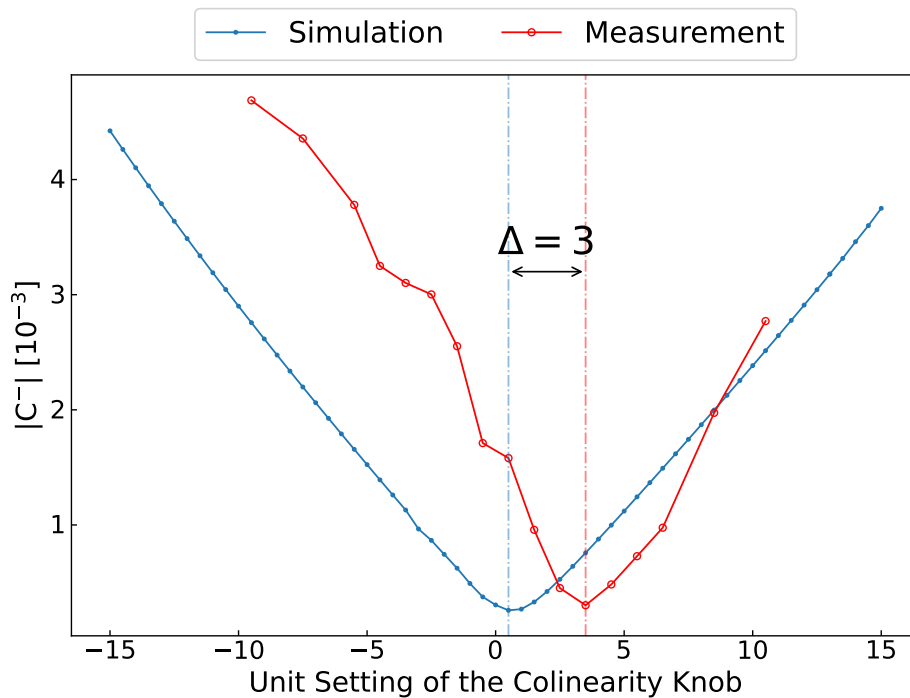


FIGURE 4.27: Measurement scan done at IR1 for beam 2 (red) and simulations for the same setup (blue). The minima of both curves are highlighted by vertical dashed lines and the delta between the two, suggesting the remaining error to correct, is displayed on the graph.

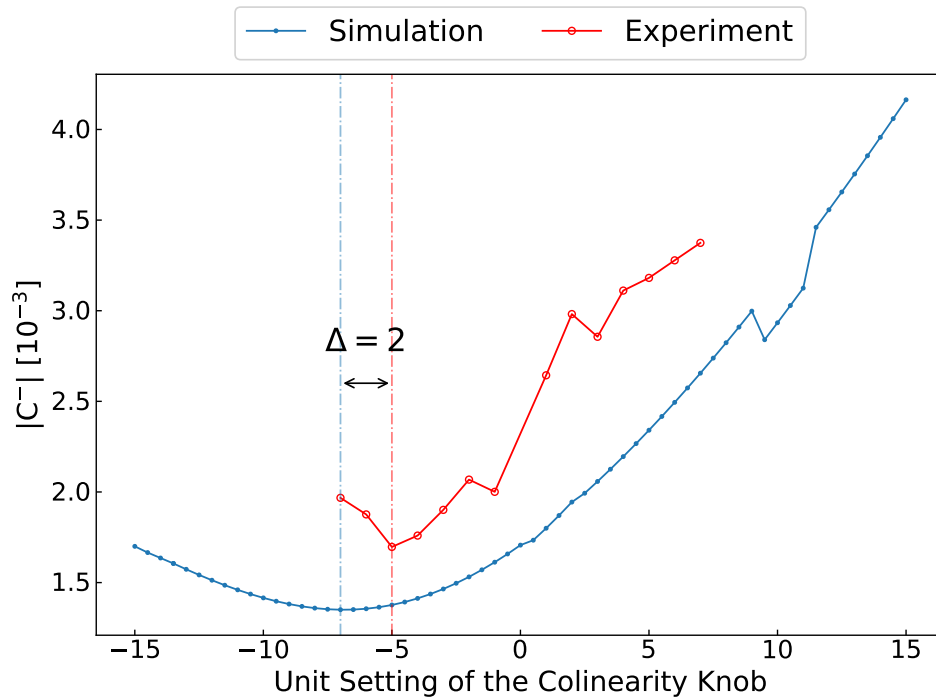


FIGURE 4.28: Measurement scan done at IR5 for beam 1 (red) and simulations for the same setup (blue). The minima of both curves are highlighted by vertical dashed lines and the delta between the two, suggesting the remaining error to correct, is displayed on the graph.

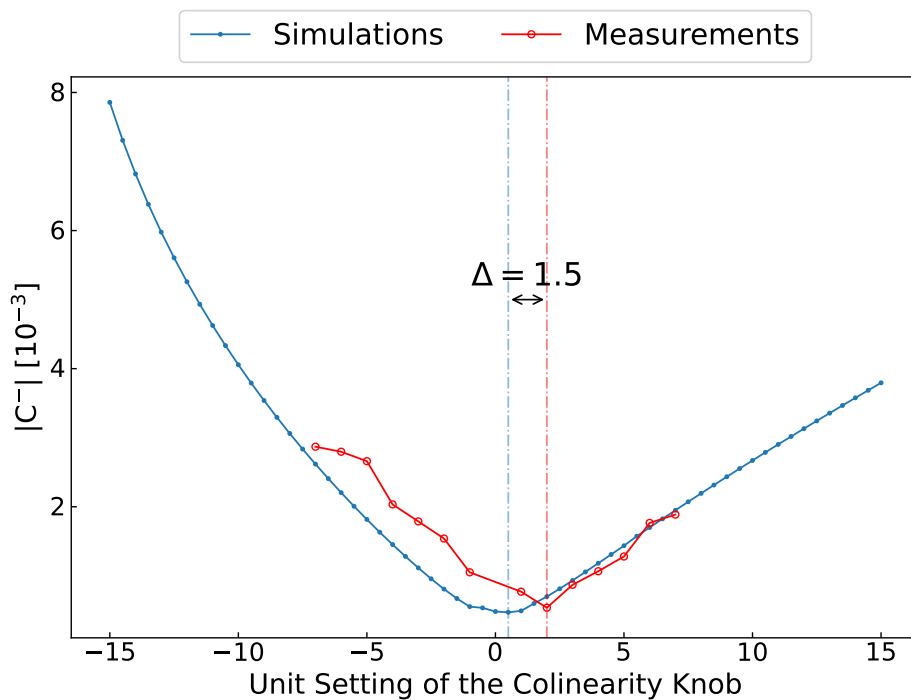


FIGURE 4.29: Measurement scan done at IR5 for beam 2 (red) and simulations for the same setup (blue). The minima of both curves are highlighted by vertical dashed lines and the delta between the two, suggesting the remaining error to correct, is displayed on the graph.

substantial, as was the case in the machine, and this highlights the need to compare the scan measurements to simulations. Overall, this comparison is needed in the case that there are significant coupling errors in the arcs. It is worth noting that both beams' measurements converge to similar correction suggestions.

Table 4.5 shows a summary of the suggested correction settings for each beam and IR. While slightly different corrections are suggested from independent scans of beam 1 and beam 2, it is possible that both values are simultaneously true. Indeed, while most of the error contribution is expected to come from the dual-beam triplet quadrupoles and be common to both beams, errors in double aperture magnets Q4 to Q10 would affect each beam individually and force a divergence of the suggested correction adjustments for each beam.

Scan	Suggested Δk [10^{-4}m^{-2}]	
	Beam 1	Beam 2
IR1	−3.5	−3
IR5	−2	−1.5

TABLE 4.5: Correction adjustments suggested from the Rigid Waist Shift scans analysis, on top of the existing segment-by-segment corrections that were in the machine (see Table 4.4).

Furthermore, the orbit and hence feed-down but also the β ratio between sources and correctors are different for both beams, which could explain part of the difference. As the main contributors to the error are the triplets, it is not unsurprising to obtain similar correction suggestions for both beams.

Some more measurements were performed with an opposite setting of the RWS in both IRs that did not yield sensible correction suggestions, which have not been shown here. For completeness, these are exposed in Appendix D together with the suspected reasons for each one's failure.

4.5.3 Luminosity Confirmation

Later on during the 2022 physics run, beam time was allocated to trim in the suggested adjustments from Table 4.5. The impact of the corrections was assessed based on instantaneous luminosity measurements at the time of the trims. Time was found to perform measurements of the efficiency of corrections in each IR at both $\beta^* = 30$ cm and $\beta^* = 42$ cm. Information on the fills used can be found in Table E.4.

For each measurement, trims around the suggested correction adjustments were also performed in order to look for the best local setting, which might not necessarily have been found by the method. Below are shown data from the trims at $\beta^* = 30$ cm only, while $\beta^* = 42$ cm results are compiled in a later table.

Figure 4.30 shows the trim performed at IR1 (blue) and subsequent measured luminosity changes at the ATLAS experiment (orange). The light blue area highlights the trim values suggested by the RWS method, which vary for beam 1 and beam 2. The instantaneous luminosity signal slightly trails up after the end of the correction adjustment

trim as the ATLAS experiment publishes a time-averaged value. A great improvement in luminosity can be observed from the trim, with an almost 10% improvement from the adjustment.

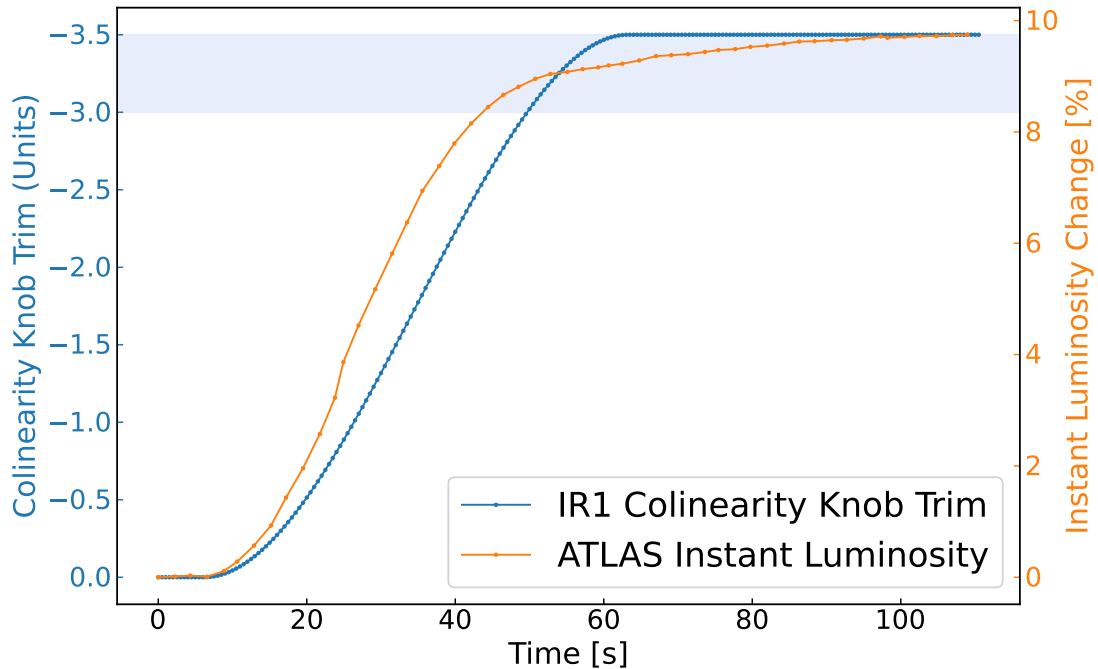


FIGURE 4.30: Trim of the colinearity knob setting (blue) and observed IP1 instantaneous luminosity change (orange) at 6.8 TeV and $\beta^* = 30$ cm. The blue area highlights the trim values suggested by the RWS method, which varies for beam 1 and beam 2.

Figure 4.31 shows the trim performed at IR5 during the same fill. Once again the trim of the colinearity knob is shown in blue and the recorded luminosity change at the CMS experiment in orange. Similarly to Fig. 4.30, the light blue area highlights the trim values suggested by the RWS method. The luminosity data outliers observed in the plot are either luminosity measurement artifacts or changes from adjustment to the head-on scheme and can be safely dismissed, as they are located outside the time periods of the trims.

Unfortunately, due to higher priority tasks for the operators at the time, the trim was not completed in a single go to the target value and as a result the luminosity decreased in the time between the different parts of the trim. Figure 4.32 shows a cut view of the data, where the downtime in between the various parts of the trim has been left out (notice the cut in the horizontal axis). The overall improvement from the complete trim is estimated from the individual observed luminosity improvements of the different parts of the trim, and amount to an almost 4% increase from the adjustment.

Table 4.6 gives a summary of the observed luminosity improvements for each performed trim, at both $\beta^* = 30$ cm and $\beta^* = 42$ cm. Overall great improvements are obtained throughout, with the largest gains recorded for IP1. It is expected that lower gains are observed at higher β^* as the $\sqrt{\beta_x \beta_y}$ term of Eq. (4.4) is substantially lower in the triplets for the less squeezed optics, resulting in a smaller effect of any tilt error. It

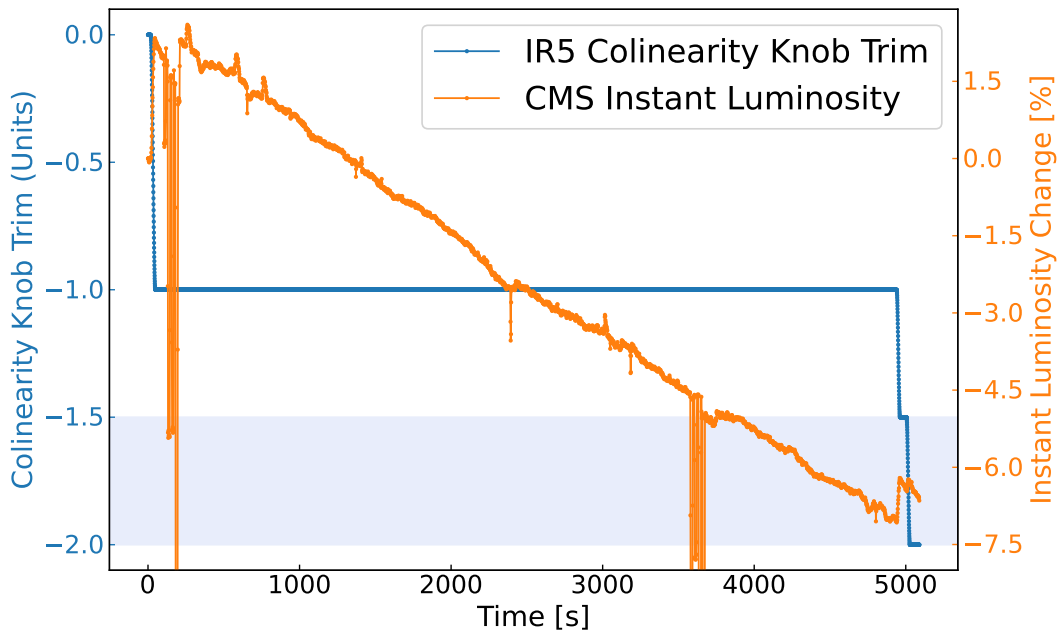


FIGURE 4.31: Trim of the colinearity knob setting (blue) and observed IP5 instantaneous luminosity change (orange) at 6.8 TeV and $\beta^* = 30$ cm. The blue area highlights the trim values suggested by the RWS method, which varies for beam 1 and beam 2.

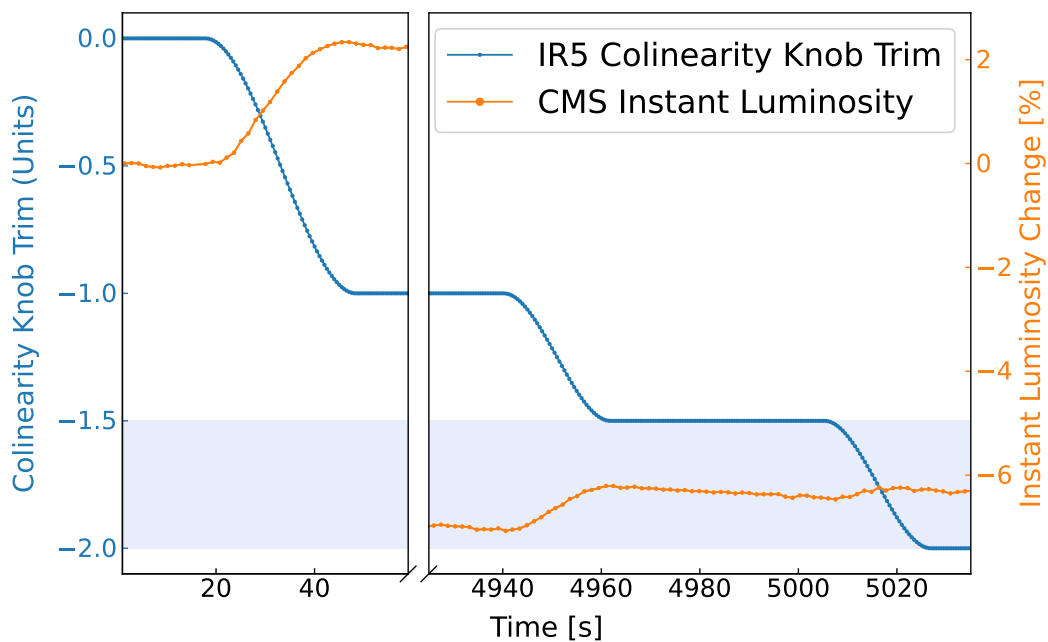


FIGURE 4.32: Zoomed view of the colinearity knob setting (blue) and observed IP5 instantaneous luminosity change (orange) at 6.8 TeV and $\beta^* = 30$ cm. The blue area highlights the trim values suggested by the RWS method, which varies for beam 1 and beam 2.

is also expected that there be a smaller improvement at the CMS detector based on the numbers in Table 4.5: a lower suggested adjustment indicates a smaller coupling error remains in IR5 than in IR1 after segment-by-segment corrections, and the subsequent smaller applied correction recovers less luminosity.

Experiment	Luminosity Gain [%]	
	$\beta^* = 30$ cm	$\beta^* = 42$ cm
ATLAS (IP1)	9.7	5.2
CMS (IP5)	3.5	1.5

TABLE 4.6: Instantaneous luminosity gains observed at the main experiments ATLAS and CMS from the method’s suggested corrections.

The adjustments determined with the RWS have been incorporated into the nominal corrector settings and the LHC now uses the resulting skew quadrupole powerings in normal operation. Table 4.7 gives a summary of the final settings at the two main LHC IRs as well as a comparison to their values in previous years, as an update of Table 4.4.

IR	Circuit	K_{1S} [10^{-4} m^{-2}]		
		2016-2018 [184]	2022 SbS	2022 RWS
IR1	RQXS.3L1	11	8	11.5
	RQXS.3R1	7	7	3.5
IR5	RQXS.3L5	7	6	4
	RQXS.3R5	7	6	8

TABLE 4.7: Final values of local IR skew quadrupole correctors powering at the two main LHC experiments, as determined with segment-by-segment (middle), compared to the values used in the LHC Run 2 (left) and the values after RWS adjustments (right).

4.5.4 Comparison to Expectations

Simulations were performed to compare the observed luminosity improvements to what one would expect from correcting the suspected local errors. As the adjustments were determined in terms of unit setting of the colinearity knob, one can consider these an accurate representation of the error that was left - and corrected - in the machine. For instance, a correction of $\Delta_{\text{colin}} = 5$ suggests that the corrected local error in the machine could be reproduced by introducing a -5 trim of the colinearity knob in simulations.

In these simulations, done at 6.8 TeV using the 2022 optics, the nominal machine setup was reproduced and the suspected errors at either IR1 or IR5 were introduced in the form of a powering of the colinearity knob with the opposite values as those from Table 4.5. Beam sizes were determined (Eq. (4.1)) for both beams in each case: with the trim of the colinearity knob, corresponding to the errored case; and without

any trim, corresponding to the corrected case. From these, instantaneous luminosities were determined according to Eq. (4.2). Figure 4.33 shows the expected values from simulations as well as the measured values as reported in Table 4.6.

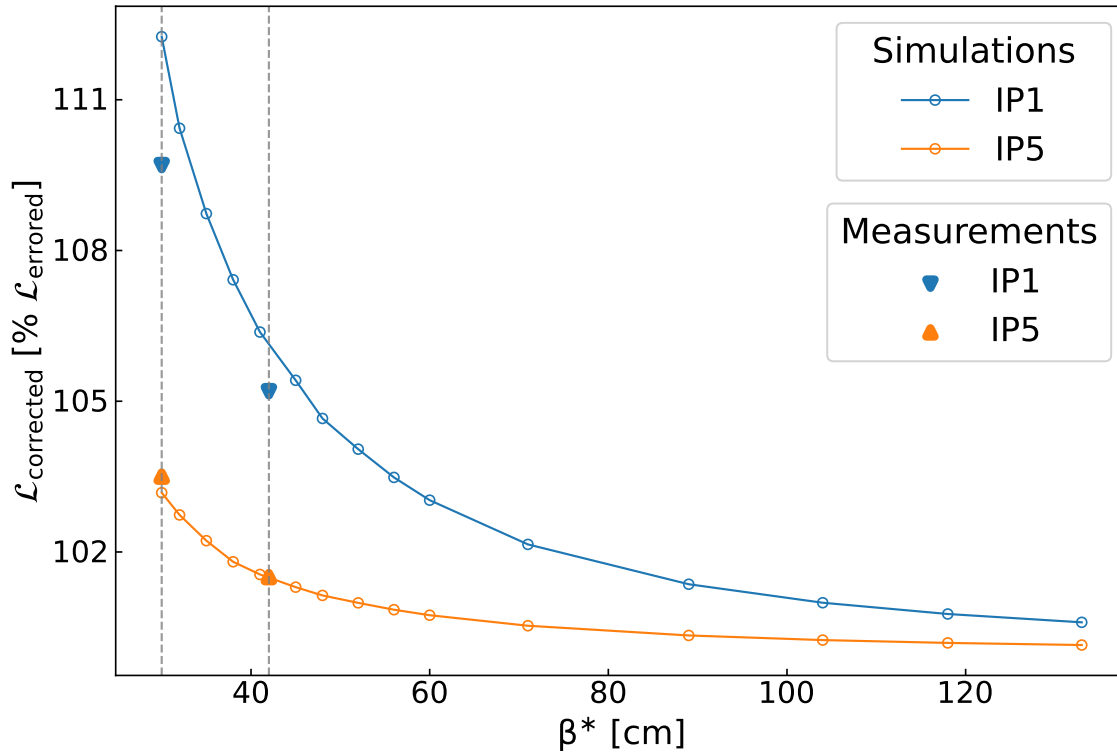


FIGURE 4.33: The expected (lines) and observed (triangular markers) instantaneous luminosity changes at 6.8 TeV for the various optics in the LHC cycle, for IP1 (blue) and IP5 (orange). Vertical dashed lines indicate the $\beta^* = 30$ cm and $\beta^* = 42$ cm data points.

While the expected luminosity gains at IP5 are in agreement with the observed ones, some discrepancies are present for IP1 data and a factor ~ 1.26 between the measurement and prediction is present.



As will be seen later on in Section 4.7, similar measurements show a much better agreement with IP1 simulation predictions using the same calculations as in Fig. 4.33. Those measurements were taken later on in the year, with higher intensity beams - thus a higher quality of the luminosity signal - and better detector setup and calibration. This leads us to believe the IP1 luminosity measurement in Fig. 4.33 is an underestimation of the actual values. The expected value for the IR1 trim, from measurements presented in Section 4.7, would be an 11.6% luminosity increase at $\beta^* = 30$ cm.

4.6 Relevance to Other Colliders

For any collider the requirement of small β -functions for collisions is a key design parameter, and leads to using a doublet or triplet of quadrupoles to achieve the

necessary intense focusing of the beams at the IP. On either side of the collision point, in the drift space leading to the first quadrupole the β -functions evolve as:

$$\beta(s) = \beta^* + s^2/\beta^* . \quad (4.6)$$

where β^* is the β -function at the IP and here s denotes the distance *from* the IP. Using L^* as the length of this drift space, the phase advance from the IP to the first quadrupole is expressed as:

$$\mu = \int_0^{L^*} \frac{1}{\beta(s)} ds = \int_0^{L^*} \frac{\beta^*}{\beta^{*2} + s^2} ds , \quad (4.7)$$

which one can integrate to obtain:

$$\mu = \beta^* \left[\frac{1}{\beta^*} \tan^{-1} \left(\frac{s}{\beta^*} \right) \right]_0^{L^*} = \tan^{-1} \left(\frac{L^*}{\beta^*} \right) . \quad (4.8)$$

Then, for traditionally $L^* \gg \beta^*$ one gets:

$$\mu \simeq \tan^{-1}(\infty) \simeq \frac{\pi}{2} . \quad (4.9)$$

As a consequence, for a typical collider layout, the phase advance from left to right doublet / triplet quadrupoles is $\sim \pi$. This can be seen in Fig. 4.34 for the FCC-ee [195] V22 lattice in the Z operation mode, which uses an asymmetric doublet of quadrupoles.

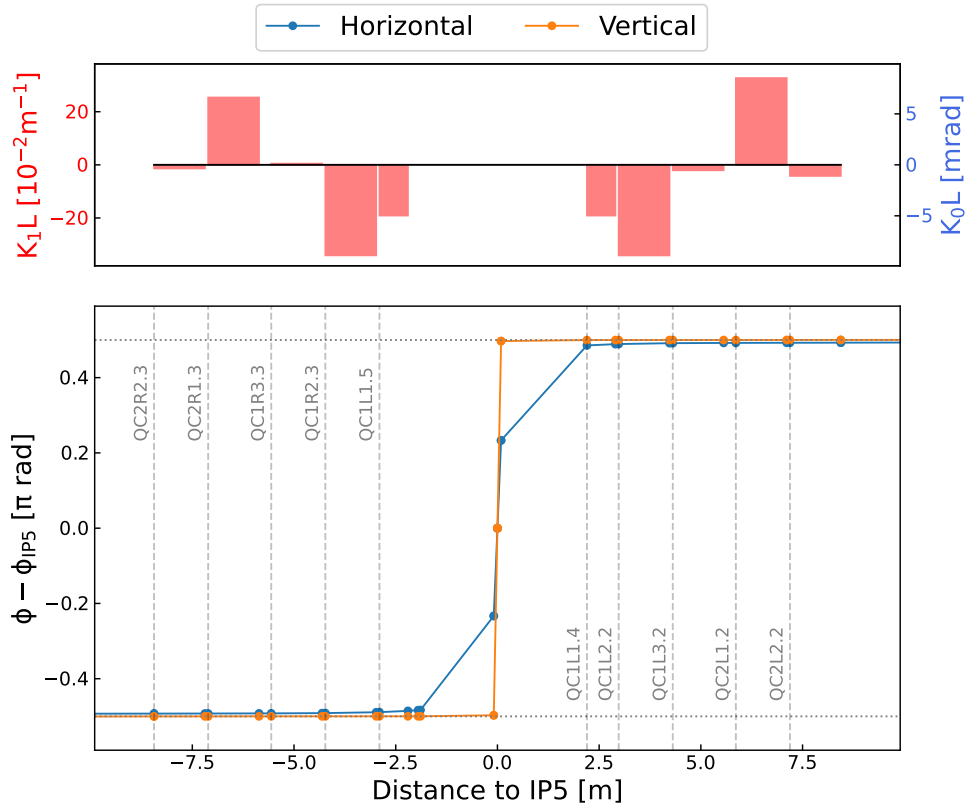


FIGURE 4.34: Phase advances relative to IP5 in the FCC-ee V22 lattice, in the Z operation mode at 45.6 GeV and $\beta^* = 10$ cm.

As a further direct consequence, tilts in these quadrupoles are likely to create a coupling bump around the IP. This can be seen, again for the FCC-ee V22 lattice, in Fig. 4.35.

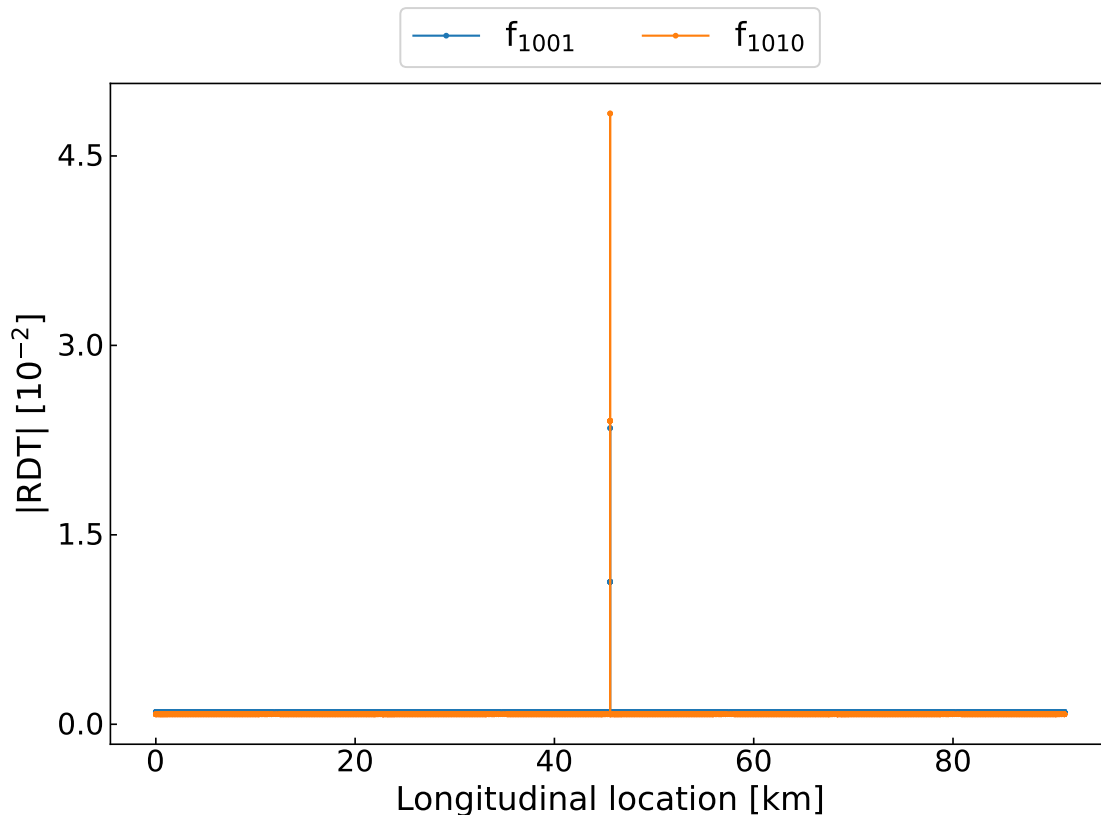


FIGURE 4.35: Simulated amplitude of coupling RDTs f_{1001} (blue) and f_{1010} (orange) from a 1 mrad tilt in the first Q1 quadrupoles around the FCC-ee's IP5.

Furthermore, the segment-by-segment limitations encountered in the LHC would also be present: no observation point is present at the IP, and due to the large β -functions in the doublet quadrupoles the phase advance from element to element close to the IP is very close to 0, making the accurate reconstruction of coupling RDTs difficult (see Section 3.3.3).

These conditions were confirmed in existing and future machines. The High-Luminosity Large Hadron Collider (HL-LHC) and FCC-hh lattices, being based on the LHC's, share the limitations that have been exposed in this chapter. The FCC-ee V22 lattice, as shown above, also exhibits these conditions and could suffer from a close coupling bump from doublet tilts. Another existing collider, SuperKEKB, has also encountered non-trivial issues with local coupling in their High Energy Ring [196].

As such, for the aforementioned accelerators but also more generally for most circular collider layouts, the presented use of a Rigid Waist Shift could provide a useful method to tackle local linear coupling.

4.7 Operation with Limited Correctors Availability

Magnet lifetime studies done during the [Long Shutdown 2 \(LS2\)](#) have projected that some magnets in the main IRs will reach their radiation dose limit during [Run 3](#) [197], including the MQSX magnets used for local coupling correction. [Table 4.8](#), reproduced from data presented in [197], shows the expected total received dose for the skew quadrupole corrector magnets in the main IRs, for various scenarios.

Magnets	Peak Dose [MGy]	
	After 395 fb ⁻¹	After 480 fb ⁻¹
MQSX (IR1)	7.5	9
MQSX (IR5)	8	9.5

TABLE 4.8: Expected total received dose of the MQSX magnets in the main IRs in Run 3. Table reproduced based on data from [197].

One can notice that the MQSXs at both IR1 and IR5 are expected to surpass their dose limit of 7 MGy during Run 3. The study itself highlights¹:

“ ” | [...] assuming a limit of 6 MGy for the corrector magnets in the triplet, this is expected to be reached in the four MCBX.1 and four MQSX by the end of 2024.

It is then warranted to prepare for one or more failures at some point during [Run 3](#), which would drastically impact the LHC’s operations, potentially shutting the machine down depending on the severity of the failures. It was therefore necessary to investigate the operational impact of losing one or more MQSX magnets in the main IRs, specifically in terms of machine safety and luminosity production. For this, different failure scenarios and containment options were investigated that would try and compensate for one or more missing correctors. The MQSX magnets in IR2 and IR8, though not considered at risk, were nonetheless included in some of these studies.

4.7.1 Operating with a Missing Corrector

Should an MQSX stop functioning, the priority is to ensure safe machine operation. In the first place, the impact of a single corrector failure around one of the main experiments was investigated.

Correction Load Carry Over

As seen in [Section 4.3](#), the contribution of one magnet can be replicated by its counterpart with a similar powering setting. For instance, looking at [Table 4.7](#), if the MQSX.3R5 were to fail the loss of contribution to global coupling would be that of an MQSX magnet with $K_{1S} = -4 \times 10^{-4} \text{ m}^{-2}$ at this location. It could be compensated by modifying the powering of MQSX.3L5 by $4 \times 10^{-4} \text{ m}^{-2}$, since the optics conditions at the correctors

¹Although this quote mentions 6 MGy this value refers to the MCBX magnets and the MQSX dose limit is indeed 7 MGy.

are identical. This compensation corresponds to a trim of -4 units of the colinearity knob around IP5 (see Table 4.1).

As such, should one MQSX fail it would still be possible to compensate for the IR's contribution to global coupling by properly powering its counterpart. It would therefore be possible to fulfill the first correction stage mentioned in Section 4.2 and to squeeze the beams down to $\beta^* = 30$ cm. Minimizing coupling at the IP, however, would not be possible anymore as it requires trimming both magnets simultaneously. The operational impact of losing one of the correctors would then be that of a potentially strong coupling at the IP.

Simulations were done with the MAD-X code to assess the impact of missing a specific corrector magnet and compensating its effect by carrying its correction setting over to its counterpart on the other side of the IP. In these simulations the power settings from Table 4.7 were used, as determined with the RWS, and beam size increases were determined from Ripken parameters according to Eq. (4.1). From these, the changes in instantaneous luminosity were calculated according to Eq. (4.2).

Figure 4.36 shows the expected instantaneous luminosity reduction from the nominal case for various trims of the colinearity knob corresponding to different missing MQSX magnets, for different β^* optics.

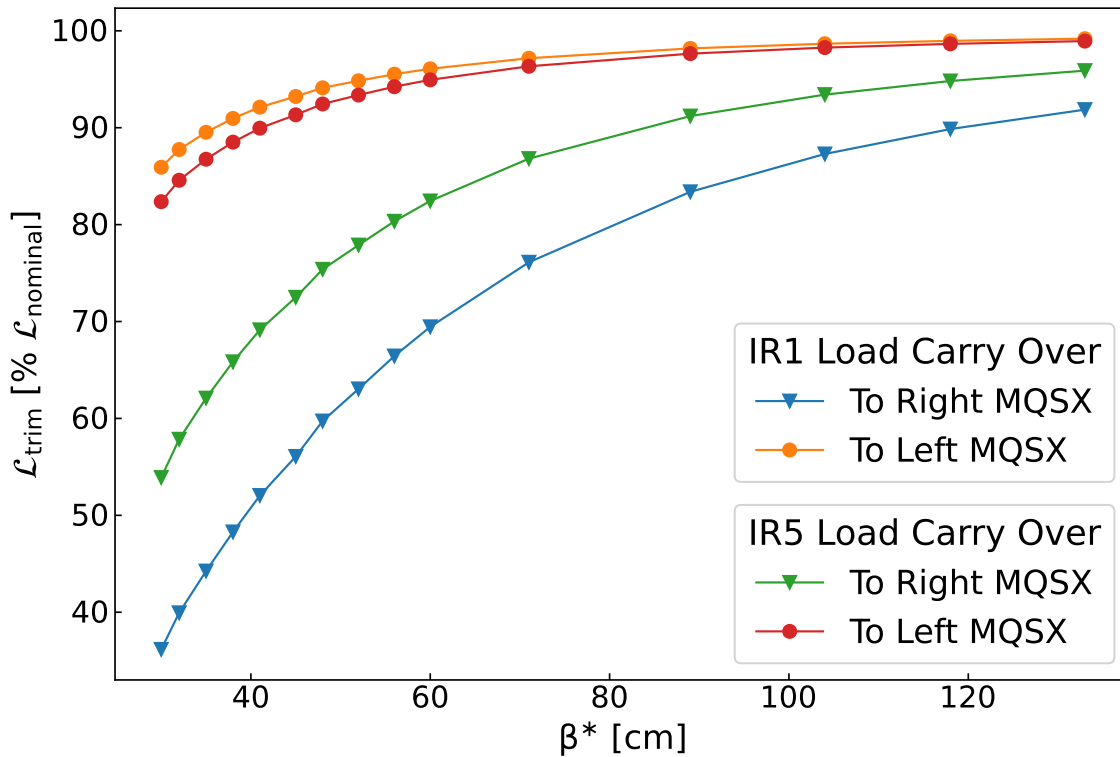


FIGURE 4.36: Expected instantaneous luminosity reduction for various trims of the colinearity knob at IP1/IP5 for different β^* optics. Each line corresponds to the trim necessary to compensate for a specific corrector's powering.

Should the most powered correctors fail, the instantaneous luminosity at the affected IP is expected to drop by up to 60% at $\beta^* = 30$ cm. Importantly, as the powering limit of the MQSXs is $K_{1S} = 30 \times 10^{-4} \text{ m}^{-2}$, it would be possible to compensate for any single failing MQSX.

The possible impact of this change on the aperture was also considered. Figure 4.37 shows the relative change in beam size around IP1 with the $\beta^* = 30$ cm optics of 2023, from the most important trim: carrying over the correction of the MQSX left of IP1 to the MQSX right of IP1.

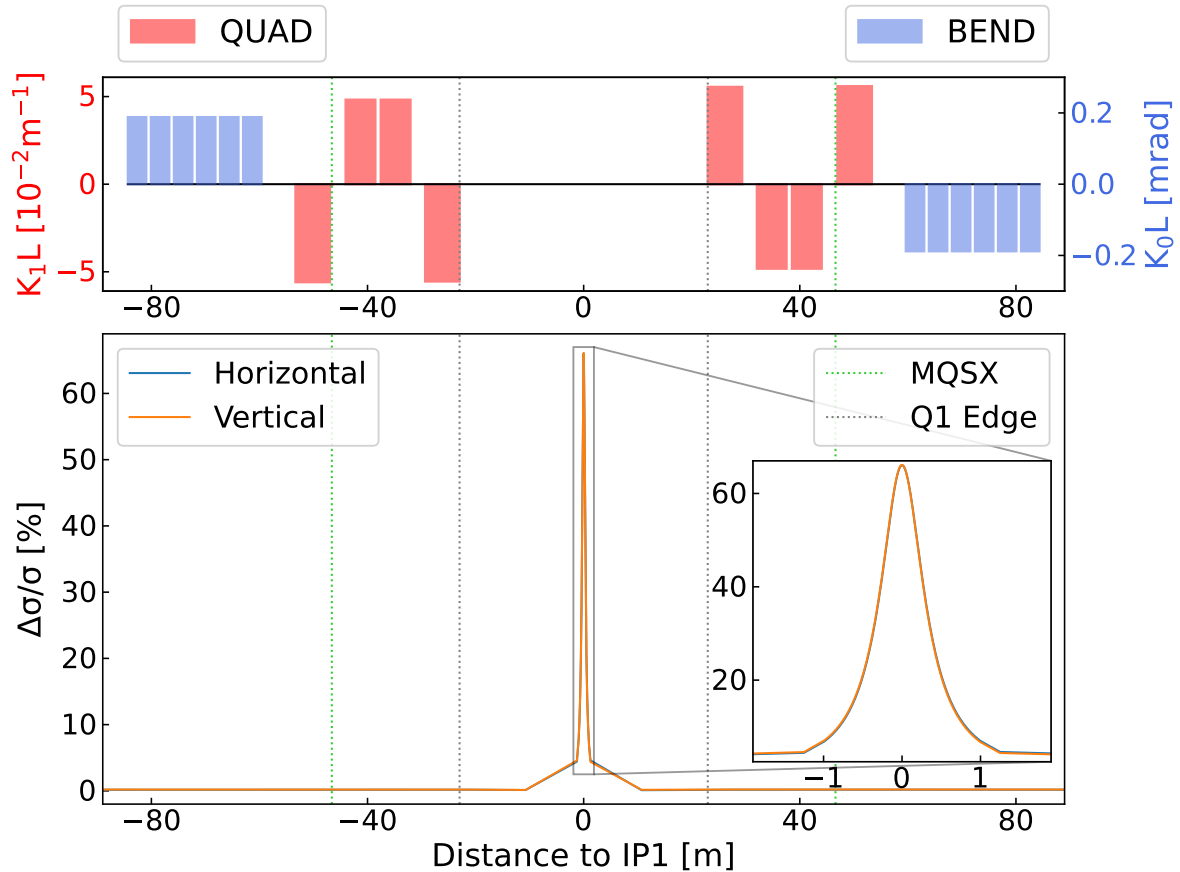


FIGURE 4.37: Relative change in horizontal (blue) and vertical (orange) beam sizes from carrying over the correction of the MQSX left of IP1 to the MQSX right of IP1.

The beam sizes in the affected case are kept very close to the nominal ones at less than a 1% deviation through the machine, being significantly affected only in the space between the left to right Q1 quadrupoles. This behavior was also observed in [186] where the coupling RDTs themselves are only significantly affected in the same space for a similar trim. Figure 4.38 shows the physical aperture limitations of elements around IP1 for the $\beta^* = 30$ cm optics, as well as representations of the beam envelopes at the same locations.

As can be seen in Fig. 4.38 the triplet elements constitute the aperture bottleneck at $\beta^* = 30$ cm, while the drift space right around the IP is not a constraint for aperture limitations. One can then conclude that the aperture would not suffer from such a compensation scheme. Similarly, the impact on Beam-Beam Long Range (BBLR) [102] interaction should be minimal as the increase is only significant within a meter of the IP location itself.

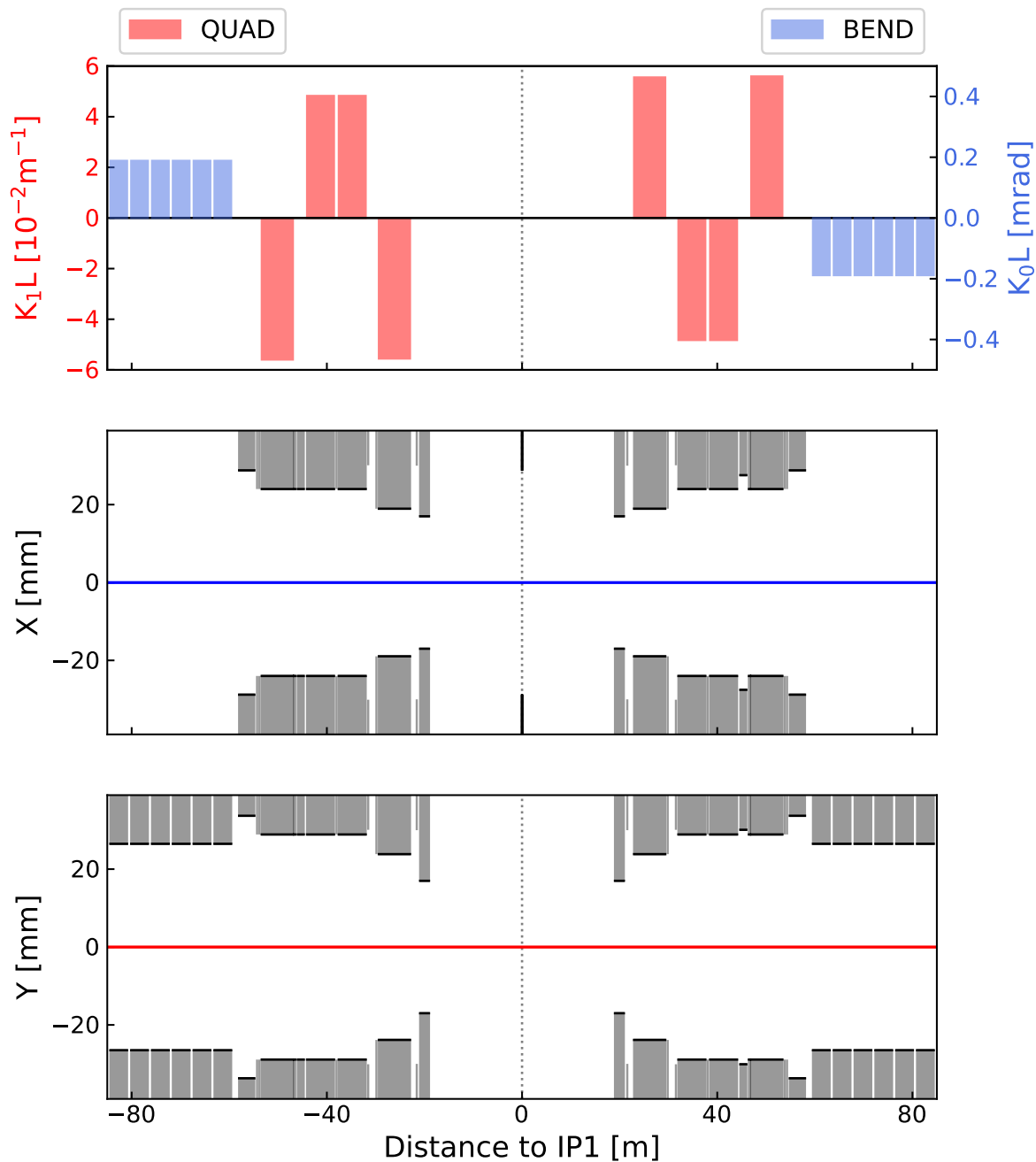


FIGURE 4.38: Magnets powering (top) and horizontal (middle) and vertical (bottom) aperture limitations around IP1, at $\beta^* = 30$ cm. The blue and red shaded areas represent, in each plane, the 3σ , 6σ and 11σ beam envelopes, from darkest to lightest respectively. The grey blocks represent the physical locations of various elements.

Experimental Measurements of Carry-Over

Measurements were conducted in late 2022 to assess the accuracy of these predictions. A comparison of instantaneous luminosity loss from carrying over the left corrector's powering to the right one at IR1 is shown in Fig. 4.39, measured at $\beta^* = 30$ cm. Carrying over the correction to the left magnet was not done due to time constraints.

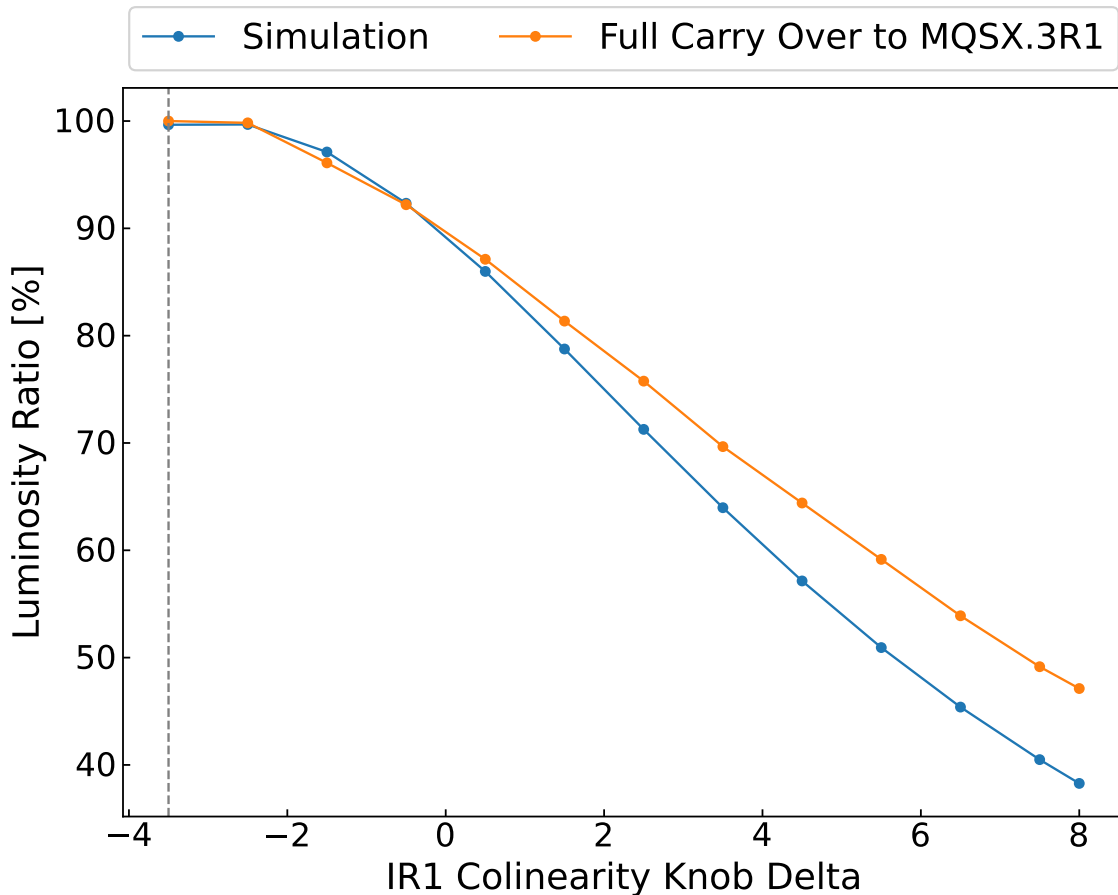


FIGURE 4.39: Instantaneous luminosity drop from correction carry-over to the right MQSX at IR1 at $\beta^* = 30$ cm. The vertical grey line indicates the nominal operating point after the RWS correction adjustments.

In Fig. 4.39, the horizontal axis indicates the colinearity knob deviation from the baseline powering of the correctors determined with the segment-by-segment technique (see Table 4.4). The vertical grey line indicates the nominal operating point after incorporating the RWS correction adjustments (see Tables 4.5 and 4.7), as well as the starting point of the scan. This means the data point at -0.5 on the horizontal axis (fourth from left) corresponds to a $\Delta_{\text{colin}} = 3$ trim from the normal operating point, and similarly the data point at 8 on the horizontal axis corresponds to a $\Delta_{\text{colin}} = 11.5$ trim, which is the full carry-over of the correction from left to right MQSX.



These are the IP1 measurements mentioned in Section 4.5.4. As one can see on Fig. 4.39, the luminosity change from a -3.5 units trim of the colinearity knob (from 0 to -3.5 on the horizontal axis) shows a good agreement with expectations and leads to an 11.6% increase in the instantaneous luminosity. It is the same trim as performed earlier in the year, which can be seen in Fig. 4.30. This time however, the luminosity change is higher than the 9.7% initially measured, and closer to the 12.25% expected in Fig. 4.33. As this measurement was performed with higher beam intensity and a better detector calibration it is more trusted.

Figure 4.40 shows a similar comparison for IR5, also at $\beta^* = 30$ cm. There again the nominal operating point corresponds to the RWS adjustment from the SbS corrections and is indicated by the vertical grey line. Due to time constraints again, however, the trim could not be fully done when carrying over the correction to the right corrector (orange line).

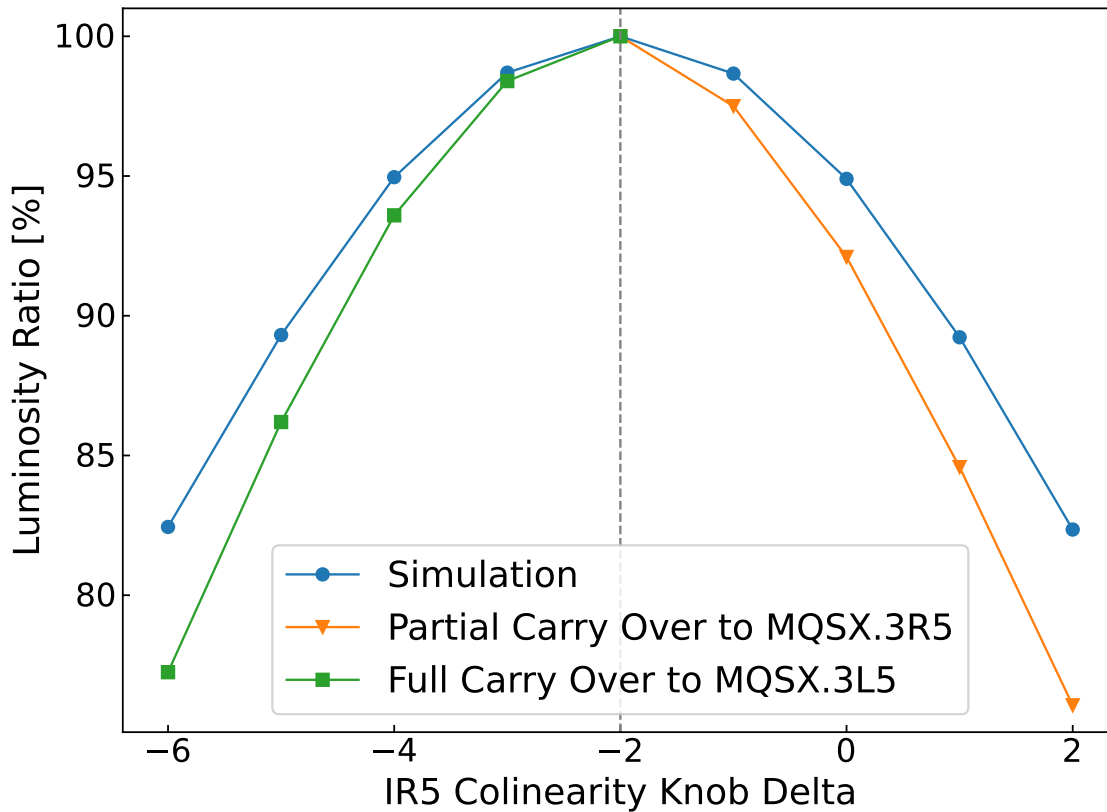


FIGURE 4.40: Instantaneous luminosity drop from correction carry-overs in both directions at IR5 at $\beta^* = 30$ cm. The vertical grey line indicates the nominal operating point after the RWS correction adjustments.

In both Figs. 4.39 and 4.40 simulations and measurements show a reasonable agreement. Simulations systematically slightly over-estimate the loss of luminosity, particularly the larger the trim is, but some discrepancy is to be expected as Eq. (4.2) is a simplified calculation.

Impact Through the Operational Cycle

In Run 3 a β^* -levelling was introduced in the LHC operational cycle to limit pile-up at the main IPs [198], as mentioned in Section 3.2. As seen in Fig. 4.36 the luminosity losses depend on the β^* , thus in order to keep operating at the pile-up limit one would have to take more frequent steps in the levelling, reducing its overall length as well as the integrated luminosity over the fill.

For instance, the levelling time would be reduced from 8.2 h to 1.23 h in the worst case, in which the MQSX.3L1 were to fail. Studies were done to assess the impact of operating with a single MQSX on the integrated luminosity over a fill, with 2023 settings. An initial bunch population of 1.8×10^{11} protons per bunch was assumed,

with 2380 bunches per beam and a β^* -levelling from 1.2 m down to 30 cm. The resulting integrated luminosity loss over a day is shown in Fig. 4.41, for each missing MQSX and for two different baselines of levelled instantaneous luminosity [199].

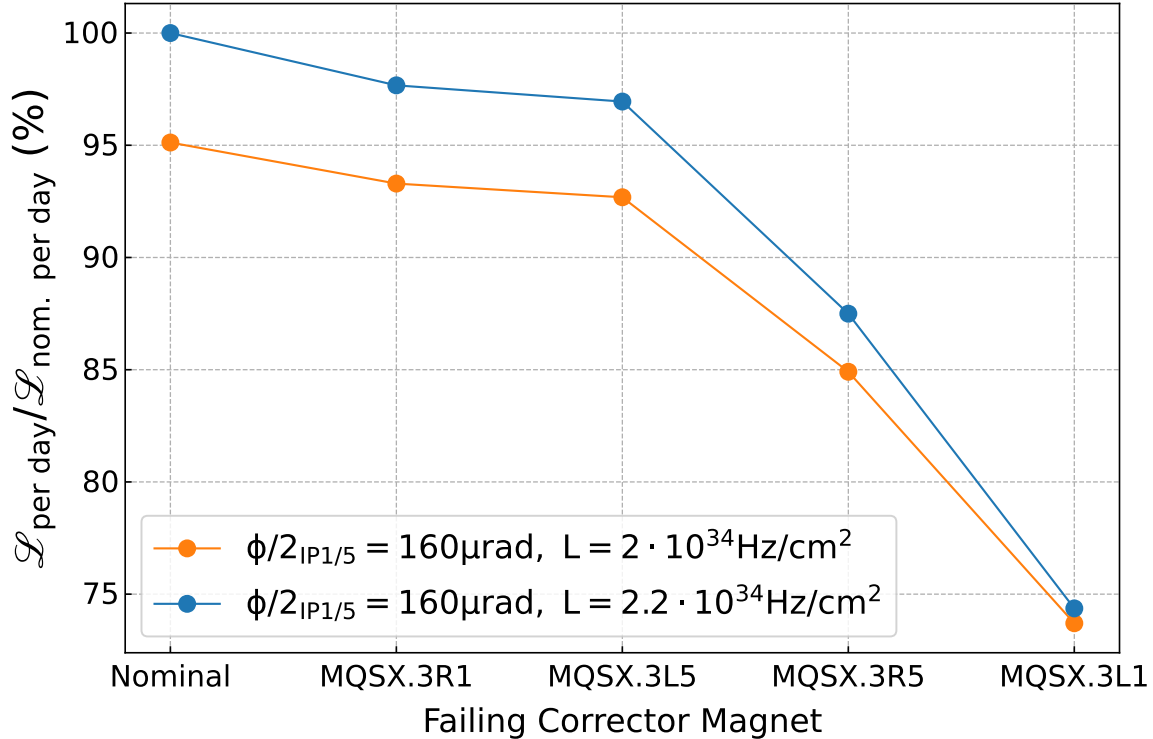



FIGURE 4.41: Integrated luminosity loss over a day for each missing MQSX and for two different baselines of instantaneous luminosity. Data is a courtesy of S. Kostoglou .

Over a day, the integrated luminosity loss reaches upwards of 25% for the worst case - failure of MQSX.3L1 -, relatively to the nominal scenario with an instantaneous luminosity target of $2.2 \times 10^{34} \text{ Hz cm}^{-2}$. Given that the impact on the instantaneous luminosity increases with decreasing β^* , as seen in Fig. 4.36, when operating with lower intensities the impact would be bigger as the levelling would have the machine stay at lower β^* for longer. It is also expected that operating with settings at the Beam-Beam Long Range limit would only improve the loss by a few percentage points in the worst case. An MD is planned in 2023 to assess both the feasibility of this approach and the accuracy of these predictions.

4.7.2 Operating with Two Missing MQSX

There is a possibility that both MQSXs in a given IR fail. In this case the compensation of a corrector's contribution by its counterpart - as described in the previous section - would no longer be possible, and the uncompensated coupling coming from the IR would be too large at small β^* for safe machine operation. Simulation results suggest that it would not be feasible to squeeze to the optics below $\beta^* = 90 \text{ cm}$, and new solutions would be needed in order to be able to provide collisions to the experiments.

Tilt of Triplet Elements

A potential solution to mitigate the impact of corrector failures is to physically tilt a close triplet quadrupole, introducing a *skew* component in the element's field and relying on this contribution to perform the correction in place of the defecting corrector.

Studies were performed to determine the amount of Q2 or Q3 tilting that would be needed to take on the coupling contribution of its closest MQSX, assuming it stops working. In each study an error was introduced in the form of the corrector's opposite powering, and a simple parametric scan was made of the introduced tilt angle. Figure 4.42 shows the coupling RDTs' amplitude at IP1 for various tilts of Q3 on the left of the IP, assuming a failure of the left *skew* quadrupole MQSX.3L1. Notice the log scale of the vertical axis.

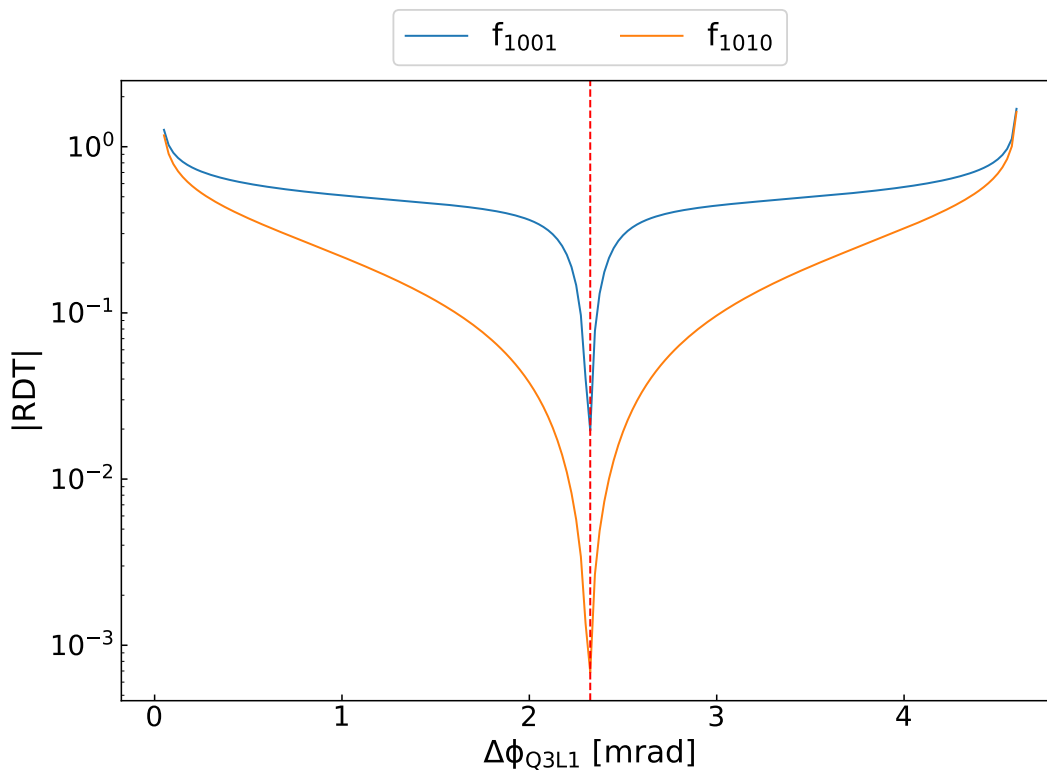


FIGURE 4.42: The amplitude of the coupling RDTs at IP1 for various tilts of the triplet quadrupole Q3 left of the IP, assuming a failure of the skew quadrupole corrector MQSX.3L1.

Figure 4.43 shows the coupling RDTs' amplitude at IP5 for various tilts of Q2 on the right of the IP, assuming a failure of the right *skew* quadrupole MQSX.3R5. On each figure, the location of the tilt setting that would minimize coupling at the IP is highlighted with a vertical red dashed line. In all studied cases a good compensation can be achieved.

Table 4.9 shows the determined tilt angles necessary for compensation for each scenario. The necessary tilts using Q2 or Q3 range between -2 and 2.85 mrad, with the most impactful ones at IR1 and IR5 - due to higher β -functions in the triplets - between -1.65 and 2.325 mrad. Note that it would also be possible to use lower values by tilting both elements simultaneously, in opposite directions.

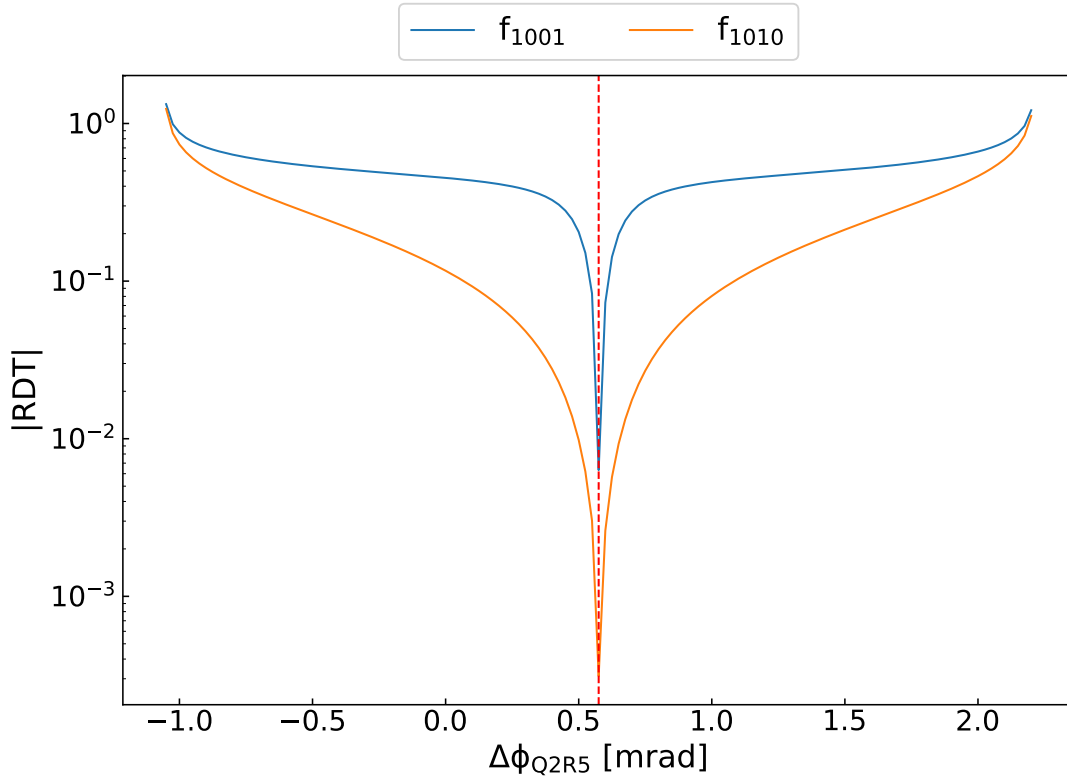


FIGURE 4.43: The amplitude of the coupling RDTs at IP5 for various tilts of the triplet quadrupole Q2 right of the IP, assuming a failure of the skew quadrupole corrector MQSX.3R5.

It is worth noting that tilting a triplet quadrupole by that much has very little impact on the optics. For instance, in the case that the MQSX.3L1 fails and is compensated by a tilt of the Q3 close to it, an additional 0.16% β -beating would be added through the machine, which is negligible.

IR	Failing Magnet	K_{1S} [10^{-4} m^{-2}]	Necessary Tilt for Compensation	
			Q2 Tilt [mrad]	Q3 Tilt [mrad]
IR1	MQSX.3L1	11.5	-1.65	2.325
	MQSX.3R1	3.5	0.5	-0.7
IR2	MQSX.3L2	-14	-1.97	2.85
	MQSX.3R2	-14	1.97	-2.85
IR5	MQSX.3L5	4	0.575	-0.8
	MQSX.3R5	8	-1.15	1.6
IR8	MQSX.3L8	-5	-0.725	1
	MQSX.3R8	-5	0.725	-1

TABLE 4.9: Necessary tilt angles of either Q2 or Q3 triplet elements to compensate for the loss of the closest skew quadrupole corrector/ Results are shown for IR2 and IR8, but only IR1 and IR5 are at risk of failure.

Discussions were engaged with the Machine Protection group to determine the practical feasibility of such a solution, and several issues were raised. Firstly, the LHC triplet alignment systems are not meant for angular alignment, but for vertical alignment of the magnet assemblies. Additionally, the alignment system relies on supporting jacks positioned at each end of the assemblies: two bellows on the IP side and one on the non IP side for Q2 triplets, for instance [200, 201]. For this reason, with only three supporting jacks it is not possible to achieve a pure tilt of the assembly, and an attempt to do so would result in both a partial tilt and misalignment of the magnet [202]. Finally, due to the possibility of damaging what is arguably the most important magnet assembly in the machine during the procedure, this solution would only be used as a last resort.

Warm Skew Quadrupole Replacement

Another solution would be to install a new warm skew quadrupole magnet as replacement either close to triplet Q3, to the separation dipole D1 or to quadrupole Q4, on the non-IP side [203]. This option is still, however, in early stages of study and will not be developed in this document.

4.8 Summary

In the Large Hadron Collider, corrections of local Interaction Region linear coupling are of importance to keep a good control of beam sizes at Interaction Points, to guarantee luminosity performance of the machine and to prevent any significant impact on the beam dynamics. So far the correction of local linear coupling has been performed by finding a powering setting of the dedicated skew quadrupole correctors with the Segment-by-Segment technique, which aims to compensate for the Interaction Region's contribution to global coupling in the machine. However, the technique suffers from inherent weaknesses that do not allow for a correction of linear coupling at the IP, and other existing methods or observables have not solved the issue.

We have presented a new method - the Rigid Waist Shift - which was developed specifically to correct for local linear coupling at the IP, and is based on the controlled perturbation of the optics in the Interaction Regions. The method allows one to determine a powering adjustment of the correctors from the values determined with Segment-by-Segment that optimizes the coupling at the IP location. The method's validity has been demonstrated in simulations and with experimental data taken in the LHC 2022 commissioning, where the determined corrections led to a measured instantaneous luminosity gain of 9.7% and 5.2% at the ATLAS and CMS experiments, respectively. These corrections are now the baseline values used in the machine for physics production. The relevance of this method was investigated for other existing and future colliders, and we have shown that for most circular collider layouts the Rigid Waist Shift could be a viable solution to tackle local linear coupling.

Magnet lifetime studies conducted during the Long Shutdown 2 have shown that the dedicated correctors are expected to reach their radiation dose limit during Run 3, and it is realistic to expect one or more failures. Studies have been performed to

determine the impact of such failures on the machine's performance and assess the viability of potential solutions. It was shown that one could compensate for the loss of a single corrector and guarantee both safe machine operation and squeezing of the beams down to collision configuration, but at the cost of luminosity. Estimates of expected instantaneous luminosity losses were determined and confirmed through experimental measurements; and the impact over a complete physics fill with the 2023 configuration was extrapolated. Potential solutions were investigated to compensate for the simultaneous loss of both correctors in a given Interaction Region, but these are still at the stage of early studies.

CHAPTER 5

Machine Learning for Interaction Region Local Coupling

Machine learning methods have found their application in a variety of fields including technology development, scientific research, medical diagnosis and business insights. The now widespread application of machine learning techniques demonstrates their applicability to various challenges and tasks.

In recent years, machine learning has been successfully applied to various areas of accelerator physics [204–214], including at the [Large Hadron Collider \(LHC\)](#) [139, 215, 216]. The primary purpose of the work presented hereafter is to explore the possibility of applying machine learning techniques to the subject of local [Insertion Region \(IR\)](#) coupling in the LHC.

5.1 Relevant Concepts of Machine Learning

Machine learning can be seen as the intersection of statistics and computer science. The key characteristics of machine learning are described by T. Mitchell as [217]:

“ ” Machine learning techniques aim to build computer programs and algorithms that automatically improve with experience by learning from examples with respect to some class of task and performance measure, without being explicitly programmed.

A key characteristic distinguishing machine learning from conventional programming is the program’s ability to automatically achieve performance improvements based on provided data. This section provides a quick introduction to some relevant machine learning paradigms and concepts, primarily derived from [217, 218] where one can find detailed discussions on the subject. The focus is kept on concepts relevant to the work presented in this chapter.

5.1.1 Defining a Machine Learning Task

In the context of machine learning, [learning](#) refers to the process of improving performance. Generally speaking a model can improve its performance by adjusting its

parameters with respect to provided data, in order to refine the approximation function that is derived from that data. It is important to note that a trained model will always remain an approximation of the relationship in the underlying data, but with good enough training this approximation should be sufficiently reliable for the specific task at hand. The requirements on the model's performance in terms of accuracy, precision and reliability depend on a particular task and application domain.

The chosen performance criteria, the type of experience to be gained through learning and the specific approach and algorithm are specific to the task that must be learned. These three parameters - task, measure of performance and source of experience - are the fundamentals of a well-defined machine learning problem. In practice, it is reflected in the selection of an appropriate learning method and function approximation algorithm, definition of the loss function and its acceptable values, as well as the preparation of data. The latter can be non-trivial and require dedicated techniques and algorithms.

5.1.2 Supervised and Unsupervised Learning

Two main approaches are available in machine learning depending on the problem definition and the availability and structure of the learning examples.

Unsupervised learning is characterized by the use of unlabeled datasets. Unsupervised learning algorithms solve tasks where only input data is available, and are used to analyze and cluster inputs by discovering patterns in data without the need for human intervention, hence they are *unsupervised*. They are suitable for tasks such as anomaly detection, signal denoising, dimensionality reduction, and feature extraction.

Supervised learning is characterized by the use of labeled datasets. These datasets are used to train - or supervise - the model to learn how to accurately classify data or predict outcomes. During the training, predictions are computed from the inputs and compared to the known corresponding outputs. By adjusting the parameters of the model - or approximation function - the quantified difference between computed predictions and correct outputs, the so-called **loss function**, is minimized. Supervised learning is typically used for **classification** and **regression** tasks. Classification tasks aim to accurately assign test data into specific categories, and regression tasks aim to understand and approximate the relationship between dependent and independent variables in order to predict the outcome of a given input.

5.1.3 Regression Models

In the case of regression problems, the regression function is what is being approximated by the model. The core model principles are outlined below.

Linear Models

Linear models compute the estimates of the output values using a linear function of the input variables [219]. For regression tasks, the estimation for the predicted output \hat{y} of a linear model is expressed as:

$$\hat{y} = w_0 + \sum_{i=1}^N w_i x_i , \quad (5.1)$$

where \vec{x} is the input vector containing N features, and \vec{w} is the vector containing the learned coefficients of the model, with w_0 being the bias. In a simple case (see Fig. 5.1 below) \hat{y} is a scalar, but it is usually a vector of dimension K . In this case the model parameters w are then represented as an $N \times K$ matrix.

Typically, linear regression models are trained using the **least squares** method, which minimizes the residual sum of squared errors between the predicted and actual output values. Given a set of N samples from the training dataset, and with y being the true output for a given sample, the linear model's parameters are updated during training with each incoming sample, minimizing:

$$RSS(\hat{w}) = \sum_{m=1}^N (y_m - \hat{y}_m)^2 . \quad (5.2)$$

After training, the resulting coefficients should be sufficiently general to generate accurate predictions for all provided data samples.

Polynomial Regression

Some learning tasks, due to the complex properties of the data, require non-linear predictors. For instance, this is the case when fitting a one dimensional polynomial function of degree n :

$$p(x) = a_0 + a_1x + a_2x^2 + \dots + a_nx^n , \quad (5.3)$$

where (a_0, \dots, a_n) is a vector of coefficients of size $n + 1$. One way to train a model to approximate such a function is to reduce the problem to linear regression [220]. To do so one can introduce a mapping such that $\psi(x) = (1, x, x^2, \dots, x^n)$, which reduces the problem to:

$$p(\psi(x)) = a_0 + a_1x + a_2x^2 + \dots + a_nx^n = \langle \vec{a}, \psi(x) \rangle , \quad (5.4)$$

and the optimal vector \vec{a} can be found by minimizing the residual sum of squares (RSS) as in Eq. (5.2).

5.1.4 Generalization, Underfitting and Overfitting

In supervised learning, one tries to train a model capable of making correct predictions on new, unseen data based on the experience and tuning acquired on the training data's known outputs. This ability to predict on new data is called **generalization**, and is the most important aspect of the built model [221, 222]. A separate and unrelated test dataset is usually used in order to evaluate the predictive power of the model. Most of the time, training and test datasets share enough similarities - properties and relations in the underlying data - such that the model can accurately predict on the test set.

However, in the case of highly complex models, high accuracy can be achieved on the training data with poor prediction performance on the test data. When too complex, models can tend to fit very closely to individual data points in the training data and extrapolate unexisting relations that will later on perform badly on new data.

This phenomenon is called **overfitting**. Similarly, when too simple for the data at hand the model will not be able to capture the underlying relations and will not be able to perform accurate predictions even on training data. This is referred to as **underfitting**.

Figure 5.1 illustrates these concepts by showing an underfitting model, a model that generalizes well, and an overfitting model. Though simple, this example highlights the importance of building a model that generalizes well.

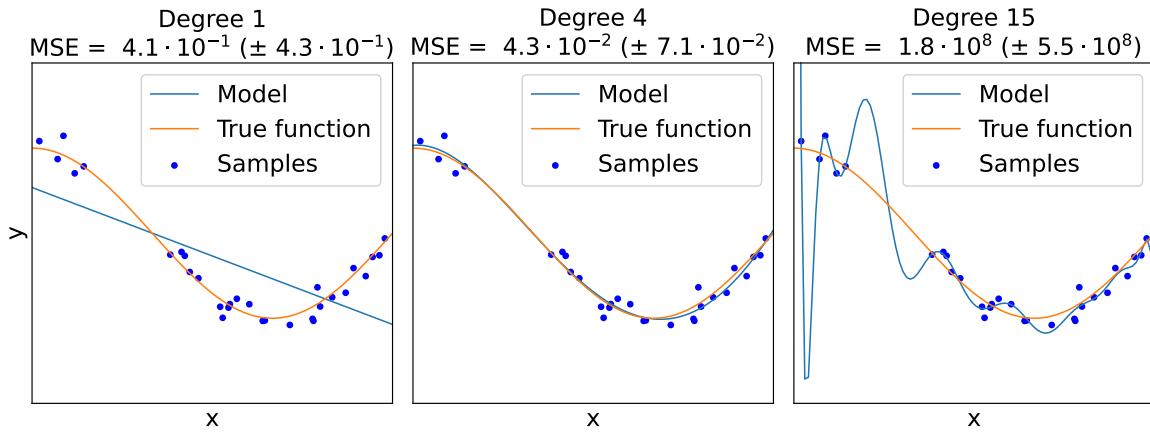


FIGURE 5.1: Three examples showcasing models approximating (blue) a true function (orange) after training on provided samples (dark blue). Of the three models one is too simple and underfits (left), one generalizes properly (middle), and one is too complex and overfits (right). This plot was reproduced from the *scikit-learn* documentation [223, 224].

One of the common ways to identify underfitting or overfitting is to provide validation data to the model in addition to the training data. The training set is then used to drive the learning procedure, and after training the error is evaluated on the validation set. When done properly, the model's performance on both training and validation sets should be nearly equal. If the performance on the training set is substantially better, the model has been overfitted and further adjustments on the model complexity are then required.

Regularized Regression

A potential approach to avoid overfitting is to apply regularization during the model training by imposing a penalty on the update of the model's parameters. As the model parameters are updated to attempt to fit every incoming input-output pair, the penalty constrains the change of these parameters such that the model becomes more robust against variations in the data. This technique is known as *L2 regularization*, and in the context of supervised regression **ridge regression** [225].

A ridge regressor minimizes the residual sum of squares introduced above by introducing a tuning parameter α which mitigates the potential linear dependencies between different input variables in the dataset. In the presence of such dependencies, parameters might be updated inappropriately during training in response to small changes in the model or the data. The regression task is formulated as:

$$\min_w \|w\vec{x} - \vec{y}\|_2^2 + \alpha \|w\|_2^2, \quad (5.5)$$

where w is the matrix containing the parameters of the model, \vec{x} is the input data vector and \vec{y} the vector of targets to be predicted by the model. With higher values of α the changes in model parameters are reduced at each update step, preventing overreactions to correlated changes in the data.

It is also possible to mitigate overfitting by decreasing the number of input features while retaining only uncorrelated features for function approximation by the model. **Lasso regression** [226] uses an $L1$ norm to drive some regression coefficients to 0, which improves the model in terms of variance and allows for automatic feature selection.

To tune additional model parameters such as the ridge penalty α or the number of input features to be retained in Lasso regression one can use **cross-validation**, a resampling method which consists of randomly dividing the dataset into equally sized parts. For instance, the dataset is divided into ten subsets and the model is fitted on nine of those while the loss is computed on the remaining subset. This procedure is repeated for each of the ten subsets to be used for loss computation, and all ten estimates of the prediction error are averaged. As the practice is part of the training process cross-validation is only applied to the training dataset, and the test dataset is still used only to evaluate a trained model's performance on unobserved data.

5.2 Identification of Local Coupling Sources

In the previous chapter, the negative impact of local **IR** linear coupling in the **LHC** has been extensively discussed, as well as the necessity of its identification and mitigation. The precise knowledge of a coupling source's location and relative strength would be a valuable asset for further correction. However, it was illustrated in **Section 4.2** how simply looking at patterns and jumps in the coupling **Resonance Driving Terms (RDTs)** was not always sufficient to accurately pinpoint the location of a source, nor can it be used in locations with little instrumentation or unfavorable conditions. As machine learning techniques have found their application in a wide range of particle accelerator control tasks in the past [139, 212, 215, 227–230], the possibility of applying machine learning techniques to the detection of local **IR** coupling sources in the **LHC** was explored.

In order to perform a prediction of **betatron coupling** sources' locations, one first needs to compute the f_{1001} and f_{1010} coupling **RDTs** which will serve as input data for the model. The strength and variations of the coupling **RDTs** throughout the machine is then used to estimate the location of coupling sources and their relative strengths. Though it was highlighted in **Section 4.2** that looking at coupling **RDTs** through the machine did not allow evaluating coupling at the **Interaction Point (IP)** (see **Fig. 4.5**), their pattern provides information on sources; and the amount of data and nature of the task fits a statistical model more than a human eye.

In terms of machine learning, this task can be defined as a regression problem that can be solved by training a model using measurements and corresponding solutions. Such a regression model requires a large dataset in order to be able to generalize and produce reliable results. As in the real machine the true location of coupling sources is unknown, no real-world data is available for model training.

5.2.1 Dataset Generation

In order to create a training dataset simulations were performed with the MAD-X [59] code, in which random rotations around the s -axis are introduced into individually powered IR quadrupoles, in each IR. The tilt generates a skew quadrupolar component at the affected element and thus turns it into a source of coupling. It has to be noted though, that in simulations only quadrupole tilts - given by the DPSI variable in MAD-X - were used to generate coupling sources, which means other potential sources such as feed-down from higher order magnets were ignored in this study.

When generating the data from simulations, the introduced tilt components form the training output and the produced coupling RDTs generated from the perturbed optics functions are the input in the training dataset. The data was generated for both Beam 1 and 2 using the $\beta^* = 30$ cm optics. Figure 5.2 shows the reconstructed coupling RDTs for a given simulation in which a truncated Gaussian distribution of tilts was assigned to all independently powered IR quadrupoles Q1 to Q11 in IRs 1, 2, 5 and 8.

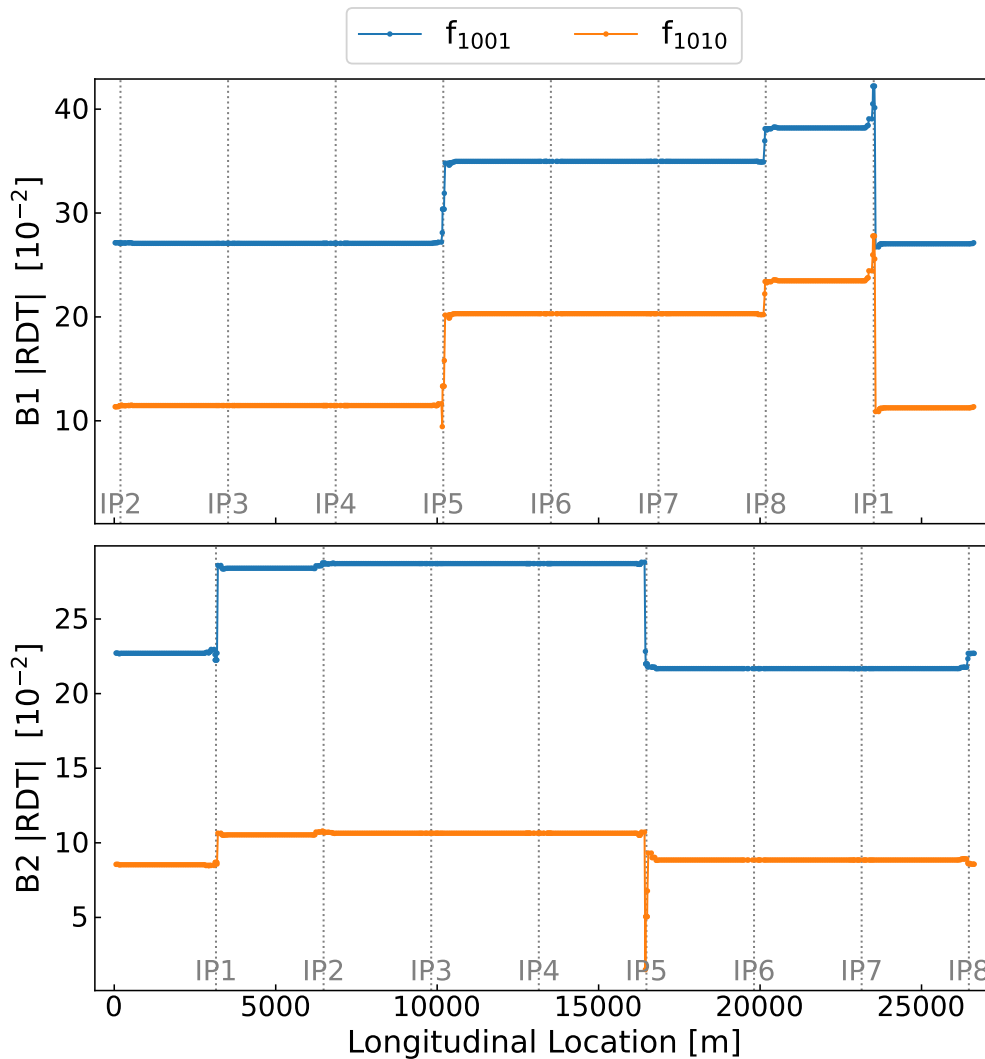


FIGURE 5.2: Beam 1 (top) and Beam 2 (bottom) coupling RDTs f_{1001} (blue) and f_{1010} (orange) after the implementation of tilt errors in the independently powered IR quadrupoles Q1 to Q11 in IRs 1, 2, 5 and 8, for the 6.8 TeV and $\beta^* = 30$ cm optics.

The standard deviation of the applied tilt errors Gaussian distribution was aligned with expected values from the element alignment precision in the LHC, after discussions with the alignment group. Each sample of the dataset is obtained by applying the following steps in simulations:

1. A truncated Gaussian distribution of tilt errors (MAD-X DPSI) is applied to quadrupoles Q1 to Q11 in IRs 1, 2, 5 and 8 for Beam 1.
2. Quadrupoles located outside the IRs are excluded as these sources can be identified and compensated by other means.
3. The coupling RDTs f_{1001} and f_{1010} are calculated at each BPM from [Twiss parameters](#) for Beam 1.
4. The DPSI values for triplets are exported and applied to Beam 2, as these are common magnets and should share the error.
5. A truncated Gaussian distribution similar to the one of step 1 is applied to the remaining quadrupoles Q4 to Q11 in IRs 1, 2, 5 and 8 for Beam 2.
6. Coupling RDTs for Beam 2 are calculated at each BPM as done for Beam 1.
7. The real and imaginary parts of the coupling RDTs at each BPM and for each beam are concatenated in order to obtain a single vector of values for a given sample.

To train the model the relation is flipped, and the introduced tilt errors have to be predicted based on given coupling RDTs computed from the perturbed optics. Therefore, the coupling RDTs reconstructed at each BPM are considered as model input and a vector containing the predicted DPSI value attributed to each affected quadrupole is the desired output. [Figure 5.3](#) shows a conceptual schematic of the dataset generation and supervised model training process for this given application.

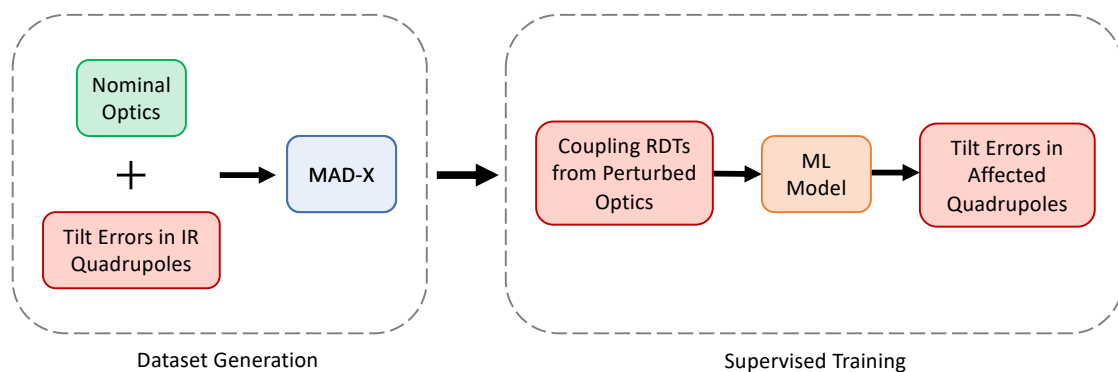


FIGURE 5.3: Conceptual representation of the dataset generation and supervised model training. This diagram is heavily inspired from [216].

A dataset of 50 000 samples (each an individual simulation following the steps above) was divided into train and test sets (75 % and 25 % respectively). Each sample pair

consists of 4424 inputs - real and imaginary parts of each coupling RDT for each BPM for each beam - and 160 outputs: one DPSI value at each affected IR quadrupole.

In addition, in order to reproduce the uncertainty of the RDTs reconstructed from measurements, both train and test datasets were augmented by adding Gaussian noise to the RDTs. The standard deviation of the added noise was determined by a statistical analysis of several measurements from the LHC Run 2. Figure 5.4 shows the standard deviation of measured coupling RDTs across Beam 1 BPMs for a batch of measurements taken on April 3, 2018.

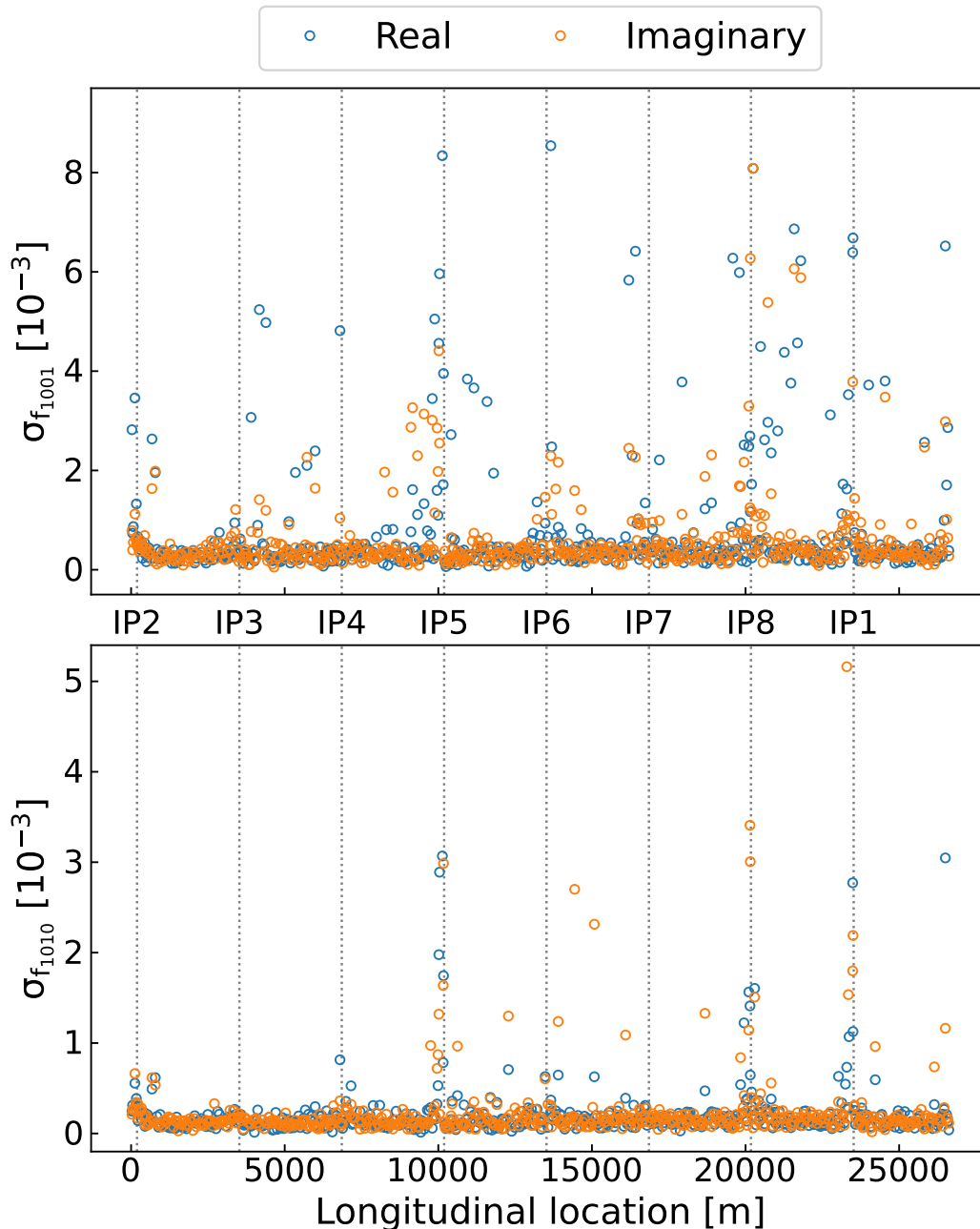


FIGURE 5.4: Standard deviation of the coupling RDTs at BPMs for Beam 1, from a batch of measurements taken on April 3, 2018. These data points were later divided into IR and arc BPMs to determine applied noise levels.

After analyzing several such batches, the following noise levels to be added were determined:

- Coupling RDTs at arc BPMs were noised with a truncated Gaussian distribution of standard deviation ranging from 0 to 10^{-5} absolute error.
- Inner BPMs located in the IRs (number 1 to 6 from the IP) were noised with a truncated Gaussian distribution of standard deviation ranging from 0 to 10^{-2} absolute error.

A new dataset was created for each combination of the noise levels mentioned above. For instance, a given set had IR BPMs noised with a standard deviation of 10^{-3} and arc BPMs with 10^{-6} . Similarly, several such datasets were created for different standard deviation of the introduced tilt errors.

5.2.2 Model Training and Evaluation

In this study models have been evaluated based on their R^2 scores, or coefficient of determination, as well as the normalized mean absolute error between the true output values and the model predictions. Several models suited for regression tasks were tested, and a minimal amount of hyperparameter tuning was performed.

Each model was trained and evaluated on the various datasets generated, in order to assess their performance and usability in various realistic contexts of noise in the data. A simple least squares linear regression [219] showed very good results on clean data, however its performance dropped drastically when applied to the noised datasets, down to unusable accuracy. A decision tree regressor [231] and a random forest regressor [232] showed poor performance on all datasets. A ridge regressor model (see Section 5.1.4) showed good performance on both clean and relatively low-noise datasets.

Figure 5.5 shows the test performance of the ridge regressor [225] on noised datasets depending on the level of noise added to different BPMs, where the impact of noise on the reconstructed coupling RDTs is apparent. In the top plot the Mean Absolute Error (MAE) - the sum of absolute errors divided by the sample size - was normalized to the standard deviation of the applied magnet tilts, $\sigma_{\text{DPSI}} = 10^{-4}$ rad in this case. In this figure each curve represents a noise level applied to arc BPMs data while each point on these curves corresponds to a noise level applied to the inner BPMs. While dense, this representation allows visualizing the performance of the model for a wide range of noised datasets, for a single given distribution of the tilt errors.

To the left of the plot are data points corresponding to low noise levels in IR BPMs, where for two of the curves (blue and orange) the model's performance is excellent. Moving up one order of magnitude in the arc BPMs noise level (green curve) leads to a significant performance drop. Points to the right of the plot, corresponding to increasing noise in IR BPMs data, show a drop in performance down to an unusable model, with $R^2 = 0.54$ in the worst case.

Figure 5.6 shows histograms of the distributions of true attributed errors, of the ridge regressor's predictions and of deviations to the true values. These were obtained by evaluating the model on a noised dataset with $\sigma_{\text{DPSI}} = 10^{-4}$ rad, $\sigma_{\text{IRs}} = 10^{-5}$ and $\sigma_{\text{arcs}} = 10^{-6}$ (corresponding to the third leftmost point on the orange curve in Fig. 5.5). One can notice the histogram of deviations much more narrowly centered on 0 than that of the attributed errors, which is the sign of good performance.

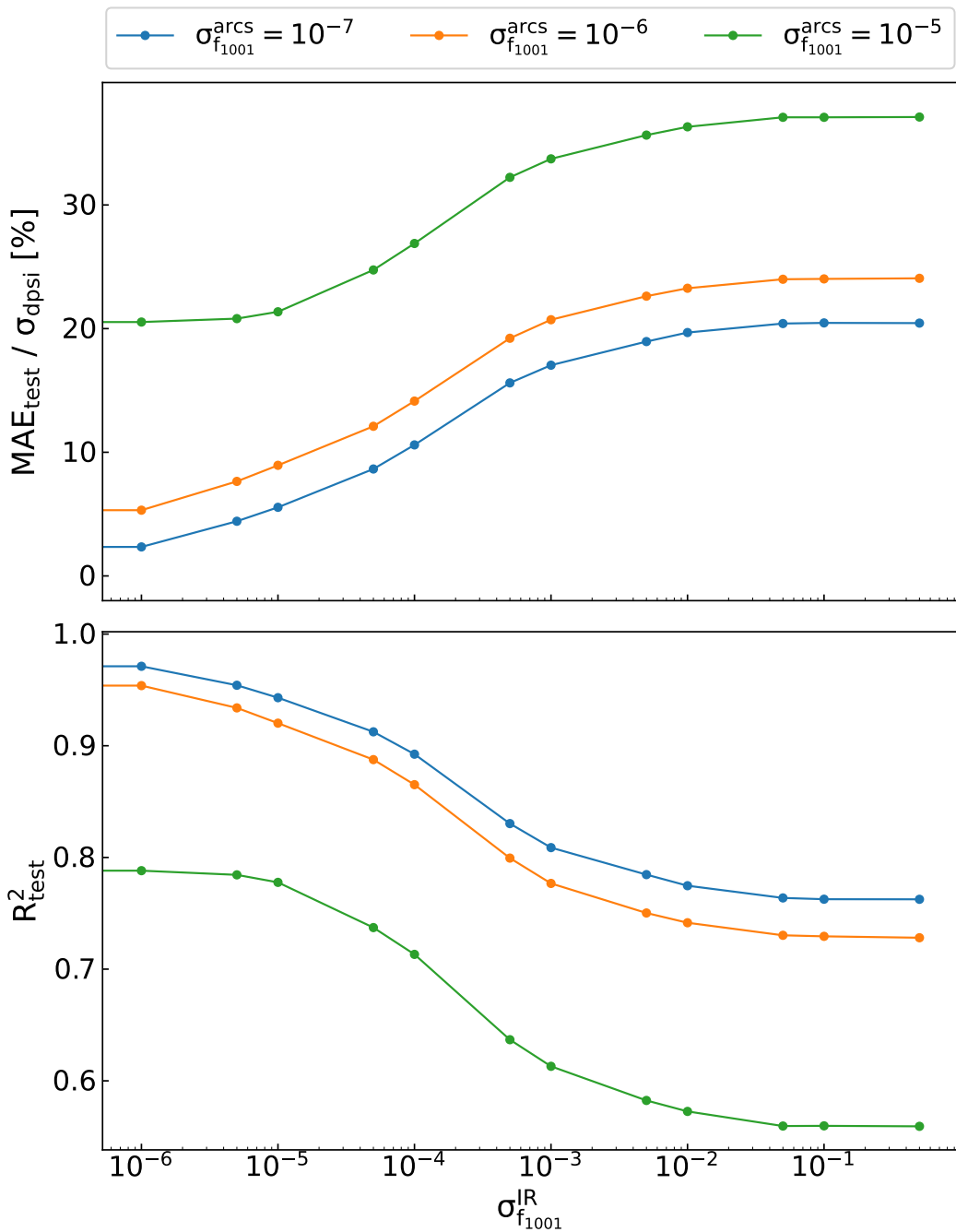


FIGURE 5.5: Normalized mean absolute error (top) and R^2 scores (bottom) of a ridge regressor on various datasets corresponding to different noise levels added to the coupling RDTs. The σ values indicated correspond to the standard deviation of the Gaussian noise distributions added to the coupling RDTs data.

Figure 5.7 shows the ridge model's predictions on a sample from the same noised test dataset ($\sigma_{DPSI} = 10^{-4}$ rad, $\sigma_{IRs} = 10^{-5}$ and $\sigma_{arcs} = 10^{-6}$), where a good agreement between the predicted and the assigned true values can be observed. Prediction performance significantly degrades with the addition of noise, with sometimes predictions being off by an order of magnitude or more in the worst cases.

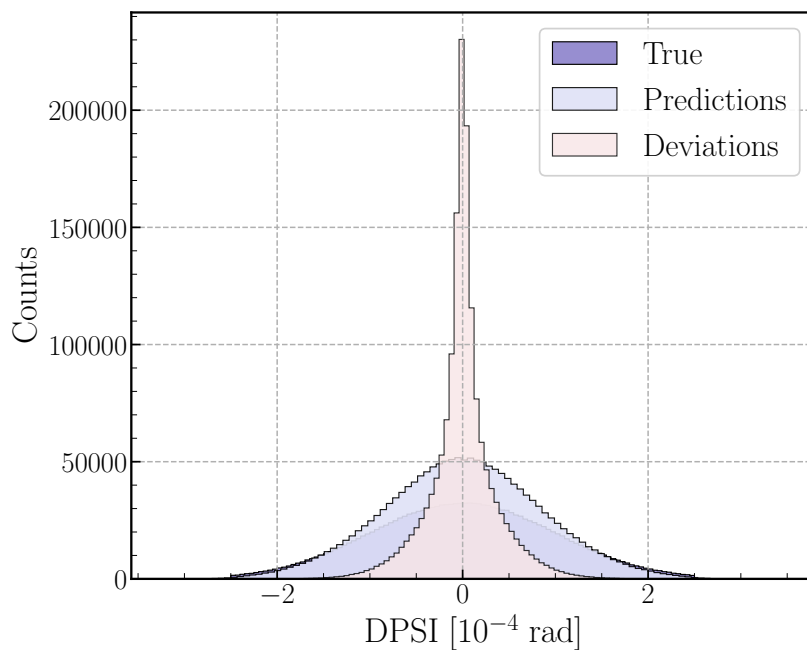


FIGURE 5.6: Histograms of the true applied DPSI values (purple), the values predicted by the Ridge model (blue) and the deviations from the predictions to the true values (pink) for a noised sample in the test dataset ($\sigma_{\text{DPSI}} = 10^{-4}$ rad and $\sigma_{\text{Arcs,IRs}} = 10^{-5}$).

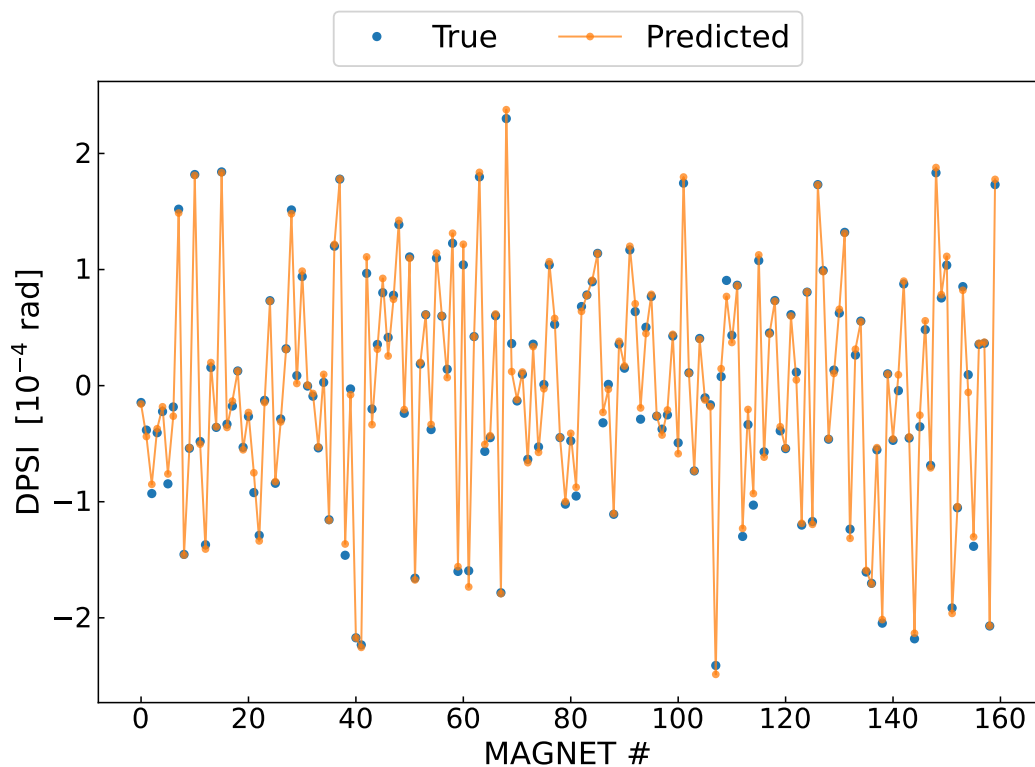


FIGURE 5.7: True assigned (blue) and predicted (orange) DPSI values with a ridge model for a given test dataset sample. Here the magnet names have been switched for numbers in order to improve clarity.

Results showing the best R^2 scores obtained by each model on both clean and noised datasets are presented in Table 5.1, where the ridge regressor clearly outperforms its counterparts.

Model	R^2 Score	
	Clean Data	Noised Data
Ridge Regressor	0.9911	0.8934
Linear Regression	0.9913	0.5638
Decision Tree Regressor	0.1385	-0.0018
Random Forest Regressor	0.0175	-0.0009

TABLE 5.1: Comparison of the R^2 score averaged over 1000 samples taken from the test dataset for different models. For the results in this table, the standard deviations of the applied noise were $\sigma = 10^{-4}$ for IR BPMs and $\sigma = 10^{-6}$ for arc BPMs. The distribution of tilt errors had a standard deviation of $\sigma = 10^{-4}$ rad.

From the results on clean data or low noise levels in Fig. 5.5 and Table 5.1, one can view this study as a good proof of principle for the application of machine learning to IR coupling sources detection. However, with realistic noise levels even the best performing model is not yet good enough to be used in operation or incorporated in correction techniques. Nonetheless, while predictions on noised data might not yield totally accurate numbers they still provide a good indication of suspected locations of coupling sources, which may be valuable for the alignment group.

There is also potential for performance improvements. Assigning more computing resources to the determination of model parameters through hyperparameter tuning is a first step towards better performance, but will not circumvent certain models' shortcomings. More complex models such as Convolutional Neural Networks (CNNs) have in the past been successfully used with impressive success on regression tasks - such as in HEP [233] and recently in optics measurements studies [234] - and would be a promising tool that could yield better prediction accuracy especially on noised datasets. Another avenue of improvements would be to create a pipeline where first a denoising step is applied on the coupling RDTs data using another model trained for the task - this has been successfully done with auto-encoder neural networks [235] - before feeding the results to the above prediction models. With good enough noise cleaning, the prediction models should reach the level of performance displayed in this study on clean or low noise datasets.

Currently, another limitation of these trained models is the fact that only skew quadrupole components were considered in the study for the introduction of coupling. In the real machine, other effects such as field errors in higher order magnets or orbit offsets in sextupoles would also lead to a coupling contribution, which the models would try to blame on a quadrupole. However, the effect of higher orders to coupling is small and assuming most contributions are in the form of tilted quadrupoles is reasonable. Circumventing the limitation would be feasible but need much more complex and inclusive simulations.

5.3 Summary

Following the successful application of machine learning methods to various tasks in particle accelerators in recent years, we explored the possibility of training machine learning models to predict linear coupling sources in the [LHC IRs](#) in the form of quadrupole tilts. Several datasets were generated for training, corresponding to realistic tilt error distributions and noise levels aiming to reproduce measurement uncertainties.

We have shown that specific machine learning models among those tested are capable of predicting the IR quadrupole tilts by assigning a representative value to specific magnets with good accuracy on datasets generated from simulations. A ridge regressor shows the best performance among the tested models, including on datasets with small amounts of noise.

While usability in operation would require better accuracy on datasets with higher noise, this is a successful proof of concept for the application of machine learning techniques to the subject of local coupling corrections in particle accelerators. Potential improvements such as using previously successful but more complex models and workflows have been identified which could allow to improve the performance of models discussed in this study. On the other hand, upgrading to better beam instrumentation that would yield more precise reconstructed coupling [RDTs](#) would also allow the use of the currently developed models with confidence.

CHAPTER 6

Optics Studies

The [luminosity](#) delivered to the [experiments](#) is not the only performance metric from the point of view of the [optics](#) in the [Large Hadron Collider \(LHC\)](#). Measuring and correcting the phase advance through the machine is crucial for optics measurements and corrections. Similarly, the measurement and correction of amplitude detuning is essential in order to understand and prevent instabilities in the machine. These are relevant not only to the [LHC](#) but for any circular accelerator.

Two further optics studies performed during the course of this thesis are presented in this chapter. The first one is a statistical analysis of the phase measurement error in the [LHC](#), that aimed to determine the influence of the [Beam Position Monitors \(BPMs\)](#) on the phase error. The second one is an investigation of the sextupolar contribution to amplitude detuning in the [LHC](#).

6.1 Phase Error Dependency on BPM Type and Location

In the [LHC](#) and many other circular accelerators, [BPM](#) measurement data constitutes the primary source for [optics](#) properties computation. Since the computation of global corrections (see [Section 3.3.4](#)) relies on obtaining the best possible phase measurement, it is valuable to understand the limitations and potential means of improvement of said measurement. As different BPM types [236] have different measurement resolution, and higher [\$\beta\$ -functions](#) lead to better signal-to-noise ratios on measurements, these measurements and the subsequent results were suspected to be substantially affected by both the type of BPM used for the measurements and the value of the β -functions at the measuring devices. This study was performed to investigate the influence of these properties on the precision of the reconstructed phase values from turn-by-turn data.

In practice, the presence of systematic errors can prevent different sets of measurements from being independent. In the following study measurements are assumed to be independent and [identically distributed normal random variables \(IIDs\)](#), meaning repeating the same BPM measurement in identical conditions will spawn a range of values forming a Gaussian distribution. As no sets of measurements were available that made use of specific groups of BPMs, a statistical analysis of the phase errors from previous measurements was needed to differentiate between BPMs of interest. Using the underlying properties of the measurement-derived distributions, one can numerically

infer the impact on the phase measurement error of specific subgroups of measuring devices.

Measurement Data and Underlying Distributions

The methods and considerations below can be applied on BPM turn-by-turn measurement data from synchrotron machines. The following analysis was done on data taken during the LHC Run 2, in 2018 and at $\beta^* = 30$ cm. Information about the measurement data used for this analysis can be found in Appendix E. Figure 6.1 shows how BPMs in the LHC are spread across a wide range of β -functions.

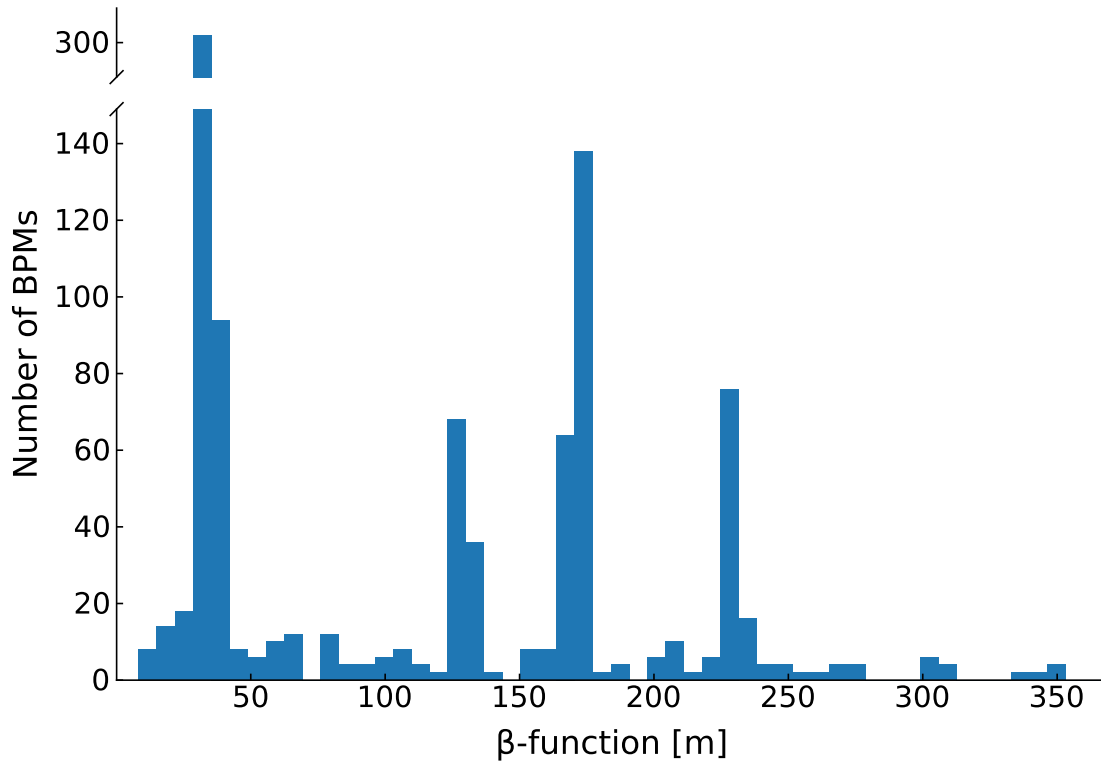


FIGURE 6.1: Distribution of BPM β -functions across the machine for the Run 2 measurements used. A small amount of BPMs located at much higher β are not shown on this plot.

The sum of two IIDs - which our measurements are assumed to be - is also normal. Using the characteristic function of a normal distribution

$$\varphi(t) = \exp\left(it\mu - \frac{\sigma^2 t^2}{2}\right), \quad (6.1)$$

and given that the characteristic function of the sum of two independent random variables X and Y is the product of their respective characteristic functions, one gets

$$\begin{aligned} \varphi_{X+Y}(t) &= \varphi_X(t)\varphi_Y(t) = \exp\left(it\mu_X - \frac{\sigma_X^2 t^2}{2}\right) \exp\left(it\mu_Y - \frac{\sigma_Y^2 t^2}{2}\right), \\ &= \exp\left(it(\mu_X + \mu_Y) - \frac{(\sigma_X^2 + \sigma_Y^2)t^2}{2}\right), \end{aligned} \quad (6.2)$$

which corresponds to a normal distribution with its mean being the sum of the two means, and its variance being the sum of the two variances. Respectively, one can deduce the same for the subtraction of two IIDs by changing the signs.

In particle accelerators, phase advances are measured from BPM to BPM and are, in the simplest form, the result of a subtraction. As a consequence, the repeated phase advance measurements obtained from a given BPM pair form a normal distribution with average phase advance $\bar{\varphi}$ and standard deviation σ_μ . Traditionally, the error on phase advance is computed via the standard deviation of N measurements:

$$\varepsilon^2 = \frac{1}{N} \sum_{i=1}^N (\varphi_i - \bar{\varphi})^2. \quad (6.3)$$

This means the squares of phase advance (and phase advance error) values ε^2 form a chi-square distribution, with a number of degrees of freedom $k = N - 1$ since the sample mean is subtracted. Therefore, grouping sufficient BPM pairs of the same type or with similar β -functions, and computing the distribution of their ε^2 one obtains a chi-square distribution. Figure 6.2 shows those chi-square distributions for different ranges of β -function combinations between measuring BPMs.

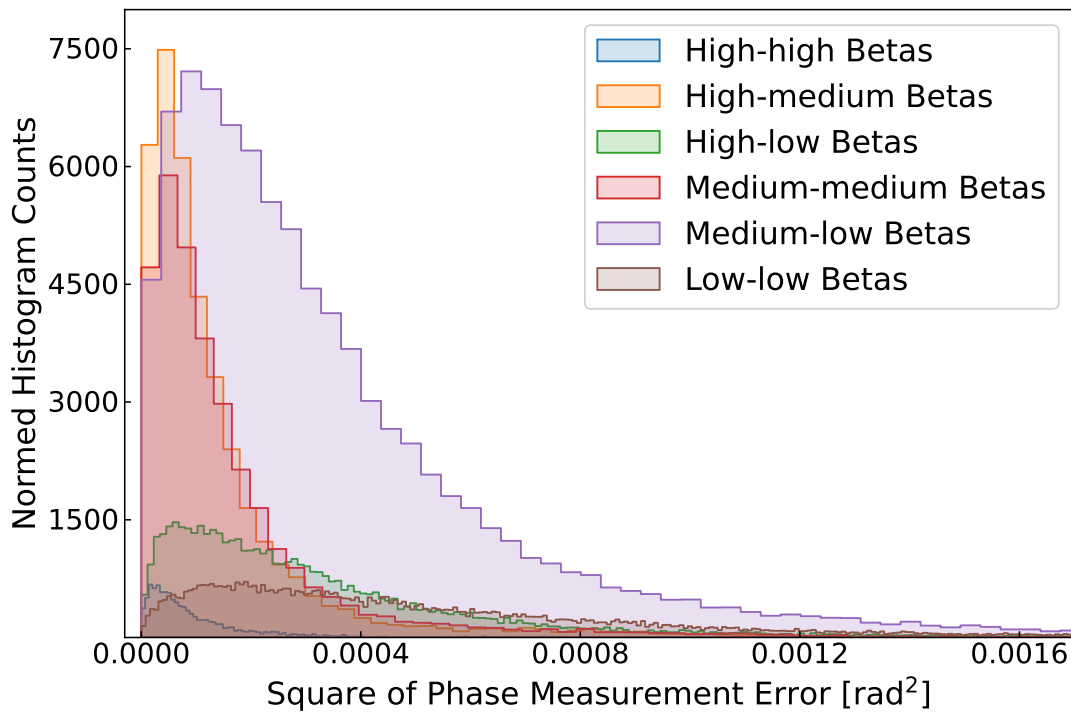


FIGURE 6.2: Chi-square distribution of the squares of phase measurement errors for different BPM combinations, differentiated by the β -functions at the locations of the measuring BPMs. For this plot a BPM was considered "low" below $\beta = 100$ m, "high" above $\beta = 200$ m and "medium" in between.

Similarly, the positive real square roots of values from this chi-square distribution form a chi distribution, which can be derived with a change of variable $x = y^2$. Figure 6.3 shows these distributions for the same β -function ranges seen in Fig. 6.2.

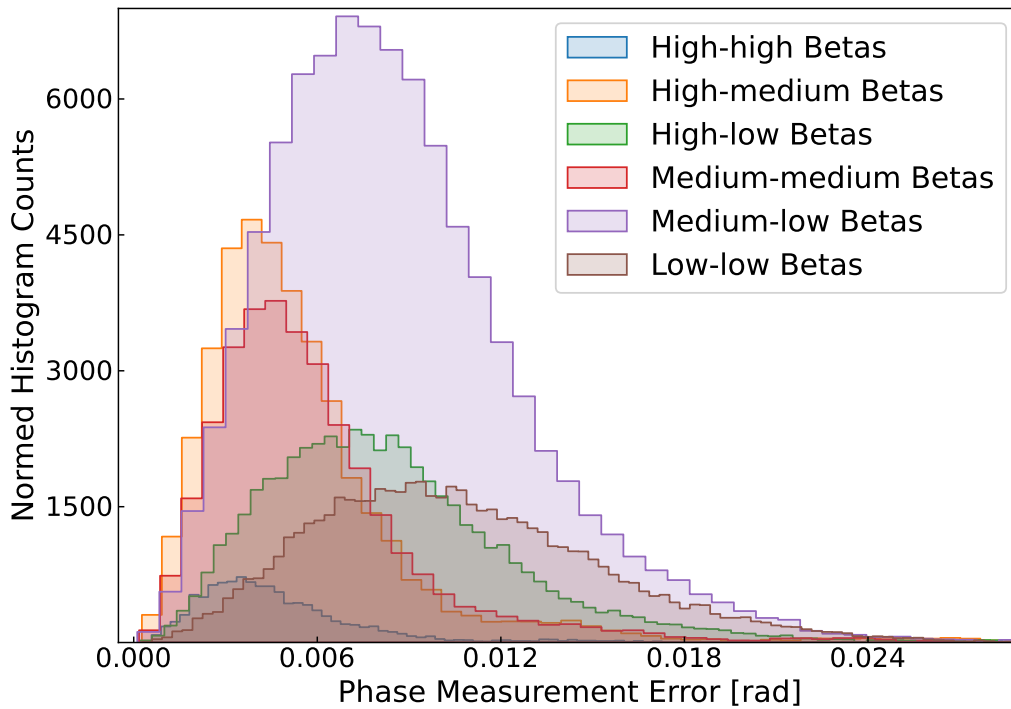


FIGURE 6.3: Distribution of the phase measurement errors for different BPM combinations, differentiated by the β -functions at the locations of the measuring BPMs. For this plot a BPM was considered "low" below $\beta = 100$ m, "high" above $\beta = 200$ m and "medium" in between.

Computing the Standard Deviation on Phase Advance

A chi-square distribution with k degrees of freedom is the distribution of a sum of the squares of k independent standard normal random variables. Let X_i represent the N normal random variables, then the associated standard deviation square is given by

$$\sigma^2 = \frac{1}{N} \sum_{i=1}^N (X_i - \bar{X})^2, \quad (6.4)$$

where \bar{X} is the sample mean of the normal distribution. In our analysis codes the standard error differs slightly from Eq. (6.4) and is defined as:

$$(SE)^2 = \frac{1}{N-1} \sum_{i=1}^N (X_i - \bar{X})^2. \quad (6.5)$$

The ensemble of σ^2 values from different sets of measurements form a chi-square distribution, such as those that can be seen in Fig. 6.2. The associated Probability Density Function (PDF) for k degrees of freedom, which is non-zero for positive values only, is given by:

$$P(x \geq 0, k) = \frac{x^{k/2-1} e^{-x/2}}{2^{k/2} \Gamma(\frac{k}{2})}. \quad (6.6)$$

The **mode** is the value x^* that maximizes the PDF. In this case, one can notice that for positive values where the PDF is defined, x^* will be the same for $P(x)$ and $\log P(x)$. When adopting the following convention:

$$\begin{aligned} A(x) &= \log P(x) , \\ C &= -\frac{k}{2} \log(2) - \log \Gamma(k/2) , \end{aligned} \quad (6.7)$$

where C is a constant of the given distribution, one can deduce the value of the mode x^* through a derivation:

$$\begin{aligned} A(x) &= C + \left(\frac{k}{2} - 1\right) \log(x) - \frac{x}{2} , \\ \frac{dA(x)}{dx} &= \left(\frac{k}{2} - 1\right) \frac{1}{x} - \frac{1}{2} = \frac{k - 2 - x}{2x} . \end{aligned} \quad (6.8)$$

Thus we find that the mode is $x^* = k - 2$. For $k \leq 2$ the mode is 0 since the PDF in that case is strictly decreasing with x . Figure 6.4 illustrates this property with a generated chi-square distribution and its PDF, highlighting the determined location of the mode from a distribution fit.

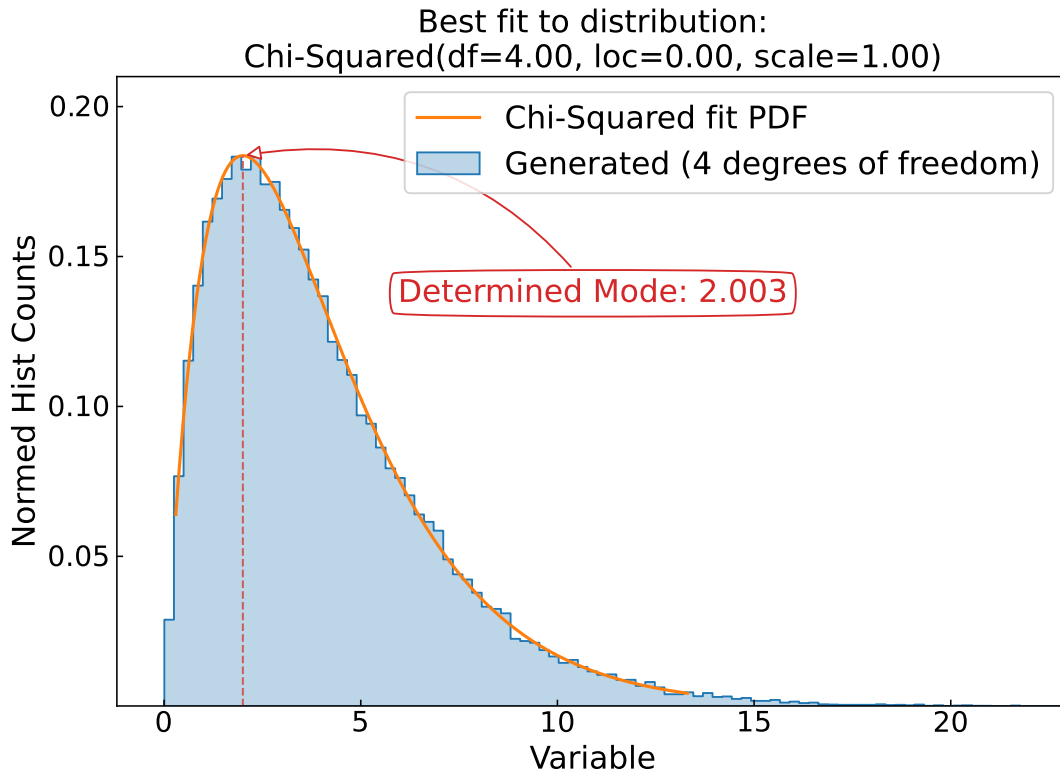


FIGURE 6.4: A randomly generated chi-square distribution (blue) with $k = 4$ degrees of freedom, and a numerically fit probability density function (orange). The determined mode (red) is indeed located at $k - 2 = 2$. Here 'df' (degrees of freedom), 'loc' (horizontal offset) and 'scale' (a scaling factor) are parameters determined during the fit. The horizontal axis is in units of σ^2 .

The standard deviation of the phase advances σ_μ is then given from the mode by:

$$\sigma_\mu = \sqrt{\frac{(\epsilon^2)^*}{k-2}} = \sqrt{\frac{(\epsilon^2)^*}{N-3}} . \quad (6.9)$$

For the chi distribution mentioned above and derived through $x = y^2$, the associated probability density function of Eq. (6.6) becomes:

$$\begin{aligned} P_\sigma(y, k) &= P(y^2, k)2y , \\ P_\sigma(y, k) &= \frac{y^{k-1} e^{-y^2/2}}{2^{k/2-1} \Gamma(\frac{k}{2})} , \end{aligned} \quad (6.10)$$

and the mode of $P_\sigma(y, k)$ is located at $y^* = \sqrt{k-1}$. The determination of the standard deviation of Eq. (6.9) above becomes:

$$\sigma_\mu = \frac{y^*}{\sqrt{k-1}} = \frac{y^*}{\sqrt{N-2}} . \quad (6.11)$$

However, for non-perfect distributions it is numerically difficult to accurately detect this mode: one can use the mode of a fitted probability density function (as done in Fig. 6.4 on a perfect chi-square distribution) but this will suffer from the quality of the fit; or try to detect the highest bins from the distribution's histogram but this suffers from bin width and outlier data points skewing the result.

It is possible to use properties other than the mode. For instance, similarly shown as previously for the mode, one can compute back the desired standard deviation using the mean of the chi distribution through:

$$\begin{aligned} \sigma_\mu &= \frac{\mu}{T} , \\ T &= \sqrt{2} \frac{\Gamma((k+1)/2)}{\Gamma(k/2)} , \end{aligned} \quad (6.12)$$

where σ_μ is the phase measurement's standard deviation, μ is the chi distribution's mean, k is the chi distribution's degrees of freedom and Γ is the Gamma function.

To summarize so far, the desired standard deviation of the phase advance measurements is not available for specific subgroups of measuring BPMs. It is however possible to compute it back from either the mode of the chi-square distribution of the phase advance errors squared, or from the mode or mean of the chi distribution of the phase advance errors, through the following steps:

1. Perform optics analysis on a set of measurements and select part of the data corresponding to the BPMs of interest.
2. Form either the chi-square or chi distribution of, respectively, their phase advance errors squared or their phase advance errors.
3. Compute the relevant property from said distribution - mode or mean, depending on the distribution - and determine the standard deviation of the phase advance measurements from that quantity.

This way, one can determine the standard deviation on the phase advance reconstruction for a given arbitrary subgroup of BPMs from the optics analysis of a set of measurements.

Application to Measurements

Due to the presence of many outliers (see Fig. 6.1) in measurement data and the lack of a sufficient number of data points in some BPM type categories, in the following the calculation from either the chi-square (Eq. (6.9)) or chi (Eq. (6.12)) distribution was used, depending on the specific BPM subgroup.

Optics analysis was run on turn-by-turn data, BPMs were categorized based on their types [236] and the value of β -functions at their locations, and both the chi distributions and the chi-square distributions were generated as detailed above. Figure 6.5 shows the distributions of phase errors for different β -function combinations among standard arc BPMs, the most common ones in the LHC.

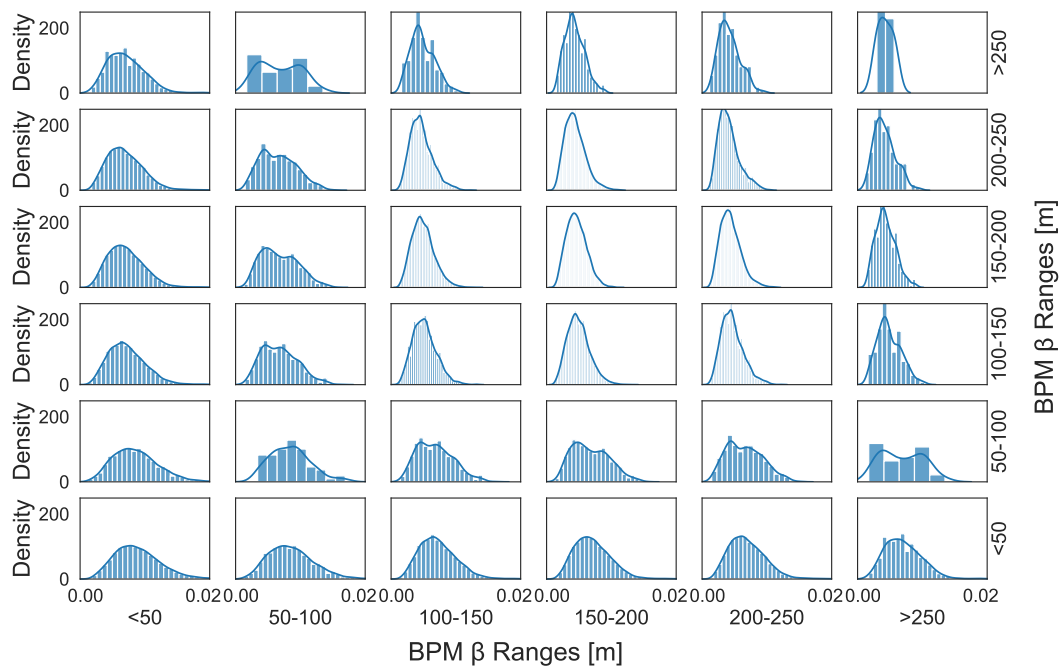


FIGURE 6.5: Phase error distributions for different BPM β combinations, between standard arc BPMs.

For each of these cases, the standard deviation on phase advance is computed using either Eq. (6.9) or Eq. (6.12). Depending on parameters set for the optics analysis one might have to apply a correcting factor of $\sqrt{N-1}$ - with N being the number of measurements used for the analysis - to compensate for this factor being already present in calculations performed by the analysis software (choosing to ignore the t -value correction and single file uncertainty makes this factor appear in the optics calculations and requires that it is removed in later on analysis). Values inferred with this method for an LHC Run 2 for standard arc BPMs can be seen in Fig. 6.6, and for *warm* type BPMs in Fig. 6.7. Results were computed for all BPM types but are not all shown.

Obtained results are in line with expectations: BPM types with lower resolution such as *warm* or *wide*-aperture BPMs consistently yield a higher standard deviation on phase advances than for instance standard BPMs. Similarly, phase advances between measuring BPMs placed at higher β -functions offer better precision.

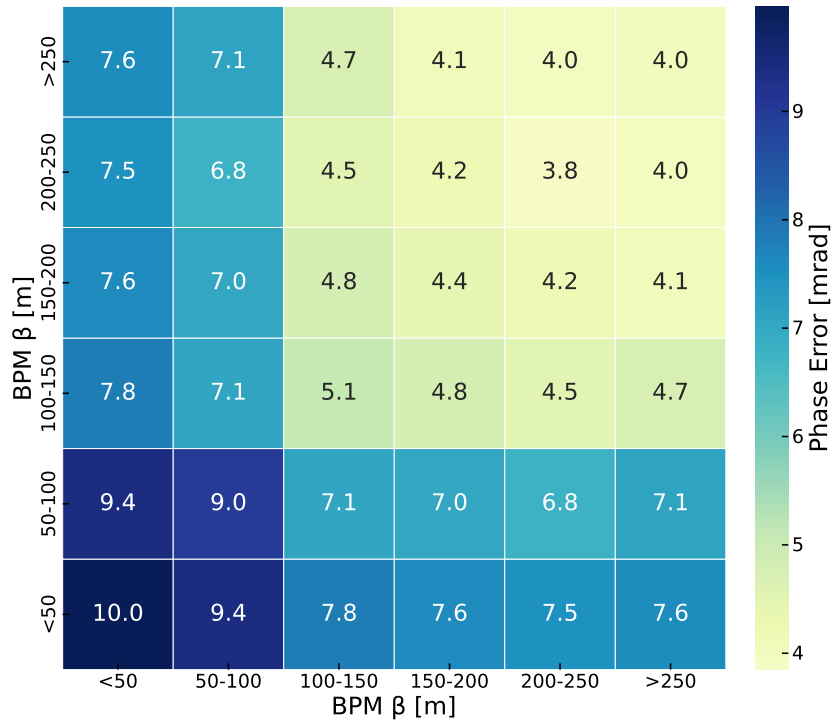


FIGURE 6.6: Computed standard deviations on phase advances between standard arc BPMs for the LHC Run 2 (2018, $\beta^* = 30$ cm) for different β -functions combinations of these BPMs.

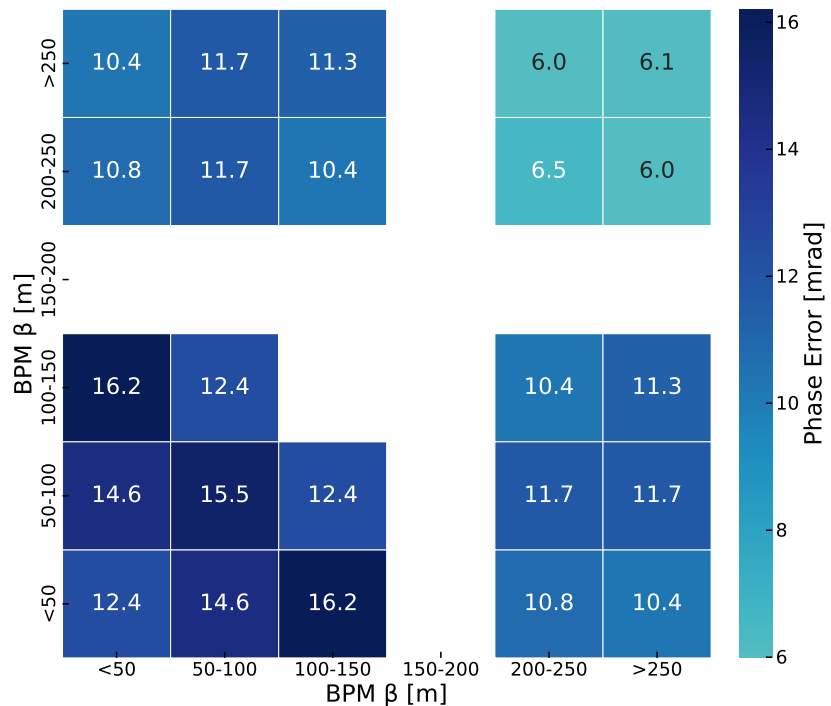


FIGURE 6.7: Computed standard deviations on phase advances between warm type BPMs for the LHC Run 2 (2018, $\beta^* = 30$ cm) for different β -functions combinations of these BPMs. Empty slots correspond to β -functions ranges where no BPMs of this type are present.

Conclusions

Assuming the normal nature of BPM measurements, one can use the underlying properties of the chi-square and chi statistical distributions in order to compute the standard deviation of phase advances while also differentiating between BPMs categories, without performing measurements involving only the BPMs of interest. The dependency of said standard deviation on both BPMs' types and their β -functions was confirmed and quantified. The ability to accurately compute key statistical values on phase advance measurements - but also potentially a number of optics values which are computed from phase - while differentiating between arbitrary BPM categories opens up potential applications in analysis algorithms, for instance refining the phase accuracy in harmonic analysis or optimizing BPM selection in the N-BPM method.

6.2 Simulations of Sextupolar Amplitude Detuning in the LHC

As mentioned in Section 2.3.5, a measurement of the machine non-linearities can be obtained by characterizing the **amplitude detuning**: the dependency of the tune on the amplitude of particle oscillations. Amplitude detuning traditionally comes from octupolar fields and is used for beam stabilization against collective effects [34, 237]. More generally, it comes from multipolar fields of even order $m = 2n$, where n is a natural number strictly higher than one since quadrupolar fields provide a linear behavior.

Analytical formulae from [29, 33, 238] show that second order terms of sextupole strengths contribute to free amplitude detuning. It has previously been suspected that the forced amplitude detuning induced by sextupolar fields would behave similarly to that already studied for octupolar fields in [239].

This study aims to first demonstrate the possibility of observing this amplitude detuning using **AC dipole** excitation, as previous works have shown that not all higher order effects can be measured with driven oscillations [240], and also to confirm the similarity of its behavior to that of the octupolar one. This will aid the understanding of the impact of our sextupolar corrections on amplitude detuning measurements, which may be non-negligible. Simulations were performed to investigate the sextupolar amplitude detuning in the LHC lattice, both through forced oscillations using AC dipole and free oscillations up to similarly high amplitudes.

Amplitude Detuning with an AC Dipole

The feasibility of direct amplitude detuning measurement with an AC dipole was demonstrated in [239], as well as its benefits compared to the previously traditional technique of exciting the beam to large amplitudes with a single kick. In the same paper, the authors go over the linear motion of particles and distinguish two cases. The parametrization of the transverse coordinate z in the case of free and forced oscillations with an AC dipole is given by Eq. (3.3) and Eq. (3.4), respectively.

Analysis of the β -function of the driven particle, β_D , can be found in [130, 134, 239]. It is derived in [239] that for multipoles of even order $m = 2n$, the amplitude detuning in the case of horizontally driven oscillations is given by

$$\begin{aligned}\Delta Q_x &= \frac{qB_{2n}}{2np} \frac{2^{-n}}{2\pi} \frac{(2n)!}{(n-1)!(n-1)!} \beta_x \beta_{D,x}^{n-1} A^{n-1}, \\ \Delta Q_y &= -\frac{qB_{2n}}{2np} \frac{2^{-n}}{2\pi} \frac{(2n)!}{(n-1)!(n-1)!} \beta_y \beta_{D,x}^{n-1} A^{n-1},\end{aligned}\tag{6.13}$$

where q is the charge of the particle, p its momentum and B_{2n} the gradient of the multipole of order $2n$ providing the detuning. Importantly, it is analytically shown that, neglecting the typically small difference between β_z and $\beta_{D,z}$:

“ ” | for multipoles of order $2n$, the direct term of the amplitude detuning measured with an AC dipole will be a factor n larger than for free oscillations while the cross terms in both cases are equal.

This means in the case of octupolar amplitude detuning that the direct term detuning $Q_x(J_x)$ under AC dipole oscillations is a factor $n = 2$ stronger than under free oscillations, while the cross term detuning $Q_y(J_x)$ will be the same in both cases. It was suspected that in the LHC sextupolar detuning can be measured with AC dipoles and that it behaves similarly with this factor 2 observed in the case of even order multipoles, while being a multipole of order 3 itself. Tracking simulations were performed to investigate this effect.

Amplitude Detuning via Particle Tracking

On-momentum particles were tracked with the [MAD-X](#) code through the [LHC](#) lattice of 2018, with $\beta^* = 30$ cm optics. In the setup, non-linearities were stripped down to the contribution of sextupoles only: no magnet errors, crossing angles or orbit bumps were included; and neither octupoles nor higher order magnets were powered. This way the only non-negligible contribution to amplitude detuning is the sextupolar one. Sextupoles were powered with strengths similar to what was used in operation.

Tracking was performed in the case of both free and AC dipole forced oscillations in the horizontal plane, with similar amplitudes. Several scenarios corresponding to different tune separations for the driven motion were explored, namely $\Delta Q_x = -10^{-2}$ and $\Delta Q_x = -5 \times 10^{-3}$, resulting in driven fractional horizontal tunes of $Q_{Dx} = 0.30$ and $Q_{Dx} = 0.305$, respectively. A small initial amplitude was applied in the vertical plane in order to enable the measurement of the vertical tune.

The AC dipole ramp-up and flattop excitation length were chosen as used in optics measurements in the LHC, to preserve the adiabaticity of the process. Turn-by-turn data was gathered at all [BPMs](#) during the tracking, and the resulting file was analyzed as done for LHC measurements. Both the natural tunes and actions were derived from harmonic and then optics analysis of the data.

[Figures 6.8](#) and [6.9](#) show the horizontal and vertical amplitude detuning results for both free and driven motion, respectively. For each result a linear regression is performed against the data to determine the detuning coefficient. In the case of simulations, where the uncertainty on the data points is negligible, this fit is enough to accurately determine the detuning coefficient. Results are compiled in [Table 6.1](#).

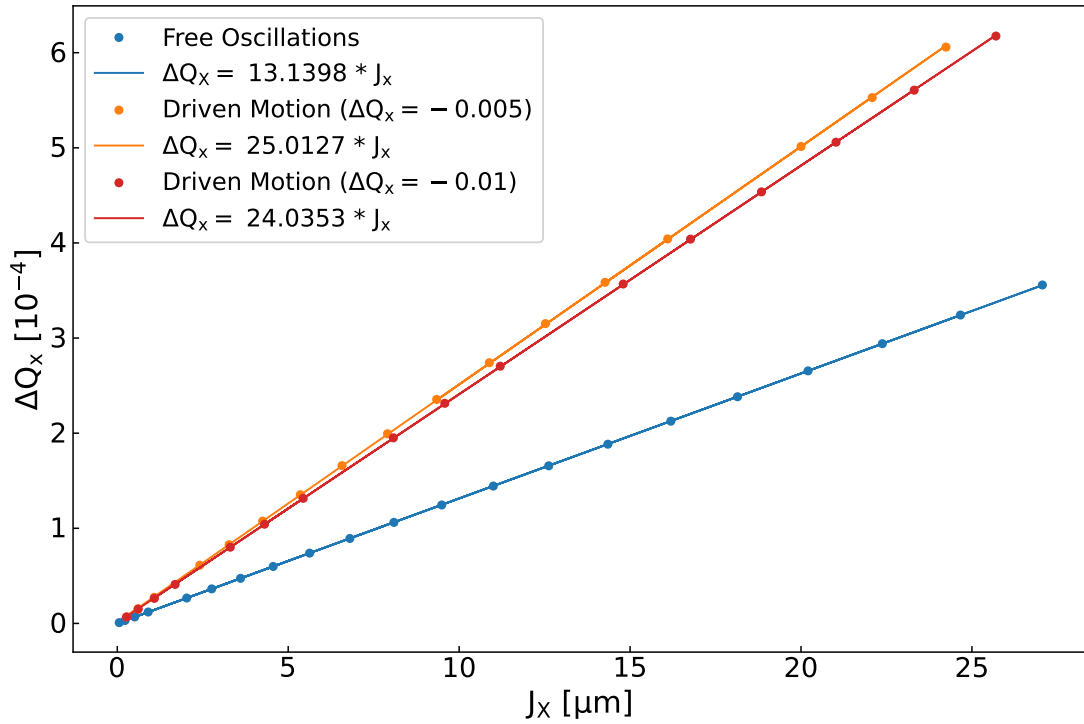


FIGURE 6.8: Natural horizontal tune Q_x shift with horizontal free or forced action (J_x or A_x), in the case of free oscillations (blue) and driven motion with $\Delta Q_x = -0.01$ (red) and $\Delta Q_x = -0.005$ (orange).

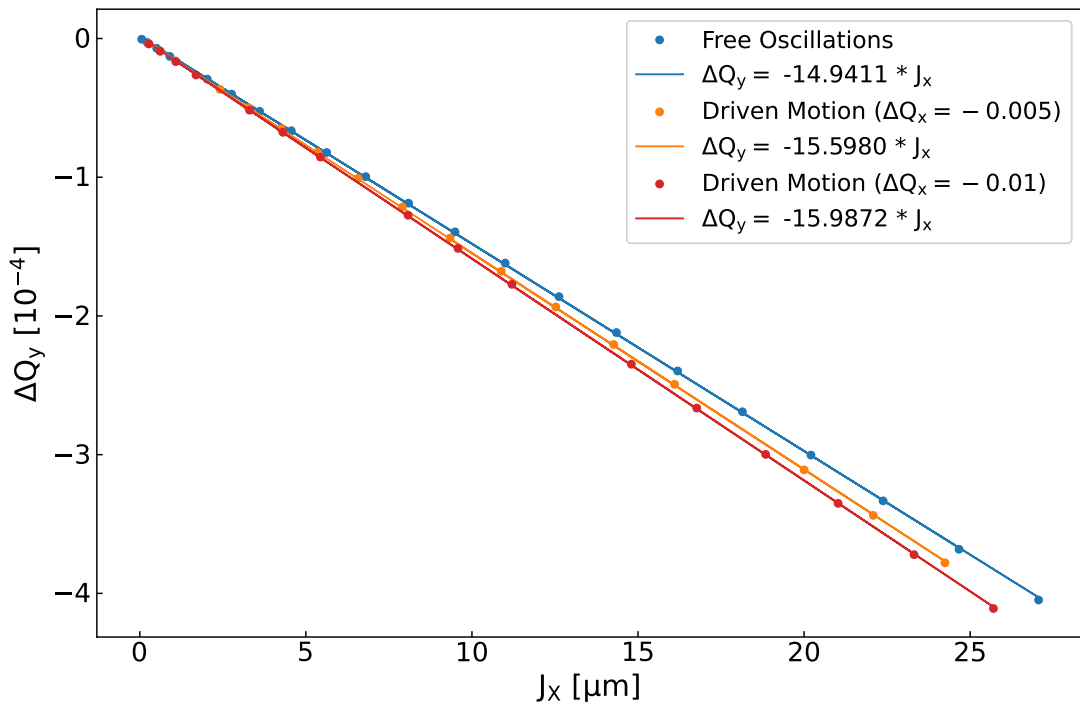


FIGURE 6.9: Natural vertical tune Q_y shift with horizontal free or forced action (J_x or A_x), in the case of free oscillations (blue) and driven motion with $\Delta Q_x = -0.01$ (red) and $\Delta Q_x = -0.005$ (orange).

For the direct detuning (Fig. 6.8), where a factor 2 is expected, the fit to free oscillations data gives a detuning coefficient of $13.14 \mu\text{m}^{-1}$, which makes the expected detuning coefficient for the forced oscillations around $26.3 \mu\text{m}^{-1}$. With a tune separation of $\Delta Q_x = -10^{-2}$, this coefficient is determined at $24.04 \mu\text{m}^{-1}$, within a 10 % margin of the expected value. Halving the tune separation to $\Delta Q_x = -5 \times 10^{-3}$ brings this coefficient closer to the factor 2, now within a 5 % margin. This change is attributed to the modification of the β -function and phase advances by the AC dipole: the $\beta_{D,z}$ term in Eq. (3.4), which is assumed close enough to β_z in the factor 2 hypothesis. As the relative difference between $\beta_{D,z}$ and β_z reduces with the tune separation, this behavior is expected.

For the cross detuning (Fig. 6.9) where a factor 1 is expected, similar results are observed: the driven motion's detuning coefficient is determined to be $-15.99 \mu\text{m}^{-1}$, reasonably close to the $-14.94 \mu\text{m}^{-1}$ in the case of free oscillations. Again, halving the tune separation to $\Delta Q_x = -5 \times 10^{-3}$ brings us closer to the factor 1.

Scenario	Detuning Coefficient [μm^{-1}]	
	Direct Term	Cross Term
Free Oscillations	13.14	-14.94
Driven ($\Delta Q_x = -0.01$)	24.04	-15.99
Driven ($\Delta Q_x = -0.005$)	25.01	-15.50

TABLE 6.1: Direct and cross term detuning coefficients for free and forced motion, determined from tracking data with a linear regression.

Conclusions

Measurement of the sextupolar amplitude detuning has not been done so far in the LHC. The negligible contribution of the sextupolar sources to the amplitude detuning in the LHC compared to other typical sources has been demonstrated, both in the presence and absence of AC dipole driven motion. Additionally, with small enough tune separation, this contribution behaves similarly to octupolar amplitude detuning when comparing the case of forced motion and free oscillations.

6.3 Summary

A statistical analysis of the phase reconstruction precision in the LHC was performed, distinguishing between BPM categories. The results confirmed the influence of both BPM type and the β -functions at the measuring device on the precision of the phase reconstruction, with up to a factor of 3 between the best and worst performing BPMs. This knowledge could be applied in optics measurements algorithms to, for instance, select a subset of BPMs to use for a given measurement. Such an analysis presents a clear improvement avenue for the reconstruction of optics functions in a circular accelerator and the improvement of computed global corrections.

A second simulation-based study was performed to investigate the sextupolar contribution to amplitude detuning in the LHC. A clear contribution, though relatively

small compared to that of other sources, was observed. The suspected behavior of this contribution in the presence of AC dipole forced oscillations, similar to that of the octupolar amplitude detuning, was confirmed.

CHAPTER 7

Conclusion

In the quest for new physics, modern particle colliders such as the [Large Hadron Collider \(LHC\)](#) are always striving to increase their [luminosity](#) - both instantaneous and integrated - in order to reduce statistical uncertainties and increase the potential for new discoveries. As a result, the machine is subject to constant upgrades and improvements in terms of hardware, software and operational configuration. In parallel to these upgrades, an ever tighter control of the [beam](#) dynamics is necessary to ensure safe operation as well as the best possible performance of the machine.

One performance limitation in the [LHC](#) is the proper handling of local [betatron coupling](#) in the [Insertion Regions \(IRs\)](#) which, if left uncorrected, has the potential to degrade or even interrupt beam operations, as well as to reduce the collision rates as was observed during an incident in 2018. The upcoming [High-Luminosity Large Hadron Collider \(HL-LHC\)](#) upgrade is bound to drastically enhance the impact of any uncorrected local coupling on the machine's performance, warranting a dedicated effort on this topic. The objective of this work has been to provide a novel approach that can measure and correct the local [IR](#) coupling and to experimentally determine corrections to improve [LHC](#) operations.

The main body of the presented work addresses the problem of measuring and correcting the local [betatron coupling](#) in the [LHC IRs](#). The shortcomings of existing local [IR](#) measurement methods for local coupling (segment-by-segment technique, k-modulation and alternative observables such as combined [Resonance Driving Terms \(RDTs\)](#)) justified the creation of new tools. The newly developed tools, the [colinearity knob](#) and [Rigid Waist Shift \(RWS\)](#), allow relevant quantities of interest to be related to strong observables such as the [RDTs](#) and the $|C^-|$ in order to drive a correction. The effect of each was demonstrated through extensive simulations, and an experimental setup to use them for the determination of corrections was laid out.

Measurements using the new experimental setup during the [LHC 2022](#) commissioning, at 6.8 TeV and $\beta^* = 30$ cm were presented, together with the determined corrections obtained by comparing the measurements to simulations. These corrections were trimmed in the machine and their efficiency assessed through instantaneous [luminosity](#) measurements. Great improvements in collision rates were observed at the main [Interaction Points \(IPs\)](#): an additional 9.7% and 3.5% instantaneous luminosity at the [ATLAS](#) and [CMS experiments](#), respectively. Comparison of these results to expectations from simulations revealed a disagreement, with the [ATLAS](#) numbers lower than expected.

This discrepancy was attributed to the early calibration setup of the detector. Luminosity predictions and measurements showed a much improved agreement at the same detector in identical measurements performed later in the year with higher intensity beams. Good agreement was observed at the CMS detector.

This new method allowed the measurement, quantification and correction, for the first time, of the local [betatron coupling](#) in the LHC IRs. It has the advantage of being applicable early on in commissioning with low intensity beams and enables distinction between the two beams, which could require different types of adjustments: magnet realignment, orbit corrections, etc. Furthermore, it has been shown to be relevant and applicable to both existing and future colliders.

As the radiation exposure of the used LHC corrector magnets is expected to surpass the allowed limit during the LHC Run 3, the impact of losing these crucial elements was studied. It was demonstrated through simulations that one could compensate for the loss of a single corrector magnet and guarantee both safe machine operation and squeezing of the beams down to collision configuration. This compensation, however, would happen at the cost of luminosity: up to a 60% loss of instantaneous luminosity in the most affected case. These expectations were confirmed through beam measurements in which the loss of correctors were simulated. Using these numbers and taking into account the β^* -leveling as well as other parameters in the 2023 configuration, up to a 25% loss of integrated luminosity over a complete physics fill is expected. Further studies are required for scenarios involving the simultaneous loss of both correctors in a given IR and to investigate potential solutions.

After the successful application of machine learning techniques to several other tasks in particle accelerators, including optics corrections, the possibility of using them for a different approach to tackle local coupling in the LHC IRs was explored. Through extensive simulation-supported data sets, specific models were trained to predict the location of coupling sources in the form of quadrupole tilts from measured RDTs. Models were obtained that achieved good prediction performance on clean data sets but did not generalize well to realistically noisy data sets. These models show promising results but improvements in the precision of the reconstructed RDTs would be necessary before they could confidently be used in the LHC. Such improvements could be achieved with better beam instrumentation, more accurate optics reconstruction methods or the use of additional, dedicated machine learning models.

Additional studies were performed that contributed to the understanding of the LHC optics and potential measurement method improvements. Through statistical analysis, the influence of both Beam Position Monitor (BPM) type and β -function at the measuring device on the precision of the phase reconstruction in the LHC was determined. The results allowed, without dedicated measurements, identification of the best conditions for phase reconstruction. This result has the potential to be applied in optics measurements algorithms to, for instance, select a subset of BPMs for better phase and potentially β -function measurements. The impact of the sextupolar contribution to the amplitude detuning in the LHC, never previously measured, was demonstrated through simulations and was shown to behave similarly to the first order octupolar amplitude detuning under forced oscillations. The determined negligible level of the contribution,

as well as its now confirmed behavior, allow it to be safely neglected from amplitude detuning measurements when characterizing the non-linearities of the machine.

The overall goal of this thesis has been to develop a new approach to the measurement and correction of local [betatron coupling](#) in the [LHC IRs](#). Different methods were developed and tested including, mainly, a new experimental setup which was used to measure and correct local coupling in the [LHC 2022 commissioning](#), improving the instantaneous luminosity at the [ATLAS](#) and [CMS experiments](#). This new method is relevant for typical conditions in an Interaction Region, and therefore relevant for other existing colliders such as SuperKEKB, but also future machines such as the [HL-LHC](#) and the [Future Circular Collider \(FCC\)](#). The work presented in this document contributes to the improved performance and understanding of the [LHC](#), but also potentially other present and future particle colliders.

APPENDIX A

Thin Kick Hamiltonian Derivation

This appendix contains the full derivation leading to the result of Eq. (2.45), showing the Hamiltonian thin kick expansion.

A.1 Multinomial Expansion

Let us start by reminding the multinomial expansion rule. For any positive integer m and non-negative integer n , the multinomial expansion describes the expansion of a sum of m numbers raised to the power n :

$$(x_1 + \dots + x_m)^n = \sum_{k_1 + \dots + k_m = n} \frac{n!}{k_1! \dots k_m!} x_1^{k_1} \dots x_m^{k_m} . \quad (\text{A.1})$$

Another form of writing the multinomial expansion is with the Kronecker delta:

$$\delta_{i,j} = \begin{cases} 0 & \text{if } i \neq j , \\ 1 & \text{if } i = j . \end{cases} \quad (\text{A.2})$$

In this case, Eq. (A.1) can be written:

$$(x_1 + \dots + x_m)^n = \sum_{k_1 + \dots + k_m \leq n} \delta_{j+k+l+m,n} \frac{n!}{k_1! \dots k_m!} x_1^{k_1} \dots x_m^{k_m} . \quad (\text{A.3})$$

Note that in this form, the indices of the summation $k_1 + k_2 + \dots + k_m$ are *less than or equal* to n . Let us illustrate with the following example:

$$\begin{aligned} (a + b + c + d)^n &= \sum_{j+k+l+m=n} \frac{n!}{j!k!l!m!} a^j b^k c^l d^m \\ &= \sum_{j+k+l+m \leq n} \delta_{j+k+l+m,n} \frac{n!}{j!k!l!m!} a^j b^k c^l d^m \\ &= \sum_{j=0}^n \sum_{k=0}^n \sum_{l=0}^n \sum_{m=0}^n \delta_{j+k+l+m,n} \frac{n!}{j!k!l!m!} a^j b^k c^l d^m . \end{aligned} \quad (\text{A.4})$$

A.2 Hamiltonian Derivation

Starting from Eq. (2.6), the transverse coordinates x and y can be expressed from action and angle variables:

$$\begin{aligned} x(s) &= \sqrt{2J_x\beta_x} \cos(\phi_x + \phi_{x,0}) , \\ y(s) &= \sqrt{2J_y\beta_y} \cos(\phi_y + \phi_{y,0}) . \end{aligned} \quad (\text{A.5})$$

Here the dependence on the longitudinal coordinate s has been removed for clarity compared to Eq. (2.6). Using Euler's formula, these can be rewritten as:

$$\begin{aligned} x &= \sqrt{2J_x\beta_x} \frac{e^{i(\phi_x + \phi_{x,0})} + e^{-i(\phi_x + \phi_{x,0})}}{2} , \\ y &= \sqrt{2J_y\beta_y} \frac{e^{i(\phi_y + \phi_{y,0})} + e^{-i(\phi_y + \phi_{y,0})}}{2} . \end{aligned} \quad (\text{A.6})$$

As seen in Section 2.2, the multipole expansion of the transverse planes Hamiltonian for a multipole of order n goes as:

$$\mathcal{H} = \text{Re} \left[(K_n + iJ_n) \frac{(x + iy)^n}{n!} \right] . \quad (\text{A.7})$$

This is a slight change over Eq. (2.37) as here the terms K_n and J_n , representing the **integrated magnet strengths**, are used over B_n and A_n . When plugging in the forms of Eq. (A.6), one gets:

$$\begin{aligned} \mathcal{H} = \text{Re} \left[\frac{1}{2^n \cdot n!} (K_n + iJ_n) \left(\sqrt{2J_x\beta_x} e^{i(\phi_x + \phi_{x,0})} \right. \right. \\ \left. \left. + \sqrt{2J_x\beta_x} e^{-i(\phi_x + \phi_{x,0})} \right. \right. \\ \left. \left. + i\sqrt{2J_y\beta_y} e^{i(\phi_y + \phi_{y,0})} \right. \right. \\ \left. \left. + i\sqrt{2J_y\beta_y} e^{-i(\phi_y + \phi_{y,0})} \right)^n \right] . \end{aligned} \quad (\text{A.8})$$

Now, we can do the multinomial expansion of last term via Eq. (A.1). Let us define a , b , c , and d such that $(a + b + c + d)^n$ equals this last term. This yields:

$$\begin{aligned} a^j &= \left(\sqrt{2J_x\beta_x} e^{i(\phi_x + \phi_{x,0})} \right)^j = (2J_x)^{\frac{j}{2}} \beta_x^{\frac{j}{2}} e^{ij(\phi_x + \phi_{x,0})} , \\ b^k &= \left(\sqrt{2J_x\beta_x} e^{-i(\phi_x + \phi_{x,0})} \right)^k = (2J_x)^{\frac{k}{2}} \beta_x^{\frac{k}{2}} e^{-ik(\phi_x + \phi_{x,0})} , \\ c^l &= \left(i\sqrt{2J_y\beta_y} e^{i(\phi_y + \phi_{y,0})} \right)^l = i^l (2J_y)^{\frac{l}{2}} \beta_y^{\frac{l}{2}} e^{il(\phi_y + \phi_{y,0})} , \\ d^m &= \left(i\sqrt{2J_y\beta_y} e^{-i(\phi_y + \phi_{y,0})} \right)^m = i^m (2J_y)^{\frac{m}{2}} \beta_y^{\frac{m}{2}} e^{-im(\phi_y + \phi_{y,0})} . \end{aligned} \quad (\text{A.9})$$

Combining these terms two by two gives:

$$\begin{aligned} a^j b^k &= (2J_x)^{\frac{j+k}{2}} \beta_x^{\frac{j+k}{2}} e^{i(j-k)(\phi_x + \phi_{x,0})} , \\ c^l d^m &= i^{l+m} (2J_y)^{\frac{l+m}{2}} \beta_y^{\frac{l+m}{2}} e^{i(l-m)(\phi_y + \phi_{y,0})} . \end{aligned} \quad (\text{A.10})$$

By combining them once more, we get:

$$a^j b^k c^l d^m = i^{l+m} (2J_x)^{\frac{j+k}{2}} (2J_y)^{\frac{l+m}{2}} \beta_x^{\frac{j+k}{2}} \beta_y^{\frac{l+m}{2}} e^{i[(j-k)(\phi_x+\phi_{x,0})+(l-m)(\phi_y+\phi_{y,0})]} . \quad (\text{A.11})$$

After isolating the terms independent of the position s , this is expressed as:

$$a^j b^k c^l d^m = i^{l+m} \beta_x^{\frac{j+k}{2}} \beta_y^{\frac{l+m}{2}} e^{i[(j-k)\phi_x+(l-m)\phi_y]} (2J_x)^{\frac{j+k}{2}} (2J_y)^{\frac{l+m}{2}} e^{i[(j-k)\phi_{x,0}+(l-m)\phi_{y,0}]} . \quad (\text{A.12})$$

Going back to the \mathcal{H} form of Eq. (A.8), using the a , b , c , and d terms defined above and the multinomial expansion rules of Eqs. (A.1) and (A.3), we get for a given element:

$$\begin{aligned} \mathcal{H} &= \text{Re} \left[\frac{1}{2^n \cdot n!} (K_n + iJ_n) (a + b + c + d)^n \right] \\ &= \text{Re} \left[\frac{1}{2^n \cdot n!} (K_n + iJ_n) \sum_{j+k+l+m=n} \frac{n!}{j!k!l!m!} a^j b^k c^l d^m \right] \\ &= \text{Re} \left[(K_n + iJ_n) \sum_{j+k+l+m=n} \frac{1}{2^{j+k+l+m} \cdot j!k!l!m!} a^j b^k c^l d^m \right] \\ &= \text{Re} \left[(K_n + iJ_n) \sum_{j+k+l+m=n} \frac{1}{2^{j+k+l+m} \cdot j!k!l!m!} \right. \\ &\quad \left. i^{l+m} \beta_x^{\frac{j+k}{2}} \beta_y^{\frac{l+m}{2}} e^{i[(j-k)\phi_x+(l-m)\phi_y]} \right. \\ &\quad \left. (2J_x)^{\frac{j+k}{2}} (2J_y)^{\frac{l+m}{2}} e^{i[(j-k)\phi_{x,0}+(l-m)\phi_{y,0}]} \right] . \end{aligned} \quad (\text{A.13})$$

Noting that i is the imaginary unit, the real part of the sum is then directly influenced by the parity of $(l + m)$. The equation can be rewritten taking this into account, effectively selecting between the two terms:

$$\Omega(i) = \begin{cases} 1 & \text{if } i \text{ is even,} \\ 0 & \text{if } i \text{ is odd.} \end{cases} \quad (\text{A.14})$$

And Eq. (A.13) becomes:

$$\mathcal{H} = \sum_{j+k+l+m=n} \left[\frac{K_n \Omega(l+m) + iJ_n \Omega(l+m+1)}{2^{j+k+l+m} \cdot j!k!l!m!} i^{l+m} \beta_x^{\frac{j+k}{2}} \beta_y^{\frac{l+m}{2}} \right. \\ \left. (2J_x)^{\frac{j+k}{2}} (2J_y)^{\frac{l+m}{2}} e^{i[(j-k)(\phi_x+\phi_{x,0})+(l-m)(\phi_y+\phi_{y,0})]} \right] . \quad (\text{A.15})$$

One can then define h_{jklm} as

$$h_{jklm} = \frac{K_n \Omega(l+m) + iJ_n \Omega(l+m+1)}{2^{j+k+l+m} \cdot j!k!l!m!} i^{l+m} \beta_x^{\frac{j+k}{2}} \beta_y^{\frac{l+m}{2}}, \quad (\text{A.16})$$

which reduces the above to Eq. (A.17):

$$\mathcal{H} = \sum_{jklm} h_{jklm} (2J_x)^{\frac{j+k}{2}} (2J_y)^{\frac{l+m}{2}} e^{i[(j-k)(\phi_x + \phi_{x,0}) + (l-m)(\phi_y + \phi_{y,0})]}, \quad (\text{A.17})$$

where $j+k+l+m = n$, which corresponds to the form of Eq. (2.45) given in Section 2.3.1.

APPENDIX B

Element Naming Conventions in the LHC

This appendix details the element naming convention in the [Large Hadron Collider \(LHC\)](#) and [High-Luminosity Large Hadron Collider \(HL-LHC\)](#). [Figure B.1](#) below illustrates the established scheme using an example segment of the LHC. A detailed listing of all LHC element and equipment names can be found at [\[236\]](#).

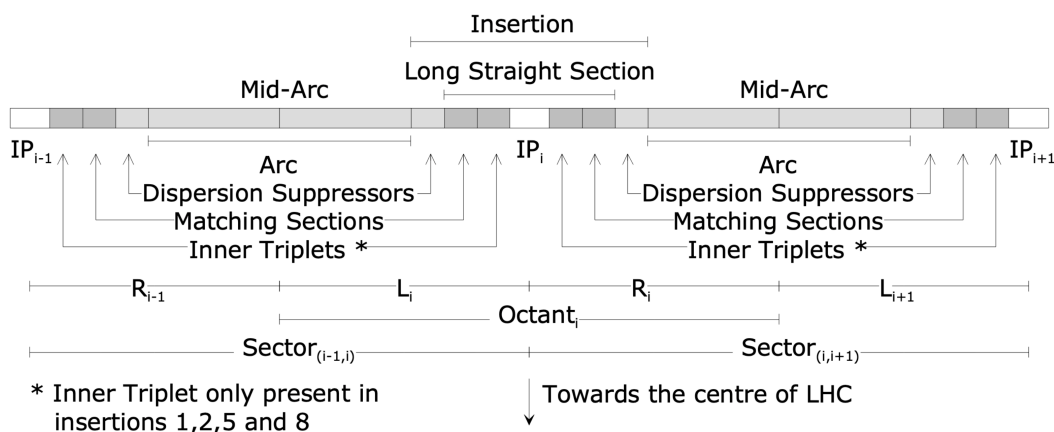


FIGURE B.1: Naming scheme in a segment of the LHC [\[241\]](#).

The general structure adheres to the following rules:

1. Each octant is divided into two **half-arcs** surrounding an **insertion**.
2. Each octant is also divided into a left side and a right side to said insertion.
3. The center point of some octants is the **Interaction Point (IP)**, with their surrounding region sometimes also referred to as **Interaction Region (IR)**.

From the standpoint of lattice definitions there are eight IPs, although this is merely for notational convenience. An **Interaction Point** in the strict sense is a location where the two beams are made to collide, which only happens in the center of octants 1, 2, 5 and 8 where **experiments** are located. It is assumed through this document that when an IP or IR is mentioned, it refers to one of these octants.

Regardless of hosting an IP, all octants have in common that they host a long straight section in the middle as part of the insertion. While the arcs can be considered generally uniform across the LHC, the various long sections differ from octant to octant.

As the base pattern of the LHC arcs is a FODO lattice, the machine can be broken up into half-cells containing one quadrupole each. As a result each half-cell is assigned a number such that the i^{th} quadrupole away from the center of its octant is associated with the i^{th} half-cell. With this in consideration, the general naming convention can be summarized as:

$$\langle\text{TYPE}\rangle\langle\text{SPECIAL}\rangle.\langle\text{EXTRA}\rangle\langle\text{HALF_CELL}\rangle\langle\text{LR}\rangle\langle\text{OCTANT}\rangle.\text{B}\langle 12\rangle$$

In the definition above the various entries are defined as follows:

- TYPE: Entry specifying the type of element. Examples are given in Table B.1.
- SPECIAL: *Optional* entry which can be used to subtype an element, e.g. H or V to signify that the element is acting on the horizontal or vertical plane.
- EXTRA: *Optional* entry used to separate between otherwise identically named elements in regard to their type and number. E.g. A, B, C to separate between three bending magnets in the same half-cell.
- LR: Entry specifying which side of the closest IP the element is on. The values for this entry are either L (left) or R (right).
- OCTANT: Entry specifying the octant the element is a part of. Valid entries are integers from 1 to 8.
- 12: *Optional* entry specifying which beam the element is part of. This is either 1 or 2, unless the element is shared between the two beams in which case the element name ends with the OCTANT entry.

B

Element Type	Prefix
Bending Magnet	MB
Quadrupole	MQ
Orbit Corrector	MCB
BPM	BPM
Crab Cavity	ACFCA
Drift	DRIFT

TABLE B.1: Example prefixes for different LHC element types. An extensive list of all elements can be found at [236].

Let us illustrate with examples. The element MQ.25L5.B1 is a quadrupole on the left side of IP5, in the 25th half-cell counting from IP5 and for beam 1.

The special identifier can be used in multiple ways. For instance MQML.10R1.B1 is a different type of quadrupole in half-cell 10, on the right side of IP1 for beam 1. Here the special identifier describes the type of quadrupole. For MCBH.21R5.B1, the special identifier H signifies that the element is a horizontal orbit corrector (MCB).

In the triplet quadrupoles one can notice for instance elements MQXB.A2L1 and MQXB.B2L1, the two elements constituting the Q2 triplet quadrupole. In this case the elements share the same type (MQXB aka middle, single aperture inner triplet quadrupole), octant, side of IP and half-cell, which is why they make use of the extra specifiers A and B to tell them apart. For this specific case these two magnets share a main power supply, but each has an additional power supply for small individual adjustments. Note that these elements skip the appendage of .B<12> as they correspond to elements common to both beams, which can only happen in the IR. This is due to the fact that when the two beams are brought to collision they are bound to travel through the same equipment pieces as they get close to the IP.

APPENDIX C

Experimental Knobs Designed for the LHC

One can find in this Appendix the full information of the different experimental [knobs](#) that were designed for the [LHC](#). The knobs are reported below as they have been implemented in the [LHC Software Architecture \(LSA\)](#) framework [242] and used in the 2022 commissioning. In each case, the values correspond to a [trim](#) factor of 1 for the knob, unless indicated otherwise, and scale linearly with the trim factor. These knobs have been designed for all beam processes of the LHC [Run 3](#) optics as they were at the time of the 2022 commissioning, for a beam energy of 6800 GeV.

C.1 Definitions of the Colinearity Knobs

[Table C.1](#) shows the settings used in [LSA](#) to define the colinearity knobs at IR1 and IR5. These knobs control the [skew](#) quadrupole correctors left and right of the [Interaction Point \(IP\)](#), the MQSX magnets.

Component	Value	Component	Value
RQSX3.L1/K1S	10^{-4}	RQSX3.L5/K1S	10^{-4}
RQSX3.R1/K1S	-10^{-4}	RQSX3.R5/K1S	-10^{-4}

(A) Colinearity knob for IR1.
(B) Colinearity knob for IR5.

TABLE C.1: Definitions of the colinearity knobs for IR1 (left) and IR5 (right) as implemented in LSA.

C.2 Definitions of the Rigid Waist Shift Knobs

[Table C.2](#) shows the settings used in [LSA](#) to define the [Rigid Waist Shift \(RWS\)](#) knobs at IR1 and IR5. These knobs control the triplet magnets left and right of the [IP](#) in order to move all four betatron waists simultaneously. A trim of the [RWS](#) acts on the common powering circuit of the triplets.



Component	Value	Component	Value
MQXA1.L1/K1	$-4.388\,91 \times 10^{-5}$	MQXA1.L5/K1	$-4.388\,91 \times 10^{-5}$
MQXA1.R1/K1	$-4.388\,91 \times 10^{-5}$	MQXA1.R5/K1	$-4.388\,91 \times 10^{-5}$
MQXB2.L1/K1	$4.388\,91 \times 10^{-5}$	MQXB2.L5/K1	$4.388\,91 \times 10^{-5}$
MQXB2.R1/K1	$4.388\,91 \times 10^{-5}$	MQXB2.R5/K1	$4.388\,91 \times 10^{-5}$
MQXA3.L1/K1	$-4.388\,91 \times 10^{-5}$	MQXA3.L5/K1	$-4.388\,91 \times 10^{-5}$
MQXA3.R1/K1	$-4.388\,91 \times 10^{-5}$	MQXA3.R5/K1	$-4.388\,91 \times 10^{-5}$

(A) RWS knob for IR1.

(B) RWS knob for IR5.

TABLE C.2: Definitions of the Rigid Waist Shift knobs for IR1 (left) and IR5 (right) as implemented in LSA.

C.3 Definitions of the Optics Rematching Knobs

Tables C.3 and C.4 show the settings used in LSA to define the optics rematching knobs needed after applying the RWS knob, at IR1. Table C.3 gives the settings that rematch the optics when the IR1 RWS knob is trimmed with a factor of 1, while Table C.4 gives the settings that rematch the optics when the IR1 RWS knob is applied with a factor of -1 . These knobs control the independent magnets Q4 to Q10 left and right of the IP for both beams.

Component	Beam 1 Value	Beam 2 Value
RQ4.L1B[12]/K1	$7.351\,348 \times 10^{-5}$	$3.132\,269 \times 10^{-7}$
RQ4.R1B[12]/K1	$4.704\,082 \times 10^{-5}$	$5.434\,962 \times 10^{-5}$
RQ5.L1B[12]/K1	$-2.142\,214 \times 10^{-4}$	$1.283\,481 \times 10^{-4}$
RQ5.R1B[12]/K1	$-2.086\,652 \times 10^{-4}$	$-1.782\,987 \times 10^{-5}$
RQ6.L1B[12]/K1	$1.252\,269 \times 10^{-4}$	$-6.654\,750 \times 10^{-5}$
RQ6.R1B[12]/K1	$2.181\,278 \times 10^{-4}$	$4.843\,161 \times 10^{-5}$
RQ7.L1B[12]/K1	$-1.654\,347 \times 10^{-5}$	$-6.727\,209 \times 10^{-6}$
RQ7.R1B[12]/K1	$-2.380\,601 \times 10^{-5}$	$7.671\,464 \times 10^{-5}$
RQ8.L1B[12]/K1	$4.701\,971 \times 10^{-5}$	$-7.422\,834 \times 10^{-6}$
RQ8.R1B[12]/K1	$-5.166\,308 \times 10^{-5}$	$2.816\,191 \times 10^{-5}$
RQ9.L1B[12]/K1	$1.183\,309 \times 10^{-4}$	$-1.835\,947 \times 10^{-4}$
RQ9.R1B[12]/K1	$1.395\,191 \times 10^{-4}$	$-6.844\,480 \times 10^{-5}$
RQ10.L1B[12]/K1	$-2.470\,503 \times 10^{-5}$	$-1.415\,361 \times 10^{-4}$
RQ10.R1B[12]/K1	$-1.960\,854 \times 10^{-5}$	$-1.257\,251 \times 10^{-4}$

TABLE C.3: Definition of the optics rematching knob for IR1 as implemented in LSA. These settings rematch the optics for a Rigid Waist Shift knob trimmed with a factor 1.

Component	Beam 1 Value	Beam 2 Value
RQ4.L1B[12]/K1	$2.890\,068 \times 10^{-5}$	$5.819\,791 \times 10^{-5}$
RQ4.R1B[12]/K1	$-3.102\,580 \times 10^{-5}$	$1.740\,345 \times 10^{-5}$
RQ5.L1B[12]/K1	$1.794\,669 \times 10^{-5}$	$-2.591\,577 \times 10^{-4}$
RQ5.R1B[12]/K1	$2.076\,919 \times 10^{-4}$	$-5.673\,007 \times 10^{-5}$
RQ6.L1B[12]/K1	$4.143\,969 \times 10^{-5}$	$3.008\,508 \times 10^{-4}$
RQ6.R1B[12]/K1	$-1.848\,040 \times 10^{-4}$	$-6.006\,251 \times 10^{-5}$
RQ7.L1B[12]/K1	$5.634\,562 \times 10^{-5}$	$-3.647\,266 \times 10^{-5}$
RQ7.R1B[12]/K1	$-8.441\,509 \times 10^{-6}$	$5.911\,061 \times 10^{-7}$
RQ8.L1B[12]/K1	$3.582\,289 \times 10^{-5}$	$-1.783\,459 \times 10^{-4}$
RQ8.R1B[12]/K1	$1.446\,909 \times 10^{-4}$	$1.123\,520 \times 10^{-4}$
RQ9.L1B[12]/K1	$-1.056\,186 \times 10^{-4}$	$6.796\,452 \times 10^{-5}$
RQ9.R1B[12]/K1	$-1.686\,284 \times 10^{-4}$	$1.143\,128 \times 10^{-4}$
RQ10.L1B[12]/K1	$-8.416\,329 \times 10^{-5}$	$-1.871\,513 \times 10^{-5}$
RQ10.R1B[12]/K1	$-4.208\,946 \times 10^{-5}$	$4.750\,863 \times 10^{-5}$

TABLE C.4: Definition of the optics rematching knob for IR1 as implemented in LSA. These settings rematch the optics for a Rigid Waist Shift knob trimmed with a factor -1 .

Similarly, [Tables C.5](#) and [C.6](#) show the settings used in [LSA](#) to define the optics rematching knobs needed after applying the Rigid Waist Shift knob, at IR5. [Table C.5](#) gives the settings that rematch the optics when the IR5 RWS knob is trimmed with a factor of 1, while [Table C.6](#) gives the settings that rematch the optics when the IR5 RWS knob is applied with a factor of -1 . These knobs control the independent magnets Q4 to Q10 left and right of the IP for both beams.

Component	Beam 1 Value	Beam 2 Value
RQ4.L5B[12]/K1	$4.732\,644 \times 10^{-5}$	$7.708\,167 \times 10^{-7}$
RQ4.R5B[12]/K1	$2.995\,622 \times 10^{-5}$	$5.229\,277 \times 10^{-5}$
RQ5.L5B[12]/K1	$-1.540\,577 \times 10^{-4}$	$1.320\,986 \times 10^{-4}$
RQ5.R5B[12]/K1	$-1.541\,586 \times 10^{-4}$	$-2.507\,269 \times 10^{-5}$
RQ6.L5B[12]/K1	$8.088\,711 \times 10^{-5}$	$-7.675\,093 \times 10^{-5}$
RQ6.R5B[12]/K1	$9.079\,173 \times 10^{-5}$	$8.686\,051 \times 10^{-5}$
RQ7.L5B[12]/K1	$-5.050\,462 \times 10^{-5}$	$6.267\,658 \times 10^{-6}$
RQ7.R5B[12]/K1	$-2.046\,442 \times 10^{-5}$	$7.702\,426 \times 10^{-5}$
RQ8.L5B[12]/K1	$8.284\,445 \times 10^{-5}$	$1.469\,226 \times 10^{-5}$
RQ8.R5B[12]/K1	$-1.498\,689 \times 10^{-5}$	$6.506\,405 \times 10^{-5}$
RQ9.L5B[12]/K1	$1.330\,684 \times 10^{-4}$	$-1.746\,977 \times 10^{-4}$
RQ9.R5B[12]/K1	$1.770\,079 \times 10^{-4}$	$-7.499\,273 \times 10^{-5}$
RQ10.L5B[12]/K1	$3.745\,423 \times 10^{-6}$	$-1.405\,645 \times 10^{-4}$
RQ10.R5B[12]/K1	$3.122\,093\,9 \times 10^{-5}$	$-1.199\,213 \times 10^{-4}$

TABLE C.5: Definition of the optics rematching knob for IR5 as implemented in LSA. These settings rematch the optics for a Rigid Waist Shift knob trimmed with a factor 1.

Component	Beam 1 Value	Beam 2 Value
RQ4.L5B[12]/K1	$3.261\,927 \times 10^{-5}$	$6.393\,201 \times 10^{-5}$
RQ4.R5B[12]/K1	$-3.059\,847 \times 10^{-5}$	$2.057\,514 \times 10^{-5}$
RQ5.L5B[12]/K1	$1.578\,156 \times 10^{-5}$	$-2.813\,483 \times 10^{-4}$
RQ5.R5B[12]/K1	$2.063\,856 \times 10^{-4}$	$-5.432\,443 \times 10^{-5}$
RQ6.L5B[12]/K1	$2.618\,065 \times 10^{-5}$	$3.291\,553 \times 10^{-4}$
RQ6.R5B[12]/K1	$-1.651\,558 \times 10^{-4}$	$-7.698\,741 \times 10^{-5}$
RQ7.L5B[12]/K1	$6.293\,434 \times 10^{-5}$	$-4.279\,221 \times 10^{-5}$
RQ7.R5B[12]/K1	$-1.308\,196 \times 10^{-5}$	$1.068\,785 \times 10^{-5}$
RQ8.L5B[12]/K1	$1.700\,830 \times 10^{-5}$	$-2.078\,329 \times 10^{-4}$
RQ8.R5B[12]/K1	$1.206\,262 \times 10^{-4}$	$1.153\,268 \times 10^{-4}$
RQ9.L5B[12]/K1	$-9.633\,770 \times 10^{-5}$	$4.971\,278 \times 10^{-5}$
RQ9.R5B[12]/K1	$-1.705\,114 \times 10^{-4}$	$1.199\,293 \times 10^{-4}$
RQ10.L5B[12]/K1	$-8.920\,503 \times 10^{-5}$	$-1.382\,229 \times 10^{-5}$
RQ10.R5B[12]/K1	$-6.293\,434 \times 10^{-5}$	$4.006\,792 \times 10^{-5}$

TABLE C.6: Definition of the optics rematching knob for IR5 as implemented in LSA. These settings rematch the optics for a Rigid Waist Shift knob trimmed with a factor -1 .

APPENDIX D

Negative Rigid Waist Shift Measurements

Results shown in [Section 4.5](#) are from measurements in which the [Rigid Waist Shift \(RWS\) knob](#) was trimmed in with a factor of 1, as defined in [Table 4.2](#). As mentioned in [Appendix C](#) and as can be seen in [Fig. 4.9](#) the knob can be trimmed with an arbitrary factor, shifting the waist of the beams left or right of the [Interaction Point \(IP\)](#).

Measurements have also been conducted in each [Insertion Region \(IR\)](#) with the [RWS](#) knobs trimmed in with a factor of -1 , which we will call a [negative RWS](#). For these, done under time constraints at the end of experimental shifts, some mistakes were made in the experimental setups and the data was deemed inconclusive after analysis. Nonetheless, for completeness these results are included below.

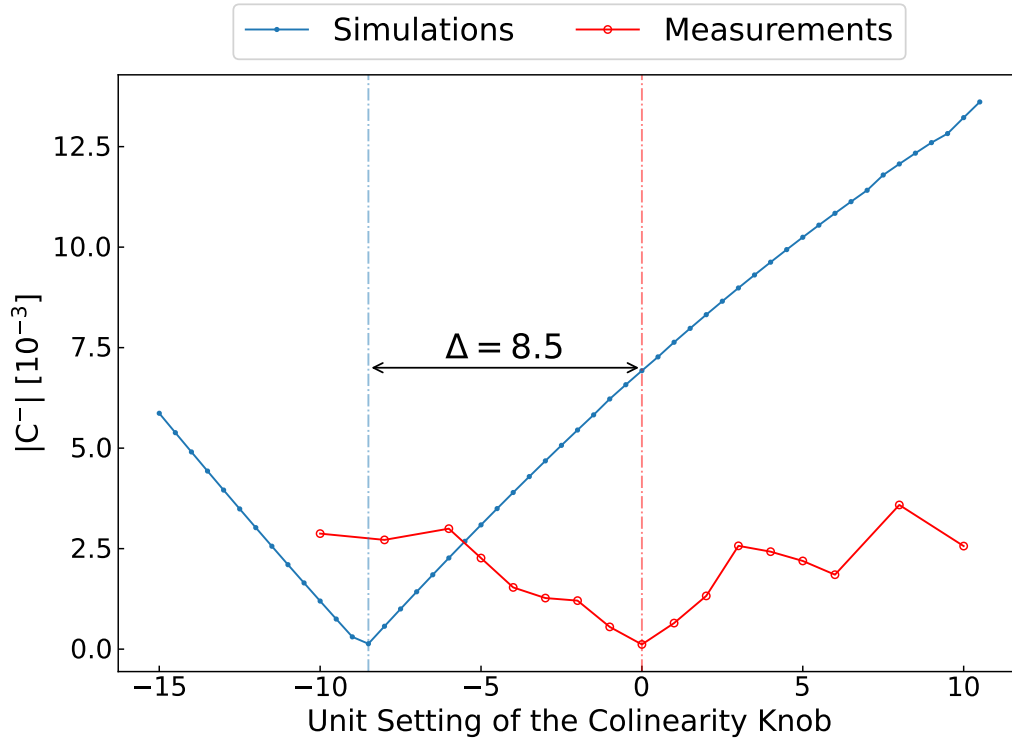


FIGURE D.1: Measurement scan with a negative RWS done at IR1 for beam 1 (red) and simulations for the same setup (blue).

Figure D.1 shows the results of a measurement scan done at IR1 for beam 1 with a negative RWS. When preparing for this scan an issue was encountered when trimming in the optics rematching knob. As the knob had been wrongly designed beforehand, it bypassed the powering limits of the Q6 magnets and thus could only be trimmed in the machine with a factor 0.7 as the LHC protection system would not allow lower currents. As a consequence a strong β -beating remained in the machine and cast doubts on the measurement data. When comparing this measurement to simulations, data suggests a *very* large error to be corrected: 8.5 units of the colinearity knob. This data was discarded when determining corrections.

Figure D.2 shows the results of a measurement scan done at IR1 for beam 2 with a negative RWS. The same issue as mentioned above was encountered, and the knob could only be trimmed in the machine with a factor 0.5, resulting once again in a strong β -beating in the machine during measurements. Comparison with simulations once again suggested a *very* large error to be corrected: 16 units of the colinearity knob, potentially more if the measurement scan was carried on for longer. This data was also discarded when determining corrections.

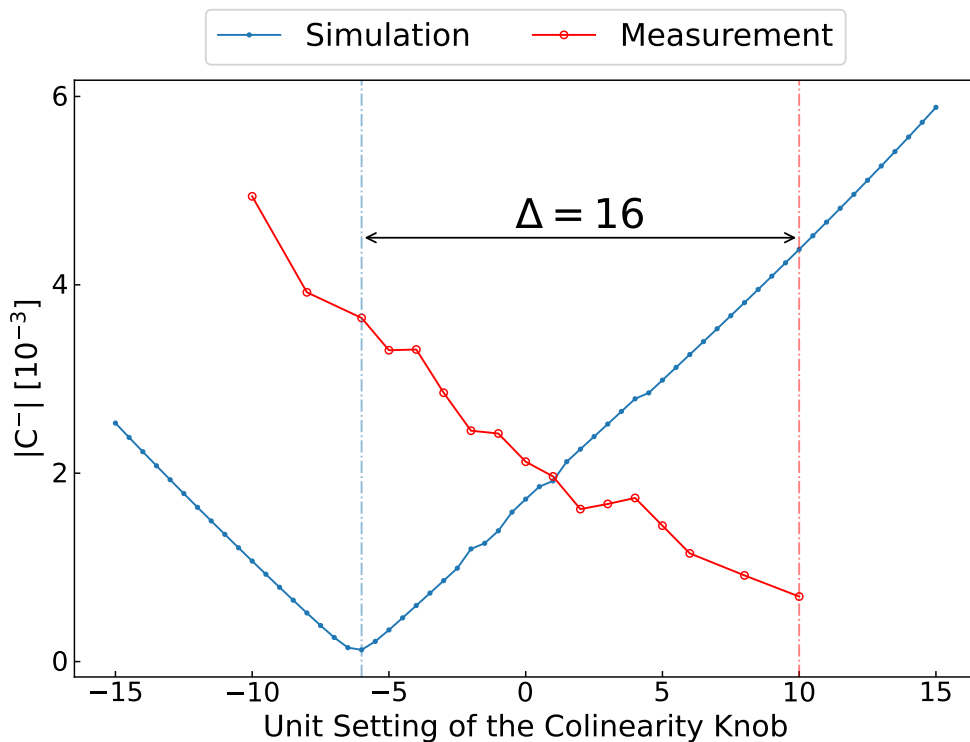


FIGURE D.2: Measurement scan with a negative RWS done at IR1 for beam 2 (red) and simulations for the same setup (blue).

Figure D.3 shows the results of a measurement scan done at IR5 for beam 1 with a negative RWS. During this scan, a mistake was made when trimming the optics rematching knob: the rematching knob from the previous scan was not trimmed out of the machine, and as a result a mix of both knobs was present during the measurements. This led to the experimental setup of the RWS not being properly implemented, and while the measurement data does not suggest an unbelievable correction as in Fig. D.2, the failed experimental setup and suspicious shape of the measurements' $|C^-|$ curve led to this data being discarded when determining corrections.

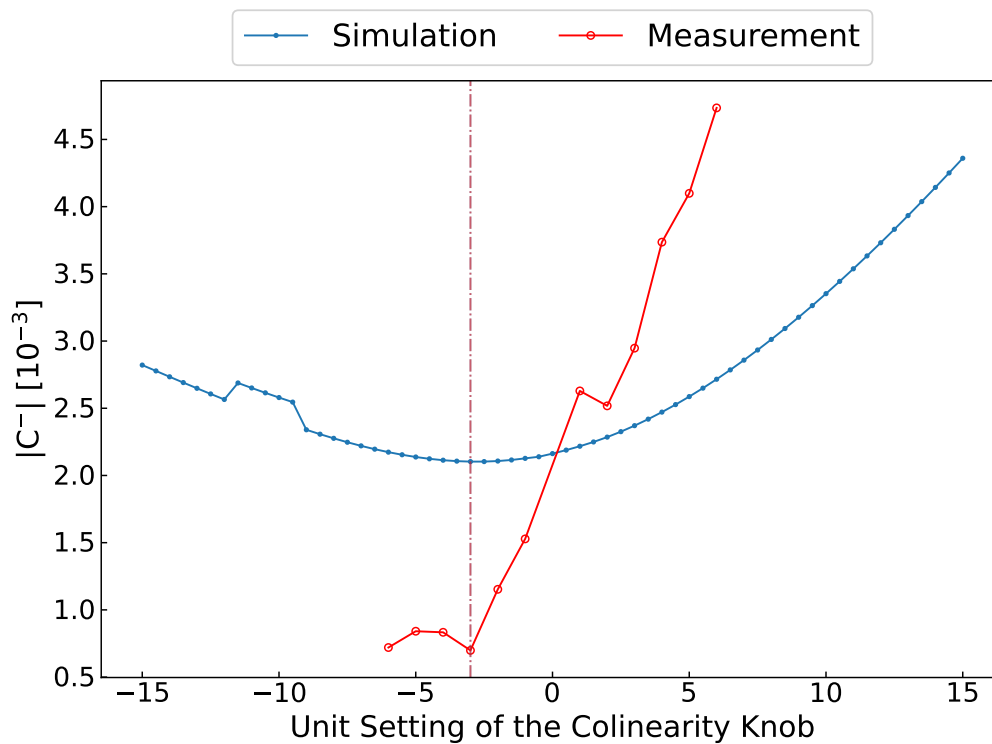


FIGURE D.3: Measurement scan with a negative RWS done at IR5 for beam 1 (red) and simulations for the same setup (blue).

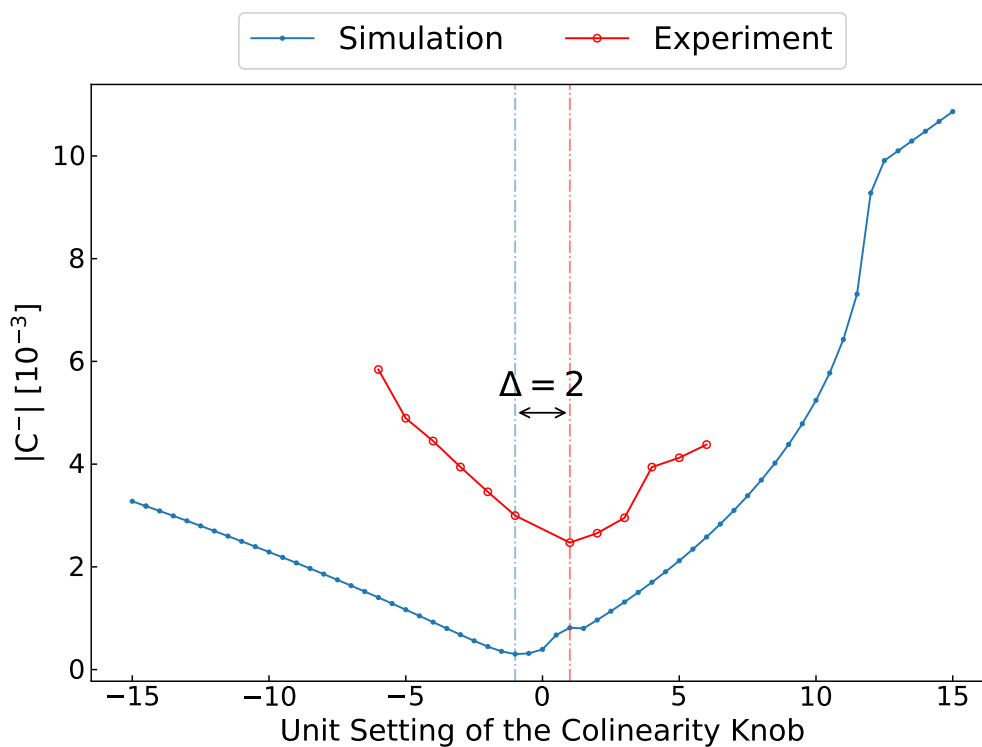


FIGURE D.4: Measurement scan with a negative RWS done at IR5 for beam 1 (red) and simulations for the same setup (blue).

Figure D.4 shows the results of a measurement scan done at IR5 for beam 1 with a negative RWS. For this measurement scan, no mistake was made in the experimental setup and the data suggests a correction similar to what was found with the scans presented in Section 4.5.2 (see Table 4.5). The success of this measurement clears some doubts on the validity of the negative RWS.

Overall, a combination of human mistakes both during the preparation of the experimental setup and during the measurement scans themselves led to the inconclusive measurements of Figs. D.1 to D.3.

APPENDIX E

List of LHC Fills Used for Measurements

One can find in this Appendix the fully detailed list of [LHC](#) fills used for the experimental campaign. In each table, the fill number, measurement date, beam energy at the time of measurement, [optics](#) configuration (β^* at IR1 and IR5) and the purpose of the measurement are indicated.

E.1 Fills Used During the LHC Run 2

[Table E.1](#) reports the fills used for the experimental campaign, for measurements taken during the [LHC Run 2](#). These relate to results presented in [Chapter 4](#) and [Chapter 6](#).

Fill #	Date	Energy	IR[15] β^*	Purpose
6537	2018/04/10	6.5 TeV	30 cm	Phase Error Analyses
7493	2018/12/02	6.37 TeV	50 cm	Colinearity Knob MD

TABLE E.1: List of the LHC fills used in the experimental campaign, during the LHC Run 2.

E.2 Fills Used During the 2021 Beam Tests

[Table E.2](#) reports the fills used for the experimental campaign, for measurements taken during the [LHC 2021 beam tests](#). These relate to results presented in [Chapter 4](#).

Fill #	Date	Energy	IR[15] β^*	Purpose
7504	2021/10/20	450 GeV	11 m	SbS Corrections Calculations
7509	2021/10/22	450 GeV	11 m	SbS Corrections Trim

TABLE E.2: List of the LHC fills used in the experimental campaign, during the LHC 2021 beam tests.

E.3 Fills Used During the LHC Run 3 2022 Commissioning

Table E.3 reports the fills used for the experimental campaign, for measurements taken during the LHC Run 3 2022 commissioning. These relate to results presented in Chapter 4.

Fill #	Date	Energy	IR[15] β^*	Purpose
7595	2022/05/09	6.8 TeV	30 cm	SbS Corrections Refinement
7598	2022/05/10	6.8 TeV	30 cm	IR5 Rigid Waist Shift
7682	2022/06/01	6.8 TeV	30 cm	IR1 Rigid Waist Shift

TABLE E.3: List of the LHC fills used in the experimental campaign, during the LHC 2022 commissioning.

E.4 Fills Used During the LHC 2022 Physics Run

Table E.4 reports the fills used for the experimental campaign, for measurements taken during the LHC 2022 physics run. These relate to results presented in Chapter 4.

Fill #	Date	Energy	IR[15] β^*	Purpose
8067	2022/07/29	6.8 TeV	30 cm	IR1 & IR5 RWS Corrections Trim
8072	2022/07/30	6.8 TeV	42 cm	IR1 & IR5 RWS Corrections Trim
8222	2022/10/02	6.8 TeV	30 cm	IR1 & IR5 Colin Knob Carry Over
8256	2022/10/12	6.8 TeV	30 cm	IR1 Colin Knob Carry Over

TABLE E.4: List of the LHC fills used in the experimental campaign, during the LHC 2022 physics Run.

APPENDIX F

Software Developments

In parallel to other works presented in this document, a substantial effort was put into software development to improve both analysis and simulation tools. Below is shown the main software development work done over the course of this PhD. For each software the main contributions are listed and references are provided.

JobSubmitter [243]. Developed with J. Dilly^{id} and M. Hofer^{id}, JobSubmitter is a Python package for easily submitting parametrized studies to the HPC queuing system HTCondor [244] used at CERN. It has quickly been adopted by colleagues due to its simplicity and efficiency.

Omc3 [187]. The omc3 Python package is our main optics analysis and correction software, developed by most members of the OMC team. Many contributions were made in the form of bug fixes, maintenance, translation of old codes to the new version, implementation of new methods or improvements to existing ones, documentation, testing and implementation of CI/CD pipelines.

OMC Documentation [245]. Together with J. Dilly^{id}, we created a website for the OMC team to serve as a wiki, resource collection and entrypoint for team members. It compiles information about the physics behind the OMC activities, experimental procedures, documentation and guides on the team's software, and resources for newcomers.

PyhDToolkit [246]. Initially designed for personal use, PyhDToolkit is a Python package for efficient simulation and visualization with the cpymad [247] and MAD-X [59] codes. It is the software used for all results in this thesis. Its core functionality was extracted into the lightweight cpymadtools [248] package, which has been adopted by colleagues for its clean and efficient API.

PyLHC [249]. Developed with J. Dilly^{id} and M. Hofer^{id}, PyLHC is a Python package holding various complementary scripts and modules to our other softwares. Contributions include knob extraction scripts, data conversion functionality between database and simulation codes formats, and quick analysis of specific measurements.

Pyrws [190]. Created for the [Large Hadron Collider \(LHC\) Run 3](#) commissioning of 2022, pyrws is a Python package to design [Rigid Waist Shift](#) configurations and knobs for any given LHC [optics](#). It was used to prepare the experimental setup leading to the main work in this thesis, described in [Chapter 4](#) and in [Appendix C](#).

Tfs-Pandas [250]. The tfs-pandas Python package is a workhorse of our codes used to handle the Table Format System (TFS) files output by both our simulation codes and analysis software. Significant effort was put into a complete rewrite of the package, speeding up its operation by up to a factor of 100 times, as well as into the addition of quality-of-life features and tests for robustness. This package is very often downloaded as its use is widespread.

Turn-by-Turn [251]. The turn-by-turn Python package handles measurement data from different formats corresponding to various machines. A contribution was made in the form of the extraction of this functionality from old codes and rewriting it to produce a clean API.

Bibliography

- [1] F. Soubelet et al. “Prospect for Interaction Region Local Coupling Correction in the LHC Run 3”. In: *Proceedings of the 12th International Particle Accelerator Conference (IPAC’21)* (Brazil). Vol. IPAC2021. JACoW Publishing, Geneva, Switzerland, 2021. ISBN: 978-3-95450-214-1. DOI: [10.18429/JACOW-IPAC2021-MOPAB007](https://doi.org/10.18429/JACOW-IPAC2021-MOPAB007).
- [2] F. Soubelet et al. “First Interaction Region Local Coupling Corrections in the LHC Run 3”. In: *Proceedings of the 13th International Particle Accelerator Conference (IPAC’22)* (Bangkok, Thailand). Vol. IPAC2022. JACoW Publishing, Geneva, Switzerland, 2022. ISBN: 978-3-95450-227-1. DOI: [10.18429/JACOW-IPAC2022-WEPOPT007](https://doi.org/10.18429/JACOW-IPAC2022-WEPOPT007).
- [3] F. Soubelet et al. “Supervised Machine Learning for Local Coupling Sources Detection in the LHC”. In: *Proceedings of the 13th International Particle Accelerator Conference (IPAC’22)* (Bangkok, Thailand). Vol. IPAC2022. JACoW Publishing, Geneva, Switzerland, 2022. ISBN: 978-3-95450-227-1. DOI: [10.18429/JACOW-IPAC2022-WEPOPT008](https://doi.org/10.18429/JACOW-IPAC2022-WEPOPT008).
- [4] F. Soubelet et al. “Rigid Waist Shift: A New Method for Local Coupling Corrections in the LHC Interaction Regions”. In: *Phys. Rev. ST Accel. Beams* 26 (May 2023). DOI: [10.1103/PhysRevAccelBeams.26.051001](https://doi.org/10.1103/PhysRevAccelBeams.26.051001).
- [5] F. Soubelet et al. “Prospect of Operating with Limited Skew Quadrupole Corrector Availability in the LHC Interaction Regions”. en. In: *Proceedings of the 14th International Particle Accelerator Conference (IPAC’23)* (Venice, Italy). Vol. IPAC2023. JACoW Publishing, Geneva, Switzerland, 2023. ISBN: 978-3-95450-231-8. DOI: [10.18429/JACoW-IPAC-23-MOPL044](https://doi.org/10.18429/JACoW-IPAC-23-MOPL044).
- [6] F. Carlier et al. “LHC Run 2 Optics Commissioning Experience in View of HL-LHC”. In: *Proceedings of the 10th International Particle Accelerator Conference (IPAC’19)* (Melbourne, Australia). JACoW Publishing, Geneva, Switzerland, June 2019. ISBN: 978-3-95450-208-0. DOI: [10.18429/JACoW-IPAC2019-MOPMP033](https://doi.org/10.18429/JACoW-IPAC2019-MOPMP033).
- [7] R. Tracey et al. “AI-Driven Holistic Approach to Energy Efficient HPC”. In: *High Performance Computing, ISC High Performance 2020 International Workshops* (Frankfurt, Germany). Springer International Publishing, 2020. ISBN: 978-3-030-59851-8. DOI: [10.1007/978-3-030-59851-8_17](https://doi.org/10.1007/978-3-030-59851-8_17).
- [8] G. Apollinari et al. *High-Luminosity Large Hadron Collider (HL-LHC) Technical Design Report*. 2020. URL: <https://cds.cern.ch/record/2749422>.

- [9] T. Persson et al. “Optics Correction Strategy for Run 3 of the LHC”. In: *Proceedings of the 12th International Particle Accelerator Conference (IPAC'21)* (Brazil). Vol. IPAC2021. JACoW Publishing, Geneva, Switzerland, 2021. ISBN: 978-3-95450-214-1. DOI: [10.18429/JACOW-IPAC2021-WEPAB027](https://doi.org/10.18429/JACOW-IPAC2021-WEPAB027).
- [10] E. H. Maclean et al. “Optics Measurement by Excitation of Betatron Oscillations in the CERN PSB”. In: *Proceedings of the 12th International Particle Accelerator Conference (IPAC'21)* (Brazil). Vol. IPAC2021. JACoW Publishing, Geneva, Switzerland, 2021. ISBN: 978-3-95450-214-1. DOI: [10.18429/JACOW-IPAC2021-THPAB168](https://doi.org/10.18429/JACOW-IPAC2021-THPAB168).
- [11] T. Persson et al. “Optics Measurements and Correction Plans for the HL-LHC”. In: *Proceedings of the 12th International Particle Accelerator Conference (IPAC'21)* (Brazil). Vol. IPAC2021. JACoW Publishing, Geneva, Switzerland, 2021. ISBN: 978-3-95450-214-1. DOI: [10.18429/JACOW-IPAC2021-WEPAB026](https://doi.org/10.18429/JACOW-IPAC2021-WEPAB026).
- [12] X. Buffat et al. *Optics Measurement and Correction Strategies for HL-LHC*. Tech. rep. Geneva: CERN, 2022. URL: <http://cds.cern.ch/record/2808650>.
- [13] T. Persson et al. “Optics Correction Strategy for Run 3 of the LHC”. In: *Proceedings of the 13th International Particle Accelerator Conference (IPAC'22)* (Bangkok, Thailand). Vol. IPAC2022. JACoW Publishing, Geneva, Switzerland, 2022. ISBN: 978-3-95450-227-1. DOI: [10.18429/JACOW-IPAC2022-WEPOST008](https://doi.org/10.18429/JACOW-IPAC2022-WEPOST008).
- [14] E. Fol et al. “Experimental Demonstration of Machine Learning Application in LHC Optics Commissioning”. In: *Proceedings of the 13th International Particle Accelerator Conference (IPAC'22)* (Bangkok, Thailand). Vol. IPAC2022. JACoW Publishing, Geneva, Switzerland, 2022. ISBN: 978-3-95450-227-1. DOI: [10.18429/JACOW-IPAC2022-MOPOPT047](https://doi.org/10.18429/JACOW-IPAC2022-MOPOPT047).
- [15] F. Carlier et al. “Challenges of k-Modulation Measurements in the LHC Run 3”. In: *Proceedings of the 14th International Particle Accelerator Conference (IPAC'23)* (Venice, Italy). Vol. IPAC2023. JACoW Publishing, Geneva, Switzerland, 2023. ISBN: 978-3-95450-231-8. DOI: [10.18429/JACOW-IPAC2023-MOPL014](https://doi.org/10.18429/JACOW-IPAC2023-MOPL014).
- [16] F. Carlier et al. “LHC Run 3 Optics Correction”. en. In: *Proceedings of the 14th International Particle Accelerator Conference (IPAC'23)* (Venice, Italy). Vol. IPAC2023. JACoW Publishing, Geneva, Switzerland, 2023. ISBN: 978-3-95450-231-8. DOI: [10.18429/JACOW-IPAC2023-MOPL015](https://doi.org/10.18429/JACOW-IPAC2023-MOPL015).
- [17] J. Dilly et al. “First Operational Dodecapole Correction in the LHC”. In: *Phys. Rev. ST Accel. Beams* 26 (Dec. 2023). DOI: [10.1103/PhysRevAccelBeams.26.121001](https://doi.org/10.1103/PhysRevAccelBeams.26.121001).
- [18] E. Lawrence and M. Livingston. “The Production of High Speed Light Ions Without the Use of High Voltages”. In: *Phys. Rev.* 40 (Apr. 1932). DOI: [10.1103/PhysRev.40.19](https://doi.org/10.1103/PhysRev.40.19).
- [19] J. D. Cockcroft and E. T. S. Walton. “Disintegration of Lithium by Swift Protons”. In: *Nature* 129 (Apr. 1932). DOI: [10.1038/129649a0](https://doi.org/10.1038/129649a0).

- [20] J. D. Cockcroft and E. T. S. Walton. “Experiments with High Velocity Positive Ions (I) - Further Developments in the Method of Obtaining High Velocity Positive Ions”. In: *Proceedings of the Royal Society of London. Series A, Containing Papers of a Mathematical and Physical Character* 136 (June 1932). DOI: [10.1098/rspa.1932.0107](https://doi.org/10.1098/rspa.1932.0107).
- [21] J. D. Cockcroft and E. T. S. Walton. “Experiments with High Velocity Positive Ions (II) - The Disintegration of Elements by High Velocity Protons”. In: *Proceedings of the Royal Society of London. Series A, Containing Papers of a Mathematical and Physical Character* 137 (July 1932). DOI: [10.1098/rspa.1932.0133](https://doi.org/10.1098/rspa.1932.0133).
- [22] ATLAS Collaboration. “Observation of a New Particle in the Search for the Standard Model Higgs Boson with the ATLAS Detector at the LHC”. In: *Physics Letters B* 716 (Sept. 2012). DOI: [10.1016/j.physletb.2012.08.020](https://doi.org/10.1016/j.physletb.2012.08.020).
- [23] CMS Collaboration. “Observation of a New Boson at a Mass of 125 GeV with the CMS Experiment at the LHC”. In: *Physics Letters B* 716 (Sept. 2012). DOI: [10.1016/j.physletb.2012.08.021](https://doi.org/10.1016/j.physletb.2012.08.021).
- [24] P. Higgs. “Broken Symmetries and the Masses of Gauge Bosons”. In: *Phys. Rev. Lett.* 13 (Oct. 1964). DOI: [10.1103/PhysRevLett.13.508](https://doi.org/10.1103/PhysRevLett.13.508).
- [25] F. Englert and R. Brout. “Broken Symmetry and the Mass of Gauge Vector Mesons”. In: *Phys. Rev. Lett.* 13 (Aug. 1964). DOI: [10.1103/PhysRevLett.13.321](https://doi.org/10.1103/PhysRevLett.13.321).
- [26] *High Luminosity LHC Project Website*. 2023. URL: <https://hilumilhc.web.cern.ch>.
- [27] *LIV.DAT Website*. 2023. URL: <https://www.liverpool.ac.uk/livdat/>.
- [28] E. Wilson. *An Introduction to Particle Accelerators*. Oxford University Press, May 2006. ISBN: 9780198508298. DOI: [10.1093/acprof:oso/9780198508298.001.0001](https://doi.org/10.1093/acprof:oso/9780198508298.001.0001).
- [29] S. Y. Lee. *Accelerator Physics*. 3rd ed. World Scientific, 2011. DOI: [10.1142/11111](https://doi.org/10.1142/11111).
- [30] H. Wiedemann. *Particle Accelerator Physics*. Springer International Publishing, 2015. DOI: [10.1007/978-3-319-18317-6](https://doi.org/10.1007/978-3-319-18317-6).
- [31] M. G. Minty and F. Zimmermann. *Measurement and Control of Charged Particle Beams*. Springer Berlin Heidelberg, 2003. ISBN: 978-3-662-08581-3. DOI: [10.1007/978-3-662-08581-3](https://doi.org/10.1007/978-3-662-08581-3).
- [32] A. Wolski. *Beam Dynamics in High Energy Particle Accelerators*. 2nd ed. Imperial College Press, 2014. DOI: [10.1142/p899](https://doi.org/10.1142/p899).
- [33] A. Chao et al. *Handbook of Accelerator Physics and Engineering*. 3rd ed. World Scientific, 2023. ISBN: 978-981-127-015-4. DOI: [10.1142/13229](https://doi.org/10.1142/13229).
- [34] A. Chao. *Physics of Collective Beam Instabilities in High Energy Accelerators*. Wiley-Interscience, 1993. ISBN: 9780471551843. URL: <https://www.slac.stanford.edu/~achao/wileybook.html>.
- [35] S. Russenschuck. *Design of Accelerator Magnets*. Tech. rep. 2005. DOI: [10.5170/CERN-2005-004.118](https://doi.org/10.5170/CERN-2005-004.118).

- [36] R. Q. Twiss and N. H. Frank. “Orbital Stability in a Proton Synchrotron”. In: *Review of Scientific Instruments* 20 (Jan. 1949). DOI: [10.1063/1.1741343](https://doi.org/10.1063/1.1741343).
- [37] E.D. Courant and H.S. Snyder. “Theory of the Alternating-Gradient Synchrotron”. In: *Annals of Physics* 3 (1958). ISSN: 0003-4916. DOI: [10.1016/0003-4916\(58\)90012-5](https://doi.org/10.1016/0003-4916(58)90012-5).
- [38] A. Müller. *Description of Beam-Matter Interaction in the Covariance Matrix Formalism: Application to Modification of Emittance and Twiss Parameters*. Tech. rep. CERN, 2001. URL: <https://cds.cern.ch/record/499590>.
- [39] J. Buon. “Beam Phase Space and Emittance”. In: *CAS - CERN Accelerator School : 5th General Accelerator Physics Course* (1992). DOI: [10.5170/CERN-1994-001.89](https://doi.org/10.5170/CERN-1994-001.89).
- [40] A. Bazzanirmando et al. *A Normal Form Approach to the Theory of Nonlinear Betatronic Motion*. CERN Yellow Reports: Monographs. Geneva: CERN, 1994. DOI: [10.5170/CERN-1994-002](https://doi.org/10.5170/CERN-1994-002).
- [41] F. Carlier. “A Nonlinear Future: Measurements and Corrections of Nonlinear Beam Dynamics Using Forced Transverse Oscillations”. Presented 2020. Amsterdam University, 2020. ISBN: 9789464022148. URL: <https://cds.cern.ch/record/2715765/files/CERN-THESIS-2020-025.pdf>.
- [42] S. Guiducci. “Chromaticity”. In: *CAS - CERN Accelerator School : 5th General Accelerator Physics Course* (1992). DOI: [10.5170/CERN-1994-001.191](https://doi.org/10.5170/CERN-1994-001.191).
- [43] R. Tomás. “Direct Measurement of Resonance Driving Terms in the Super Proton Synchrotron (SPS) of CERN using Beam Position Monitors”. Presented on 30 Mar 2003. Universitat de València, 2003. URL: <https://cds.cern.ch/record/615164>.
- [44] A. Franchi. “Studies and Measurements of Linear Coupling and Nonlinearities in Hadron Circular Accelerators”. Presented 2006. Johann Wolfgang Goethe-Universität, 2006. URL: <https://d-nb.info/981264875/34>.
- [45] E. H. Maclean. “Modelling and correction of the non-linear transverse dynamics of the LHC from beam-based measurements”. Presented 2014. Herford College, University of Oxford, 2014. URL: <https://cds.cern.ch/record/1951379>.
- [46] T. Persson. “Beam-Based Error Identification and Correction Methods for Particle Accelerators”. Presented on 10 Jun 2014. Chalmers University of Technology, 2014. URL: <https://cds.cern.ch/record/2054059>.
- [47] A. Franchi et al. “First Simultaneous Measurement of Sextupolar and Octupolar Resonance Driving Terms in a Circular Accelerator from Turn-by-Turn Beam Position Monitor Data”. In: *Phys. Rev. ST Accel. Beams* 17 (July 2014). DOI: [10.1103/PhysRevSTAB.17.074001](https://doi.org/10.1103/PhysRevSTAB.17.074001).
- [48] E. Forest. “A Hamiltonian-Free Description of Single Particle Dynamics for Hopelessly Complex Periodic Systems”. In: *Journal of Mathematical Physics* 31 (May 1990). DOI: [10.1063/1.528795](https://doi.org/10.1063/1.528795).
- [49] B. Hall. *Lie Groups, Lie Algebras, and Representations: An Elementary Introduction*. 2nd ed. Graduate Texts in Mathematics. Cham, Switzerland: Springer International Publishing, May 2015. DOI: [10.1007/978-3-319-13467-3](https://doi.org/10.1007/978-3-319-13467-3).

- [50] R. Bartolini and F. Schmidt. *Normal Form via Tracking or Beam Data*. Tech. rep. 1998. URL: <https://cds.cern.ch/record/333077>.
- [51] J. Bengtsson. “Non-linear transverse dynamics for storage rings with applications to the low-energy antiproton ring (LEAR) at CERN”. Presented on 1 Aug 1988. Lund University, 1988. DOI: [10.5170/CERN-1988-005](https://doi.org/10.5170/CERN-1988-005). URL: <http://cds.cern.ch/record/190442>.
- [52] A. Franchi, E. Métral, and R. Tomás. “Emittance Sharing and Exchange Driven by Linear Betatron Coupling in Circular Accelerators”. In: *Phys. Rev. ST Accel. Beams* 10 (June 2007). DOI: [10.1103/PhysRevSTAB.10.064003](https://doi.org/10.1103/PhysRevSTAB.10.064003).
- [53] G. Ripken and F. Willeke. “On the Impact of Linear Coupling on Nonlinear Dynamics”. In: *Part. Accel.* 27 (1990). URL: <https://cds.cern.ch/record/204506>.
- [54] F. Soubelet. “Towards an LHC Octupole Optics model for PyHEADTAIL”. Presented 25 Sep 2017. Grenoble Institute of Technology - Phelma, 2017.
- [55] L. R. Carver et al. “Transverse Beam Instabilities in the Presence of Linear Coupling in the Large Hadron Collider”. In: *Phys. Rev. ST Accel. Beams* 21 (Apr. 2018). DOI: [10.1103/PhysRevAccelBeams.21.044401](https://doi.org/10.1103/PhysRevAccelBeams.21.044401).
- [56] D. A. Edwards and L. C. Teng. “Parametrization of Linear Coupled Motion in Periodic Systems”. In: *IEEE Transactions on Nuclear Science* 20 (1973). DOI: [10.1109/TNS.1973.4327279](https://doi.org/10.1109/TNS.1973.4327279).
- [57] F. Willeke and G. Ripken. “Methods of Beam Optics”. In: AIP, 1989. DOI: [10.1063/1.38050](https://doi.org/10.1063/1.38050).
- [58] A. Wolski. *Dynamical Maps for Linear Elements*. Cockcroft Institute. 2012. URL: <https://www.cockcroft.ac.uk/wp-content/uploads/2014/12/wolski-4.pdf>.
- [59] H. Grote and F.C. Iselin. *The MAD Program*. Tech. rep. CERN, 2016. URL: http://mad.web.cern.ch/mad/madx.old/PTC_proper/special_papers/madX_latest/doc/mad8usrguide/maduser.pdf.
- [60] G. Ripken. *Untersuchungen zur Strahlführung und Stabilität der Teilchenbewegung in Beschleunigern und Storage-Ringen unter strenger Berücksichtigung einer Kopplung der Betatronschwingungen*. Tech. rep. DESY, 1970.
- [61] I. Borchardt et al. “Calculation of Beam Envelopes in Storage Rings and Transport Systems in the Presence of Transverse Space Charge Effects and Coupling”. In: *Zeitschrift für Physik C Particles and Fields* (1988). DOI: [10.1007/BF01548283](https://doi.org/10.1007/BF01548283).
- [62] V. A. Lebedev and S. A. Bogacz. “Betatron Motion with Coupling of Horizontal and Vertical Degrees of Freedom”. In: *Journal of Instrumentation* (2010). DOI: [10.1088/1748-0221/5/10/p10010](https://doi.org/10.1088/1748-0221/5/10/p10010).
- [63] F. Schmidt, E. Forest, and E. McIntosh. *Introduction to the Polymorphic Tracking Code: Fibre Bundles, Polymorphic Taylor Types and "Exact Tracking"*. Tech. rep. Geneva: CERN, 2002. URL: <https://cds.cern.ch/record/573082>.

- [64] Y. Cai. “Luminosity of Asymmetric e+e- Collider with Coupling Lattices”. In: *Proceedings of EPAC 2000* (Vienna, Austria). JACoW Publishing, Geneva, Switzerland, 2000. URL: <https://accelconf.web.cern.ch/e00/PAPERS/MOP5B10.pdf>.
- [65] G. Guignard. “Betatron Coupling and Related Impact of Radiation”. In: *Phys. Rev. E* 51 (June 1995). DOI: [10.1103/PhysRevE.51.6104](https://doi.org/10.1103/PhysRevE.51.6104).
- [66] P. Bryant. “A Simple Theory for Weak Betatron Coupling”. In: *CAS - CERN Accelerator School : 5th General Accelerator Physics Course* (1992). DOI: [10.5170/CERN-1994-001.207](https://doi.org/10.5170/CERN-1994-001.207).
- [67] J. Keintzel. “Beam Optics Design, Measurement and Correction Strategies for Circular Colliders at the Energy and Luminosity Frontier”. Presented 2022. Vienna University of Technology, 2022. URL: <https://cds.cern.ch/record/2804868>.
- [68] T. Persson and R. Tomás. “Improved Control of the Betatron Coupling in the Large Hadron Collider”. In: *Phys. Rev. ST Accel. Beams* 17 (May 2014). DOI: [10.1103/PhysRevSTAB.17.051004](https://doi.org/10.1103/PhysRevSTAB.17.051004).
- [69] W. Herr and B. Muratori. “Concept of Luminosity”. In: *CAS - CERN Accelerator School : Intermediate Course on Accelerator Physics* (2006). DOI: [10.5170/CERN-2006-002.361](https://doi.org/10.5170/CERN-2006-002.361).
- [70] M. Hostettler. *LHC Luminosity Lifetime*. 2012. URL: https://lhc-beam-operation-committee.web.cern.ch/minutes/Meeting52-30_10_2012/LBOC_LumiLifetimeADT.pdf.
- [71] F. Landua. *The CERN Accelerator Complex Layout in 2022. Complexe des Accélérateurs du CERN en Janvier 2022*. 2022. URL: <https://cds.cern.ch/record/2813716>.
- [72] The ATLAS Collaboration. “The ATLAS Experiment at the CERN Large Hadron Collider”. In: *Journal of Instrumentation* 3 (Aug. 2008). DOI: [10.1088/1748-0221/3/08/s08003](https://doi.org/10.1088/1748-0221/3/08/s08003).
- [73] *ATLAS Experiment Website*. 2022. URL: <https://atlas.cern>.
- [74] *CERN Document Server: ATLAS*. 2022. URL: <https://cds.cern.ch/collection/ATLAS>.
- [75] The ALICE Collaboration. “The ALICE Experiment at the CERN LHC”. In: *Journal of Instrumentation* 3 (Aug. 2008). DOI: [10.1088/1748-0221/3/08/s08002](https://doi.org/10.1088/1748-0221/3/08/s08002).
- [76] *ALICE Experiment Website*. 2022. URL: <https://alice.cern>.
- [77] *CERN Document Server: ALICE*. 2022. URL: <https://cds.cern.ch/collection/ALICE>.
- [78] The CMS Collaboration. “The CMS experiment at the CERN LHC”. In: *Journal of Instrumentation* 3 (Aug. 2008). DOI: [10.1088/1748-0221/3/08/s08004](https://doi.org/10.1088/1748-0221/3/08/s08004).
- [79] *CMS Experiment Website*. 2022. URL: <https://cms.cern>.
- [80] *CERN Document Server: CMS*. 2022. URL: <https://cds.cern.ch/collection/CMS>.

- [81] The LHCb Collaboration. “The LHCb Detector at the LHC”. In: *Journal of Instrumentation* 3 (Aug. 2008). DOI: [10.1088/1748-0221/3/08/s08005](https://doi.org/10.1088/1748-0221/3/08/s08005).
- [82] *LHCb Experiment Website*. 2022. URL: <https://lhcb.web.cern.ch>.
- [83] *CERN Document Server: LHCb*. 2022. URL: <https://cds.cern.ch/collection/LHCb>.
- [84] The LHCf Collaboration. “The LHCf Detector at the CERN Large Hadron Collider”. In: *Journal of Instrumentation* 3 (Aug. 2008). DOI: [10.1088/1748-0221/3/08/s08006](https://doi.org/10.1088/1748-0221/3/08/s08006).
- [85] *LHCf Experiment Page*. 2022. URL: <https://home.cern/science/experiments/lhcf>.
- [86] *CERN Document Server: LHCf*. 2022. URL: <https://cds.cern.ch/collection/LHCf>.
- [87] C. Alpigiani et al. *A Letter of Intent for MATHUSLA: A Dedicated Displaced Vertex Detector Above ATLAS or CMS*. Tech. rep. Geneva: CERN, 2018. eprint: [1811.00927](https://cds.cern.ch/record/2631491). URL: <https://cds.cern.ch/record/2631491>.
- [88] *MATHUSLA Experiment Page*. 2023. URL: <https://mathusla-experiment.web.cern.ch/>.
- [89] *CERN Document Server: MATHUSLA*. 2023. URL: <https://cds.cern.ch/search&sc=1&p=MATHUSLA>.
- [90] J. L. Feng et al. “ForwArd Search ExpeRiment at the LHC”. In: *Phys. Rev. D* 97 (Feb. 2018). DOI: [10.1103/PhysRevD.97.035001](https://doi.org/10.1103/PhysRevD.97.035001).
- [91] *FASER Experiment Website*. 2023. URL: <https://faser.web.cern.ch/>.
- [92] *CERN Document Server: FASER*. 2023. URL: <https://cds.cern.ch/collection/FASER>.
- [93] The SND Collaboration. *Scattering and Neutrino Detector at the LHC*. Tech. rep. Geneva: CERN, 2020. URL: <https://cds.cern.ch/record/2729015>.
- [94] *SND Experiment Page*. 2023. URL: <https://snd-lhc.web.cern.ch/>.
- [95] *CERN Document Server: SND*. 2023. URL: <https://cds.cern.ch/search&sc=1&p=SND>.
- [96] The TOTEM Collaboration. “The TOTEM Experiment at the CERN Large Hadron Collider”. In: *Journal of Instrumentation* 3 (Aug. 2008). DOI: [10.1088/1748-0221/3/08/s08007](https://doi.org/10.1088/1748-0221/3/08/s08007).
- [97] *TOTEM Experiment Page*. 2022. URL: <https://totem.web.cern.ch/Totem>.
- [98] *CERN Document Server: TOTEM*. 2022. URL: <https://cds.cern.ch/collection/TOTEM>.
- [99] J. L. Pinfold. “The MoEDAL Experiment - Searching for Highly Ionizing Particles at the LHC”. In: *NATO Science for Peace and Security Series B: Physics and Biophysics*. Springer Netherlands, 2009. DOI: [10.1007/978-90-481-2287-5_21](https://doi.org/10.1007/978-90-481-2287-5_21).
- [100] *MOEDAL Experiment Page*. 2022. URL: <https://moedal.web.cern.ch>.
- [101] *CERN Document Server: MOEDAL*. 2022. URL: <https://cds.cern.ch/collection/MoEDAL>.

- [102] A. Poyet. “Beam-Beam Long-Range Wire Compensation For Enhancing CERN LHC Performance.” Presented 18 May 2021. Université Grenoble-Alpes, 2021. URL: <https://cds.cern.ch/record/2773329>.
- [103] O. Brüning et al. *LHC Design Report v.1: the LHC Main Ring*. CERN Yellow Reports: Monographs. Geneva: CERN, 2004. DOI: [10.5170/CERN-2004-003-V-1](https://doi.org/10.5170/CERN-2004-003-V-1).
- [104] O. Brüning et al. *LHC Design Report v.2: the LHC Infrastructure and General Services*. CERN Yellow Reports: Monographs. Geneva: CERN, 2004. DOI: [10.5170/CERN-2004-003-V-2](https://doi.org/10.5170/CERN-2004-003-V-2).
- [105] M. Benedikt et al. *LHC Design Report v.3: the LHC Injector Chain*. CERN Yellow Reports: Monographs. Geneva: CERN, 2004. DOI: [10.5170/CERN-2004-003-V-3](https://doi.org/10.5170/CERN-2004-003-V-3). URL: <https://cds.cern.ch/record/823808>.
- [106] J. Keintzel. “Optics Design and Performance Aspects of the HE-LHC”. Presented 2018. Vienna University of Technology, 2018. URL: <https://cds.cern.ch/record/2640684>.
- [107] R. Ostojic and T. Taylor. *Proposal for an Improved Optical and Systems Design of the LHC Low- β Triplets*. Tech. rep. Geneva: CERN, 1994. URL: <https://cds.cern.ch/record/273752/files/at-94-038.pdf>.
- [108] T. D’Amico and G. Guignard. *Analysis of Generic Insertions Made of Two Symmetric Triplets*. Tech. rep. Geneva: CERN, 1998. URL: <https://cds.cern.ch/record/363832>.
- [109] F. Bordry and H. Thiesen. “LHC Inner Triplet Powering Strategy”. In: (Chicago, Illinois, USA). JACoW Publishing, Geneva, Switzerland, 2001. ISBN: 0-7803-7191-7. URL: <https://accelconf.web.cern.ch/p01/PAPERS/ROPB012.PDF>.
- [110] O. Brüning et al. *Dynamic Aperture Studies for the LHC Separation Dipoles*. Tech. rep. Geneva: CERN, 2004. URL: <https://cds.cern.ch/record/742967>.
- [111] G. Vanbavinckhove. “Optics Measurements and Corrections for Colliders and Other Storage Rings”. Presented on 16 Jan 2013. Amsterdam University, 2013. URL: <https://cds.cern.ch/record/1533084>.
- [112] S. Fartoukh. *An Achromatic Telescopic Squeezing (ATS) Scheme For The LHC Upgrade*. Tech. rep. Geneva: CERN, 2011. URL: <https://cds.cern.ch/record/1382077>.
- [113] S. Fartoukh. “Achromatic Telescopic Squeezing Scheme and Application to the LHC and its Luminosity Upgrade”. In: *Phys. Rev. ST Accel. Beams* 16 (Nov. 2013). DOI: [10.1103/PhysRevSTAB.16.111002](https://doi.org/10.1103/PhysRevSTAB.16.111002).
- [114] M. Pojer et al. “LHC Operational Experience of the 6.5 TeV Proton Run with ATS Optics”. In: *Proceedings of the 9th International Particle Accelerator Conference (IPAC’18)* (Vancouver, BC, Canada). JACoW Publishing, Geneva, Switzerland, June 2018. ISBN: 978-3-95450-184-7. DOI: [10.18429/JACoW-IPAC2018-MOPMF050](https://doi.org/10.18429/JACoW-IPAC2018-MOPMF050).
- [115] S. Fartoukh et al. *Round Telescopic Optics with Large Telescopic Index*. Tech. rep. Geneva: CERN, 2018. URL: <https://cds.cern.ch/record/2643258>.

- [116] J. Wenninger, M. Lamont, and S. Page. *Functional Specification: LHC Modes*. Tech. rep. CERN, 2019. URL: <https://edms.cern.ch/ui/file/1070479/2.1/LHC-OP-ES-0022-V2.1.pdf>.
- [117] L. Bottura et al. *Pre-Cycles of the LHC Magnets During Operation*. Tech. rep. Geneva: CERN, 2010. URL: <https://cds.cern.ch/record/1283477>.
- [118] R. Bailey and P. Collier. *Standard Filling Schemes for Various LHC Operation Modes*. Geneva, Switzerland: CERN, 2003. URL: http://cds.cern.ch/record/691782/files/project-note-323_v1.pdf.
- [119] M. Solfaroli Camillocci et al. “Combined Ramp and Squeeze to 6.5 TeV in the LHC”. In: *Proceedings of the 7th International Particle Accelerator Conference (IPAC’16)* (Busan, Korea). Vol. IPAC2016. JACoW, 2016. ISBN: 978-3-95450-147-2. DOI: [10.18429/JACoW-IPAC2016-TUPMW031](https://doi.org/10.18429/JACoW-IPAC2016-TUPMW031).
- [120] S. Fartoukh et al. *LHC Configuration and Operational Scenario for Run 3*. Tech. rep. Geneva: CERN, 2021. URL: <https://cds.cern.ch/record/2790409>.
- [121] G. Ferlin et al. “Cryogenics Experience During Run 2 and Impact of LS2 on Next Run”. In: *Proceedings of the 9th LHC Evian Workshop on Beam Operations*. CERN. 2019. URL: <https://cds.cern.ch/record/2706427/>.
- [122] O. Brüning and S. Fartoukh. *Field Quality Specification for the LHC Main Dipole Magnets*. Tech. rep. Geneva: CERN, 2001. URL: <https://cds.cern.ch/record/522049>.
- [123] R. Tomás et al. “Record Low β -Beating in the LHC”. In: *Phys. Rev. ST Accel. Beams* (2012). DOI: [10.1103/PhysRevSTAB.15.091001](https://doi.org/10.1103/PhysRevSTAB.15.091001).
- [124] T. Persson et al. “LHC Optics Commissioning: A journey Towards 1% Optics Control”. In: *Phys. Rev. ST Accel. Beams* (June 2017). DOI: [10.1103/PhysRevAccelBeams.20.061002](https://doi.org/10.1103/PhysRevAccelBeams.20.061002).
- [125] A. Boccardi et al. *An overview of the LHC Transverse Diagnostics Systems*. Tech. rep. Geneva: CERN, 2009. URL: <https://cds.cern.ch/record/1156346>.
- [126] A. Boccardi et al. *First Results from the LHC BBQ Tune and Chromaticity Systems*. Tech. rep. Geneva: CERN, 2009. URL: <https://cds.cern.ch/record/1156349>.
- [127] R. Barlow et al. *Control of the MKQA Tuning and Aperture Kickers of the LHC*. Tech. rep. Geneva: CERN, 2009. URL: <https://cds.cern.ch/record/1232062>.
- [128] E. Carlier, L. Ducimetiere, and E. Vossenberg. “A Kicker Pulse Generator for Measurement of the Tune and Dynamic Aperture in the LHC”. In: *Conference Record of the 2006 Twenty-Seventh International Power Modulator Symposium* (Arlington, VA, USA). 2006. DOI: [10.1109/MODSYM.2006.365284](https://doi.org/10.1109/MODSYM.2006.365284).
- [129] R. Meller et al. *Decoherence of Kicked Beams*. Tech. rep. May 1987. URL: <https://inspirehep.net/files/0af8ccfb6a5da1a4b0a03420d3107115>.
- [130] R. Miyamoto. “Diagnostics of the Fermilab Tevatron Using an AC Dipole”. en. Presented 2008. University of Texas, 2008. URL: <https://repositories.lib.utexas.edu/bitstream/handle/2152/18189/miyamotor70709.pdf>.
- [131] J. Serrano and M. Cattin. *The LHC AC Dipole System: An Introduction*. Tech. rep. Geneva: CERN, 2010. URL: <https://cds.cern.ch/record/1263248>.

- [132] R. Tomás. “Adiabaticity of the Ramping Process of an AC Dipole”. In: *Phys. Rev. ST Accel. Beams* 8 (Feb. 2005). DOI: [10.1103/PhysRevSTAB.8.024401](https://doi.org/10.1103/PhysRevSTAB.8.024401).
- [133] R. Tomás. “Normal Form of Particle Motion Under the Influence of an AC Dipole”. In: *Phys. Rev. ST Accel. Beams* 5 (May 2002). DOI: [10.1103/PhysRevSTAB.5.054001](https://doi.org/10.1103/PhysRevSTAB.5.054001).
- [134] R. Miyamoto et al. “Parametrization of the Driven Betatron Oscillation”. In: *Phys. Rev. ST Accel. Beams* (Aug. 2008). DOI: [10.1103/PhysRevSTAB.11.084002](https://doi.org/10.1103/PhysRevSTAB.11.084002).
- [135] R. Miyamoto et al. “Measurement of Coupling Resonance Driving Terms in the LHC with AC Dipoles”. In: *Proceedings of the 2nd International Particle Accelerator Conference (IPAC'11)* (San Sebastián, Spain). Vol. IPAC2011. JACoW Publishing, Geneva, Switzerland, 2011. URL: <https://accelconf.web.cern.ch/ipac2011/papers/wepc030.pdf>.
- [136] R. Calaga and R. Tomás. “Statistical Analysis of RHIC Beam Position Monitors Performance”. In: *Phys. Rev. ST Accel. Beams* 7 (Apr. 2004). DOI: [10.1103/PhysRevSTAB.7.042801](https://doi.org/10.1103/PhysRevSTAB.7.042801).
- [137] L. Malina. “Novel Beam-Based Correction and Stabilisation Methods for Particle Accelerators”. Presented 21 Nov 2018. University of Oslo, 2018. URL: <https://cds.cern.ch/record/2677131>.
- [138] L. Malina. “Harpy: A Fast, Simple and Accurate Harmonic Analysis with Error Propagation”. In: *Proceedings of the 13th International Particle Accelerator Conference (IPAC'22)* (Bangkok, Thailand). Vol. IPAC2022. JACoW Publishing, Geneva, Switzerland, 2022. ISBN: 978-3-95450-227-1. DOI: [10.18429/JACoW-IPAC2022-WEPOMS035](https://doi.org/10.18429/JACoW-IPAC2022-WEPOMS035).
- [139] E. Fol. et al. “Detection of Faulty Beam Position Monitors Using Unsupervised Learning”. In: *Phys. Rev. ST Accel. Beams* 23 (Oct. 2020). DOI: [10.1103/PhysRevAccelBeams.23.102805](https://doi.org/10.1103/PhysRevAccelBeams.23.102805).
- [140] P. Castro. “Luminosity and Beta Function Measurement at the Electron-Positron Collider Ring LEP”. Presented on 25 Nov 1996. Universitat de València, 1996. URL: <https://cds.cern.ch/record/316609>.
- [141] A. Langner et al. “Utilizing the N Beam Position Monitor Method for Turn-by-Turn Optics Measurements”. In: *Phys. Rev. ST Accel. Beams* 19 (Sept. 2016). DOI: [10.1103/PhysRevAccelBeams.19.092803](https://doi.org/10.1103/PhysRevAccelBeams.19.092803).
- [142] A. Wegscheider et al. “Analytical N Beam Position Monitor Method”. In: *Phys. Rev. ST Accel. Beams* 20 (2017). ISSN: 2469-9888. DOI: [10.1103/PhysRevAccelBeams.20.111002](https://doi.org/10.1103/PhysRevAccelBeams.20.111002).
- [143] A. Langner and R. Tomás. “Optics Measurement Algorithms and Error Analysis for the Proton Energy Frontier”. In: *Phys. Rev. ST Accel. Beams* (Mar. 2015). DOI: [10.1103/PhysRevSTAB.18.031002](https://doi.org/10.1103/PhysRevSTAB.18.031002).
- [144] A. García-Tabarés and R. Tomás. “Optics-Measurement-Based Beam Position Monitor Calibrations in the LHC Insertion Regions”. In: *Phys. Rev. ST Accel. Beams* (Apr. 2020). DOI: [10.1103/PhysRevAccelBeams.23.042801](https://doi.org/10.1103/PhysRevAccelBeams.23.042801).

- [145] L. Malina and J. Coello de Portugal. “Optics Measurements in Storage Rings Based on Simultaneous 3-Dimensional Beam Excitation”. In: *Proceedings of the 9th International Particle Accelerator Conference (IPAC'18)* (Vancouver, BC, Canada). Vol. IPAC2018. JACoW Publishing, Geneva, Switzerland, June 2018. ISBN: 978-3-95450-184-7. DOI: [10.18429/JACoW-IPAC2018-THPAF046](https://doi.org/10.18429/JACoW-IPAC2018-THPAF046).
- [146] R. Calaga, R. Tomás, and F. Zimmermann. “BPM Calibration Independent LHC Optics Correction”. In: *Proceedings of the 22nd Particle Accelerator Conference (PAC'07)* (Albuquerque, New Mexico, USA). JACoW Publishing, Geneva, Switzerland, 2007. ISBN: 1-4244-0917-9. URL: <https://accelconf.web.cern.ch/p07/PAPERS/THPAS091.PDF>.
- [147] R. Calaga et al. “Beta* Measurement in the LHC Based On K-Modulation”. In: *Proceedings of the 2nd International Particle Accelerator Conference (IPAC'11)* (San Sebastián, Spain). Vol. IPAC2011. JACoW Publishing, Geneva, Switzerland, 2011. ISBN: 978-92-9083-366-6. URL: <https://accelconf.web.cern.ch/IPAC2011/papers/TUPZ027.pdf>.
- [148] F. Carlier and R. Tomás. “Accuracy and Feasibility of the β^* Measurement for LHC and High Luminosity LHC Using k Modulation”. In: *Phys. Rev. ST Accel. Beams* 20 (Jan. 2017). DOI: [10.1103/PhysRevAccelBeams.20.011005](https://doi.org/10.1103/PhysRevAccelBeams.20.011005).
- [149] A. Franchi, R. Tomás, and G. Vanbavinckhove. *Computation of the Coupling Resonance Driving term f_{1001} and the Coupling Coefficient C from Turn-by-Turn single-BPM Data*. Tech. rep. Geneva: CERN, 2010. URL: <https://cds.cern.ch/record/1264111>.
- [150] R. Tomás et al. “CERN Large Hadron Collider Optics Model, Measurements, and Corrections”. In: *Phys. Rev. ST Accel. Beams* 13 (Dec. 2010). DOI: [10.1103/PhysRevSTAB.13.121004](https://doi.org/10.1103/PhysRevSTAB.13.121004).
- [151] M. Benedikt et al. “Driving Term Experiments at CERN”. In: *Phys. Rev. ST Accel. Beams* (Mar. 2007). DOI: [10.1103/PhysRevSTAB.10.034002](https://doi.org/10.1103/PhysRevSTAB.10.034002).
- [152] T. Persson et al. “Automatic Correction of Betatron Coupling in the LHC Using Injection Oscillations”. In: *Proceedings of the 4th International Particle Accelerator Conference (IPAC'13)* (Shanghai, China). Vol. IPAC2013. JACoW Publishing, Geneva, Switzerland, 2013. URL: <https://accelconf.web.cern.ch/ipac2013/papers/tupwo049.pdf>.
- [153] A. Wegscheider and R. Tomás. “Forced Coupling Resonance Driving Terms”. In: *Proceedings of the 12th International Particle Accelerator Conference (IPAC'21)* (Brazil). Vol. IPAC2021. JACoW Publishing, Geneva, Switzerland, 2021. ISBN: 978-3-95450-214-1. DOI: [10.18429/JACoW-IPAC2021-WEPAB400](https://doi.org/10.18429/JACoW-IPAC2021-WEPAB400).
- [154] R. Miyamoto. *Measurement of Coupling Resonance Driving Terms with the AC Dipole*. Tech. rep. Brookhaven National Laboratory, 2010. DOI: [10.2172/1013520](https://doi.org/10.2172/1013520).
- [155] A. Wegscheider and R. Tomás. “An N-BPM Momentum Reconstruction for Linear Transverse Coupling Measurements in LHC and HL-LHC”. In: *Proceedings of the 13th International Particle Accelerator Conference (IPAC'22)* (Bangkok, Thailand). Vol. IPAC2022. JACoW Publishing, Geneva, Switzerland, 2022. ISBN: 978-3-95450-227-1. DOI: [10.18429/JACoW-IPAC2022-MOPOTK032](https://doi.org/10.18429/JACoW-IPAC2022-MOPOTK032).

- [156] R. Tomás et al. “Review of Linear Optics Measurement and Correction for Charged Particle Accelerators”. In: *Phys. Rev. ST Accel. Beams* (May 2017). DOI: [10.1103/PhysRevAccelBeams.20.054801](https://doi.org/10.1103/PhysRevAccelBeams.20.054801).
- [157] M. Aiba et al. “First β -beating Measurement and Optics Analysis for the CERN Large Hadron Collider”. In: *Phys. Rev. ST Accel. Beams* (Aug. 2009). DOI: [10.1103/PhysRevSTAB.12.081002](https://doi.org/10.1103/PhysRevSTAB.12.081002).
- [158] R. Tomás et al. “Procedures and Accuracy Estimates for Beta-Beat Correction in the LHC”. In: *Proceedings of EPAC 2006* (Edinburgh, Scotland). JACoW Publishing, Geneva, Switzerland, 2006. URL: <https://accelconf.web.cern.ch/e06/PAPERS/WEPCH047.PDF>.
- [159] R. Miyamoto et al. “Measurement of Coupling Resonance Driving Terms in the LHC with AC Dipoles”. In: *Proceedings of the 2nd International Particle Accelerator Conference (IPAC'11)* (San Sebastián, Spain). Vol. IPAC2011. JACoW Publishing, Geneva, Switzerland, 2011. ISBN: 978-92-9083-366-6. URL: <https://accelconf.web.cern.ch/ipac2011/papers/wepc030.pdf>.
- [160] R. Calaga, R. Tomás, and A. Franchi. “Betatron Coupling: Merging Hamiltonian and Matrix Approaches”. In: *Phys. Rev. ST Accel. Beams* 8 (Mar. 2005). DOI: [10.1103/PhysRevSTAB.8.034001](https://doi.org/10.1103/PhysRevSTAB.8.034001).
- [161] E. H. Maclean et al. “First Measurement and Correction of Nonlinear Errors in the Experimental Insertions of the CERN Large Hadron Collider”. In: *Phys. Rev. ST Accel. Beams* 18 (Dec. 2015). DOI: [10.1103/PhysRevSTAB.18.121002](https://doi.org/10.1103/PhysRevSTAB.18.121002).
- [162] E. H. Maclean et al. “New Approach to LHC Optics Commissioning for the Nonlinear Era”. In: *Phys. Rev. ST Accel. Beams* 22 (June 2019). DOI: [10.1103/PhysRevAccelBeams.22.061004](https://doi.org/10.1103/PhysRevAccelBeams.22.061004).
- [163] T. Persson et al. “Chromatic Coupling Correction in the Large Hadron Collider”. In: *Phys. Rev. ST Accel. Beams* 16 (Aug. 2013). DOI: [10.1103/PhysRevSTAB.16.081003](https://doi.org/10.1103/PhysRevSTAB.16.081003).
- [164] R. Tomás, T. Persson, and E. H. Maclean. “Amplitude Dependent Closest Tune Approach”. In: *Phys. Rev. ST Accel. Beams* 19 (July 2016). DOI: [10.1103/PhysRevAccelBeams.19.071003](https://doi.org/10.1103/PhysRevAccelBeams.19.071003).
- [165] E. H. Maclean, T. Persson, and R. Tomás. “Amplitude Dependent Closest Tune Approach Generated by Normal and Skew Octupoles”. In: *Proceedings of the 8th International Particle Accelerator Conference (IPAC'17)* (Copenhagen, Denmark). JACoW Publishing, Geneva, Switzerland, May 2017. ISBN: 978-3-95450-182-3. DOI: [10.18429/JACoW-IPAC2017-WEPIK091](https://doi.org/10.18429/JACoW-IPAC2017-WEPIK091).
- [166] N. Biancacci and R. Tomás. “Using AC Dipoles to Localize Sources of Beam Coupling Impedance”. In: *Phys. Rev. ST Accel. Beams* (May 2016). DOI: [10.1103/PhysRevAccelBeams.19.054001](https://doi.org/10.1103/PhysRevAccelBeams.19.054001).
- [167] E. H. Maclean et al. *Demonstration of Coupling Correction Below the Per-Mil Limit in the LHC*. Tech. rep. Geneva: CERN, 2016. URL: <https://cds.cern.ch/record/2210530>.
- [168] K. Tian, J. Safranek, and Y. Yan. “Machine Based Optimization Using Genetic Algorithms in a Storage Ring”. In: *Phys. Rev. ST Accel. Beams* (Feb. 2014). DOI: [10.1103/PhysRevSTAB.17.020703](https://doi.org/10.1103/PhysRevSTAB.17.020703).

- [169] Y. Ohnishi et al. “Measurement of Chromatic X – Y Coupling”. In: *Phys. Rev. ST Accel. Beams* (Sept. 2009). DOI: [10.1103/PhysRevSTAB.12.091002](https://doi.org/10.1103/PhysRevSTAB.12.091002).
- [170] C. Michele et al. “Local Transverse Coupling Impedance Measurements in a Synchrotron Light Source from Turn-by-Turn Acquisitions”. In: *Phys. Rev. ST Accel. Beams* (Dec. 2016). DOI: [10.1103/PhysRevAccelBeams.19.121002](https://doi.org/10.1103/PhysRevAccelBeams.19.121002).
- [171] X. Shen et al. “Application of Independent Component Analysis to AC Dipole Based Optics Measurement and Correction at the Relativistic Heavy Ion Collider”. In: *Phys. Rev. ST Accel. Beams* (Nov. 2013). DOI: [10.1103/PhysRevSTAB.16.111001](https://doi.org/10.1103/PhysRevSTAB.16.111001).
- [172] ATLAS Collaboration. “Betatron Phase and Coupling Measurements at the Cornell Electron/Positron Storage Ring”. In: *Phys. Rev. ST Accel. Beams* (Sept. 2000). DOI: [10.1103/PhysRevSTAB.3.092801](https://doi.org/10.1103/PhysRevSTAB.3.092801).
- [173] W. Fischer. “Robust Linear Coupling Correction with N -Turn Maps”. In: *Phys. Rev. ST Accel. Beams* (June 2003). DOI: [10.1103/PhysRevSTAB.6.062801](https://doi.org/10.1103/PhysRevSTAB.6.062801).
- [174] A. Franchi. “Error Analysis of Linear Optics Measurements via Turn-by-Turn Beam Position Data in Circular Accelerators”. In: *arXiv* (2016). DOI: [10.48550/arxiv.1603.00281](https://doi.org/10.48550/arxiv.1603.00281).
- [175] R. Tomás et al. “Measurement of Global and Local Resonance Terms”. In: *Phys. Rev. ST Accel. Beams* 8 (Feb. 2005). DOI: [10.1103/PhysRevSTAB.8.024001](https://doi.org/10.1103/PhysRevSTAB.8.024001).
- [176] Y. Xi and H. Xiaobiao. “A Method for Simultaneous Linear Optics and Coupling Correction for Storage Rings with Turn-by-Turn Beam Position Monitor Data”. In: *Nuclear Instruments and Methods in Physics Research Section A: Accelerators, Spectrometers, Detectors and Associated Equipment* (2016). ISSN: 0168-9002. DOI: <https://doi.org/10.1016/j.nima.2016.05.020>.
- [177] H. Xiaobiao et al. “An Algorithm for Online Optimization of Accelerators”. In: *Nuclear Instruments and Methods in Physics Research Section A: Accelerators, Spectrometers, Detectors and Associated Equipment* (2013). ISSN: 0168-9002. DOI: <https://doi.org/10.1016/j.nima.2013.05.046>.
- [178] E. C. Raka. “Measurement of the Linear Coupling in the Brookhaven AGS”. In: *IEEE Transactions on Nuclear Science* (1975). DOI: [10.1109/tns.1975.4328033](https://doi.org/10.1109/tns.1975.4328033).
- [179] A. Franchi et al. “Vertical Emittance Reduction and Preservation in Electron Storage Rings via Resonance Driving Terms Correction”. In: *Phys. Rev. ST Accel. Beams* (Mar. 2011). DOI: [10.1103/PhysRevSTAB.14.034002](https://doi.org/10.1103/PhysRevSTAB.14.034002).
- [180] M. Aiba et al. “Ultra Low Vertical Emittance at SLS Through Systematic and Random Optimization”. In: *Nuclear Instruments and Methods in Physics Research Section A: Accelerators, Spectrometers, Detectors and Associated Equipment* (2012). ISSN: 0168-9002. DOI: <https://doi.org/10.1016/j.nima.2012.08.012>.
- [181] E. H. Maclean et al. “Effect of Linear Coupling on Nonlinear Observables at the LHC”. In: *Proceedings of the 8th International Particle Accelerator Conference (IPAC'17)* (Copenhagen, Denmark). JACoW Publishing, Geneva, Switzerland, May 2017. ISBN: 978-3-95450-182-3. DOI: [10.18429/JACoW-IPAC2017-WEPIK092](https://doi.org/10.18429/JACoW-IPAC2017-WEPIK092).

- [182] E. Métral, G. Hoffstaetter, and F. Willeke. “Destabilising Effect of Linear Coupling in the HERA Proton Ring”. In: *Proceedings of EPAC 2002* (Paris, France). JACoW Publishing, Geneva, Switzerland, 2002. URL: <https://accelconf.web.cern.ch/e02/PAPERS/WEPRI045.pdf>.
- [183] M. Hostettler et al. “Large Hadron Collider Optics Repository, 2022 Optics”. In: *GitLab repository* (2022). URL: <https://gitlab.cern.ch/acc-models/acc-models-lhc/-/tree/2022>.
- [184] T. Persson et al. “LHC Optics Corrections in Run 2”. In: *9th LHC Operations Evian Workshop*. 2019. URL: https://indico.cern.ch/event/751857/contributions/3259376/attachments/1781875/3033022/optics_corrections_run2.pdf.
- [185] J.M. Jowett et al. “The 2018 Heavy-Ion Run of the LHC”. In: *Proceedings of the 10th International Particle Accelerator Conference (IPAC’19)* (Melbourne, Australia). JACoW Publishing, Geneva, Switzerland, June 2019. ISBN: 978-3-95450-208-0. DOI: [10.18429/JACoW-IPAC2019-WEYYPLM2](https://doi.org/10.18429/JACoW-IPAC2019-WEYYPLM2).
- [186] M. Hofer and R. Tomás. “Effect of Local Linear Coupling on Linear and Nonlinear Observables in Circular Accelerators”. In: *Phys. Rev. ST Accel. Beams* 23 (2020). DOI: [10.1103/PhysRevAccelBeams.23.094001](https://doi.org/10.1103/PhysRevAccelBeams.23.094001).
- [187] OMC-Team. “omc3: Python 3 Codes for Beam Optics Measurements and Corrections in Circular Particle Accelerators”. In: *GitHub repository* (2020). DOI: [10.5281/zenodo.5705625](https://doi.org/10.5281/zenodo.5705625). URL: <https://github.com/pylhc/omc3>.
- [188] T. Persson et al. *MD4944: Local Linear Coupling Measurement at the IPs*. Tech. rep. Geneva: CERN, 2020. URL: <https://cds.cern.ch/record/2710101>.
- [189] S. Fartoukh et al. *First High-Intensity Beam Tests with Telescopic Flat Optics at the LHC*. Tech. rep. Geneva: CERN, 2019. URL: <https://cds.cern.ch/record/2687343>.
- [190] F. Soubelet. “pyrws, Python Package to Prepare Rigid Waist Shift Operations in the CCC”. In: *GitHub repository* (2022). DOI: [10.5281/zenodo.6517667](https://doi.org/10.5281/zenodo.6517667). URL: <https://github.com/fsoubelet/pyrws>.
- [191] R. Tomás. *Optimizing the global coupling knobs for the LHC*. Tech. rep. Geneva: CERN, 2012. URL: <https://cds.cern.ch/record/1422434>.
- [192] T. Persson. *Transverse Coupling, OMC-OP Worhsop*. 2019. URL: https://indico.cern.ch/event/828284/contributions/3467292/attachments/1921190/3178244/transverse_coupling_omc_op_v2.pdf.
- [193] T. Persson. *Stability of Linear Coupling in Run 2*. 2019. URL: https://indico.cern.ch/event/844692/contributions/3546747/attachments/1909102/3153959/coupling_stability.pdf.
- [194] A. Wegscheider et al. “Analytical N Beam Position Monitor Method”. In: *Phys. Rev. ST Accel. Beams* 20 (Nov. 2017). DOI: [10.1103/PhysRevAccelBeams.20.111002](https://doi.org/10.1103/PhysRevAccelBeams.20.111002).
- [195] A. Abada et al. “FCC-ee: The Lepton Collider”. In: *The European Physical Journal Special Topics* 228 (June 2019). DOI: [10.1140/epjst/e2019-900045-4](https://doi.org/10.1140/epjst/e2019-900045-4).

- [196] A. Morita et al. “Optics Corrections including IP Local Coupling at SuperKEKB”. In: *Proceedings of the 62nd ICFA ABDW on High Luminosity Circular e^+e^- Colliders (eeFACT’18)* (Hong Kong, China). JACoW Publishing, Geneva, Switzerland, Apr. 2019. ISBN: 978-3-95450-216-5. DOI: [10.18429/JACoW-eeFACT2018-TUOAB04](https://doi.org/10.18429/JACoW-eeFACT2018-TUOAB04).
- [197] F. Cerutti. *Triplet Luminosity Lifetime*. 2021. URL: <https://indico.cern.ch/event/1077835/contributions/4533356/attachments/2352134/4012821/Evian.pdf>.
- [198] S. Fartoukh. *Machine Configuration and Performance For the Rest of Run 3*. 2023. URL: <https://indico.cern.ch/event/1224987/>.
- [199] S. Kostoglou. *Impact on Luminosity Due to MQSX Loss*. 2023. URL: <https://indico.cern.ch/event/1255433/>.
- [200] F. Micolon et al. “Mechanical Consolidation of the LHC Inner Triplet Magnet Supporting System for Remote Alignment”. In: *Proceedings of the 12th International Particle Accelerator Conference (IPAC’21)* (Campinas, SP, Brazil). Vol. IPAC2021. JACoW Publishing, Geneva, Switzerland, 2021. ISBN: 978-3-95450-214-1. DOI: [10.18429/JACoW-IPAC2021-TUPAB308](https://doi.org/10.18429/JACoW-IPAC2021-TUPAB308).
- [201] H. Durand et al. “The Remote Positioning of the LHC Inner Triplet”. In: *Proceedings of the 10th International Workshop on Accelerator Alignment (IWAA’10)* (KEK, Tsukuba, Japan). Vol. IWAA10. 2008. URL: <https://www.slac.stanford.edu/econf/C0802113/papers/P018.pdf>.
- [202] C. Garion and S. Le Naour. *Roll Application on Q3 or Q2 to Compensate a MQSX Failure*. 2023. URL: <https://indico.cern.ch/event/1326841/>.
- [203] T. Persson. *Status of the Studies on Possible Mitigation in Case of MQSX Failure*. 2023. URL: <https://indico.cern.ch/event/1229356/>.
- [204] A. Edelen et al. “Machine Learning for Orders of Magnitude Speedup in Multiobjective Optimization of Particle Accelerator Systems”. In: *Phys. Rev. ST Accel. Beams* (Apr. 2020). DOI: [10.1103/PhysRevAccelBeams.23.044601](https://doi.org/10.1103/PhysRevAccelBeams.23.044601).
- [205] Y. Gao et al. “Bayesian Optimization Experiment for Trajectory Alignment at the Low Energy RHIC Electron Cooling System”. In: *Phys. Rev. ST Accel. Beams* (Jan. 2022). DOI: [10.1103/PhysRevAccelBeams.25.014601](https://doi.org/10.1103/PhysRevAccelBeams.25.014601).
- [206] A. Ivanov and I. Agapov. “Physics-Based Deep Neural Networks for Beam Dynamics in Charged Particle Accelerators”. In: *Phys. Rev. ST Accel. Beams* (July 2020). DOI: [10.1103/PhysRevAccelBeams.23.074601](https://doi.org/10.1103/PhysRevAccelBeams.23.074601).
- [207] R. Roussel et al. “Phase Space Reconstruction from Accelerator Beam Measurements Using Neural Networks and Differentiable Simulations”. In: *Phys. Rev. Lett.* (Apr. 2023). DOI: [10.1103/PhysRevLett.130.145001](https://doi.org/10.1103/PhysRevLett.130.145001).
- [208] M. Kranjčević et al. “Multiobjective Optimization of the Dynamic Aperture Using Surrogate Models Based on Artificial Neural Networks”. In: *Phys. Rev. ST Accel. Beams* 2021 (). DOI: [10.1103/PhysRevAccelBeams.24.014601](https://doi.org/10.1103/PhysRevAccelBeams.24.014601).
- [209] S. J alas et al. “Bayesian Optimization of a Laser-Plasma Accelerator”. In: *Phys. Rev. Lett.* 2021 (). DOI: [10.1103/PhysRevLett.126.104801](https://doi.org/10.1103/PhysRevLett.126.104801).

- [210] J. Duris et al. “Bayesian Optimization of a Free-Electron Laser”. In: *Phys. Rev. Lett.* 2020 (). DOI: [10.1103/PhysRevLett.124.124801](https://doi.org/10.1103/PhysRevLett.124.124801).
- [211] S. Biedron. “Adding Data Science and More Intelligence to Our Accelerator Toolbox”. en. In: *Proceedings of the 10th International Particle Accelerator Conference (IPAC'19)* (Melbourne, Australia). Vol. IPAC2019. JACoW Publishing, Geneva, Switzerland, 2019. ISBN: 978-3-95450-208-0. DOI: [10.18429/JACoW-IPAC2019-TUZPLM1](https://doi.org/10.18429/JACoW-IPAC2019-TUZPLM1).
- [212] A. Edelen et al. “Neural Networks for Modeling and Control of Particle Accelerators”. In: *IEEE Transactions on Nuclear Science* 63 (Apr. 2016). DOI: [10.1109/TNS.2016.2543203](https://doi.org/10.1109/TNS.2016.2543203).
- [213] C. Emma et al. “Machine Learning-Based Longitudinal Phase Space Prediction of Particle Accelerators”. In: *Phys. Rev. ST Accel. Beams* 2018 (). DOI: [10.1103/PhysRevAccelBeams.21.112802](https://doi.org/10.1103/PhysRevAccelBeams.21.112802).
- [214] X.Y. Xu, Y.B. Leng, and Y.M. Zhou. “Machine Learning Image Processing Technology Application in Bunch Longitudinal Phase Data Information Extraction”. en. In: *Proceedings of the 8th International Beam Instrumentation Conference (IBIC'19)* (Malmö, Sweden). Vol. IBIC2019. JACoW Publishing, Geneva, Switzerland, 2019. ISBN: 978-3-95450-204-2. DOI: [10.18429/JACoW-IBIC2019-WEPP021](https://doi.org/10.18429/JACoW-IBIC2019-WEPP021).
- [215] E. Fol, R. Tomás, and G. Franchetti. “Supervised Learning-Based Reconstruction of Magnet Errors in Circular Accelerators”. In: *The European Physical Journal Plus* (Apr. 2021). DOI: [10.1140/epjp/s13360-021-01348-5](https://doi.org/10.1140/epjp/s13360-021-01348-5).
- [216] E. Fol. “Application of Machine Learning in Beam Optics Measurements and Corrections”. Presented 2021. Goethe University Frankfurt, 2021. URL: <https://cds.cern.ch/record/2799999>.
- [217] T. Mitchell. *Machine Learning*. McGraw-Hill series in computer science. New York, NY: McGraw-Hill Professional, Mar. 1997. ISBN: 978-0070428072.
- [218] T. Hastie, J. Friedman, and R. Tibshirani. *The Elements of Statistical Learning*. Springer New York, 2001. DOI: [10.1007/978-0-387-21606-5](https://doi.org/10.1007/978-0-387-21606-5).
- [219] T. L. Lai and H. Robbins. “Strong Consistency of Least-Squares Estimates in Regression Models”. In: *Proceedings of the National Academy of Sciences* 74 (July 1977). DOI: [10.1073/pnas.74.7.2667](https://doi.org/10.1073/pnas.74.7.2667).
- [220] S. Shalev-Shwartz and S. Ben-David. *Understanding Machine Learning: From Theory to Algorithms*. Cambridge University Press, 2014. ISBN: 9781107298019. DOI: [10.1017/CB09781107298019](https://doi.org/10.1017/CB09781107298019).
- [221] F. Rosenblatt. “The perceptron: A probabilistic Model for Information Storage and Organization in the Brain”. In: *Psychological Review* 65 (1958). DOI: [10.1037/h0042519](https://doi.org/10.1037/h0042519).
- [222] C. M. Bishop. *Neural Networks for Pattern Recognition*. Oxford University Press, Inc., 1995. ISBN: 0198538642. URL: <https://people.sabanciuniv.edu/berrin/cs512/lectures/Book-Bishop-Neural%20Networks%20for%20Pattern%20Recognition.pdf>.

- [223] F. Pedregosa et al. “Scikit-learn: Machine Learning in Python”. In: *Journal of Machine Learning Research* 12 (2011).
- [224] F. Pedregosa et al. *Scikit-Learn Documentation, Underfitting vs. Overfitting*. 2022. URL: https://scikit-learn.org/stable/auto_examples/model_selection/plot_underfitting_overfitting.html.
- [225] R. Rifkin and R. Lippert. *Notes on Regularized Least-Squares*. Tech. rep. Computer Science and Artificial Intelligence Laboratory, 2007.
- [226] R. Tibshirani. “Regression Shrinkage and Selection Via the Lasso”. In: *Journal of the Royal Statistical Society: Series B (Methodological)* 58 (Jan. 1996). DOI: [10.1111/j.2517-6161.1996.tb02080.x](https://doi.org/10.1111/j.2517-6161.1996.tb02080.x).
- [227] E. Fol et al. “Machine Learning Methods for Optics Measurements and Corrections at LHC”. In: *Proceedings of the 9th International Particle Accelerator Conference (IPAC’18)* (Vancouver, BC, Canada). JACoW Publishing, Geneva, Switzerland, 2018. ISBN: 978-3-95450-184-7. DOI: [10.18429/JACoW-IPAC2018-WEPAF062](https://doi.org/10.18429/JACoW-IPAC2018-WEPAF062).
- [228] E. Bozoki and A. Friedman. “Neural Networks and Orbit Control in Accelerators”. In: *Proceedings of EPAC 1994* (London, United Kingdom). JACoW Publishing, Geneva, Switzerland, 1994. URL: https://accelconf.web.cern.ch/e94/PDF/EPAC1994_1589.PDF.
- [229] E. Meier, G. LeBlanc, and Y. E. Tan. “Orbit Correction Studies using Neural Networks”. In: *Proceedings of the 3rd International Particle Accelerator Conference (IPAC’12)* (New Orleans, LA, USA). Vol. IPAC2012. JACoW Publishing, Geneva, Switzerland, 2012. ISBN: 978-3-95450-115-1. URL: <https://jacow.org/IPAC2012/papers/WEPPP057.pdf>.
- [230] Y. Kijima et al. “A Beam Diagnostic System for Accelerator using Neural Networks”. In: *Proceedings of EPAC 1992* (Berlin, Germany). JACoW Publishing, Geneva, Switzerland, 1992. ISBN: 9782863321140. URL: https://accelconf.web.cern.ch/e92/PDF/EPAC1992_1155.PDF.
- [231] L. Breiman et al. *Classification And Regression Trees*. Routledge, Oct. 2017. DOI: [10.1201/9781315139470](https://doi.org/10.1201/9781315139470).
- [232] L. Breiman. “Random Forests”. In: *Machine Learning* 45 (2001). DOI: [10.1023/a:1010933404324](https://doi.org/10.1023/a:1010933404324).
- [233] A. Aurisano et al. “A Convolutional Neural Network Neutrino Event Classifier”. In: *Journal of Instrumentation* 11 (Sept. 2016). DOI: [10.1088/1748-0221/11/09/p09001](https://doi.org/10.1088/1748-0221/11/09/p09001).
- [234] E. Fol et al. “Optics Corrections Using Machine Learning in the LHC”. en. In: *Proceedings of the 10th International Particle Accelerator Conference (IPAC’19)* (Melbourne, Australia). Vol. IPAC2019. JACoW Publishing, Geneva, Switzerland, 2019. ISBN: 978-3-95450-208-0. DOI: [10.18429/JACoW-IPAC2019-THPRB077](https://doi.org/10.18429/JACoW-IPAC2019-THPRB077).
- [235] E. Fol and R. Tomás. “Denoising of Optics Measurements Using Autoencoder Neural Networks”. en. In: *Proceedings of the 12th International Particle Accelerator Conference (IPAC’21)* (Brazil). Vol. IPAC2021. JACoW Publishing, Geneva, Switzerland, 2021. ISBN: 978-3-95450-214-1. DOI: [10.18429/JACoW-IPAC2021-THPAB068](https://doi.org/10.18429/JACoW-IPAC2021-THPAB068).

- [236] CERN. *Equipment Codes Main Systems*. 2023. URL: <https://edms5.cern.ch/pls/cedar/codes.systems>.
- [237] I. Karpov, T. Argyropoulos, and E. Shaposhnikova. “Thresholds for Loss of Landau Damping in Longitudinal Plane”. In: *Phys. Rev. ST Accel. Beams* (Jan. 2021). DOI: [10.1103/PhysRevAccelBeams.24.011002](https://doi.org/10.1103/PhysRevAccelBeams.24.011002).
- [238] J. Bengtsson and J. Irwin. “Analytical Calculations of Smear and Tune Shift”. In: *Report No. SSC-232* (Feb. 1990). URL: <https://www.osti.gov/servlets/purl/6876278>.
- [239] S. White, Maclean E, and R. Tomás. “Direct Amplitude Detuning Measurement with AC Dipole”. In: *Phys. Rev. ST Accel. Beams* 16 (July 2013). DOI: [10.1103/PhysRevSTAB.16.071002](https://doi.org/10.1103/PhysRevSTAB.16.071002).
- [240] T. Persson, R. Tomás, and E. H. Maclean. “Suppression of Amplitude Dependent Closest Tune Approach and its Behavior Under Forced Oscillations”. In: *Phys. Rev. ST Accel. Beams* (May 2019). DOI: [10.1103/PhysRevAccelBeams.22.051001](https://doi.org/10.1103/PhysRevAccelBeams.22.051001).
- [241] R. Saban. *Equipment Naming Conventions*. 2006. URL: <https://twiki.cern.ch/twiki/pub/FlukaTeam/FlukaLHCSVNRepositories/LHC-PM-QA-204-32-00.pdf>.
- [242] D. Jacquet et al. “LSA - The High Level Application Software of the LHC and its Performance During the First 3 Years of Operation”. In: *Proceedings of ICALEPCS2013* (San Francisco, CA, USA). Vol. ICALEPCS2013. JACoW Publishing, Geneva, Switzerland, 2013. ISBN: 978-3-95450-139-7. URL: <https://accelconf.web.cern.ch/ICALEPCS2013/papers/thppc058.pdf>.
- [243] OMC-Team et al. “PyLHC-Submitter”. In: *GitHub repository* (2020). DOI: [10.5281/zenodo.4818454](https://doi.org/10.5281/zenodo.4818454). URL: <https://github.com/pylhc/submitter>.
- [244] D. Thain, T. Tannenbaum, and M. Livny. “Distributed Computing in Practice: the Condor Experience”. In: *Concurrency - Practice and Experience* 17 (2005). URL: <https://chtc.cs.wisc.edu/doc/condor-practice.pdf>.
- [245] *OMC Website*. URL: <https://pylhc.github.io/>.
- [246] F. Soubelet. “PyHDTToolkit, An all-in-one package for Python work in my PhD”. In: *GitHub repository* (2020). DOI: [10.5281/zenodo.4268804](https://doi.org/10.5281/zenodo.4268804). URL: <https://fsoubelet.github.io/PyHDTToolkit/>.
- [247] T. Gläkle et al. *cpymad*. 2021. DOI: [10.5281/zenodo.4724857](https://doi.org/10.5281/zenodo.4724857). URL: <https://github.com/hibtc/cpymad>.
- [248] F. Soubelet. “cpymadtools, Lightweight Pythonic Wrapper Around cpymad”. In: *GitHub repository* (2022). DOI: [10.5281/zenodo.7339939](https://doi.org/10.5281/zenodo.7339939). URL: <https://beamoptyicsanalysis.github.io/cpymadtools/>.
- [249] OMC-Team et al. “PyLHC: Additional Tools for Particle Accelerator Data Analysis and Machine Information”. In: *GitHub repository* (2020). DOI: [10.5281/zenodo.5643602](https://doi.org/10.5281/zenodo.5643602). URL: <https://github.com/pylhc/PyLHC>.
- [250] OMC-Team et al. “TFS-Pandas: A Pandas-based TFS File Handler”. In: *GitHub repository* (2020). DOI: [10.5281/zenodo.5070986](https://doi.org/10.5281/zenodo.5070986). URL: <https://github.com/pylhc/tfs>.

-
- [251] OMC-Team et al. “Turn-by-Turn”. In: *GitHub repository* (2020). DOI: [10.5281/zenodo.5554916](https://doi.org/10.5281/zenodo.5554916).. URL: https://github.com/pylhc/turn_by_turn.